

Scanning Tunneling Spectroscopy Studies of High-Temperature Cuprate Superconductors

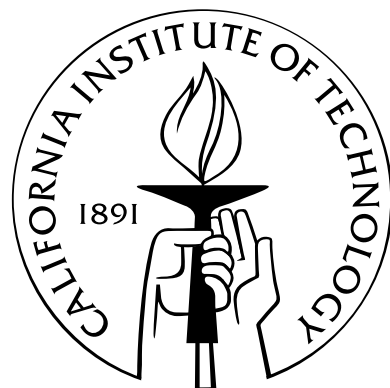
Thesis by

Ching-Tzu Chen

In Partial Fulfillment of the Requirements

for the Degree of

Doctor of Philosophy



California Institute of Technology

Pasadena, California

2006

(Defended May 19, 2006)

© 2006

Ching-Tzu Chen

All Rights Reserved

*To my parents
for their unconditional love and support*

Acknowledgements

This thesis would not have been completed without the help of many individuals. First of all, I would like to thank my advisor Professor Nai-Chang Yeh, for her guidance of my adventure into the vast high-temperature superconductivity field, for the enlightening discussions, her constant encouragement, and incomparable optimism despite frequent setbacks with instrumentation and fundings. Nai-Chang is unique in her comprehension and implementation of the theory that complements her experimentalist's intuition. Therefore, she has supported both the theoretical and experimental aspects of the thesis project, which makes this Ph.D. experience exceptional.

In the lab, I have been very fortunate to have "The Magician" Nils as a colleague and, more importantly, a great friend. Not only that the scanning tunneling microscope built for this thesis research would not have been realized without his expertise in the arts of machining, but also that I would not have learned so much more about life beyond physics. I am also thankful to Ted, for the interesting exchange of ideas, information and knowledge in science and culture; to Andy, for introducing me to both the techniques of cryogenic experiments and the American lifestyle outside the lab; to Andrew, for the fruitful collaboration I enjoyed during our endeavor into the phenomenological theory and for his great help with the experiments; to Cameron, for feeding me well with all sorts of homemade pastries and for sharing his passion toward the arts of cooking; to Slobodan and Marcus, for the witty discussions that show their terrific sense of dark humor; and to every Yeh group member for the friendship and support.

Aside from research, my life has been tremendously enriched by the numerous interesting friends whom I met in the States. Special thanks to Shing-Lin, for patiently listening to my (often immature) whining, providing to-the-point advice, and sharing her experience, wisdom, and philosophy; to

James, for his generosity and help in setting up the prototype interferometer; to Shao-Ching, for reaching out and helping me through the first two years at Caltech; to Hsin-Ying, for sharing the enthusiasm in physics; and to Hwa-Jen and Ivy, for all the fun discussions and the refreshing perspective on sociology and music.

Finally, I'd like to express my deepest gratitude to my parents, for their unconditional love and for letting me explore my interests and capability freely; to my best friend Yuan-Yu, for his companionship through the darkest period of my life; and to Pei-Ying, who can always bring a smile to my face.

Abstract

This thesis presents the scanning tunneling spectroscopic studies of the non-universal electronic properties among electron- and hole-doped cuprates. Tunneling spectra of the electron-doped $\text{Sr}_{0.9}\text{La}_{0.1}\text{CuO}_2$ and the hole-doped $\text{YBa}_2\text{Cu}_3\text{O}_{6+\delta}$ reveal distinctly different behavior in the pairing symmetries, pseudogap phenomena, satellite features, and low-energy excitations. While underdoped and optimally doped $\text{YBa}_2\text{Cu}_3\text{O}_{6+\delta}$ exhibits *d*-wave and overdoped Ca-doped $\text{YBa}_2\text{Cu}_3\text{O}_{6+\delta}$ (*d+s*)-wave pairing symmetry, the electron-doped $\text{Sr}_{0.9}\text{La}_{0.1}\text{CuO}_2$ shows fully gapped *s*-wave pairing symmetry. The absence of the satellite features and pseudogap in tunneling spectra of electron-doped cuprates sharply contrasts with their general presence in hole-doped cuprates. Furthermore, the subgap low-energy spectral characteristics of $\text{Sr}_{0.9}\text{La}_{0.1}\text{CuO}_2$ deviate substantially from the mean-field Bardeen-Cooper-Schrieffer theory, while those of $\text{YBa}_2\text{Cu}_3\text{O}_{6+\delta}$ can be fully accounted for by the mean-field generalized Blonder-Tinkham-Klapwijk formalism.

Despite the aforementioned disparities, several experimental results reveal important connections between the two types of cuprates. For instance, the coexistence of the pseudogap and superconducting spectra in hole-doped cuprates and the observations of the current- and field-induced pseudogap in electron-doped cuprates suggest that competing orders, manifested as the pseudogap, coexist with superconductivity in both types of cuprates. In addition, by comparing the tunneling spectra with the high-field vortex dynamics measurements, we find that the quasiparticle spectral characteristics of $\text{Sr}_{0.9}\text{La}_{0.1}\text{CuO}_2$ and $\text{YBa}_2\text{Cu}_3\text{O}_{6+\delta}$ correlate with the degree of field-induced quantum phase fluctuations of the two compounds.

Based on these findings, we propose a simple model of coexisting density waves with superconductivity to unify the apparent non-universal phenomena among cuprate superconductors. By

incorporating quantum phase fluctuations and adopting realistic band structures, numerical simulations of the quasiparticle tunneling spectra demonstrate excess subgap low-energy excitations, which is consistent with the empirical observations in $\text{Sr}_{0.9}\text{La}_{0.1}\text{CuO}_2$. Furthermore, by tuning the ratio of the density waves to superconductivity, the theoretical calculations reproduce the absence of pseudogap phenomena in electron-doped cuprates and the general presence of the pseudogap in hole-doped cuprates. Thereby, we conclude that the competing orders that coexist with superconductivity in cuprate superconductors contribute to the rich cuprate phenomenology.

Contents

Acknowledgements	iv
Abstract	vi
1 Introduction	1
1.1 Crystalline structures and electronic phase diagram of high-temperature superconductors	1
1.1.1 Crystalline and electronic structures of parent compounds	1
1.1.2 Electronic phase diagrams	3
1.1.3 Effective single-band Hubbard model and $t - J$ model	6
1.2 Electron-doped vs. hole-doped cuprates: review of current experimental and theoretical status	9
1.2.1 Pairing symmetry	9
1.2.2 Pseudogap	11
1.2.3 Orders in cuprate superconductors	15
1.3 Overview of the thesis	18
2 Physics of Tunneling Spectroscopy	21
2.1 Tunneling Hamiltonian	21
2.1.1 Normal-insulator-superconductor tunneling	26
2.2 Pairing symmetry and tunneling spectra: generalized Blonder-Tinkham-Klapwijk (BTK) model	30

2.2.1	Generalized Blonder-Tinkham-Klapwijk formalism—A mean-field description	32
2.2.2	Tunneling spectra of a <i>d</i> -wave superconductor and the Andreev bound state .	36
3	Scanning Tunneling Microscopy: Principle and Instrumentation	43
3.1	Brief review	44
3.2	Instrumentation of a cryogenic STM	46
3.2.1	STM head	47
3.2.2	STM electronics	50
3.2.3	Cryogenic probe and dewar	53
3.2.4	Noise reduction	56
3.3	Comparison with other experimental techniques	60
3.3.1	Tunneling spectroscopy	60
3.3.2	Angle-resolved photoemission spectroscopy	63
3.3.3	Neutron scattering	65
4	Tunneling Spectra of Hole-Doped $\text{YBa}_2\text{Cu}_3\text{O}_{6+\delta}$	67
4.1	Introduction	67
4.2	Sample preparation	70
4.3	Results of directional tunneling spectroscopy	71
4.3.1	Doping dependence of the pairing symmetry and pairing potential	71
4.3.2	Impurity effect	77
4.4	Discussion	78
4.4.1	Pairing symmetry	78
4.4.2	Spatial spectral homogeneity, pseudogap, and competing orders	81
4.4.3	Satellite features	85
4.4.4	Quantum impurities	86
4.5	Summary	87

5 Tunneling Spectra of Electron-Doped $\text{Sr}_{1-x}\text{La}_x\text{CuO}_2$	88
5.1 Introduction	88
5.2 Crystalline structure and sample preparation	91
5.3 Results of scanning tunneling spectroscopy	92
5.3.1 Pairing symmetry and pairing potential of pure $\text{Sr}_{1-x}\text{La}_x\text{CuO}_2$	94
5.3.2 Spectral characteristics of pure $\text{Sr}_{1-x}\text{La}_x\text{CuO}_2$	96
5.3.3 Tunneling spectra of Zn- and Ni-doped $\text{Sr}_{1-x}\text{La}_x\text{CuO}_2$	98
5.4 Discussion	102
5.4.1 Pairing symmetry	102
5.4.2 Impurity substitution and pairing symmetry	103
5.4.3 Satellite features, pseudogap phenomena, and competing orders	105
5.4.4 Low-energy excitations, quantum fluctuations, and quantum criticality	108
5.5 Summary	110
6 Competing Orders, Quantum Phase Fluctuations, and Quasiparticle Tunneling Spectra	111
6.1 Introduction	111
6.2 Competing orders and quantum phase fluctuations on low-energy excitations	113
6.2.1 Formalism	114
6.2.2 Numerical results	117
6.2.3 Summary	122
6.3 Collective modes and quasiparticle interference on the local density of states of cuprate superconductors	123
6.3.1 Model	123
6.3.2 Numerical results	127
6.3.3 Summary	131
6.4 Conclusion	131

Conclusion	134
Appendices	135
A Blonder-Tinkham-Klapwijk Formalism	136
B Tip Preparation, Piezo Calibration, and Thermal Drifting	141
B.1 Tip preparation	141
B.2 Piezo calibration and HOPG images	142
B.3 Thermal drifting calibration and gold images	143
C Modeling the STS data in the presence of impurities	146

List of Figures

1.1	Crystalline structures of three representative cuprates	2
1.2	The zero-field temperature (T) vs. doping (x) phase diagram	4
1.3	Schematic diagram of a single CuO ₄ cluster	7
1.4	Order parameter of d and $(d + s)$ -pairing symmetry	10
1.5	Nernst region and the pseudogap phase	12
2.1	Schematic diagram of scattering processes at the N-I-S interface	34
2.2	Momentum dependence of a d -wave pairing potential	36
2.3	Simulated tunneling spectra of a d -wave superconductor	37
2.4	Trajectories of the Andreev bound states	38
2.5	Tunneling spectra along the {110}-axis for various pairing symmetries	39
2.6	Tunneling spectra along the c -axis for various pairing symmetries	40
3.1	Schematic diagram of an STM system	45
3.2	Schematic diagram of STM coarse movement control	46
3.3	Schematic diagram of the STM head	48
3.4	Principle of the coarse approach mechanism	49
3.5	Schematic diagram of the STM feedback controller	51
3.6	Schematic diagram of the sequential triggering circuit	52
3.7	Schematic diagram of the STM cryogenic probe	54
3.8	Transmitted vibrational noise spectra	57
3.9	Low-frequency acoustic noise spectra	58

3.10	Transmission of the cryogenic microwave powder filter.	59
4.1	The generic phase diagram of the hole-doped cuprate superconductors	68
4.2	Spatially resolved (dI_{NS}/dV) vs. V spectra of YBCO	72
4.3	Normalized (dI_{NS}/dV) vs. V spectra of YBCO	73
4.4	Normalized tunneling spectra of YBCO and BTK fitting curves	74
4.5	Representative c -axis tunneling spectra of YBCO	75
4.6	Normalized c -axis tunneling spectra of impurity-doped YBCO	77
4.7	YBCO c -axis tunneling spectra near a non-magnetic impurity	78
4.8	Numerical simulation of {110} tunneling spectra for various pairing symmetries	79
4.9	Doping dependence of the spectral gap Δ_d and $2\Delta_d/k_B T_c$ ratio in YBCO	83
5.1	Comparison of the crystalline structures	92
5.2	Representative surface topography of pure SLCO	93
5.3	Representative quasiparticle tunneling spectra of SLCO	95
5.4	Temperature dependence of the spectral gap in SLCO	97
5.5	Current dependence of tunneling spectra in SLCO	97
5.6	Tunneling spectra of Zn-SLCO	99
5.7	Tunneling spectra of Ni-SLCO	100
5.8	The spatial evolution of the spectral difference	101
5.9	Tunneling spectra of anisotropic s -wave pairing	102
5.10	Magnetic susceptibility data of pure and impurity doped SLCO	104
5.11	Current-induced pseudogap in SLCO	107
5.12	Vortex phase diagram of SLCO	108
5.13	Field-induced quantum phase transition	109
6.1	Ring diagram and Dyson's equation	116
6.2	Calculated quasiparticle DOS: s -wave electron-doped cuprates	118
6.3	Spectral evolution with V/Δ for s -wave superconductors	120

6.4	Calculated quasiparticle DOS: <i>d</i> -wave hole-doped cuprates	121
6.5	Model of the pinned density waves	124
6.6	Calculated energy-dependent FT-LDOS: non-magnetic impurities	128
6.7	Evolution of the relative intensities of FT-LDOS with energy	129
6.8	Calculated energy-dependent FT-LDOS: pinned SDW	130
6.9	Calculated real space LDOS modulations	131
6.10	Calculated temperature-dependent FT-LDOS	132
A.1	Schematic diagram of energy vs. momentum at N-S interface	138
A.2	Differential tunneling conductance vs. bias voltage for various barrier heights	140
B.1	SEM images of STM tips	142
B.2	STM topographic images of highly ordered pyrolytic graphite	142
B.3	The temperature dependence of the piezo coefficient	143
B.4	Comparison of STM images before and after tip re-approach	144
B.5	STM topographic images of gold at various temperatures	145

Chapter 1

Introduction

Twenty years have passed since the discovery of the first copper-oxide high-temperature superconductor $\text{La}_{2-x}\text{Ba}_x\text{CuO}_4$ in 1986, and the intriguing physics of cuprate superconductors continues to fascinate scientists. Coherent comprehension of the underlying mechanism remains elusive. Nevertheless, a number of superconducting and normal-state properties are now understood in great detail from the comparison of experimental findings to theoretical analyses of simple models. In this chapter, we review the basic properties of the cuprate superconductors, survey the current experimental and theoretical progress, and conclude with a brief outline of the thesis.

1.1 Crystalline structures and electronic phase diagram of high-temperature superconductors

1.1.1 Crystalline and electronic structures of parent compounds

Cuprate superconductors are generally referred to as doped Mott insulators. To understand the origin of this terminology, we begin with an investigation of the cuprate crystalline and electronic structures. All high T_c superconductors share the following two elements: the CuO_2 planes that form single-layer or multilayer conducting blocks per unit cell, and the “charge reservoirs” in between the CuO_2 planes that are responsible for contributing either electrons or holes to the CuO_2 planes. In Fig. 1.1, three representative cuprate superconductors, the one-layer hole-doped $\text{La}_{2-x}\text{Sr}_x\text{CuO}_4$ (LSCO), the one-layer electron-doped $\text{Nd}_{2-x}\text{Ce}_x\text{CuO}_{4\pm\delta}$ (NCCO), and the infinite-

layer $\text{Sr}_{1-x}\text{La}_x\text{CuO}_2$ (SLCO), are illustrated as examples. It is understood that the electronic states of the CuO_2 planes control the physics of high T_c superconductivity. By doping with substitution elements or by changing the oxygen content (as in $\text{YBa}_2\text{Cu}_3\text{O}_{6+\delta}$) in the charge reservoirs, the carrier density in the CuO_2 planes can be controlled.

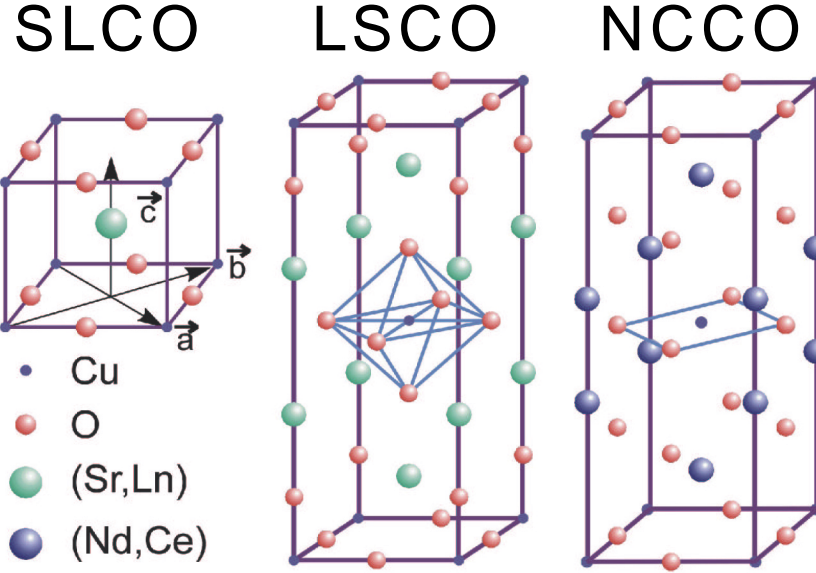


Figure 1.1: Crystalline structures of representative hole-doped and electron-doped cuprates: electron-doped $\text{Sr}_{1-x}\text{La}_x\text{CuO}_2$ (SLCO), hole-doped $\text{La}_{2-x}\text{Sr}_x\text{CuO}_4$ (LSCO), and electron-doped $\text{Nd}_{2-x}\text{Ce}_x\text{CuO}_{4\pm\delta}$ (NCCO). We note the absence of apical oxygen in all electron-doped cuprates, in contrast to the presence of CuO_6 octahedron in hole-doped cuprates. Furthermore the infinite-layer system differs from all others in that no excess charge reservoir exists between consecutive CuO_2 planes.

In the undoped parent compound, the electronic states of the Cu on the plane are in the d^9 configuration. The presence of oxygen octahedron sounding the central Cu ion and the associated Jahn-Teller distortion split the degenerate e_g orbitals of Cu d^9 with the resulting highest partially occupied orbital being $d_{x^2-y^2}$. The Cu $d_{x^2-y^2}$ -orbital and the doubly occupied O p_x , p_y -orbitals form a strong covalent bonding. In the absence of interaction among electrons, the hybridization of these three orbitals gives rise to the bonding, non-bonding and half-filled anti-bonding bands and predicts a good metal, in sharp contrast to the large charge gap observed in the undoped compounds.

The failure of the band theory, and hence that of the conventional Fermi liquid approach to high T_c problems, stems from the existence of a large on-site Coulomb interaction that well exceeds the bandwidth of the tight-binding anti-bonding band. If a charge carrier were to hop onto a partially

filled Cu $d_{x^2-y^2}$ orbital, the two Cu $d_{x^2-y^2}$ carriers would experience a large energy penalty, and, hence, it is energetically more favorable to localize the electrons. Electronic systems with half-filled states and strong localizations are known as Mott insulators. Specifically, the strong on-site Coulomb repulsion suppresses charge fluctuations, splits the half-filled anti-bonding band into an empty upper-Hubbard band and a filled lower-Hubbard band, thereby turning a band metal into a Mott insulator with an optical gap of a few eV.

More precisely, in the cuprate systems, the energy penalty of having a second hole in the Cu d -orbital is much larger than the energy separation between the Cu $d_{x^2-y^2}$ and O p -orbitals. Thus, the extra hole primarily goes to the O p_x , p_y orbitals, and the energy cost ($E_p - E_d$), of the order of ~ 2 eV, is named the charge transfer gap. Because the hybridization integral, t_{dp} , is much smaller than the energy barrier ($E_p - E_d$), the electrons in the undoped compounds form localized moments on the Cu sites. These spins are anti-ferromagnetically aligned via the super-exchange interaction that involves virtual hopping to the neighboring O p -orbitals. As a result, the parent compounds of high T_c materials are referred to as anti-ferromagnetic Mott insulators.

1.1.2 Electronic phase diagrams

When charge carriers are introduced to the CuO₂ planes, several novel phases appear as exemplified in Fig. 1.2. This section provides an overview of the electronic phase diagrams of cuprates and summarizes the most important phenomena shared among all cuprate superconductors. We remark that the physics of cuprate superconductors is extremely rich, and therefore a simplified phase diagram such as that shown in Fig. 1.2 cannot capture many interesting details that take place in different cuprate systems. Since the physics behind these non-universal phenomena is the main theme of the thesis, we shall discuss these issues in more detail later in this chapter [§1.2].

As mentioned in the previous section, at zero doping, the electronic state of the parent compound is an anti-ferromagnetic Mott insulating state for both the n-type (electron-doped) and the p-type (hole-doped) cuprates. Chronologically, soon after the discovery of La₂CuO₄, long-range Néel spin ordering in this system was experimentally determined [1]. Strictly speaking however,

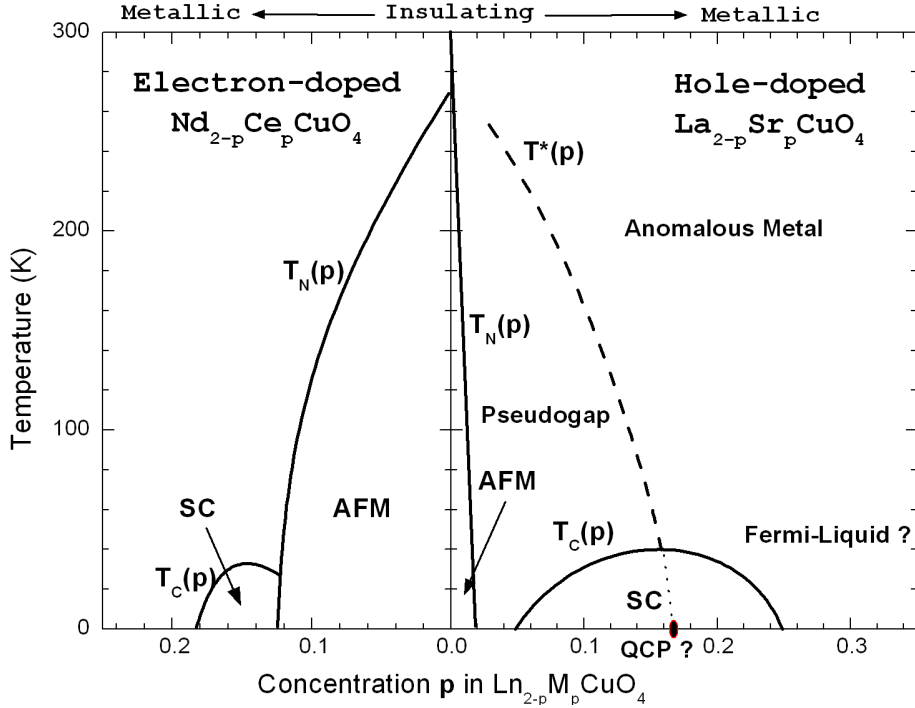


Figure 1.2: The zero-field temperature (T) vs. doping (x) phase diagram of representative electron-doped (n-type) and hole-doped (p-type) cuprate superconductors. AFM: long-range commensurate anti-ferromagnetic order. SC: superconducting state. PG: pseudogap region. FL: Fermi liquid. T_N , T_c , and T^* are respectively the Néel temperature, the superconducting transition temperature, and pseudogap temperature.

the Hohenberg-Mermin-Wagner theorem asserts that an ideal two-dimensional (2D) magnetic system with isotropic anti-ferromagnetic Heisenberg couplings would remain magnetically disordered at finite temperature. The finding of long-range anti-ferromagnetic ordering in real systems can be reconciled with theory by relaxing the strict 2D picture and incorporating three-dimensional (3D) anisotropic effects. The anisotropic effects in cuprate can arise through many different ways. For instance, in addition to the dominant 2D Heisenberg term, there are small interlayer coupling, Dzyaloshinski-Moriya (DM) anisotropic coupling and easy-plane (x - y) anisotropic coupling terms in the real and spin space Hamiltonian [2]. In orthorhombic systems, such as La_2CuO_4 , DM and interlayer anisotropies stabilize the 3D long-range anti-ferromagnetic phase [3, 4]. In tetragonal systems, such as Nd_2CuO_4 , where the former two anisotropies are absent, x - y anisotropy results in a crossover from the 2D Heisenberg behavior to the 2D XY regime, followed by a crossover to the 3D XY regime, and hence stabilizes the long-range Néel order [5, 4].

As holes are introduced to the CuO₂ planes, the Néel temperature of the system decreases rapidly upon doping and the commensurate anti-ferromagnetic (AFM) long-range order disappears completely at around $p \sim 0.02$, where p is the number of doped holes per Cu. Above this doping level, various types of spin fluctuations replace the original commensurate AFM order and continue to survive in the superconducting phase. In La_{2-x}Sr_xCuO₄ ($x = p$ for the one-layer systems), static incommensurate spin fluctuations develop beyond the Néel state and persist in the superconducting state, while in other compounds, such as YBa₂Cu₃O_{6+δ}, commensurate magnetic resonance modes and significant dynamic spin fluctuations coexist with superconductivity in the underdoped and optimally doped region.

When hole-doping is further increased, superconductivity sets in at $p \sim 0.05$ and lasts up to $p \sim 0.25$. There is general consensus that the pairing symmetry of the superconducting order parameter of hole-doped cuprates is predominantly $d_{x^2-y^2}$ -like in the underdoped and optimally doped¹ region [6, 7]. In the heavily overdoped limit, on the other hand, a significant s -wave component in addition to the $d_{x^2-y^2}$ component has been revealed [8] [§1.2.1].

In the normal state of the underdoped cuprates, various phenomena associated with a partially suppressed density of states around the Fermi level and an opening of the spectral gap in the spin and charge fluctuations have been observed [9]. This state is termed as the pseudogap phase [§1.2.2]. Near the optimal doping, the pseudogap phase crosses over to an anomalous non-Fermi-liquid region where quantum critical scaling behavior in the spin and charge density fluctuations is suggested [10, 11]. As we further increase the doping to the overdoped range, conventional Fermi-liquid physics is eventually recovered.

On the electron-doping side, despite an overall similarity, we notice that the AFM state exists over a wider doping range and the superconducting region is much narrower in comparison with that of the hole-doped cuprates. An intuitive way to visualize the robustness of the AFM order in the electron-doping phase diagram is the spin-dilution picture. While the hole doping introduces carriers to the O p -orbitals, the electron doping takes place in the Cu d -orbital. The resulting mobile spinless

¹The optimal doping $p_0 \approx 0.16$ is defined as the doping concentration with the highest transition temperature $T_c(p_0)$. Underdoping refers to the doping level where $p < p_0$, and overdoping refers to $p > p_0$.

Cu $3d^{10}$ configuration dilutes the background anti-ferromagnetic coupling and leads to a gradual reduction of the Néel temperature [12]. The suppression of T_N is comparable to that observed in the Zn-doped La_2CuO_4 [13, 14] where the doped Zn with a localized $3d^{10}$ configuration dilutes the AFM order of the Cu spins. In contrast, the doped holes in the O orbitals induce ferromagnetic coupling between adjacent Cu spins, strongly frustrating the anti-ferromagnetic background [15]. Therefore, the Néel temperature drops rapidly with increasing hole doping, and the resulting AFM phase is much narrower in the hole-doped cuprates.

In the normal state of the n-type cuprates, no discernible zero-field low-energy pseudogap is observed by the tunneling and photoemission spectroscopy measurements, although, upon the application of a large magnetic field that fully suppresses superconductivity, a partial tunneling gap is again detected [16, 17, 18] [§1.2.2]. Besides, the electronic properties of the normal state measured by the transport and zero-field tunneling experiments are more conventional, similar to what the Fermi-liquid region in the overdoped p-type cuprates exhibits.

1.1.3 Effective single-band Hubbard model and $t - J$ model

The electronic states responsible for the essential physics in cuprate superconductors are the Cu $d_{x^2-y^2}$ orbital and the O p_x, p_y orbitals. Therefore, to understand the generic features of the cuprate phase diagram, a sensible starting point may be a three-band Hubbard model [19], which includes both the Cu and O orbitals. However, there is strong evidence that the single-band Hubbard model suffices to account for many important aspects of cuprate physics [20], even though it is not apparent why one could safely ignore the oxygen orbitals when constructing a low-energy Hamiltonian. This issue was addressed by the insight of Zhang and Rice [21], which brings forward the importance of the singlet formation between the doped O hole and the Cu hole originally residing at the half-filled central Cu^{2+} ions [Fig. 1.3]. It is by considering the low-energy theory of the singlet motion in the CuO_2 planes that we arrive at an effective single-band model proposed by Anderson [20].

In the hole-doped cuprates, the primary driving force of the singlet formation is the reduction in kinetic energy from phase coherence and from Cu – O hybridization. According to the second-

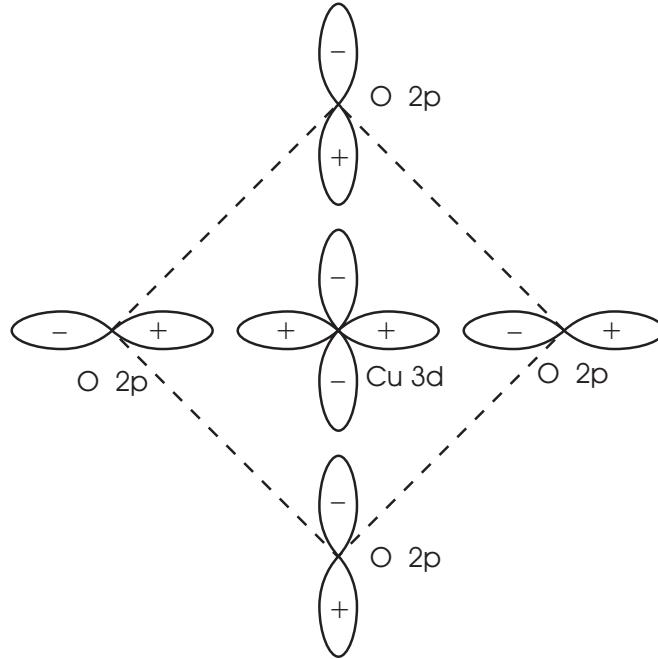


Figure 1.3: Schematic diagram of a single CuO₄ cluster and the hybridization of the Cu 3d⁹ hole with the surrounding O 2p hole states.

order perturbation calculation [21], to maximize the energy gain, a doped hole first spreads out as a symmetric coherent superposition of the four O 2p hole states surrounding the Cu²⁺ ion and then hybridizes with the central Cu $d_{x^2-y^2}$ hole to form a Zhang-Rice singlet [Fig. 1.3]. Since the symmetric O hole states localized at different CuO₄ clusters are not orthogonal, a proper set of Wannier functions for the whole lattice has to be constructed from the localized states. By hybridizing the symmetric O Wannier states with the central Cu $d_{x^2-y^2}$ states, the original three-band Hamiltonian can be rewritten in terms of this new basis.

The resulting low-energy effective Hamiltonian of the Zhang-Rice singlets in the CuO₂ plane reduces to a single-band Hubbard model, which contains an effective singlet hopping matrix element $t_{i,j,\sigma}$ and an effective potential term $U \sim (E_d - E_p)$ where E_d (E_p) is the energy of the Cu $d_{x^2-y^2}$ (O 2p_x, 2p_y) holes,

$$H = - \sum_{\langle i,j \rangle, \sigma} \left[t_{i,j,\sigma} c_{i,\sigma}^\dagger c_{j,\sigma} + h.c. \right] + \sum_{i,\sigma} U n_{i,\sigma} n_{i,\sigma}. \quad (1.1)$$

In Eq. (1.1), i and j label the lattice sites, and the first summation is over the nearest neighbors.

In the high U (strong-coupling) limit, Hubbard model is reduced to the $t - J$ model:

$$H = P \left(- \sum_{\langle i,j \rangle, \sigma} [t_{i,j,\sigma} c_{i,\sigma}^\dagger c_{j,\sigma} + h.c.] + J \sum_{\langle i,j \rangle} \left[(\vec{S}_i \cdot \vec{S}_j - \frac{1}{2} n_i n_j) \right] \right) P, \quad (1.2)$$

where the exchange coupling is given by $J = 4t^2/U$, and P is the projection operator that projects out the double occupancy states. For the electron-doped cuprates, mapping from the three-band model to the one-band Hubbard model is more apparent because the doped charge carriers, instead of going to the O sites, fill up the Cu 3d-orbitals. By replacing the hybridization hopping t_{pd} with a second-order effective hopping element and assuming that U is large, we arrive at exactly the same single-band $t - J$ model (1.2). In this case, the effective Hamiltonian characterizes the hopping of the Cu 3d¹⁰ configuration, in contrast to that of the Zhang-Rice singlets for hole doping.

We note that, although in the lowest-order approximation the three-band Hubbard model reduces to the single-band $t - J$ model for both electron- and hole-doped cuprates, this theory cannot account for the asymmetry in the phase diagram between the two types of cuprates [Fig. 1.2] because the one-band $t - J$ model with nearest-neighbor hopping is electron-hole symmetric. Introducing further neighbor couplings into the one-band model could break the symmetry [22, 23, 24]. However, when solved on finite clusters, the three-band Hubbard model with parameters derived from the *ab initio* local density functional theory generates similar nearest-neighbor t and next-nearest-neighbor t' hopping elements in the effective model for both types of doping [25]. This difficulty can be circumvented if an additional Cu 4s orbital is taken into account [26]. It is known that the apical oxygens in the hole-doped cuprates modulate the Cu 4s orbital [27] and thus change the t'/t ratio significantly. Since electron-doped cuprates have no apical oxygen atoms, it may explain why they have a different t'/t value and thus a disparate phase diagram from that of the hole-doped cuprates. At the time of writing, we do not know what the suitable microscopic model is for electron-doped cuprates. More theoretical effort is necessary to better elucidate the *microscopic* origin of the asymmetry in the phase diagram.

1.2 Electron-doped vs. hole-doped cuprates: review of current experimental and theoretical status

As a first-order description, the one-band Hubbard model and its derivative $t - J$ model capture the essential physics of the doped anti-ferromagnetic Mott insulators, *i.e.*, the competition between the kinetic energy (t) that favors the delocalization of charge carriers and the anti-ferromagnetic exchange interaction (J) originated from the strong on-site Coulomb repulsion. Mean field theory of the $t - J$ model supplemented by an off-site Coulomb potential reveals a plethora of possible ground states closely spaced in energy [28], characterized by their respective broken symmetries and their distinctive low-energy excitations. A central objective of the high T_c research is to determine which orders are responsible for the cuprate phenomenology. In this section, we review the experimental findings that uncover the competing gound states and comment on related theoretical proposals advocating for specific orders. We focus on contrasting the pairing symmetry and the pseudogap phenomena between the electron- and hole-doped cuprates and discuss how these apparent non-universal phenomena are linked to the presence of competing orders.

1.2.1 Pairing symmetry

The identification of the pairing symmetry is an important step toward determining the pairing mechanism of high-temperature superconductivity because it poses great constraints on the microscopic theory. Empirically, the Knight shift and spin-lattice relaxation measurements by the nuclear magnetic resonance (NMR) technique have shown that carriers in cuprate superconductors form singlet pairing below the transition temperature [29, 30]. Consequently, from a symmetry consideration the parity of the (orbital) order parameter must be even. In a quasi-two-dimensional system where interlayer coupling is sufficiently weak and electron motion is strongly confined in the CuO₂ planes, d -wave pairing is preferable because it minimizes the on-site Coulomb repulsion while retaining 2D confinement. When the interlayer coupling strength increases, however, s -wave pairing becomes more favorable as the system gains a larger condensation energy at the expense of the Coulomb

energy.

It is well established that the pairing symmetry of the underdoped and optimally doped p-type cuprates is predominately *d*-wave [6, 7] [Fig. 1.4(a)]. Preponderant evidence from non-phase-sensitive experiments such as the angular-resolved photoemission spectroscopy (ARPES) [31], thermal conductivity [32], and penetration depth measurements [33] has revealed the anisotropy of the pairing potential, the presence of line nodes, and the existence of low-energy nodal quasiparticles. Additionally, ingenious phase-sensitive techniques such as the SQUID interferometry [34], single-Josephson-junction modulation [34, 35], and tricrystal scanning SQUID magnetometry [36] experiments have confirmed the change of phase across the line nodes, which is consistent with a *d*-pairing symmetry.

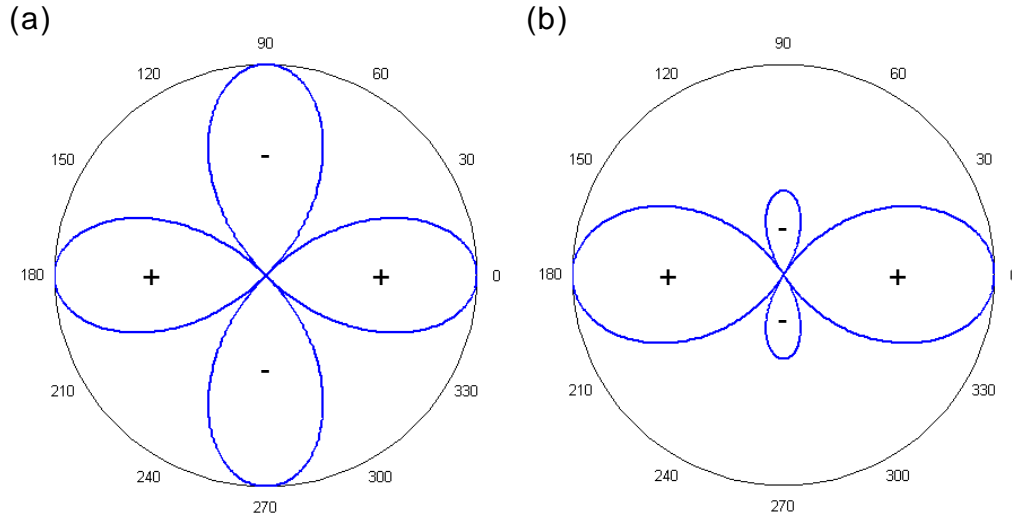


Figure 1.4: Magnitude and phase of the superconducting order parameter as a function of direction in the momentum space. The superconducting order parameter of (a) a *d*-wave superconductor is given by $\Delta_d(\mathbf{k}) = \Delta \cos 2\theta_{\mathbf{k}}$, where Δ is the maximum gap value and $\theta_{\mathbf{k}}$ is the angle between the quasiparticle wavevector \mathbf{k} and the antinode direction, while that of (b) a $(d+s)$ -wave superconductor is $\Delta_{(d+s)}(\mathbf{k}) = \Delta [(1 - x) \cos 2\theta_{\mathbf{k}} + x]$. In figure (b), $x = 30\%$ *s*-wave admixture is assumed.

Curiously, in the heavily overdoped cuprates, there is a significant *s*-wave component mixing into the *d*-wave order parameter [Fig. 1.4(b)]. Our tunneling results on the overdoped $(Y_{0.7}Ca_{0.3})Ba_2Cu_3O_{6+\delta}$ (Ca-YBCO, doping level $p \approx 0.22$) thin films [8] find a substantial Δ_s/Δ_d ratio [§4], where Δ_s and Δ_d are the magnitudes of the *s*-wave and *d*-wave components. Subsequent ARPES measurements on overdoped $YBa_2Cu_3O_{6.993}$ (YBCO) ($p \approx 0.18$) reconfirms the large in-plane gap anisotropy [37]. In addition, Raman spectroscopy results on tetragonal $Bi_2Sr_2CaCu_2O_{8+\delta}$ (Bi -

2212) [38] and $Tl_2Ba_2CuO_{6+\delta}$ (Tl -2201) [39] single crystals suggest that the *s*-wave mixing with overdoping is a generic feature of high T_c superconductors regardless of the crystalline symmetry.

In the electron-doped cuprates, the determination of the pairing symmetry has been more controversial. While quasiparticle tunneling spectroscopy [40, 41] and earlier Raman spectroscopy [42] indicate an *s*-wave pairing in nearly optimally doped one-layer $Nd_{2-x}Ce_xCuO_{4-\delta}$ (NCCO) and $Pr_{2-x}Ce_xCuO_{4-\delta}$ (PCCO), tricrystal SQUID magnetometry [43], ARPES measurements [44, 45], and recent Raman spectroscopy results [46] are more consistent with *d*-wave pairing.² Recently, doping-dependent pairing symmetry is observed by point-contact spectroscopy [47] and penetration depth measurements [48], where the change from *d*-wave pairing in the underdoped to *s*-wave in the optimally doped and overdoped one-layer PCCO is reported. Furthermore, scanning tunneling spectroscopy studies of the infinite-layer $Sr_{0.9}La_{0.1}CuO_2$ (SLCO) [49] have identified an *s*-wave pairing [§5] in this simplest cuprate compound that is free of the complications from the Cu – O chain effect as in YBCO and the oxygen inhomogeneity induced disorder as in NCCO, PCCO, and Bi-2212.

The non-universal pairing symmetry observed in electron-doped and hole-doped cuprates indicates that, instead of being a ubiquitous property of high-temperature superconductors, the symmetry of the order parameter varies with material-dependent properties including the anisotropy ratio, the on-site Coulomb repulsion and the anti-ferromagnetic coupling strength. Thus, the pairing symmetry is possibly a mere consequence of the compromise between different competing energy scales [50] rather than a sufficient condition of cuprate superconductivity.

1.2.2 Pseudogap

The first experiments showing evidence for a normal state gap-like feature in the hole-doped cuprates are the temperature-dependent NMR spin-lattice relaxation rate and Knight shift measurements of underdoped YBCO [51, 52]. The spectral weight of the low-frequency spin fluctuations is transferred to the high-frequency range in the normal state, and a “spin gap” is developed well above

²We note that the *d*-wave pairing observed in ARPES [45] and Raman scattering [46] is not an exact $d_{x^2-y^2}$ symmetry, since the maximum gap is displaced away from the $[\pi, 0]$ to where the Fermi surface crosses the magnetic Brillouin zone boundary, indicating a strong coupling to the background anti-ferromagnetic fluctuations in the one-layer electron-doped cuprates.

the transition temperature T_c . Other measurements probing the charge, spin, and single-particle excitations of underdoped p-type cuprates all hint at an opening of low-energy spectral gaps above T_c . The development of spectral gaps in spin fluctuations (as measured by the NMR spin-lattice relaxation rate), in charge fluctuations (as measured by the optical conductivity spectra via infrared reflectance [53]), and in single-particle excitation spectra (as measured by the tunneling spectroscopy [54] and ARPES [55, 56]) all takes place at different temperatures. In the phase diagram given by Fig. 1.2, we define the pseudogap temperature $T^*(p)$ as the temperature below which a suppression of electronic density of states around the Fermi level develops.

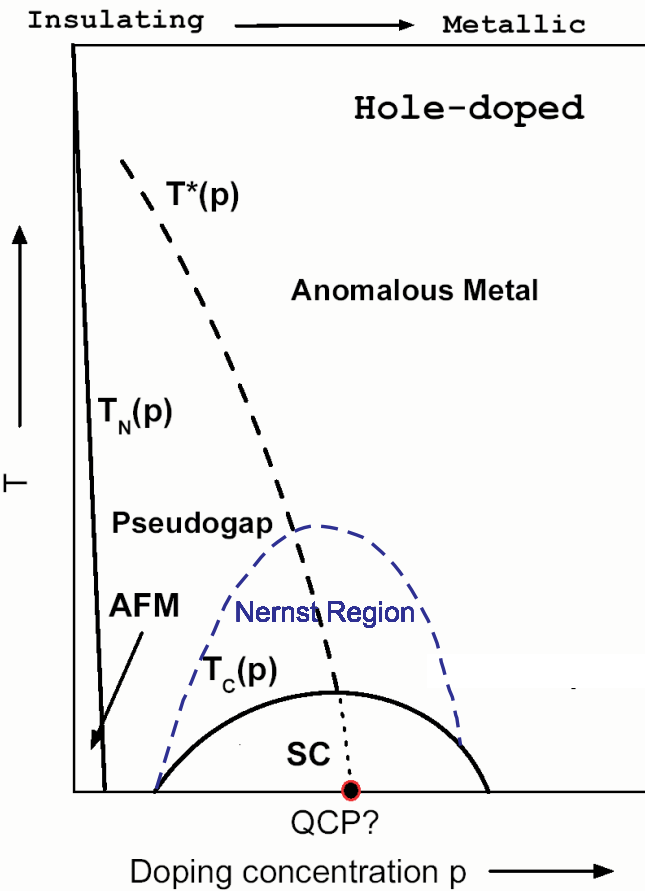


Figure 1.5: Schematic phase diagram for the hole-doped cuprates showing that the Nernst region only covers a small part of the pseudogap phase. Note that the “normal” metal coincides with the anomalous metal state shown in Fig. 1.2.

While NMR, neutron scattering, transport, and optical conductivity measurements probe the reduced spin and charge scattering rates, tunneling spectroscopy and ARPES probe directly the

loss of single-particle density of states. ARPES measurements of underdoped Bi-2212 reveal a normal state (leading edge) spectral gap whose magnitude and momentum anisotropy resembles the superconducting gap [55, 56], and the earlier tunneling spectroscopy measurements observe a smooth evolution of the superconducting gap into the pseudogap [57, 54]. Based on these results, some physicists speculate that the pseudogap is a precursor to the superconducting gap.

There are two main categories of theories under the precursor scenario: the “pre-formed magnetic pairing” conjecture and the “pre-formed Cooper pairing” conjecture. Representative theories of pre-formed magnetic pairs include the resonating valence bond (RVB) theory and its derivative, the $SU(2)$ gauge theory [20, 58], which view the pseudogap as a spin gap opening up upon the singlet pairing below a pseudogap temperature T^* . In the theory, the singlet pairing fluctuates and resonates among different pairs, thus restoring translational symmetry of the CuO_2 planes. This ground state is known as an RVB spin liquid state. The orbital wavefunction of such a pseudogap phase could display staggered-flux correlations [58, 59], equivalent to the d -wave superconducting correlations in the zero-doping limit [60]. By cooling the pre-formed magnetic-pair system below T_c , the singlet pairs would turn into Cooper pairs, so that long-range superconductivity becomes established. Experimental data suggestive of this scenario have been reported by the observation of a normal state spin gap in NMR measurements [61]. However, direct observation of the proposed staggered flux phase (in which orbital currents circulate in a staggered pattern) remains elusive. Furthermore, that there is no apparent broken symmetry in an RVB spin liquid cannot be easily reconciled with numerous experimental reports on the observation of broken symmetries in cuprates [§1.2.3]. Another version of the pre-formed magnetic pairing scenario suggests that the singlet pairing would result in a valence-bond solid (spin-Peierls state) instead of the RVB spin liquid [62]. At low temperatures, the conjecture of the bond-ordered states seems to be consistent with several experimental phenomena. However, a finite-temperature theory directly applicable to the pseudogap phase is still lacking.

In the preformed Cooper pair scenario, the pseudogap phase is regarded as a state with strong superconducting phase fluctuations resulting from the small phase stiffness in high T_c cuprates [63].

The pairing potential in the pseudogap phase is non-vanishing, and hence the spectral gap is non-zero, though the phase coherence is lost. The supporting experimental evidence for the fluctuating superconducting order above T_c is provided by the Nernst experiments, where the short-range superconducting correlations are manifested as the non-zero Nernst signals [64, 65, 66]. However, the Nernst region where local superconducting order persists and phase fluctuation scenario applies is much smaller than the observed pseudogap region [Fig. 1.5]. Therefore, phase fluctuations of the pre-formed Cooper pairs alone cannot account for the wide range of the pseudogap phase.

Another viewpoint concerning the nature of pseudogap is based on Landau's symmetry-breaking theory where a competing order is assumed to be responsible for the pseudogap phenomena. In contrast to earlier tunneling spectroscopy with limited spatial resolution that shows smooth transition from the superconducting phase to the pseudogap phase [57, 54], recent spatially resolved scanning tunneling spectroscopy measurements indicate that there are two types of single-particle spectra with different gap values coexisting in the underdoped and optimally doped Bi-2212 samples [67, 68]. Furthermore, the interlayer tunneling spectra of Bi-2212 mesa samples demonstrate that the sharp superconducting coherence peaks coexist with a gradual hump feature at $T \ll T_c$, and that the superconducting gap vanishes above T_c while the higher energy hump background persists till $T^* > T_c$ [69]. The ARPES measurements on $\text{La}_{2-x}\text{Sr}_x\text{CuO}_4$ [70] and the bulk specific heat measurements [71] also support the conjecture of the pseudogap phase as a competing order phase. Candidates for the competing order include (fluctuating) stripe order [72, 73], circulating current order [74] also known as d -density wave order [75], (dynamic) anti-ferromagnetic order [76], and valence-bond-solid order [62]. Determining which orders are present in the superconducting and the pseudogap phases is one of the most important current topics of cuprate physics [62, 58, 73, 76].

In contrast to the ubiquitous presence of pseudogap above T_c in underdoped p-type cuprates [55, 56, 9], *no* discernible normal state single-particle excitation gap has been observed in the zero-field tunneling spectroscopy of n-type one-layer NCCO and PCCO [16, 17, 18], and *no* discernible normal state leading edge gap has been seen within the resolution of ARPES [77]. Nernst measurement on NCCO also exhibits negligible superconducting fluctuations above T_c [65, 78]. Furthermore, scanning

tunneling spectra of infinite-layer SLCO indicate complete absence of any normal state tunneling gap [§5], and the NMR spin-lattice relaxation rate and Knight shift measurements show that there is no normal state spin gap in this compound [79]. Only when a magnetic field exceeding the upper critical field is applied, would a normal state “pseudogap” appear in the tunneling spectra [17, 18]. However, such a “pseudogap” in n-type cuprates only appears below T_c , which apparently contradicts the precursor Cooper pairing scenario.

To explain the absence of the zero-field pseudogap and the field-induced pseudogap in the electron-doped systems, we propose that the strength of the competing order in the n-type cuprates is smaller than the superconducting gap, which is opposite to their counterparts in the p-type cuprates. Only when the superconducting order is suppressed and the competing order enhanced by a large external field would the single-particle spectral gap associated with the competing order be revealed. In Chapter 6, we present a simple model that implements this conjecture in the calculation of the tunneling spectra for both *s*- and *d*-wave cuprate superconductors. Numerical simulations based on this model confirm that our conjecture is consistent with the observed spectral characteristics of the infinite-layer SLCO [§6]. Moreover, it can be shown that, by varying the gap ratio of the two competing orders, the appearance of pseudogap phenomena in hole-doped cuprates can be reconciled with the absence of pseudogap in the electron-doped cuprates.

1.2.3 Orders in cuprate superconductors

One way to differentiate between numerous theories of high-temperature superconductivity is to identify the (static or fluctuating) quantum order that each theory prescribes for the pseudogap and the superconducting phases. Experimentally, spin correlations of several cuprate families have been studied in detail by means of inelastic and elastic neutron scattering for comparison with theoretical predictions. One of the most conspicuous features observed in LSCO and YBCO is the presence of incommensurate spin fluctuations, which are static in the underdoped LSCO with doping $0.055 < p < 0.14$ [80, 81, 82], dynamic in LSCO with $p > 0.14$, and dynamic in YBCO throughout the entire superconducting doping range [83]. In Nd-doped LSCO, Bragg peaks related to static

spin and charge orders are revealed with a charge modulation periodicity half of that of the spin modulation [84]. This observation is consistent with the “stripe” picture where the doped holes self-organize into charge stripes that are the anti-phase domain walls between Néel ordered regions [72]. Similar static stripe-like orders are also detected in $\text{La}_{1.875}\text{Ba}_{0.125}\text{CuO}_4$ [85].

In the stripe phenomenology, the incommensurability δ_q of the spin fluctuations is related to the doping level by $\delta_q = p$, exactly what is observed in underdoped LSCO for $0.055 < p < 0.125$ ³ [86]. Therefore, it is proposed that the static incommensurate spin density waves in LSCO are spin stripes, even though the corresponding charge Bragg peaks have never been identified (presumably due to the weak intensity). Furthermore, the dynamic incommensurate spin fluctuations that take place beyond 1/8 doping are interpreted as slowly fluctuating stripes. In comparison, earlier neutron scattering results on YBCO do not provide as strong evidence for stripe formation. Most experimental data on YBCO exhibit dynamic spin fluctuations with a more complicated doping-dependent incommensurability [83]. Recently, one-dimensional incommensurate spectral features have been observed in highly ordered underdoped $\text{YBa}_2\text{Cu}_3\text{O}_{6.5}$, in which the spin fluctuations are incommensurate along the {100} axis and commensurate along the {010} direction [87, 88]. The one-dimensional incommensurate scattering is taken as strong evidence of stripe-like modulations in underdoped YBCO. We remark, in passing, that the neutron scattering experiments on electron-doped cuprates show dynamic *commensurate* spin fluctuations [89, 90, 91, 92], in contrast to the incommensurate scattering of hole-doped cuprates.

Other types of orders that appear in some theories of cuprate superconductivity include the *d*-density wave order [75] (or the circulating current order [74]) branded as the hidden order of the pseudogap phase. The orbital currents flowing in the CuO_2 planes break the time-reversal symmetry and produce a *c*-axis moment. This phase should be visible in the neutron scattering experiments if it exists. To date, the only supportive evidence for the static *c*-axis moment comes from a set of experiments on underdoped $\text{YBa}_2\text{Cu}_3\text{O}_{6.6}$ [93, 94]. However, contradictory results have also been reported for highly ordered $\text{YBa}_2\text{Cu}_3\text{O}_{6.5}$ [87, 88]. Whether the dynamic orbital current fluctuations

³Beyond the 1/8 doping, the observed incommensurability of LSCO saturates at 0.125.

of the staggered flux state predicted by the $SU(2)$ slave-boson theory exist or not is yet to be verified.

While spin orders couple directly to neutron magnetic moments, charge correlations can only be detected indirectly through neutron scattering of the induced lattice distortion. The ideal probe for static charge orderings of quasi-two-dimensional samples is the scanning tunneling spectroscopy (STS). Low-temperature scanning tunneling spectra taken on highly anisotropic Bi-2212 have revealed a number of interesting phenomena, including a checkerboard-like charge ordering in the vortex core of nearly optimally doped samples [95], dispersive modulations in the local density of states in nearly optimal doped and slightly underdoped samples [96, 97], and non-dispersive incommensurate modulations in heavily underdoped samples [98]. In addition, it is found that above the superconducting transition temperature, four non-dispersive modulation peaks along the anti-nodal direction survive [99]. These results imply the presence of the checkerboard or stripe order in the pseudogap phase and its coexistence with the superconducting order in the vortex core of the superconducting phase. Another cuprate compound that exhibits incommensurate charge density wave order is the highly two-dimensional Na-doped $\text{Ca}_2\text{CuO}_2\text{Cl}_2$ [100]. In the underdoped samples, all tunneling spectra below T_c reveal pseudogap-like density of states without sharp superconducting coherence peaks, similar to those taken on the non-superconducting samples. Thus, it is tempting to attribute the pseudogap spectra to the presence of charge ordering. An alternative interpretation of the density of states modulation is to view it as a manifestation of the bond-ordered states among which the stripe order is a special case [62]. To distinguish between different bond orders of the same periodicity, the phase information of the Fourier-transformed local density of states must be retained and carefully analyzed [101]. To date, no definitive result has been obtained from such analysis [73].

Up to this point, we have only discussed the orders that break explicit symmetries such as the spin-rotational symmetry, the lattice symmetry, or the time-reversal symmetry. There are other theories that conjecture more subtle topological orders as the relevant orders that characterize the pseudogap phase. These theories are based on the RVB scenario [20] that postulates a common origin for the pseudogap and the superconducting phases as a doped spin liquid state. Two types of spin

liquids most discussed in the context of cuprate superconductivity are the Z_2 [102] and $U(1)$ spin liquids [103, 58] characterized by their respective low-energy gauge groups. At the time of writing, the experiments designed to detect the non-trivial fluxes [104] associated with the topological order have not produced any positive result [105, 106]. Therefore, we shall restrict our discussion to the symmetry-breaking orders in this thesis.

1.3 Overview of the thesis

This thesis presents scanning tunneling spectroscopic studies of two families of cuprate superconductors, the hole-doped cuprate YBCO, and the electron-doped cuprate $\text{Sr}_{0.9}\text{La}_{0.1}\text{CuO}_2$ (SLCO). Their contrasting properties, such as the pairing symmetries and pseudogap phenomena, are highlighted, and a proposal to unify these apparent non-universal phenomena in terms of coexisting orders is put forward. The theoretical model based on this proposal is solved by numerical methods, and the results are found to reconcile the findings in the low-energy quasiparticle spectral characteristics of different cuprates.

The thesis is organized as follows. Chapter 2 first describes the fundamental physics of tunneling spectroscopy within the tunneling Hamiltonian formalism. The Blonder-Tinkham-Klapwijk (BTK) theory is then introduced to treat the tunneling spectra of superconducting electrodes with a variable junction barrier [Appendix A]. For superconductors of unconventional pairing symmetries, the generalized BTK theory is derived in order to account for the Andreev bound state developed at the sample surface along the nodal direction. Tunneling spectra of d -wave superconductors along the nodal, anti-nodal, and c -axis are summarized, and comparisons are drawn among the spectra of various mixed pairing symmetry superconductors.

Chapter 3 begins with a brief review of the scanning tunneling microscopy (STM) technique, followed by detailed description for the instrumentation of the cryogenic STM built for the thesis research. The working principle of the STM and the essential components are outlined. The specifications of the STM electronics and the high-voltage circuitry for piezoelectric control are provided, and the cryogenic probe design is illustrated. Additional elements necessary for a fully functional

STM are documented, which include the improvement of thermal response and measures taken for the vibrational, acoustic, and electrical noise reduction.

Chapter 4 presents the STS results on the hole-doped YBCO with a range of doping. The pairing symmetry and the pairing potential are extracted by fitting to the BTK formalism. Predominantly *d*-wave pairing is found in underdoped and optimally doped pure YBCO, and in overdoped Ca-YBCO a significant *s*-wave admixture is revealed by STS. In addition, tunneling spectra of optimally doped YBCO with a small concentration of non-magnetic impurities are studied, which exhibit strong suppression of the superconducting gap and a single resonance peak at the impurity site, consistent with the *d*-wave pairing symmetry around optimal doping. The implication of the doping-dependent pairing symmetry in the context of quantum criticality and the existence of fluctuating competing orders is discussed.

Chapter 5 presents the tunneling spectra of the electron-doped SLCO. In contrast to the predominantly *d*-wave pairing in hole-doped cuprates, the order parameter of SLCO is found to be momentum-independent with a single-particle excitation gap substantially exceeding the BCS value. Above T_c , the spectral gap closes, indicating the absence of zero-field pseudogap. The single-particle spectral response to the quantum impurities (Zn and Ni) further corroborates the finding of the *s*-wave pairing in SLCO. Moreover, it is found that the mean-field Bogoliubov quasiparticle based description fails to account for several important spectral characteristics of SLCO: the excess low-energy excitations, the rapid decrease of the spectral gap with increasing temperatures, and the current-induced pseudogap-like features. These observations are in contrast to the applicability of the mean-field BTK theory to YBCO tunneling spectra and can be understood in terms of the presence of strong quantum fluctuations in SLCO that results from its proximity to a quantum critical point. Additional evidence for strong quantum phase fluctuations have been obtained from studies of high-field vortex dynamics [107] in various cuprates and will be discussed and compared with microscopic quasiparticle spectra.

In Chapter 6, a theoretical model for coexisting density waves with superconductivity is investigated by numerical methods. By incorporating quantum phase fluctuations and using realistic band

structures, we find that the resulting quasiparticle spectra exhibit excess low-energy excitations consistent with empirical results [§5.3.1]. Furthermore, by tuning the ratio of the strength of the competing order to that of the superconducting order, the absence of pseudogap in n-type cuprates, the current-induced pseudogap-like spectra in SLCO [§5.3.2], and the general presence of pseudogap phenomena in hole-doped cuprates [§1.2.2] are reproduced. An additional theoretical manifestation of competing orders is also investigated by considering the interference of quasiparticles scattered off pinned density waves, and the numerical results are found to compare favorably with experimental data in Bi-2212 [95, 97, 99]. Finally, we conclude that competing orders are important in understanding the cuprate phenomenology. Further experiments that investigate the varying proximity to quantum criticality of different cuprate superconductors are proposed for future studies.

Chapter 2

Physics of Tunneling Spectroscopy

Electron tunneling spectroscopy in artificial solid-state tunneling structures was pioneered by the work of Esaki on semiconductor p-n junctions in 1958 [108]. Shortly after, Fisher and Giaever succeeded in fabricating thin-film metal-insulator-metal junctions with reproducible behavior in 1959 [109]. Furthermore, by cooling to below the transition temperature of lead, Giaever [110] directly observed the superconducting energy gap in the differential tunneling conductance (dI/dV vs. V) of an aluminum-oxide-lead junction. The importance of this discovery is two-fold. For one thing, this is the first unequivocal evidence that tunneling current in a well-formed junction accounts entirely for the total current across the junction. For another, it demonstrates that tunneling spectroscopy is a powerful high-energy-resolution tool to study the electronic structures of superconducting material. In this thesis, we employed a specific configuration of tunneling technique, the scanning tunneling spectroscopy, with a normal-metal tip as the counter-electrode to study high-temperature superconductors. To set the foundation for understanding the physics encoded in the tunneling spectra, we first review the theories related to the normal-metal-insulator-superconductor (N-I-S) tunneling process and summarize the equations relevant to data analysis and numerical simulations in later chapters.

2.1 Tunneling Hamiltonian

The most commonly adopted approach to solving the tunneling problem in a many-body system is the transfer Hamiltonian formalism [111, 112, 113]. The central assumption of the theory is that the

tunneling barrier separates the two electrodes into two nearly independent subsystems, H_L and H_R , with a weak residual perturbation, H_T , coupling the ground state to the excited states in which a bare electron is transferred from one electrode to the other. The Hamiltonians for the uncoupled left and right electrodes are

$$H_L = \sum_{\mathbf{p}} \epsilon_{\mathbf{p}} c_{\mathbf{p}}^\dagger c_{\mathbf{p}} = \mu_L \hat{N}_L + \sum_p \xi_{\mathbf{p}} c_{\mathbf{p}}^\dagger c_{\mathbf{p}} \quad (2.1)$$

and

$$H_R = \sum_{\mathbf{q}} \epsilon_{\mathbf{q}} c_{\mathbf{q}}^\dagger c_{\mathbf{q}} = \mu_R \hat{N}_R + \sum_q \xi_{\mathbf{q}} c_{\mathbf{q}}^\dagger c_{\mathbf{q}} \quad (2.2)$$

where $c_{\mathbf{p}}$ and $c_{\mathbf{q}}^\dagger$ are the particle operators, $\{c_{\mathbf{p}}, c_{\mathbf{q}}^\dagger\} = 0$, and

$$H_T = \sum_{\mathbf{p}, \mathbf{q}} T_{\mathbf{p}, \mathbf{q}} \{c_{\mathbf{p}}^\dagger c_{\mathbf{q}} + c_{\mathbf{q}}^\dagger c_{\mathbf{p}}\} \quad (2.3)$$

is the tunneling Hamiltonian, also called the transfer Hamiltonian. In Eqs. (2.1)–(2.3), $\epsilon_{\mathbf{p}}$ and $\epsilon_{\mathbf{q}}$ are the single-particle eigen-energies, μ_L and μ_R the chemical potentials, \hat{N}_L and \hat{N}_R the number operators and $\xi_{\mathbf{p}}$ and $\xi_{\mathbf{q}}$ the single-particle eigen-energies referenced to μ_L and μ_R respectively. The tunneling matrix element, $T_{\mathbf{p}, \mathbf{q}}$, is the probability amplitude to transfer an electron across the insulating barrier. Using first-order time-dependent perturbation theory, Bardeen [111] showed that $T_{\mathbf{p}, \mathbf{q}}$ is determined by the quantum mechanical current density operator evaluated within the barrier,

$$T_{\mathbf{p}, \mathbf{q}} = -\frac{\hbar^2}{2m} \int \{\psi_{\mathbf{p}}^* \nabla^2 \psi_{\mathbf{q}} - \psi_{\mathbf{q}}^* \nabla^2 \psi_{\mathbf{p}}\} d\tau = -\frac{\hbar^2}{2m} \int \{\psi_{\mathbf{p}}^* \nabla \psi_{\mathbf{q}} - \psi_{\mathbf{q}}^* \nabla \psi_{\mathbf{p}}\} \cdot d\vec{S}, \quad (2.4)$$

where $d\tau$ is the volume element, and $d\vec{S}$ is the area element.

After summing over all relevant states, the total tunneling current at the bias voltage V given by the Fermi golden rule is

$$I(V) = \frac{4\pi e}{\hbar} \sum_{\mathbf{p}, \mathbf{q}} |T_{\mathbf{p}, \mathbf{q}}|^2 [f(\xi_{\mathbf{p}}) - f(\xi_{\mathbf{q}})] \delta(\xi_{\mathbf{p}} - \xi_{\mathbf{q}} + eV), \quad (2.5)$$

where $\psi_{\mathbf{p}}$ and $\psi_{\mathbf{q}}$ are the single-particle wavefunctions of the left and right electrodes, and f is the Fermi function, $f(\xi) = \frac{1}{1+e^{-\xi/k_B T}}$.

Equation (2.5) is valid only in a non-interacting, single-particle approximation. When generalized to an interacting system that contains all the many-body effects, the tunneling current should be written in terms of the spectral functions of the two electrodes $A_L(p, \omega_{\mathbf{p}})$ and $A_R(q, \omega_{\mathbf{q}})$ [114, 113],

$$I(V) = \frac{4\pi e}{\hbar} \sum_{\mathbf{p}, \mathbf{q}} |T_{\mathbf{p}, \mathbf{q}}|^2 \int \frac{d\omega_{\mathbf{p}}}{2\pi} \int \frac{d\omega_{\mathbf{q}}}{2\pi} [f(\omega_{\mathbf{p}}) - f(\omega_{\mathbf{q}})] A_L(p, \omega_{\mathbf{p}}) A_R(q, \omega_{\mathbf{q}}) \delta(\omega_{\mathbf{p}} - \omega_{\mathbf{q}} + eV) \quad (2.6)$$

where $\omega_{\mathbf{p}}$ and $\omega_{\mathbf{q}}$ are two dummy energy variables to be integrated over. In the non-interacting limit, $A_L(p, \omega_{\mathbf{p}}) = 2\pi\delta(\omega_{\mathbf{p}} - \xi_{\mathbf{p}})$, $A_R(q, \omega_{\mathbf{q}}) = 2\pi\delta(\omega_{\mathbf{q}} - \xi_{\mathbf{q}})$, and (2.6) reduces to (2.5).

It is generally assumed that the junction surface is sufficiently smooth so that barrier transmission is specular and that the band structure varies sufficiently slowly so that the WKB approximation is valid [115, 116]. In this case, the evaluation of the matrix element, $T_{\mathbf{p}, \mathbf{q}}$, reduces to a one-dimensional tunneling problem. For metallic electrodes with parabolic band structures,

$$\begin{aligned} |T_{\mathbf{p}, \mathbf{q}}|^2 &\approx \frac{\partial \xi_{\mathbf{p}}}{\partial \mathbf{p}_L} \frac{\partial \xi_{\mathbf{q}}}{\partial \mathbf{q}_L} |D(\xi_{\mathbf{p}}, \mathbf{p}_T)|^2 \delta(\mathbf{p}_T - \mathbf{q}_T) \\ D(\xi_{\mathbf{p}}, \mathbf{p}_T) &= \exp \left[- \int dx \kappa(x, \xi_{\mathbf{p}}, \mathbf{p}_T) \right] \\ \kappa(x, \xi_{\mathbf{p}}, \mathbf{p}_T) &= \sqrt{2m [U(x, V) - \xi_{\mathbf{p}} + \hbar^2 \mathbf{p}_T^2 / 2m]} \end{aligned} \quad (2.7)$$

where the subscript L indicates the longitudinal component of the momentum, T indicates the transverse component, D is the transmission coefficient, and κ is the wave vector inside the tunneling barrier $U(x, V)$. Under the assumption that the longitudinal energy ($\xi_{\mathbf{p}} - \hbar^2 \mathbf{p}_T^2 / 2m$) of the tunneling particle is sufficiently smaller than the barrier height $U(x, V)$, the barrier transmission $D(\xi_{\mathbf{p}}, \mathbf{p}_T)$ is approximately a constant.

With Eq. (2.7), when converting the summation over momenta in (2.5) into energy integrals, the

longitudinal band structure is eliminated by the group velocity factors $\frac{\partial \xi_{\mathbf{p}_L}}{\partial p_L}$ and $\frac{\partial \xi_{\mathbf{q}_L}}{\partial q_L}$. As a result,

$$I(V) = \frac{4\pi e}{\hbar} \sum_{\mathbf{p}_T} \int d\xi_{\mathbf{p}} |D_{\xi_{\mathbf{p}}, \mathbf{p}_T}|^2 [f(\xi_{\mathbf{p}}) - f(\xi_{\mathbf{p}} + eV)] \propto |D|^2 \int d\xi [f(\xi) - f(\xi + eV)], \quad (2.8)$$

where the normal state band structure drops out entirely from the expression,¹ and the tunneling current is ohmic at low-bias voltages, $I(V) \propto |D|^2 eV$. For electrodes with more complicate band structures, the cancellation between the Jacobian and the group velocity factors in the tunneling matrix element $T_{\mathbf{p}, \mathbf{q}}$ are not complete. Therefore, the tunneling conductance generally contains *convoluted* information of the band structure.²

In contrast to the subtleties involved in the interpretation of metal-insulator-metal (N-I-N) tunneling and metal-insulator-semiconductor tunneling spectra in terms of band structure anomalies [115, 117], the N-I-S tunneling current has a surprisingly simple form [110],

$$I(V) \propto \int_{-\infty}^{\infty} d\xi |D|^2 [f(\xi) - f(\xi + eV)] N_S(\xi + eV), \quad (2.9)$$

where $N_S(\xi) \propto \frac{|\xi|}{\sqrt{\xi^2 - \Delta^2}}$ is the density of states of the superconducting electrode, and Δ is the energy gap of the superconductor. Assuming D varies slightly with energy, the differential conductance measures directly the BCS (Bardeen-Cooper-Schrieffer) density of states in the low-temperature limit,

$$\begin{aligned} \frac{dI}{dV}(V) &\propto |D|^2 \int_{-\infty}^{\infty} d\xi N_S(\xi) \left[-\frac{\partial f(eV + \xi)}{\partial(eV)} \right] \\ &\propto |D|^2 N_S(eV). \end{aligned} \quad (2.10)$$

This simple relation between the tunneling conductance and the BCS density of states arises

¹More precisely, the summation over the transverse momentum \mathbf{p}_T in Eq. (2.8) still contains transverse band structure information. However, for tunneling process between simple metals where a large number of transverse momentum states are available, the exponential function in $D(\xi_{\mathbf{p}}, \mathbf{p}_T)$ limits the effective tunneling to electrons at nearly normal incidence. Consequently, the transverse band structure effect is also suppressed [116].

²Most textbooks on many-body physics or superconductivity treat the the tunneling matrix element $T_{\mathbf{p}, \mathbf{q}}$ as a constant and pull it out of the momentum summation in Eqs. (2.5) and (2.6). As a result, converting the momentum sum into energy integrals lumps the band structure effect into two density of states factors N_L and N_R in the tunneling current expression

$$I(V) \propto |T|^2 \int d\xi N_L(\xi) N_R(\xi + eV) [f(\xi) - f(\xi + eV)],$$

which strictly speaking is *incorrect*. Using tunneling spectroscopy to determine single-particle band structure information, such as the band edge of semiconductors, generally suffers from the complicated functional form of the tunneling matrix element and other model-dependent uncertainties. More details are given in the classic books on tunneling by Wolf [117] and Duke [115].

from the fact that, although tunneling current does not probe the bare band structure directly, it contains direct information about the spectral function of the many-body system. More explicitly, by identifying $A_L(p, \omega_p)$ and $A_R(q, \omega_q)$ in (2.6) with the free electron and the superconducting spectral functions, respectively,

$$\begin{aligned} A_L(p, \omega_p) &= 2\pi\delta(\omega_p - \xi_p) \\ A_R(q, \omega_q) &= 2\pi u_q^2\delta(\omega_q - E_q) + 2\pi v_q^2\delta(\omega_q + E_q), \end{aligned} \quad (2.11)$$

where u_q and v_q are the coherence factors and $E_q = \sqrt{\xi_q^2 + \Delta^2}$ the quasiparticle eigen-energy, Eq. (2.6) can be shown to be equivalent to (2.9) under some general assumptions. Interestingly, in the final result, the coherence factors u and v drop out, and a naive semiconductor representation works in the N-I-S tunneling problem.

We postpone the derivation of Eqs. (2.6) and (2.9) to §2.1.1 and end this section by pointing out the limitations of the tunneling Hamiltonian formalism. There are three primary difficulties with the theory [118, 119]. First, there are ambiguities in decomposing the Hamiltonian into H_L , H_R , and H_T . Second, it is impossible to find a set of single-particle wavefunctions that are complete on the left (right) electrode and, at the same time, orthogonal to all the wavefunctions on the right (left) electrode, so that H_L and H_R commute. Third, the first-order time-dependent perturbation theory does not provide an estimate of the errors. Feuchtwang studied these issues thoroughly to investigate the validity of tunneling Hamiltonian formalism [119]. In the report [119], a procedure to calculate Bardeen's transfer matrix element was established and the matrix element was interpreted as a pseudopotential representing the boundary conditions at the interface. The resulting expression for computing the tunneling current formally agrees with the results obtained from the tunneling Hamiltonian approach. Thus, despite the aforementioned problems, the simple tunneling Hamiltonian picture gives us an answer both easy to understand and consistent with the result of a more sophisticated theory. More details are given in [119] and references therein.

2.1.1 Normal-insulator-superconductor tunneling

Giaever's N-I-S tunneling result [110] that states that the differential conductance is directly proportional to the BCS density of states is somewhat surprising because, when calculating most transition rates in a BCS superconductor, the BCS coherence factors generally have important consequences. It is therefore remarkable that they drop out completely from the expression for the tunneling process. This interesting fact stems from normal electrons tunneling into both electron- and hole-branches of the quasiparticles in the superconductors. We now derive (2.6) and (2.9) via the tunneling Hamiltonian approach [112].

The total Hamiltonian is $H = H_N + H_S + H_T$ (N: normal metal, S: superconductor), where $H_T = \sum_{\mathbf{p}, \mathbf{q}, \sigma} \{T_{\mathbf{p}, \mathbf{q}} c_{\mathbf{p}, \sigma}^\dagger c_{\mathbf{q}, \sigma} + T_{\mathbf{p}, \mathbf{q}}^* c_{\mathbf{q}, \sigma}^\dagger c_{\mathbf{p}, \sigma}\}$. Current flowing through the junction equals to

$$I = \langle \hat{I} \rangle = e \langle \dot{\hat{N}}_S \rangle = \frac{e}{i\hbar} \left\langle [\hat{N}_S, H] \right\rangle = \frac{e}{i\hbar} \left\langle [\hat{N}_S, H_T] \right\rangle = \frac{e}{i\hbar} \sum_{\mathbf{p}, \mathbf{q}, \sigma} \langle T_{\mathbf{p}, \mathbf{q}} c_{\mathbf{p}, \sigma}^\dagger c_{\mathbf{q}, \sigma} - T_{\mathbf{p}, \mathbf{q}}^* c_{\mathbf{q}, \sigma}^\dagger c_{\mathbf{p}, \sigma} \rangle. \quad (2.12)$$

To first-order in H_T , linear response theory gives

$$I = \frac{e}{\hbar^2} \sum_{\mathbf{p}, \mathbf{q}, \sigma} \int_{-\infty}^{\infty} dt' \Theta(t - t') \langle [H_T(t'), T_{\mathbf{p}, \mathbf{q}} c_{\mathbf{p}, \sigma}^\dagger(t) c_{\mathbf{q}, \sigma}(t) - T_{\mathbf{p}, \mathbf{q}}^* c_{\mathbf{q}, \sigma}^\dagger(t) c_{\mathbf{p}, \sigma}(t)] \rangle, \quad (2.13)$$

in which $c_{q, \sigma}^\dagger(t)$, $c_{\mathbf{q}, \sigma}(t)$, $c_{\mathbf{p}, \sigma}^\dagger(t)$, and $c_{\mathbf{p}, \sigma}(t)$ are defined in the interaction picture. The first two operators are the creation and annihilation operators for electrons in the superconducting electrodes, while the last two are those for the electrons in the normal metal.

In the tunneling process where a definite number of electrons are transferred into a superconductor, Josephson's definition [120] of the quasiparticle operators ($\gamma_{e(h), \sigma}$ and $\gamma_{e(h), \sigma}^\dagger$) proved to be superior to the ordinary Bogoliubov operators, for the former create an exact charge e or $-e$ in the

superconductor. The Josephson quasiparticle operators are defined by

$$\begin{aligned}
\gamma_{e,\mathbf{q}\uparrow}^\dagger &= u_{\mathbf{q}} c_{\mathbf{q}\uparrow}^\dagger - v_q S^\dagger c_{-\mathbf{q}\downarrow} \\
\gamma_{h,\mathbf{q}\uparrow}^\dagger &= u_{\mathbf{q}} S c_{\mathbf{q}\uparrow}^\dagger - v_q c_{-\mathbf{q}\downarrow} = S \gamma_{e,\mathbf{q}\uparrow}^\dagger \\
\gamma_{e,\mathbf{q}\downarrow}^\dagger &= u_{\mathbf{q}} c_{-\mathbf{q}\downarrow}^\dagger + v_q S^\dagger c_{\mathbf{q}\uparrow} \\
\gamma_{h,\mathbf{q}\downarrow}^\dagger &= u_{\mathbf{q}} S c_{-\mathbf{q}\downarrow}^\dagger + v_q c_{\mathbf{q}\uparrow} = S \gamma_{e,\mathbf{q}\downarrow}^\dagger,
\end{aligned} \tag{2.14}$$

where S^\dagger and S are the pair creation and annihilation operators. The inverse operators of (2.14) are

$$\begin{aligned}
c_{\mathbf{q}\uparrow}^\dagger &= u_{\mathbf{q}} \gamma_{e,\mathbf{q}\uparrow}^\dagger + v_{\mathbf{q}} \gamma_{h,\mathbf{q}\downarrow} \\
c_{-\mathbf{q}\downarrow}^\dagger &= u_{\mathbf{q}} \gamma_{e,\mathbf{q}\downarrow}^\dagger - v_{\mathbf{q}} \gamma_{h,\mathbf{q}\uparrow}.
\end{aligned} \tag{2.15}$$

Taking into account the chemical potential difference with a bias voltage, $\mu_N - \mu_S = eV$, the unperturbed Hamiltonian and the operators in the interaction picture are written out as

$$\begin{aligned}
H_N &= \mu_N \hat{N}_N + \sum_{p\sigma} \xi_{\mathbf{p}} c_{\mathbf{p}\sigma}^\dagger c_{\mathbf{p}\sigma} \\
H_S &= \mu_S \hat{N}_S + \sum_{q\sigma} E_{\mathbf{q}} \left(\gamma_{e,\mathbf{q}\sigma}^\dagger \gamma_{e,\mathbf{q}\sigma} + \gamma_{h,\mathbf{q}\sigma}^\dagger \gamma_{h,\mathbf{q}\sigma} \right)
\end{aligned} \tag{2.16}$$

$$\begin{aligned}
c_{\mathbf{p}\sigma}^\dagger(t) &= e^{\frac{i}{\hbar} H_N t} c_{\mathbf{p}\sigma}^\dagger e^{-\frac{i}{\hbar} H_N t} = e^{\frac{i}{\hbar} (\xi_{\mathbf{p}} + \mu_N) t} c_{\mathbf{p}\sigma}^\dagger \\
c_{\mathbf{p}\sigma}(t) &= e^{\frac{i}{\hbar} H_N t} c_{\mathbf{p}\sigma} e^{-\frac{i}{\hbar} H_N t} = e^{-\frac{i}{\hbar} (\xi_{\mathbf{p}} + \mu_N) t} c_{\mathbf{p}\sigma}
\end{aligned} \tag{2.17}$$

$$\begin{aligned}
c_{\mathbf{q}\uparrow}^\dagger(t) &= u_{\mathbf{q}} \gamma_{e,\mathbf{q}\uparrow}^\dagger(t) + v_{\mathbf{q}} \gamma_{h,\mathbf{q}\downarrow}(t) = u_{\mathbf{q}} e^{\frac{i}{\hbar} (E_{\mathbf{q}} + \mu_S) t} \gamma_{e,\mathbf{q}\uparrow}^\dagger + v_{\mathbf{q}} e^{-\frac{i}{\hbar} (E_{\mathbf{q}} - \mu_S) t} \gamma_{h,\mathbf{q}\downarrow} \\
c_{\mathbf{q}\uparrow}(t) &= u_{\mathbf{q}} \gamma_{e,\mathbf{q}\uparrow}(t) + v_{\mathbf{q}} \gamma_{h,\mathbf{q}\downarrow}^\dagger(t) = u_{\mathbf{q}} e^{-\frac{i}{\hbar} (E_{\mathbf{q}} + \mu_S) t} \gamma_{e,\mathbf{q}\uparrow} + v_{\mathbf{q}} e^{\frac{i}{\hbar} (E_{\mathbf{q}} - \mu_S) t} \gamma_{h,\mathbf{q}\downarrow}^\dagger \\
c_{\mathbf{q}\downarrow}^\dagger(t) &= u_{\mathbf{q}} \gamma_{e,\mathbf{q}\downarrow}^\dagger(t) - v_{\mathbf{q}} \gamma_{h,\mathbf{q}\uparrow}(t) = u_{\mathbf{q}} e^{\frac{i}{\hbar} (E_{\mathbf{q}} + \mu_S) t} \gamma_{e,\mathbf{q}\downarrow}^\dagger - v_{\mathbf{q}} e^{-\frac{i}{\hbar} (E_{\mathbf{q}} - \mu_S) t} \gamma_{h,\mathbf{q}\uparrow} \\
c_{\mathbf{q}\downarrow}(t) &= u_{\mathbf{q}} \gamma_{e,\mathbf{q}\downarrow}(t) - v_{\mathbf{q}} \gamma_{h,\mathbf{q}\uparrow}^\dagger(t) = u_{\mathbf{q}} e^{-\frac{i}{\hbar} (E_{\mathbf{q}} + \mu_S) t} \gamma_{e,\mathbf{q}\downarrow} - v_{\mathbf{q}} e^{\frac{i}{\hbar} (E_{\mathbf{q}} - \mu_S) t} \gamma_{h,\mathbf{q}\uparrow}^\dagger.
\end{aligned} \tag{2.18}$$

In Eqs (2.16)–Eqs (2.18), $E_{\mathbf{q}} = \sqrt{\xi_{\mathbf{q}}^2 + \Delta_q^2}$ is the quasiparticle excitation energy, μ_N and μ_S are the chemical potentials of the normal metal and the superconductor, $\xi_{\mathbf{p}}$ and $\xi_{\mathbf{q}}$ are the single-particle energies referenced to μ_N and μ_S , respectively, and \hat{N}_N and \hat{N}_S are the number operators of the

normal and superconducting electrodes.

Substituting (2.17) and (2.18) into (2.13) and keeping in mind that $\langle c_{\mathbf{p}\sigma}^\dagger c_{\mathbf{p}\sigma} \rangle = f(\xi_{\mathbf{p}})$, $\langle c_{\mathbf{p}\sigma} c_{\mathbf{p}\sigma}^\dagger \rangle = 1 - f(\xi_{\mathbf{p}})$, $\langle \gamma_{e,\mathbf{q}\sigma}^\dagger \gamma_{e,\mathbf{q}\sigma} \rangle = \langle \gamma_{h,\mathbf{q}\sigma}^\dagger \gamma_{h,\mathbf{q}\sigma} \rangle = f(E_{\mathbf{q}})$, and $\langle \gamma_{e,\mathbf{q}\sigma} \gamma_{e,\mathbf{q}\sigma}^\dagger \rangle = \langle \gamma_{h,\mathbf{q}\sigma} \gamma_{h,\mathbf{q}\sigma}^\dagger \rangle = 1 - f(E_{\mathbf{q}})$, we find that the integral in (2.13), $\int_{-\infty}^{\infty} dt' \theta(t-t') \langle [H_T(t'), T_{\mathbf{p},\mathbf{q}} c_{\mathbf{p},\sigma}^\dagger(t) c_{\mathbf{q},\sigma}(t) - T_{\mathbf{p},\mathbf{q}}^* c_{\mathbf{q},\sigma}^\dagger(t) c_{\mathbf{p},\sigma}(t)] \rangle$, equals to

$$\begin{aligned} i\hbar \frac{u_q^2 f(\xi_{\mathbf{p}})[1-f(E_{\mathbf{q}})]}{\xi_{\mathbf{p}}-E_{\mathbf{q}}+eV+i\delta} &+ i\hbar \frac{v_q^2 f(\xi_{\mathbf{p}})f(E_{\mathbf{q}})}{\xi_{\mathbf{p}}+E_{\mathbf{q}}+eV+i\delta} \\ -i\hbar \frac{u_q^2 f(\xi_{\mathbf{p}})[1-f(E_{\mathbf{q}})]}{\xi_{\mathbf{p}}-E_{\mathbf{q}}+eV-i\delta} &- i\hbar \frac{v_q^2 f(\xi_{\mathbf{p}})f(E_{\mathbf{q}})}{\xi_{\mathbf{p}}+E_{\mathbf{q}}+eV-i\delta} \\ -i\hbar \frac{u_q^2 f(E_{\mathbf{q}})[1-f(\xi_{\mathbf{p}})]}{\xi_{\mathbf{p}}-E_{\mathbf{q}}+eV+i\delta} &- i\hbar \frac{v_q^2 [1-f(\xi_{\mathbf{p}})][1-f(E_{\mathbf{q}})]}{\xi_{\mathbf{p}}+E_{\mathbf{q}}+eV+i\delta} \\ +i\hbar \frac{u_q^2 f(E_{\mathbf{q}})[1-f(\xi_{\mathbf{p}})]}{\xi_{\mathbf{p}}-E_{\mathbf{q}}+eV-i\delta} &+ i\hbar \frac{v_q^2 [1-f(\xi_{\mathbf{p}})][1-f(E_{\mathbf{q}})]}{\xi_{\mathbf{p}}+E_{\mathbf{q}}+eV-i\delta}, \end{aligned} \quad (2.19)$$

Recall $\frac{1}{x-x_0 \pm i\delta} = P \frac{1}{x-x_0} \mp i\pi\delta(x-x_0)$. The principal integrals in (2.19) cancel each other. Only the delta functions are left. Thus,

$$\begin{aligned} I = & \frac{4\pi e}{\hbar} \sum_{\mathbf{p},\mathbf{q}} |T_{\mathbf{p},\mathbf{q}}|^2 \{ u_q^2 [f(\xi_{\mathbf{p}}) - f(E_{\mathbf{q}})] \delta(\xi_{\mathbf{p}} - E_{\mathbf{q}} + eV) \\ & - v_q^2 [1 - f(\xi_{\mathbf{p}}) - f(E_{\mathbf{q}})] \delta(\xi_{\mathbf{p}} + E_{\mathbf{q}} + eV) \}. \end{aligned} \quad (2.20)$$

For a state \mathbf{q}^+ with $E_{\mathbf{q}^+}$ and $u_{\mathbf{q}^+}$, there is another state \mathbf{q}^- with the same energy $E_{\mathbf{q}^-} = E_{\mathbf{q}^+}$ but $\xi_{\mathbf{q}^-} = -\xi_{\mathbf{q}^+}$, such that $|u_{\mathbf{q}^+}|^2 + |u_{\mathbf{q}^-}|^2 = |u_{\mathbf{q}^+}|^2 + |v_{\mathbf{q}^+}|^2 = 1$, and $|v_{\mathbf{q}^+}|^2 + |v_{\mathbf{q}^-}|^2 = |v_{\mathbf{q}^+}|^2 + |u_{\mathbf{q}^+}|^2 = 1$. Moreover, because \mathbf{q}^+ and \mathbf{q}^- are both near the same point on the Fermi surface, $|T_{\mathbf{p},\mathbf{q}^+}| \approx |T_{\mathbf{p},\mathbf{q}^-}|$. Thus, when summing over all possible \mathbf{q} values, the coherence factors u_q^2 and v_q^2 drop out, and

$$I = \frac{4\pi e}{\hbar} \sum_{\mathbf{p},\mathbf{q}} |T_{\mathbf{p},\mathbf{q}}|^2 [f(\xi_{\mathbf{p}}) - f(E_{\mathbf{q}})] \delta(\xi_{\mathbf{p}} - E_{\mathbf{q}} + eV) - [1 - f(\xi_{\mathbf{p}}) - f(E_{\mathbf{q}})] \delta(\xi_{\mathbf{p}} + E_{\mathbf{q}} + eV). \quad (2.21)$$

Recall that in Eq. (2.7), assuming specular transmission and bare parabolic band structures, the tunneling matrix element is approximately

$$|T_{\mathbf{p},\mathbf{q}}|^2 \approx \frac{\partial \xi_{\mathbf{p}}}{\partial \mathbf{p}_L} \frac{\partial \xi_{\mathbf{q}}}{\partial \mathbf{q}_L} |D(\xi_{\mathbf{p}}, \mathbf{p}_T)|^2 \delta(\mathbf{p}_T - \mathbf{q}_T), \quad (2.22)$$

where the subscript L indicates the longitudinal component and T the transverse component of the momenta. When converting the momentum summation in (2.21) into energy integrals, assuming $|D|^2$ varies slowly, the tunneling current can be expressed as

$$\begin{aligned} I(V) \propto & |D|^2 N_S(0) \int_{-\infty}^{\infty} d\xi_p \int_0^{\infty} dE_q \left(\frac{\partial \xi_q}{\partial E_q} \right) \{ [f(\xi_p) - f(E_q)] \delta(\xi_p - E_q + eV) \\\\ & - [1 - f(\xi_p) - f(E_q)] \delta(\xi_p + E_q + eV) \}, \end{aligned} \quad (2.23)$$

where $N_S(0)$ is the density of states of the superconducting electrode around the Fermi level. Define

$$\frac{N_S(E_q)}{N_S(0)} = \left| \frac{\partial \xi_q}{\partial E_q} \right| = \begin{cases} \frac{|E_q|}{\sqrt{E_q^2 - \Delta^2}} & (|E_q| > \Delta) \\ 0 & (|E_q| < \Delta), \end{cases} \quad (2.24)$$

where we have assumed an s -wave superconductor so that Δ is independent of \mathbf{q} . We note that by using $1 - f(-\xi_p - eV) = f(\xi_p + eV)$, we arrive at the Giaever's simple formula:

$$\begin{aligned} I(V) \propto & |D|^2 \int_{-\infty}^{\infty} d\xi_p \{ N_S(\xi_p + eV) [f(\xi_p) - f(\xi_p + eV)] \Theta(\xi_p + eV) \\\\ & - N_S(-\xi_p - eV) [1 - f(\xi_p) - f(-\xi_p - eV)] [1 - \Theta(\xi_p + eV)] \} \\\\ \propto & |D|^2 \int_{-\infty}^{\infty} d\xi N_S(\xi + eV) [f(\xi) - f(\xi + eV)], \end{aligned} \quad (2.25)$$

The subscript \mathbf{p} is dropped in the very last equation. At low temperatures, (2.25) reduces to

$$\frac{dI}{dV}(V) \propto |D|^2 N_S(eV). \quad (2.26)$$

Thus, measuring the differential conductance spectrum is equivalent to measuring the superconducting density of states.

The transfer Hamiltonian formalism, and hence Eq.(2.26), applies only to tunneling processes with a large barrier height. Furthermore, in deriving (2.26) we sum over the momenta values for both electrodes, so the momentum-dependent information of the tunneling spectral weight is lost. As a result, Eqs.(2.25) and (2.26) are valid only for tunneling into a conventional superconductor whose pairing potential is isotropic, or to those processes that sample over all possible momentum

distribution in an unconventional superconductor, such as the c -axis tunneling of a d -wave superconductor where the surface normal direction of the superconducting electrode aligns along its c crystalline axis.

In the following section, we will introduce another formalism, the generalized Blonder-Tinkham-Klapwijk (BTK) theory, that goes beyond the tunneling limit and analyzes tunneling processes with an arbitrary barrier strength within the same framework. More importantly, BTK theory allows us to simulate the tunneling spectra that retain the momentum-dependent information of an unconventional superconductor. For instance, the zero-bias conductance peak that appears in the tunneling spectrum taken on a $\{110\}$ -oriented d -wave superconductor reveals existence of nodes and the phase change of the d -wave order parameter, while the U-shape spectral gap in the $\{100\}$ tunneling spectra of a d -wave superconductor reveals the maximum value of the pairing potential. Thus, BTK theory serves as an important tool to extract the pairing symmetry and pairing potential of any unconventional superconducting order parameter.

2.2 Pairing symmetry and tunneling spectra: generalized Blonder-Tinkham-Klapwijk (BTK) model

Another way of treating the N-I-S tunneling process is to view it as a scattering problem. Analogous to solving the Schrodinger equation in the N-I-N scattering problem, here we solve the Bogoliubov–de Gennes (BdG) equation where the superconducting order parameter serves as a position-dependent off-diagonal potential $\Delta(x)$ and the interface as a diagonal delta-function potential with a variable barrier strength $H\delta(x)$. This approach has the advantage of capturing an important process that the tunneling Hamiltonian failed to, *i.e.*, the Andreev reflection in the low-barrier N-S tunneling limit [121]. Andreev realized that, when an electron (or hole) of energy E approaches the N/S interface from the N region, it will be reflected as a hole (or electron) where $|\Delta|$ rises above E , provided that the length scale over which Δ varies is much larger than the Fermi wavelength. Andreev reflection arises naturally from the Bogoliubov–de Gennes (BdG) equation with a spatially

slowly varying order parameter and a vanishing barrier strength [121].

To take into account the Andreev process and to generalize the N-I-S tunneling problem to account for arbitrary barrier strength, Blonder *et al.* [122] proposed to calculate the tunneling current through the use of the BdG equation. In the BTK formalism, the BdG equation is set up such that the interface between N and S is modeled as a delta function with a variable dimensionless barrier strength $Z = mH/\hbar^2 k_f$. The order parameter $\Delta(x)$ is approximately zero on the N side and a constant on the S side. By matching the boundary conditions, the probability current of normal reflection $B(E)$ and that of Andreev reflection $A(E)$ are derived [Appendix A]. The tunneling current as a function of the bias voltage V is given in terms of $A(E)$ and $B(E)$,

$$I \propto N_N \int_{-\infty}^{\infty} dE [f(E - eV) - f(E)] [1 + A(E) - B(E)]. \quad (2.27)$$

While ordinary reflection associated with $B(E)$ reduces the tunneling current, Andreev reflection associated with $A(E)$ enhances it by transmitting a Cooper pair over the interface for one incident electron.

The Andreev process not only plays an important role in the N-I-S tunneling for a conventional BCS *s*-wave superconductor in the low-barrier limit, but is also fundamental in the formation of a novel zero-energy surface state of an unconventional superconductor [123]. Kashiwaya and Tanaka generalized the BTK formalism [124, 125, 126] to study the important consequence of this bound state—the zero-bias conductance peak (ZBCP) in the tunneling spectra. It is the ZBCP feature that makes tunneling spectroscopy a phase-sensitive measurement for superconductors with unconventional pairing symmetries.

In this section, we will review the generalized BTK formalism, discuss the origin of the zero-energy bound state and the ZBCP, and present the numerical simulations of the quasiparticle tunneling spectra on a *d*-wave superconductor along different crystalline orientations. We will also discuss the tunneling results of mixed pairing symmetry superconductors and point out the important signatures in the spectra. A summary of the original BTK formalism for tunneling into an *s*-wave

superconductor is provided in Appendix A as a reference.

2.2.1 Generalized Blonder-Tinkham-Klapwijk formalism—A mean-field description

The Bogoliubov–de Gennes (BdG) equation generalizes the BCS formalism to treat superconductors with spatially varying pairing strength, chemical potential, and Hartree potential. In an inhomogeneous anisotropic even-parity (such as *d*-wave) superconductor, the Bogoliubov–de Gennes (BdG) equation reads [127]

$$\begin{aligned} Ef(\mathbf{r}_1) &= \hat{h}_0(\mathbf{r}_1)f(\mathbf{r}_1) + \int d\mathbf{r}_2 \Delta(\mathbf{r}_1, \mathbf{r}_2)g(\mathbf{r}_2) \\ Eg(\mathbf{r}_1) &= -\hat{h}_0(\mathbf{r}_1)g(\mathbf{r}_1) + \int d\mathbf{r}_2 \Delta(\mathbf{r}_1, \mathbf{r}_2)f(\mathbf{r}_2). \end{aligned} \quad (2.28)$$

To be consistent with the notation of [124, 125], the quasiparticles wavefunction is written as two-component column vector,

$$\Psi(\mathbf{r}_1) = \begin{bmatrix} f(\mathbf{r}_1) \\ g(\mathbf{r}_1) \end{bmatrix}. \quad (2.29)$$

In (2.28), $\hat{h}_0(\mathbf{r}_1) = -\hbar^2 \nabla_{\mathbf{r}_1}^2 / 2m - \mu + V(\mathbf{r}_1)$, μ is the chemical potential, $V(\mathbf{r}_1)$ the Hartree potential, and $\Delta(\mathbf{r}_1, \mathbf{r}_2)$ the pairing potential.

Rewrite the pairing potential in terms of the relative coordinates $\mathbf{r} = \mathbf{r}_1 - \mathbf{r}_2$ and $\mathbf{R} = (\mathbf{r}_1 + \mathbf{r}_2)/2$,

$$\Delta(\mathbf{r}_1, \mathbf{r}_2) = \tilde{\Delta}(\mathbf{r}, \mathbf{R}),$$

and Fourier transform $\tilde{\Delta}(\mathbf{r}, \mathbf{R})$ into

$$\Delta(\mathbf{k}, \mathbf{R}) = \int d\mathbf{r} e^{-i\mathbf{k}\cdot\mathbf{r}} \tilde{\Delta}(\mathbf{r}, \mathbf{R}) \equiv \Delta(\hat{\gamma}, \mathbf{R}), \quad (2.30)$$

where $\hat{\gamma} = \mathbf{k}/|\mathbf{k}| \approx \mathbf{k}/k_f$ denotes the direction of the quasiparticle momentum and k_f is the magnitude of the Fermi momentum. Then $\Delta(\mathbf{k}, \mathbf{R})$ describes, in the quasiclassical approximation,

the pairing potential which quasiparticles with momentum \mathbf{k} experience at position \mathbf{R} . Introducing two envelope functions $u(\hat{\gamma}, \mathbf{r}_1)$ and $v(\hat{\gamma}, \mathbf{r}_1)$ to factor away the fast atomic-scale oscillations

$$\Psi(\mathbf{r}_1) = \begin{bmatrix} f(\mathbf{r}_1) \\ g(\mathbf{r}_1) \end{bmatrix} = e^{ik_f \hat{\gamma} \cdot \mathbf{r}_1} \begin{bmatrix} u(\hat{\gamma}, \mathbf{r}_1) \\ v(\hat{\gamma}, \mathbf{r}_1) \end{bmatrix} \quad (2.31)$$

and using Eqs. (2.30) and (2.31), the BdG equation (2.28) is recast into

$$\begin{aligned} Eu(\hat{\gamma}, \mathbf{r}_1) &= -i\frac{\hbar^2 k_f}{m} \hat{\gamma} \cdot \nabla_{\mathbf{r}} u(\hat{\gamma}, \mathbf{r}_1) + \Delta(\hat{\gamma}, \mathbf{r}_1) v(\hat{\gamma}, \mathbf{r}_1) \\ Ev(\hat{\gamma}, \mathbf{r}_1) &= i\frac{\hbar^2 k_f}{m} \hat{\gamma} \cdot \nabla_{\mathbf{r}} v(\hat{\gamma}, \mathbf{r}_1) + \Delta^*(\hat{\gamma}, \mathbf{r}_1) u(\hat{\gamma}, \mathbf{r}_1). \end{aligned} \quad (2.32)$$

In deriving (2.32) only terms of the lowest order in $(k_f \xi_0)^{-1}$ are retained, since the scale for spatial variation of the pairing potential given by the coherence length ξ_0 is much larger than k_f^{-1} .

Following the logic of the original BTK theory [Appendix A], we first identify the allowed elastic tunneling processes across the N-I-S junction and write down the incident, reflected, and transmitted wavefunctions in the normal and the superconducting electrode. By matching the boundary conditions at the interface, the Andreev reflection coefficient $a(E, \theta)$ and the normal reflection coefficient $b(E, \theta)$ are extracted to compute the differential tunneling conductance.

For electrons incident from the normal-metal side with energy E and an angle of incidence θ_N , there are four possible trajectories [Fig. 2.1]. They can be Andreev reflected as holes (A) with an angle θ_N , normal reflected as electrons (B) with an angle of reflection $\theta'_N = \theta_N$, transmitted as electron-like quasiparticles (C) with an angle of refraction θ_S , or transmitted as hole-like quasiparticles (D) with an angle $\theta_S = \theta'_S$. In the normal electrode, the unit vector of the momentum of the incident electrons is denoted as $\hat{\gamma}_N$, that of the reflected electrons as $\hat{\gamma}'_N$, and the pairing potential $\Delta(\hat{\gamma}_N, \mathbf{R}) = \Delta(\hat{\gamma}'_N, \mathbf{R}) = 0$. Solving (2.32) gives us the form of the wavefunction on the N side

$$\Psi_N(\mathbf{r}) = e^{ik_f \hat{\gamma}_N \cdot \mathbf{r}} e^{i\frac{E}{\hbar k_f N/m} \hat{\gamma}_N \cdot \mathbf{r}} \begin{bmatrix} 1 \\ 0 \end{bmatrix}$$

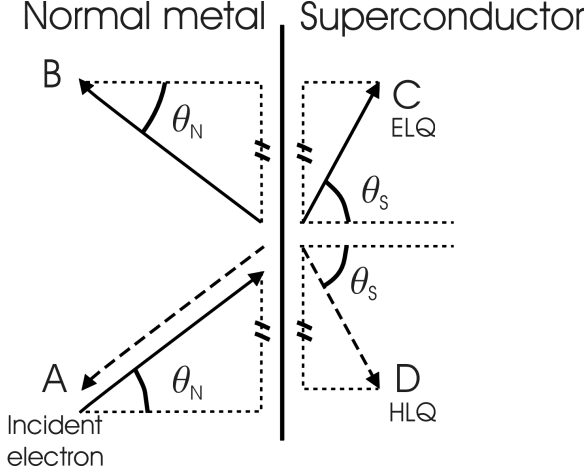


Figure 2.1: Adapted from Fig. 1(b) of [125]. Schematic diagram of the transmission and reflection processes at the N-I-S interface. For an electron incident from the normal metal with an angle of incidence θ_N , it can be Andreev-reflected as a hole (A), normal-reflected as an electron (B) with an angle θ_N , transmitted as an electron-like quasiparticle (ELQ) (C) with an angle θ_S , or transmitted as a hole-like quasiparticle (HLQ) (D). All the electron-like excitations are denoted by solid lines and hole-like excitations dashed lines. The arrows indicate the directions of the group velocities of the particles, and note that, for hole-like quasiparticles, the wave vector and the group velocity point in the opposite directions. The components of the wave vectors parallel to the interface are conserved.

$$+a(E) e^{ik_{fN} \hat{\gamma}_N \cdot \mathbf{r}} e^{-i\frac{E}{\hbar k_{fN}/m} \hat{\gamma}_N \cdot \mathbf{r}} \begin{bmatrix} 0 \\ 1 \end{bmatrix} + b(E) e^{ik_{fN} \hat{\gamma}'_N \cdot \mathbf{r}} e^{i\frac{E}{\hbar k_{fN}/m} \hat{\gamma}'_N \cdot \mathbf{r}} \begin{bmatrix} 1 \\ 0 \end{bmatrix}, \quad (2.33)$$

where a is the amplitude for Andreev reflection, b the amplitude for normal reflection, and k_{fN} the Fermi momentum in the normal electrode. Since $k_{fN} \gg Em/\hbar k_{fN}$, (2.33) is approximately

$$\Psi_N(\mathbf{r}) \approx e^{ik_{fN} \hat{\gamma}_N \cdot \mathbf{r}} \begin{bmatrix} 1 \\ 0 \end{bmatrix} + a(E) e^{ik_{fN} \hat{\gamma}_N \cdot \mathbf{r}} \begin{bmatrix} 0 \\ 1 \end{bmatrix} + b(E) e^{ik_{fN} \hat{\gamma}'_N \cdot \mathbf{r}} \begin{bmatrix} 1 \\ 0 \end{bmatrix}. \quad (2.34)$$

In the superconducting electrode, we denote the unit vector of the momentum of the transmitted electron-like quasiparticles (ELQ) as $\hat{\gamma}_S$, that of the transmitted hole-like quasiparticles (HLQ) as $\hat{\gamma}'_S$, the pairing potential experienced by the "ELQ's" as $\Delta(\hat{\gamma}_S, \mathbf{R}) = |\Delta(\hat{\gamma}_S, \mathbf{R})| e^{i\phi(\hat{\gamma}_S)} = |\Delta_+| e^{i\phi_+}$, and that experienced by the "HLQ's" as $\Delta(\hat{\gamma}'_S, \mathbf{R}) = |\Delta(\hat{\gamma}'_S, \mathbf{R})| e^{i\phi(\hat{\gamma}'_S)} = |\Delta_-| e^{i\phi_-}$. Then the

wavefunction for the transmitted electron-like and hole-like quasiparticles reads

$$\Psi_S(\mathbf{r}) = c(E) e^{ik_{fS}\hat{\gamma}_S \cdot \mathbf{r}} e^{i\frac{\sqrt{E^2 - |\Delta_+|^2}}{\hbar k_{fS}/m} \hat{\gamma}'_S \cdot \mathbf{r}} \begin{bmatrix} \sqrt{\frac{E + \sqrt{E^2 - |\Delta_+|^2}}{2E}} \\ e^{-i\phi_+} \sqrt{\frac{E - \sqrt{E^2 - |\Delta_+|^2}}{2E}} \end{bmatrix} \\ + d(E) e^{ik_{fS}\hat{\gamma}'_S \cdot \mathbf{r}} e^{-i\frac{\sqrt{E^2 - |\Delta_-|^2}}{\hbar k_{fS}/m} \hat{\gamma}'_S \cdot \mathbf{r}} \begin{bmatrix} e^{i\phi_-} \sqrt{\frac{E - \sqrt{E^2 - |\Delta_-|^2}}{2E}} \\ \sqrt{\frac{E + \sqrt{E^2 - |\Delta_-|^2}}{2E}} \end{bmatrix} \quad (2.35)$$

$$\Psi_S(\mathbf{r}) \approx c(E) e^{ik_{fS}\hat{\gamma}_S \cdot \mathbf{r}} \begin{bmatrix} \sqrt{\frac{E + \sqrt{E^2 - |\Delta_+|^2}}{2E}} \\ e^{-i\phi_+} \sqrt{\frac{E - \sqrt{E^2 - |\Delta_+|^2}}{2E}} \end{bmatrix} + d(E) e^{ik_{fS}\hat{\gamma}'_S \cdot \mathbf{r}} \begin{bmatrix} e^{i\phi_-} \sqrt{\frac{E - \sqrt{E^2 - |\Delta_-|^2}}{2E}} \\ \sqrt{\frac{E + \sqrt{E^2 - |\Delta_-|^2}}{2E}} \end{bmatrix}, \quad (2.36)$$

where k_{fS} is the Fermi momentum in the superconducting electrode.

The insulating interface is modeled as a δ -function Hartree potential $V(\mathbf{r}) = H\delta(\mathbf{r})$. By solving for the coefficients $a(E) - d(E)$ under the boundary conditions (1) $\Psi^N(0) = \Psi^S(0) = \Psi(0)$ and (2) $\frac{\hbar}{2m} \frac{d\Psi^S(0)}{dx} - \frac{\hbar}{2m} \frac{d\Psi^N(0)}{dx} = H\Psi(0)$, and taking into account the momentum conservation parallel to the interface, we arrive at the following expression for the probability current tunneling across the N-I-S junction at zero temperature:

$$\sigma_S(E, \theta_N) \equiv \sigma_N \left[1 + |a(E, \theta_N)|^2 - |b(E, \theta_N)|^2 \right] = \sigma_N \frac{1 + \sigma_N |\Gamma_+|^2 + (\sigma_N - 1) |\Gamma_+ \Gamma_-|^2}{|1 + (\sigma_N - 1) \Gamma_+ \Gamma_- e^{i(\phi_- - \phi_+)}|^2}, \quad (2.37)$$

where

$$\begin{aligned} \Gamma_\pm &= \frac{E - \sqrt{E^2 - |\Delta_\pm|^2}}{|\Delta_\pm|}, \\ \sigma_N &= \frac{4 \frac{k_{fS}}{k_{fN}} \frac{\cos\theta_S}{\cos\theta_N}}{(1 + \frac{k_{fS}}{k_{fN}} \frac{\cos\theta_S}{\cos\theta_N})^2 + 4(\frac{Z}{\cos\theta_N})^2}, \\ Z &= \frac{mH}{\hbar^2 k_{fN}}. \end{aligned}$$

In an s -wave superconductor where $\Delta_+ = \Delta_- = \Delta$, Eq.(2.37) reduces to the original BTK formula (A.12), (A.13), and (A.14).

2.2.2 Tunneling spectra of a d -wave superconductor and the Andreev bound state

Having derived (2.37), we can now calculate the tunneling conductance spectra of superconductors with unconventional pairing symmetries in a real scanning tunneling spectroscopy (STS) experiment. Taking into account a finite transverse momentum distribution for the incident particles by considering a finite tunneling cone β , the resulting tunneling conductance is

$$\frac{dI}{dV}(V) \propto \int d\theta \left[1 + |a(E, \theta)|^2 - |b(E, \theta)|^2 \right] e^{-\frac{\theta^2}{\beta^2}}. \quad (2.38)$$

For simplicity, $k_{f_S}/k_{f_N} \approx 1$ is assumed, and thus $\theta_N \approx \theta_S \equiv \theta$. Since in the STS configuration we usually operate in the tunneling limit, the following simulations are done with a large effective barrier height. We focus on the spectra of d -, $(d+s)$ -, $(d+is)$ -, and $(d+id')$ -wave superconductors which are the most relevant to later chapters on the hole-doped cuprates.

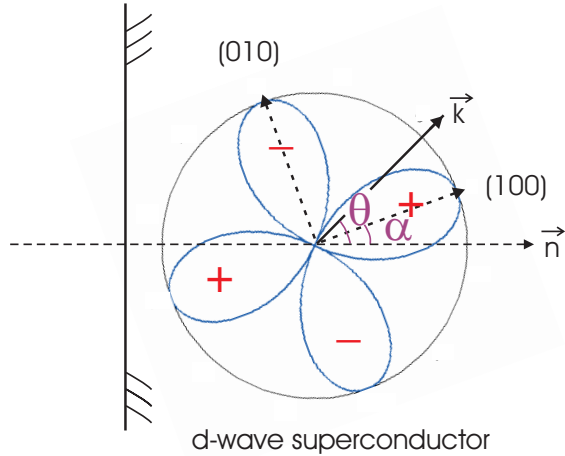


Figure 2.2: Momentum dependence of a d -wave pairing potential. $\Delta(\mathbf{k}) = \Delta(\theta) = \Delta_d \cos(2\theta - 2\alpha)$. θ is the angle between the surface normal and the wave vector \mathbf{k} , and α is the angle between the surface normal and (100) -axis of the superconductor.

In a d -wave superconductor, $\Delta(\mathbf{k}) = \Delta(\theta) = \Delta_d \cos(2\theta)$ [Fig. 2.2]. The pairing potentials Δ_+

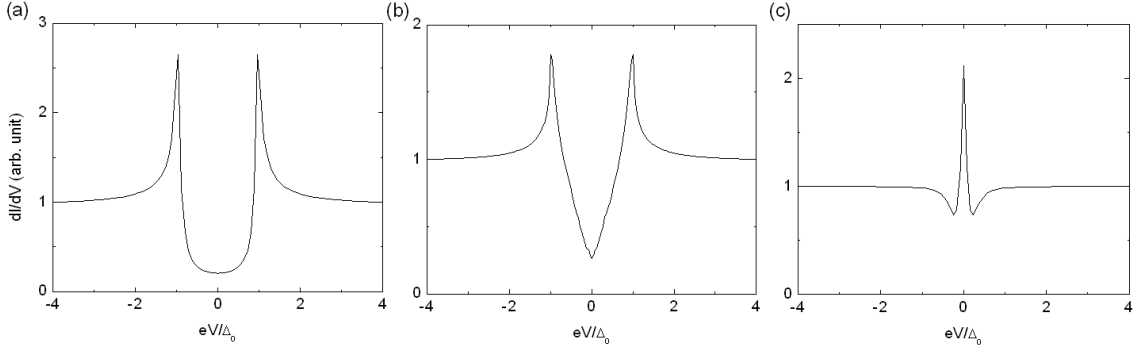


Figure 2.3: Simulated tunneling spectra of a d -wave superconductor taken with the average quasi-particle momentum parallel to (a) the anti-nodal (100) direction, (b) the c -axis (001) direction, and (c) the nodal (110) direction. The scanning tunneling spectroscopy configuration is usually operated in the tunneling limit. Thus, these BTK simulation curves are carried out with a large effective barrier height.

and Δ_- that the ELQ's and the HLQ's experience are

$$\begin{aligned}\Delta_+ &= \Delta_d \cos(2\theta - 2\alpha) \\ \Delta_- &= \Delta_d \cos(2\theta + 2\alpha),\end{aligned}\tag{2.39}$$

where α is the angle between the normal vector of the interface and (100)-axis of the superconductor. When the normal vector \vec{n} of the interface is oriented along the anti-nodal (100) or (010) direction (*i.e.*, $\alpha = 0$ and $\Delta_+ = \Delta_-$), the tunneling spectrum shows a U-shape feature as in a BCS superconductor, with two coherence peaks located at the maximal pairing potential $\pm\Delta_d$ and no density of states found within the gap [Fig. 2.3(a)]. When \vec{n} is parallel to the (001)-axis, the incident electrons sample over all possible θ values and hence the tunneling cone completely opens up in this case ($\beta \approx \infty$). In addition, the conservation of the momentum parallel to the interface implies that $\Delta_+ = \Delta_-$ for c -axis tunneling. The resulting spectrum has a V-shape feature with the coherence peaks located at $\pm\Delta_d$ [Fig. 2.3(b)].

Most interestingly, when the normal vector \vec{n} of the junction surface is oriented along the nodal (110) direction, the pairing potentials experienced by the ELQ's and the HLQ's are opposite in sign, $\Delta_+ = -\Delta_-$. Consequently, the tunneling spectrum displays a conductance peak at zero bias [Fig. 2.3(c)]. In the high-barrier low-transmission limit ($\sigma_N \rightarrow 0$), the normalized tunneling conductance reduces to the surface density of states [125, 126]. Therefore, the zero-bias conductance

peak (ZBCP) reflects the existence of a zero-energy surface state, called the Andreev bound state (ABS), at the superconductor-insulator interface.

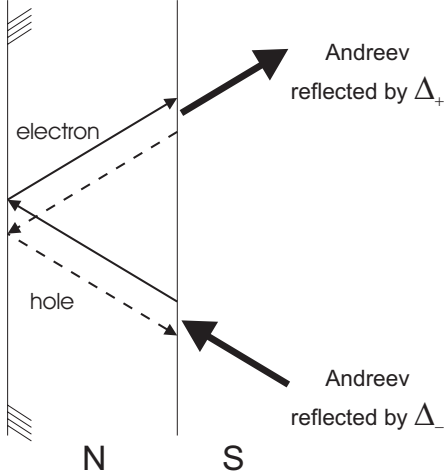


Figure 2.4: Trajectories of the Andreev bound states at the surface of a d -wave superconductor. (Taken from Fig. 7 of [126].) The existence of the surface states is stable even in the limit of vanishing normal metallic layer. The solid lines denote the trajectories of the electrons, and the dashed lines the trajectories of the holes. When the electrons Andreev reflected from the N/S interface, they experience a pairing potential Δ_+ , while the Andreev reflection of holes experiences Δ_- . When the normal vector of the interface is parallel to the nodal (110) direction, the two pairing potentials have equal magnitude but opposite signs, giving rise to a bound state at $E = 0$.

Mathematically, the energy of the bound state is determined by the zero of the denominator in (2.37),

$$1 - \Gamma_+ \Gamma_- e^{i(\phi_- - \phi_+)} = 0, \sigma_N \rightarrow 0. \quad (2.40)$$

Given that $\phi_- - \phi_+ = \pi$ and $|\Delta_+| = |\Delta_-|$, the bound state energy is always at $E = 0$. Physically, an intuitive visualization of the formation of ABS at the surface of a d -wave superconductor is given by [126]. As illustrated in Fig. 2.4, assume that the surface of the superconductor is capped with a thin layer of normal metal of thickness d_N . The trajectories of the quasiparticles form closed loops through two Andreev reflections at the N/S interface (one converting electrons to holes and the other converting holes to electrons) and two specular reflections at the surface. Applying the quantization condition that the phase shift is a multiple of 2π for a bound quasiparticle along a closed path of the classical trajectory, and taking into account that the phase shifts picked up by the two Andreev reflections are different because of different pairing potentials the ELQ's and the HLQ's experience,

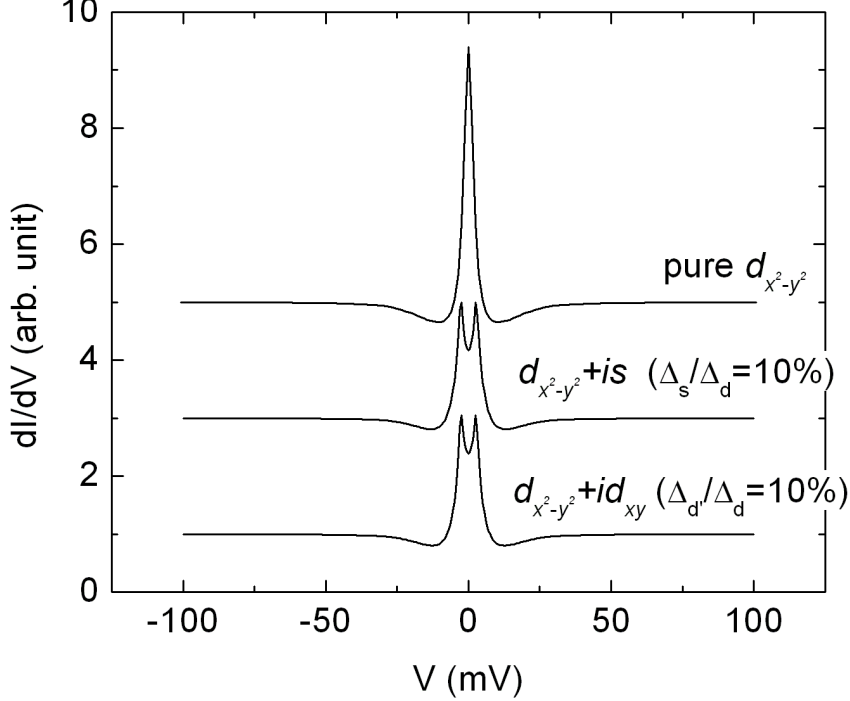


Figure 2.5: Tunneling spectra taken along the nodal direction for different pairing symmetries. The spectra of pure d -wave and $(d + is)$ -wave superconductors have been shifted for clarity. As shown in the figure, a small imaginary component (*e.g.*, 10% the gap value of a 30 meV d -wave superconductor) can produce appreciable splitting (> 6 meV) of the zero-bias conductance peak (ZBCP). For a $(d + id')$ superconductor, the amount of the ZBCP splitting is comparable to that of a $(d + is)$ superconductor, provided that the percentage of symmetry mixing is the same. For a $(d + s)$ -wave superconductor (not shown), the shape and width of the ZBCP is indistinguishable from that of a pure d -wave superconductor within experimental resolution.

we obtain the equation that dictates the bound state energy:

$$-\tan^{-1}\left(\frac{\sqrt{|\Delta_+|^2 - E^2}}{E}\right) - \tan^{-1}\left(\frac{\sqrt{|\Delta_-|^2 - E^2}}{E}\right) - (\phi_+ - \phi_-) + 2\phi_N = 2n\pi, \quad (2.41)$$

where n is an integer and ϕ_N is the phase shift accumulated when traveling around the metallic layer, $\phi_N = md_N E / (\hbar^2 k_{fN})$. In a real system where the thickness of the metallic layer is vanishingly small, the quantization condition (2.41) reduces to (2.40), and N-I-S tunneling along (110) into these zero-energy surface states gives rise to the ZBCP in the conductance spectrum.

In the presence of a small imaginary component mixed to the predominantly d -wave order parameter, *e.g.*, $d + is$, the degeneracy of the zero-energy bound states is lifted because of broken time-reversal symmetry. The resulting splitting in the ZBCP provides an estimate of the weight of

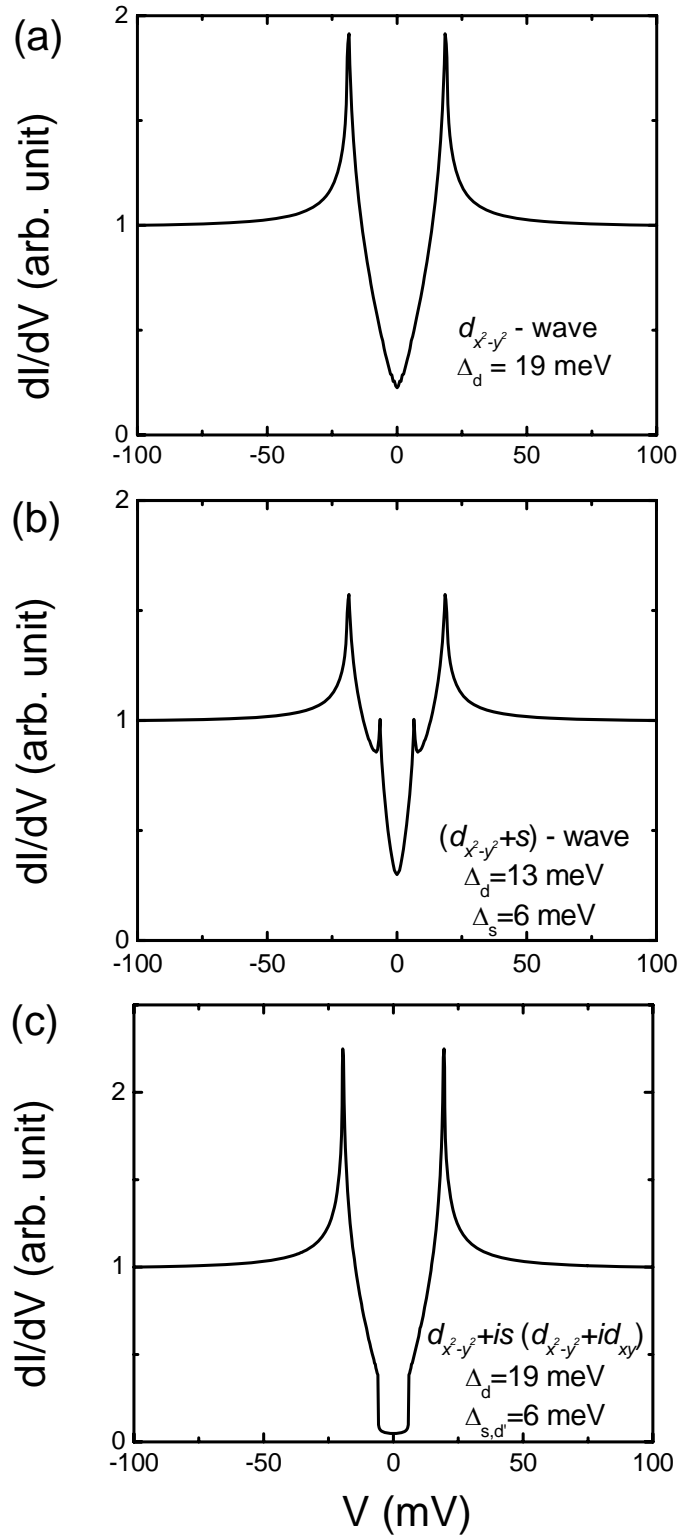


Figure 2.6: Tunneling spectra taken along the c -axis. (a) Tunneling spectrum of a pure d -wave, (b) a $(d+s)$ -wave, and (c) a $(d+is)$ or $(d+id')$ superconductor. The gap values are chosen so that the position of the coherence peaks and the subgap features stays the same for all three figures.

the imaginary component [Fig. 2.5(a)]. On the contrary, as shown in [Fig. 2.5(b)], because time-reversal symmetry is still respected, a small real s -component mixing does not break the degeneracy. Therefore, tunneling spectra taken along the nodal direction cannot distinguish between d -wave and $d+s$ -wave pairing symmetry.

Although the existence of a small s -wave component does not modify the shape and the magnitude of the ZBCP, it does have other observational consequences on the tunneling spectra. For example, tunneling spectra along (100) and (010) reveal two different gap values, $\Delta_d \pm \Delta_s$. Similarly, the c -axis tunneling spectrum of a $(d+s)$ -wave superconductor shows two corresponding sets of coherence peaks [Fig. 2.6(b)] in contrast to that of the pure d -wave superconductor [Fig. 2.6(a)]. For comparison, the c -axis tunneling spectrum of a $(d+is)$ -wave superconductor is plotted in Fig. 2.6(c). Owing to the small imaginary component mixing, the low-energy excitation is fully gapped within the secondary pairing potential Δ_s (or $\Delta_{d'}$). Therefore, around zero bias the c -axis tunneling shows a small U-shape feature [Fig. 2.6(c)] in contrast to the V-shape feature in the d - and $(d+s)$ -wave cases.

As a final remark, we note that the generalized BTK theory is based on the mean-field Bogoliubov-de Gennes equation. Therefore, quantum/thermal fluctuations and residual interactions, such as quasiparticle scattering and quasiparticle coupling with the bosonic modes of the system, are not accounted for.

In conclusion, the existence of a zero-energy Andreev surface state turns quasiparticle tunneling spectroscopy into a phase-sensitive technique to uncover the sign change of the order parameter across the nodal axis in an unconventional superconductor. At the mean-field level, the symmetry of the order parameter, the magnitude of the pairing potential and the amount of secondary symmetry mixing can be extracted by means of the generalized Blonder-Tinkham-Klapwijk formalism. We will present an example of applying the BTK formalism to study the tunneling spectra of the hole-doped cuprate $\text{YBa}_2\text{Cu}_3\text{O}_{6+\delta}$ [§4], which demonstrates that, for YBCO, mean-field theory is a good approximation and the Bogoliubov quasiparticle description captures most of the important physics in the superconducting state. In contrast, deviation from the BTK formalism is observed in the

electron-doped $\text{Sr}_{1-x}\text{La}_x\text{CuO}_2$, indicating that the mean-field approximation is not adequate for this compound. The implication of the breakdown will be discussed in detail in §5 and §6.

Chapter 3

Scanning Tunneling Microscopy: Principle and Instrumentation

Scanning tunneling microscopy (STM) has been proven to be an extremely powerful tool for studying the electronic structures of solid-state systems. The STM topographic images, assisted by other surface analysis techniques with chemical specificity, lead to the structural determination of clean and adsorbate-covered surfaces. For example, the first atomically resolved STM image in history confirmed the Si(111) 7×7 surface reconstruction [128] and identified Takayanagi's dimer-adatom-stacking-fault model [129] as the correct Si(111) 7×7 surface structure. Combining scanning tunneling microscopy with spectroscopy, a number of beautiful experiments were carried out, *e.g.*, to visualize the standing wave pattern of the two-dimensional surface state electrons in an artificial quantum corral [130, 131], to provide the first direct spectroscopic signature of the Kondo resonance of an isolated magnetic impurity in a non-magnetic host [132], and to map out the electronic density of states inside a single vortex core of the Abrikosov flux lattice for a conventional type II superconductor [133, 134]. Furthermore, spatially resolved tunneling spectroscopy gave invaluable insights into open questions in the physics of strongly correlated electronic systems, such as the correlation between charge ordering and the metal-insulator transition in magnetic manganites [135] and the various ordering phases in high-temperature cuprate superconductors. In this chapter, we summarize the operating principles of scanning tunneling microscopy/spectroscopy and then present our development of a magnetic-field-compatible, cryogenic, variable-temperature STM for the study of cuprate superconductors.

3.1 Brief review

Scanning tunneling microscopy (STM) was invented by Binnig and Rohrer in 1981 [136, 137]. By integrating scanning capacity into vacuum tunneling capability, STM enables us to image the surfaces of conducting samples and study their local electronic properties down to atomic scales. Useful information on the physics of STM, general design and instrumentation principles, and the extension to other scanning probe techniques can be found in references [138, 139].

The essential components of an STM include a sharp probing tip; a piezoelectric scanning unit, which controls the vertical and lateral movement of the tip; a coarse positioning unit, which brings the tip-sample separation to within the tunneling range ($\sim \text{\AA}$); a vibration isolation stage; and a set of electronics, which detects the small tunneling current ($\sim 10 \text{ pA} - 1 \text{ nA}$), controls the piezo-tube scanner with feedback, and drives the coarse positioning [Fig. 3.1].

Figure 3.1 is a schematic diagram of our STM system. The arrows denote the travel direction of the commands and the electronic signals. For instance, the STM digital feedback controller takes the output signal from the current pre-amp, compares the signal level with the preset value, calculates the response according to the user-defined feedback parameters, and sends the feedback voltage through an analog to digital converter to the high-voltage amplifier, which then magnifies the input signal to drive the piezo scanner. On the one hand, the controller communicates with the computer to change the experimental settings, such as the bias voltage, the tunneling current set point, the scanning range, scanning speed and the proportional/integral (P-I) gain for the feedback algorithm. On the other hand, it also transfers the feedback signal and tunneling current signal back to the computer to generate topographic images and tunneling spectra.

To initiate the tunneling process, the STM tip is brought to within several angstroms from the sample surface by the coarse approach walker. Applying a bias voltage between the sample and the tip electrode gives rise to a quantum mechanical tunneling current. Since the tunneling probability amplitude is an exponential function of the tip-sample separation, the value of the tunneling current is extremely sensitive to the sample surface corrugation. For instance, given a work function $\sim 1 \text{ eV}$, a decrease in separation of 1 \AA increases the tunneling current by a factor of ~ 3 . During topographical

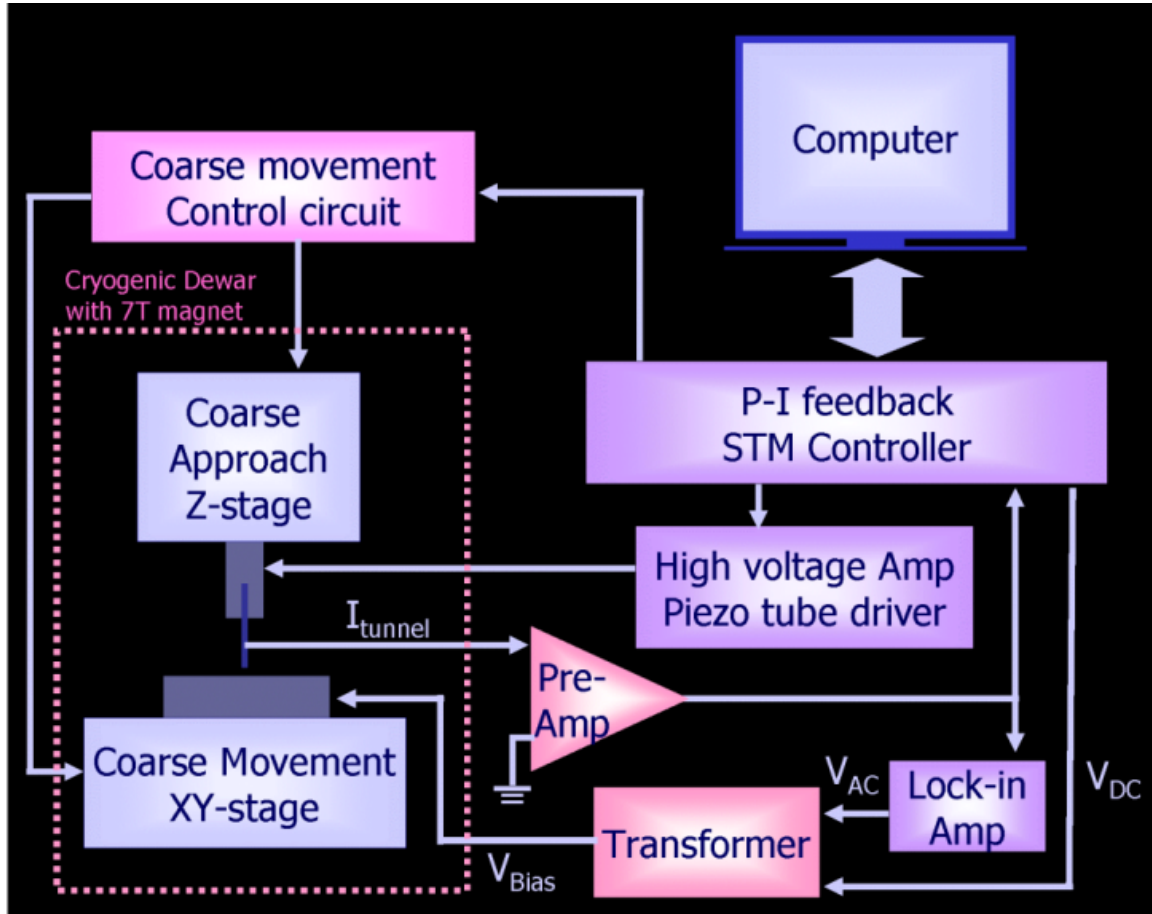


Figure 3.1: Block diagram of an STM system. The arrows denote the traveling direction of the commands and the signals. The STM head is schematically represented by the coarse approach z -stage and the sample translation xy -stage. The feedback controller, the current pre-amplifier, the high-voltage amplifier for the scanner, the high-voltage control circuit for coarse approach and the Stanford Research Systems lock-in amplifier (SR-830) form a complete set of electronics for STM control and data acquisition. The coarse movement control circuit includes a Physik Instrumente E-420 high-voltage amplifier and a homemade sequential triggering circuit [Fig. 3.2].

image scanning, by keeping the tunneling current constant with the feedback adjustment, the output voltages from the feedback loop to the z -electrode of the piezo tube are converted to deduce the vertical position of the tip as a function of its lateral position, $z(x, y)$. This is called constant-current topographic imaging.

Via constant-current imaging, we can identify the feature of interest and zoom in to investigate its local electronic structure, more specifically, its local density of states (LDOS), with the tunneling spectroscopy capability. As derived in Chapter 2, by studying the differential conductance (dI/dV) in a planar-junction-type of tunneling experiment, the averaged DOS of the sample is extracted. To

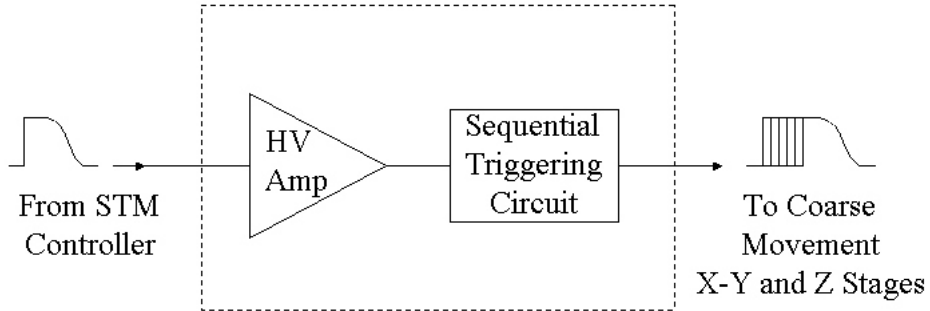


Figure 3.2: Schematic diagram of the STM coarse movement control unit.

obtain the spatially resolved LDOS, we measure the tunneling spectra point by point on target areas. During a set of scanning tunneling spectroscopy measurements, a constant tip-sample separation is first established by fixing the set-point current at a given bias voltage. Next, the feedback is turned off and a small sinusoidal modulation is added to the DC bias voltage. The resulting current modulation ($\propto dI/dV$) is then read off from a lock-in amplifier, into which the tunneling current signal from the current pre-amplifier is fed. We record the output signal from the lock-in amplifier as a function of the DC bias voltage to generate a tunneling spectrum $\frac{dI}{dV}(\vec{r}, V)$, and hence the LDOS. By taking dI/dV along a line or by taking a two-dimensional dI/dV map, changes in LDOS around a impurity, across a step-edge, or among grains with different crystalline orientations can be revealed and compared with theoretical predictions.

3.2 Instrumentation of a cryogenic STM

For an STM to perform spectroscopy measurements with atomic scale resolution reliably, several instrumentation challenges must be overcome. The coarse approach mechanism has to bring the probing tip smoothly into the tunneling range ($\sim 5 \text{ \AA}$) without crashing onto the sample. Secondly, the tip-sample separation has to remain constant to within $\sim 0.1\text{\AA}$ throughout any measurement. That is to say, mechanically the design of the STM should be rigid enough to prevent vibrational couplings from changing the tip-sample distance. The mechanical disturbance from the environment and acoustic vibrations should be decoupled as much as possible from the STM head.

Electronically, tunneling currents generally range from \sim pA to \sim nA. To avoid artifacts in tunneling spectra due to noise contamination, the electronics must be well shielded from ambient electromagnetic interference. Ground loops must be avoided, and cross-talk between the high-voltage piezo driving signals, the temperature controller output and the low-level tunneling/bias signals need be minimized.

Thermally, to track the evolution of cuprate electronic properties from the low-temperature superconducting state to above the transition temperatures, it is required that the STM system have good thermal stability, low thermal drift, good thermal isolation when operating at high temperatures, and sufficient cooling power to attain low base temperatures. Furthermore, problems associated with gas desorption and sample contamination at elevated temperatures must be addressed.

This section describes the design of our STM head and the cryogenic probe, and the measures taken to counter the aforementioned technical challenges under a modest budget. Other information related to the preparation of STM tips, the calibration of the shear piezos and the piezo-tube scanner, and the STM images on highly ordered pyrolytic graphite and gold samples for calibration purposes is given in Appendix B.

3.2.1 STM head

The STM built as part of this thesis work is intended to operate at variable cryogenic temperatures, in high vacuum, and in high magnetic fields. To compensate for the undesirable noisy environment of the lab and to fit the system into a 3" bore magnet, we adopted Pan's STM design [140, 141] with some variation because this design ensures a compact, rigid, high-vacuum and high-field-compatible STM head. There is a variety of distinct STM designs. In general, they differ in how the coarse approach is implemented and in their rigidity against vibrations. Pan's design employs a modified "stick-slip" coarse approach mechanism that exploits the friction between parts to hold the unit against vibrational noise coupling.

The STM head [Fig. 3.3] consists of a Macor¹ housing (1), six shear-piezo stacks² (2) with alumina

¹A machinable ceramic manufactured by Corning Inc.

²0.040" thick EBL-2 shear piezos purchased from Staveley Sensor.

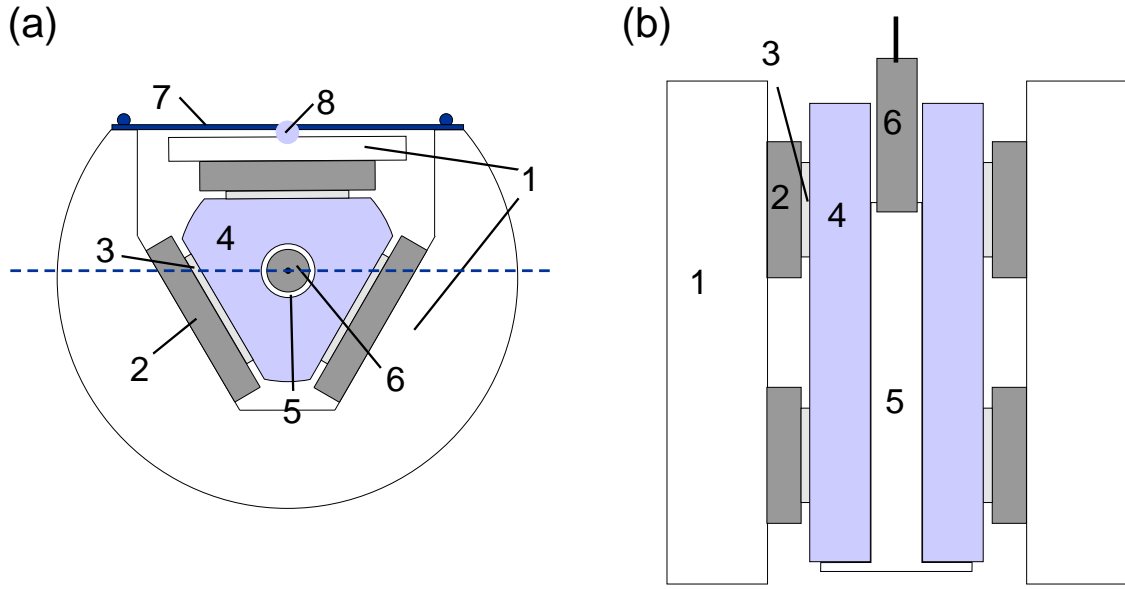


Figure 3.3: Schematics of the STM head, not to scale. (The sample holder is omitted.) (a) Top view. (b) Side view along the cut denoted by the dotted line. (1) Macor body, (2) shear-piezo stacks, (3) alumina plate contacts, (4) sapphire prism, (5) Macor insert of the scanning unit, (6) piezo-tube scanner, (7) Be-Cu spring plate, (8) sapphire ball bearing.

plate contacts³ (3), a sapphire prism⁴(4) that carries the scanning unit, and a Be-Cu spring plate (7). The scanning unit is made of a Macor insert (5), a piezo-tube scanner⁵(6), and a metallic tip holder. The metallic tip holder is attached to the center of the piezo-tube scanner, and the scanner is glued to the top of the Macor insert with Torr Seal.⁶ The Macor piece fits tightly to the central hole of the sapphire prism, and the scanning unit is locked to the sapphire with screws and TorrSeal. By pressing down a 1/8" diameter sapphire ball (8) against the top Macor block (1), the Be-Cu spring plate (7) holds the sapphire prism firmly between six piezo stacks. All of the materials chosen are non-magnetic and ultra-high-vacuum compatible. The overall dimension of the STM head is about 1.5" in diameter and 2" in height.

The operating principle of the shear-piezo motor is shown in Fig. 3.4. To move the sapphire one step forward, we apply six sharp high-voltage steps sequentially to the six shear-piezo stacks, so that the piezos move backward one stack at a time, while the other stacks hold the sapphire

³0.020" thick Superstrates manufactured by Coors Ceramic Company.

⁴Purchased from Insaco, Inc.

⁵0.020" thick, 0.125" OD, EBL-2 piezo tube purchased from Staveley Sensor.

⁶Purchased from Varian Inc.

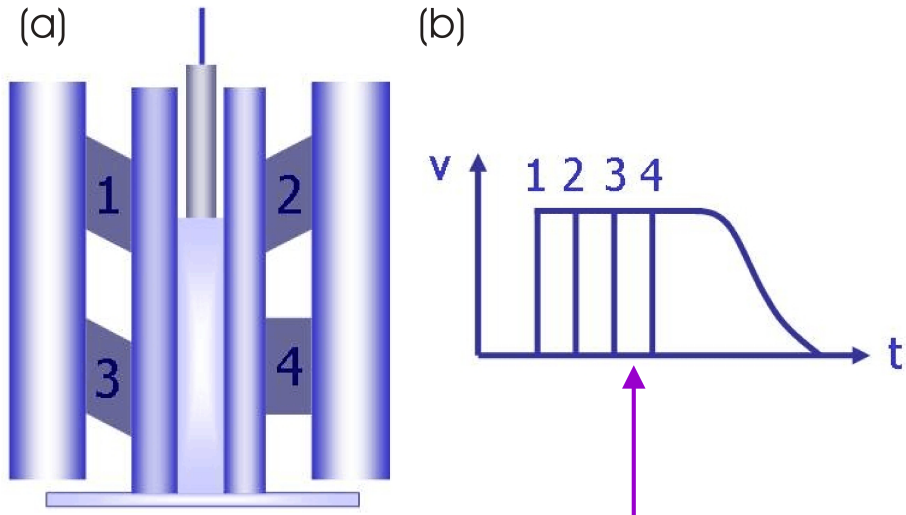


Figure 3.4: Principle of the coarse approach mechanism. (a) Snapshot of the configuration of the piezo stacks during a coarse movement cycle. (Only four of the six stacks are shown.) (b) Voltage waveform applied to the piezo stacks as a function of time. The arrow indicates when the snapshot is taken.

prism steady by friction. After every piezo stack is displaced from its resting position, we slowly decrease the applied voltages to zero. As a result, the six piezo legs simultaneously relax back to their neutral positions and, through friction, bring the prism forward by one step. The size of each step is determined by the shear-coefficient of the piezos ($\sim 8 \text{ \AA/V}$ at room temperature, and $\sim 1.5 \text{ \AA/V}$ at 4.2 K), the applied voltages and the number of piezos per stack. Typically, at room temperatures, one coarse step is about $0.4 - 0.8 \mu\text{m}$ with an applied voltage between $150 - 300 \text{ V}$, while the vertical probing range of the piezo-tube is over $1.0 \mu\text{m}$, larger than the coarse approach step size. Therefore, by applying feedback voltages to the piezo-tube, we can safely advance the tip forward without crashing onto the sample.

This design is superior in its stability against external mechanical perturbations. The sapphire prism and the tip it carries are held steady by friction between the alumina contacts and the prism. The strength of the friction can be adjusted by varying the curvature of the thin Be-Cu spring. Therefore, there is very little relative motion between the Macor body and the tip. Furthermore, after each step is completed, all piezos return to their neutral positions. Thus, no voltage is needed to hold the prism in place, and the vibrational noises transmitted through the voltage noises applied

to the piezos are eliminated.

One additional advantage of the design is its stability against thermal expansion. The STM head is designed to be concentric with the tip and sample located at the center. Therefore, it minimizes thermal drifting and enhances the STM performance at variable cryogenic temperatures. Besides, the Be-Cu plate is heat-treated to retain its springing strength during thermal cycling. Therefore, the rigidity of the STM head is guaranteed throughout the temperature range from 4K to ~ 100 K.

3.2.2 STM electronics

The STM control and data acquisition electronics consist of a high-gain low-noise current pre-amplifier⁷, a digital P-I feedback controller⁸, a set of high-voltage amplifiers that control the piezo-tube scanner, a high-power high-voltage amplifier⁹ and a homemade triggering circuit that controls the coarse approach piezo motor. A block diagram of the STM is given in Fig. 3.1.

The low-noise current pre-amp has a variable gain up to 1×10^{12} . We operate the pre-amp mostly at a gain of 1×10^9 for data acquisition and at 1×10^6 for field-emission tip cleaning. When operated at 1×10^9 , the output voltage noise is below 4 mV (peak-to-peak), equivalent to a ≤ 4 pA (peak-to-peak) input referred noise.

The STM digital feedback controller [Fig. 3.5] is built around two 32-bit floating point digital signal processors.¹⁰ One of them is designated for the feedback control and the other for imaging, data collection, data buffering, and data transfer. There are four 20-bit digital-to-analog converters (DAC's) for the high-voltage scanner control and the low-level sample bias voltage, and there are five 16-bit 100 kHz analog-to-digital converters (ADC's). The tunneling current signal from the pre-amp is connected to one of the ADC's with programmable gain (2 – 16) and a digital filter (2 – 20 Hz). The remaining four auxiliary analog input ports can be used to perform simultaneous data acquisition, *e.g.*, from the lock-in amplifier output during constant-current imaging.

To coordinate the coarse approach with the fine scanner control, there is an additional DAC that

⁷Model 1211 from DL Instruments.

⁸Purchased from Custom Vacuum System.

⁹E-420 from Physik Instrumente.

¹⁰ADSP-21062—SHARC manufactured by Analog Devices.

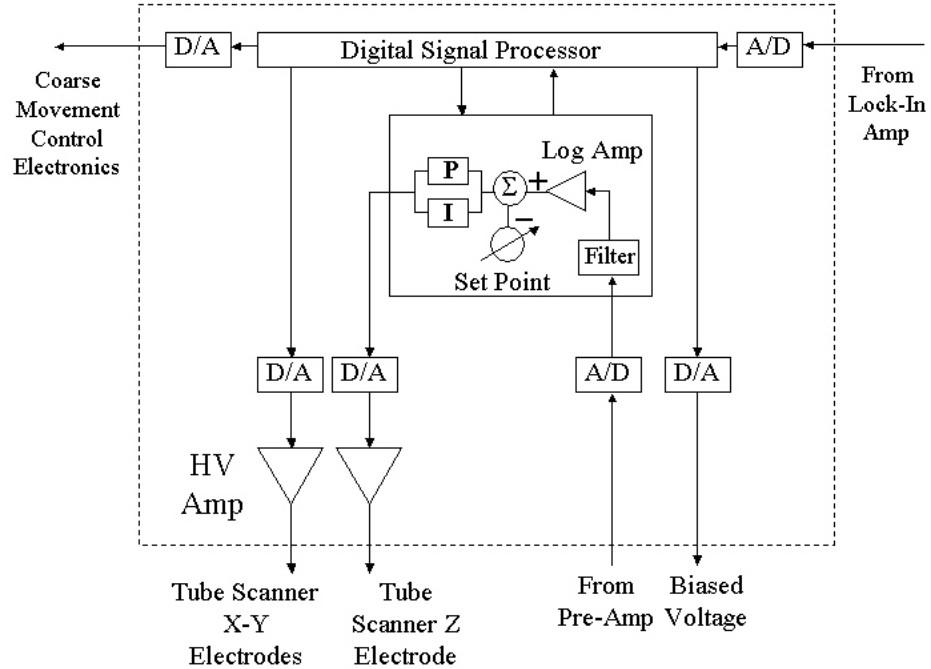


Figure 3.5: Schematic of the proportional/integral gain (P/I) digital STM feedback controller.

generates the triggering waveform for the coarse movement control of the shear-piezo walker. When the tip is brought within the tunneling range, under a constant sample bias voltage, the controller takes the amplified current signals from the pre-amp, performs the P/I feedback algorithm and, finally, outputs a voltage signal to the z -electrode of the piezo-tube to maintain a constant tunneling current. The five built-in monolithic high-voltage amplifiers (± 220 V) drive the scanning tube to manipulate the raster and vertical motion while the ADC's and the second digital signal processor record the data and transfer them to the computer.

Another important component of the STM electronics is the coarse movement control electronics. It includes a high-voltage high-power amplifier purchased from the Physik Instrumente (E-420) and a homemade sequential triggering circuit that gates the high-voltage output from E-420 to the coarse approach piezo stacks [Fig. 3.2]. For the slip-stick coarse approach mechanism to function properly, we need the capability of charging the piezo stacks (~ 4 nF each) to 400 V within $1 \mu\text{s}$ [Fig. 3.4] in order to overcome the huge static friction between the sapphire prism and the piezo stacks. Since no commercial high-voltage amplifier could provide such a large instantaneous current, we add to the

triggering circuit two large capacitors¹¹ as charge reservoirs to supply additional currents in each pulse cycle.

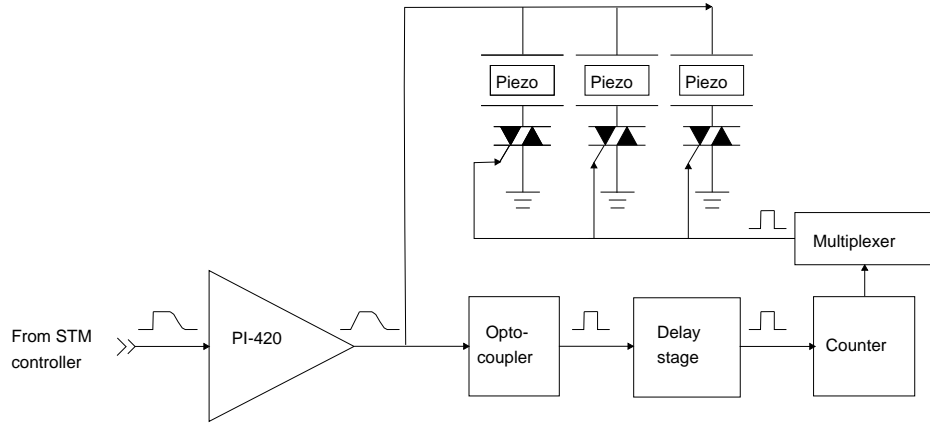


Figure 3.6: Schematic diagram of the sequential triggering circuit. (Only three of the six ports are shown for simplicity.) The high-voltage signal from E-420 is decoupled from the low-level digital circuitry via an optocoupler. The clock frequency of the counter that controls the sequential charging interval is set by a variable resistor. The oscillator consists of two inverters and two capacitors in addition to the resistor.

The schematics of the high-voltage triggering circuit is shown in Fig. 3.6. During each cycle, the delay stage receives a trigger signal from the optocoupler and waits until the capacitors are fully charged before it sends a pulse to the timer. After receiving the pulsing signal, the timer counts from one to eight with a user-defined time interval and sends the output number to the multiplexer. Then, the multiplexer sends a triggering signal to the gate electrode of the corresponding high-voltage-sensitive-gate triac to charge up the individual piezo stack. Consequently, the piezos are activated sequentially with the specified time interval and a very high instantaneous current. In our design, the time interval and the delay are set by variable resistors to be $\sim 50 \mu\text{s}$ and $\sim 0.5 \text{ ms}$, respectively, while the duration of the entire pulse is programmed to be $\sim 3 \text{ ms}$.

Overall, the speed of the coarse approach is limited by the bandwidth of the feedback to $\sim 1 \text{ step/sec}$. At room temperatures, it takes less than an hour to move the tip $\sim 3 \text{ mm}$ forward into tunneling range. At helium temperatures, because of the reduced piezo coefficient and the increased friction between the sapphire prism and the alumina contacts, it usually takes overnight to reach the tunneling range.

¹¹2 μF , rated at 630 V, purchased from Digi-Key Corporation

3.2.3 Cryogenic probe and dewar

The STM probe [Fig. 3.7] used in this thesis work is adapted from an old probe made for a gas-cooled, solenoid-driven STM head. The backbone of the probe is a 1 in. diameter, 3.5 ft. long thin-wall stainless steel (SS) tubing (6), situated in a 2.5 in. diameter stainless steel vacuum can (5). A charcoal pump (8) is installed at the bottom of the vacuum can to absorb the residual gas from any virtual leaks of the STM head at low temperatures. Otherwise, the high-voltage-driven coarse approach may cause undesirable discharge and damage the piezo motor. For the same reason, we have to eliminate the use of helium exchange gas for cooling to protect the STM head. At room temperature, we routinely reach $\leq 5 \times 10^{-6}$ torr by using a turbo pump without having to bake out the charcoal. When the probe is immersed in liquid helium or liquid nitrogen, the pressure is maintained below the scale of our ion gauge ($\leq 10^{-8}$ torr) because of the extra pumping power received from the charcoal pump.

In the absence of exchange gas, the original design of the probe is not able to provide enough cooling power, and the thermal load from the room temperature end becomes detrimental. We address this problem by reducing the thermal radiation and conduction and by increasing the thermal link to the helium bath. For example, Be-Cu springs (3) are attached to the bottom two stainless steel (SS) baffles (2) around the SS backbone tubing to ensure that the baffles are in good contact with the vacuum can and, hence, the liquid helium bath. In addition, ten Cu baffles (1) are added to the center of the SS tubing to reflect the thermal radiation down the tubing. These two measures combine to improve the radiation shielding, establish a uniform thermal gradient along the probe, and shunt the thermal conduction through the backbone tubing.

Next, we minimize the thermal conduction of the electrical wires. For example, 36 AWG man-ganin wires,¹² known to have low thermal conductivity are used for wiring the piezo stacks, piezo-tube scanner, and the copper foil heater¹³ and 36 AWG phosphor bronze Quad-Twist wires.¹⁴ are used for the Cernox temperature sensor¹⁴ The bias voltage lead is a 4" long stranded 304 SS flexible

¹²Purchased from the California Fine Wire Company.

¹³Purchased from Minco Co.

¹⁴Purchased from Lakeshore Cryotronics, Inc.

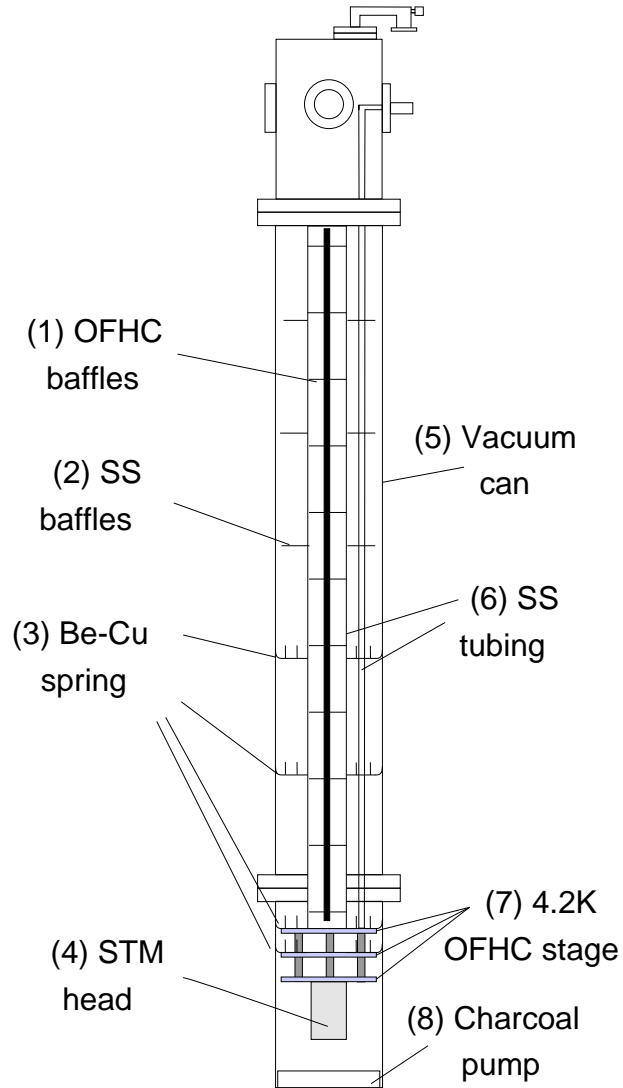


Figure 3.7: STM cryogenic probe. (Not to scale.)

mini-coaxial cable¹⁴ with a negligible thermal load ($\ll 1 \text{ mW}$).

The remaining heat load comes from the thermal conduction through the lead carrying the tunneling current. To reduce the coupling of vibrational noises through the microphone effect, we use a 0.141" diameter rigid coaxial cable for the tunneling signals. Ideally, the 20 mil semi-rigid mini-coax from Lakeshore is a better choice because of its low thermal conduction. However, it is difficult to attach SMA connectors to the cable without partially pinching its extremely thin insulating layer. As a result, the cables always come with a partial short on the order of $\sim 10^{10} \Omega$,

unacceptable for any high-impedance tunneling experiment. Thus, we compromise on the thermal performance and settle for a 3.5' long 0.141" coaxial cable with Cu inner conductor and SS outer shielding.

To reduce the heat leak through the inner conductor of the coax, we replace the bottom section of the cable with a 0.5' long 36 AWG manganin wire, and the resulting thermal load is suppressed to below 1 mW. Next, we tackle the ~ 6 mW heat leak through the SS outer conductor by thermal anchoring it with four gold-coated copper wires to the bottom radiation baffle. One end of the wires is wrapped around the manganin section of the coaxial cable and held in place with VGE-7031 varnish, while the other end is firmly attached to the bottom baffle. For more than 5 liters of liquid helium left in the dewar, the estimated temperature difference across the copper wires is ~ 70 K, and therefore the thermal anchoring provides at least ~ 10 mW of cooling power, sufficient to compensate for the heat load through the SS outer conductor.

To reduce the heat load further, we anchor the wires of the piezo motor, the piezo-tube scanner, and the temperature sensor to two 4.2 K stages made of oxygen-free high-conductivity copper (OFHC) before connecting them to the STM head. In addition, we pass the bias voltage and the tunneling current leads through the cryogenic microwave powder filters [142] attached to the bottom OFHC stage. Several Be-Cu spring contacts (3) firmly establish the thermal link between the 4.2 K stages and the outer can, thus providing enough cooling power for the entire STM head. After the installation of baffles and heat sinks, base temperature significantly improves from ~ 30 K to ~ 9 K.

The Oxford dewar housing the STM probe holds up to ~ 35 liters of liquid helium. It comes with a 3" bore superconducting magnet. The upper section of the magnet leads are thin-wall brass tubing with copper wires soldered along their circumference, which extend to the bottom magnet. These leads are designed to be in direct contact with the helium bath and are not retractable from the flange of the dewar. Consequently, the boil-off rate of liquid helium reaches ~ 10 liters per day, which corresponds to 3–4 days of experiment between refilling.

3.2.4 Noise reduction

For an STM to achieve its best performance, noise contamination must be minimized. For example, in the constant-current topography mode, we need to restrict the lateral vibrational noise coupling to $\leq 0.5 \text{ \AA}$ and the vertical vibrations to $\leq 0.1 \text{ \AA}$ in order to have good atomic resolution. In the spectroscopy mode where feedback is disabled, the rigidity of the STM head against vibrations is even more crucial. A disturbance of $\sim 1 \text{ \AA}$ in the vacuum tunneling gap typically would cause the tunneling current to fluctuate by a factor of ~ 5 , so it would wash out whatever information encoded in the spectrum. Thus, we first address the reduction of mechanical coupling to the lab environment and acoustic vibrations before turning to the issue of minimizing electrical interference.

The STM lab is located in the sub-basement where the floor vibration is presumably the least severe. Nevertheless, as we set up the accelerometer¹⁵ and physically measure its noise spectrum, several sharp resonant peaks below 100 Hz are found [Fig. 3.8(a)], among which noises of $\sim 50 \text{ Hz}$ are the most pronounced.¹⁶ To suppress the coupling to these resonance modes, the dewar holding the STM probe is bolted to a 3" thick aluminum plate and placed on a four-post Newport air damper, which serves as a low-pass filter of the floor vibrations. Additional lead bricks and lead shot bags are placed around the table to increase the loading and suppress the corner frequency of the air damper. When the table is inflated, the transmitted vibrational noises are suppressed to less than 2% of its original amplitude at the resonant frequencies [Fig. 3.8].

Another type of vibrational noise is transmitted through acoustic coupling. The acoustic noises that plague the STM system mostly come from the room ventilation motors. This type of low-frequency noises are generally difficult to remove because they either drive the plaster wall or indirectly couple through the ceiling to vibrate the whole lab. In our case, the two main sources are the ventilation pipeline mounted directly to the lab side wall and another big motor facing the lab entrance.

The following two measures are taken to contain these noises: the maximization of sound absorption and the minimization of sound transmission. We cover all of the side walls of the STM lab

¹⁵ENTEK 9200L accelerometer purchased from Rockwell Automation.

¹⁶Data in Fig. 3.8 were taken by Timothy Ward during his SURF study at Caltech in the summer of 2004.

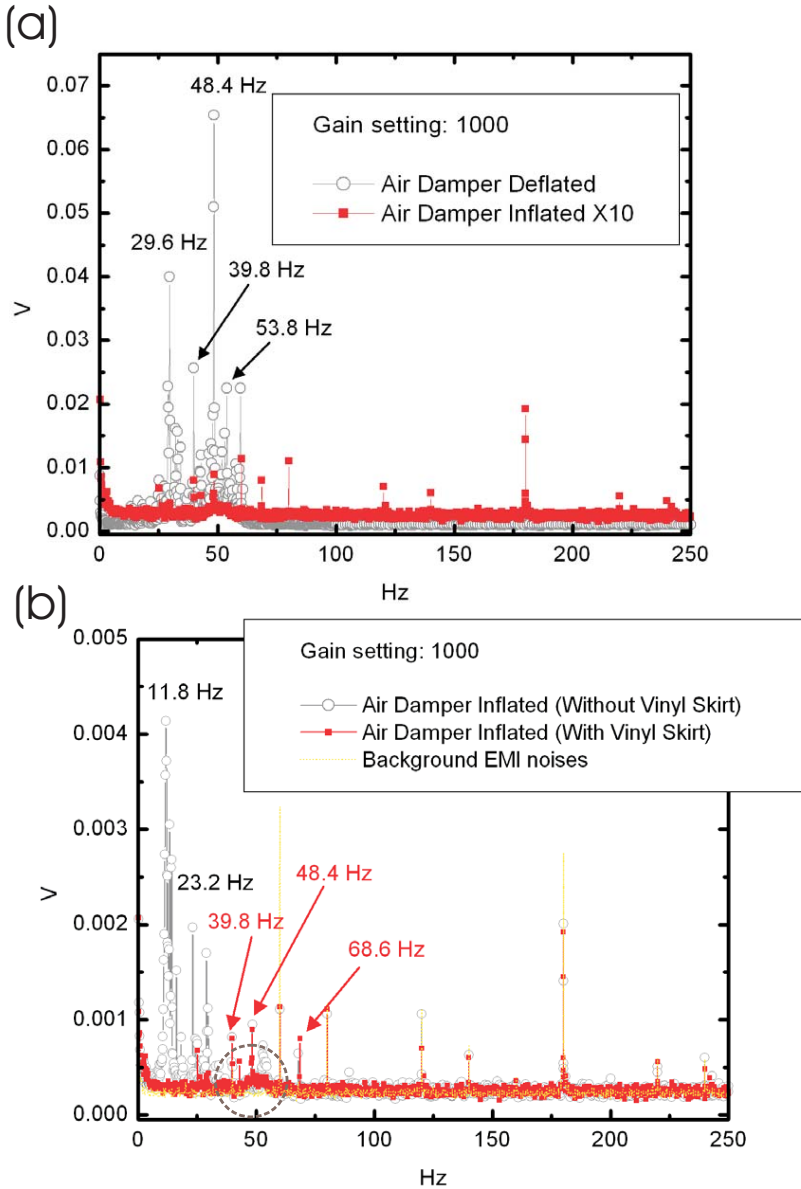


Figure 3.8: Transmitted vibrational noise spectra. (a) A comparison between noise spectrum taken with the air table deflated and that with the air table inflated. Note that the magnitude of the latter has been multiplied by 10 for clarification. The resonance modes of the building (denoted by the gray open circle), ranging from 25 – 55 Hz, are greatly suppressed when the air damper is inflated. However, there is residual spectral weight (denoted by the red solid square) centered around 50 Hz that couples to the STM probe. Noise peaks at 60, 80, 120, 140, 180, 220, and 240 Hz are line noise contaminations and Nyquist ghost artifacts, as demonstrated in (b). (b) Noise spectra taken while the air damper is inflated, with (red solid square) and without (gray open circle) the vinyl skirts attached to the edge of the table. Also shown is the noise spectrum of the background electromagnetic interference (yellow dotted line). The vinyl skirts help stabilize the air table and further reduce the low-frequency noises ranging from 5–35 Hz. Most of the remaining spectral weight is distributed around 50 Hz within the black dotted circle. For a close view of the spectrum below 150 Hz, please refer to the inset of Fig 3.9. All noise spectra are calculated by fast Fourier transforming the traces of time-varying output voltages from the piezo-electric accelerometer, ENTEK 9200L. The sensitivity of the sensor is 500 mV/g, and the sensor output is post-amplified with a gain of 1000.

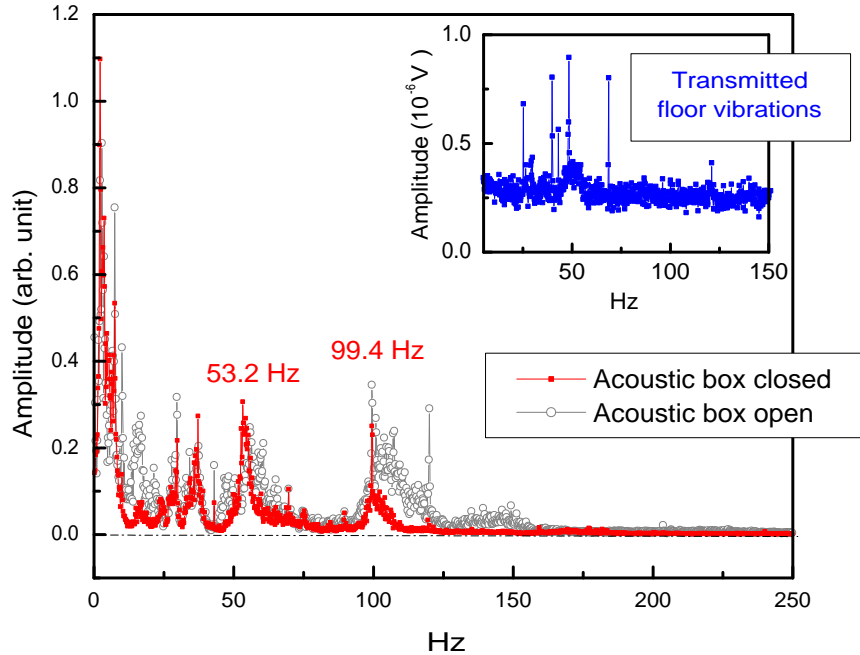


Figure 3.9: Low-frequency acoustic noise spectrum taken in the acoustic housing surrounding the STM cryostat with and without the lid closed. Above 100 Hz, the acoustic noise is mostly filtered away, while there is a substantial residual spectral weight around 50 Hz, which coincides with the residual floor vibrational noise shown in the inset.

with flat foam absorbers,¹⁷ and place crater-shaped acoustic foam above the fluorescent lights and the wire conduits to intercept noises rebounding from the ceiling. A bass tube¹⁸ is installed in the corner of the lab to absorb the low-frequency acoustic waves. To minimize the transmission of noise generated by the ventilation machines, rubber buffers are inserted on the pipelines connected to the side-wall. Thick vinyl curtains¹⁹ are hung in front of the entrance facing the other motor to reflect the noises, and vinyl sheets are tailored to attach to the edges of the aluminum table. These vinyl skirts keep acoustic noises from impinging upon the dewar and also provide more weight and better balance to the table. In Fig. 3.8(b), it is shown that the low-frequency vibrational noises around 12 Hz and 25 Hz are further suppressed after the installation of the skirts.

To isolate the STM system from the residual acoustic noises, a double-layer acoustic housing is built around the STM table. The inner layer is made of composite wood and the outer layer of concrete boards. Both are covered with acoustic absorption foam. The spectra of the residual

¹⁷1" thick, flat sound absorbing foam distributed by McMaster Carr.

¹⁸16" OD tube trap purchased from Silent Source.

¹⁹2 lb/ft² sound barriers from Silent Source.

acoustic noise taken via a simple microphone circuit show that the acoustic box filters away most frequencies above 100 Hz, but, around its natural frequencies, the noises are mostly transmitted [Fig. 3.9]. One of the resonant frequencies lies within 50 – 60 Hz, which coincides with the vibration frequency of the side-wall driven by the venting pipeline. Since the transmitted floor vibrations also show significant spectral weight within the same frequency range [Fig. 3.9 inset], Teflon blocks are placed irregularly between baffles to break up the resonance in order to avoid the cryogenic dewar from enhancing this mode.

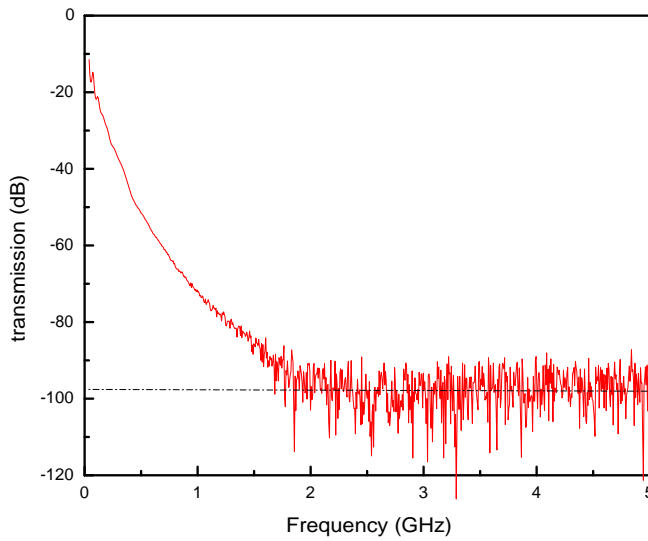


Figure 3.10: Transmission of the cryogenic microwave powder filter.

Finally, to minimize the contamination of tunneling current signals through cross-talks and environmental electromagnetic interference, we run wires of different purposes through separate thin-wall SS tubes; the latter serve as additional shielding [Fig. 3.7]. As a result, the high voltages driving the piezo-tube and shear-piezo motor are decoupled from the low-level bias voltage and the tunneling current leads. The coaxial cables carrying the bias and the tunneling signal are passed through a room-temperature RF filter²⁰ and a cryogenic powder filter²¹ [Fig. 3.10] before being connected to the STM head. To reduce the excess high-frequency noises during experiments, the high-voltage

²⁰Model BLP-1.9 from Mini-Circuits.

²¹For a brief description of the construction and modeling of cryogenic powder filters, please refer to [143].

amplifier, E-420, is turned off when coarse approach is completed and the tip is in tunneling range. Furthermore, all grounding and shielding wires are carefully arranged to avoid ground loops. After all is done, the noise floor of our system reaches about $15 - 20 \text{ pA}_{\text{p-p}}$ ($3 - 4 \text{ pA}_{\text{rms}}$) at helium temperatures.

3.3 Comparison with other experimental techniques

In this section, we briefly review other spectroscopic tools frequently applied to the study of high-temperature superconductivity.

3.3.1 Tunneling spectroscopy

Scanning tunneling spectroscopy (STS) is a local probe that measures the local density of states convoluted with the tunneling matrix element. It has superior spatial and energy resolution. On the other hand, issues such as characterizing the tip structures, preserving a good sample surface that represents the bulk properties, and determining the tunneling matrix elements can be challenging.

In addition to STS, there are several other configurations of tunnel junctions commonly seen in the high T_c community. These techniques generally sample over a much larger area than STM to yield a spatially averaged spectra. In this sense, they complement the results of STS experiments. In the following, we discuss the relative strength and the limitations of four representative tunneling techniques: planar junction spectroscopy, point contact spectroscopy, break-junction spectroscopy, and interlayer tunneling spectroscopy.

Planar junction

Planar junctions are fabricated by depositing the two electrode materials as cross strips separated by a thin layer ($\sim 10 - 40 \text{\AA}$) of insulating material. The first N-I-S tunneling experiment [110] was carried out on planar junctions in 1960. Because of their long history, planar junctions are probably the most studied among the tunneling spectroscopy techniques. However, a number of possible pitfalls associated with these junctions have been identified, including junction contam-

ination, Coulomb blockade, Schottky barrier, heating, and barrier breakdown due to pinholes in the insulating layer. A complete set of diagnostics must be run before these potential problems can be ruled out. Schottky barrier and Coulomb blockade problems are also common for STS and point-contact spectroscopy if the sample surface has degraded. Both phenomena have distinct I-V characteristics that help identify defective junctions and avoid interpreting artifacts as real features.

In theory, one could have well-defined crystalline orientation of the thin-film samples used in the planar junctions by varying the substrate material and the growth conditions. Therefore, planar junctions have been employed to study the Andreev bound state of {110}-oriented cuprate films [144]. However, the presence of interface roughness over a large junction area poses another complication for data analysis besides the aforementioned problems.

Point-contact spectroscopy

A point-contact is formed by pressing a sharp metallic electrode, such as Au or Pt/Ir, onto the sample of interest. By varying the spring loading applied to the tip, the tunneling barrier, and hence the junction impedance($\sim 1\Omega - 1k\Omega$), can be adjusted to probe the conductance spectrum from the point-contact limit to near the tunneling limit. Compared to STM, point-contact experiments are much easier to set up for variable temperature and variable magnetic field measurements. In addition, they do not have the problem of pinholes or shorts through the insulating layer as in the planar junctions. However, the preparation for a clean tip and a good sample surface is non-trivial. The large springing force needed to form a good contact also poses a problem for maintaining the sample surface integrity and the mechanical stability of the system. A recent review of the application of point-contact spectroscopy to studies of the Andreev process in cuprate superconductors can be found in an article by Deutscher [145].

Break-junction

In a break-junction setup, a thin piece of sample is glued to a flexible support. By carefully bending the support, the sample is broken into two pieces, and, by slowly reducing the stress, the two parts are brought back to establish a tunnel junction. Compared with planar junctions and

point-contact spectroscopy, break junctions have the advantage of retaining fresh junction surfaces because the junctions are generally formed in vacuum at cryogenic temperatures. The down side is that the intrinsic randomness in the break surface and the reformation process renders it almost impossible to control the orientations of the junction electrodes. Thus, it is not a good choice for measuring orientation-dependent properties, such as tunneling into the Andreev bound states.

Break junctions on the nearly two-dimensional Bi-2212 samples have been prepared in two different ways. One is by applying the bending method as mentioned above to fabricate in-plane tunnel junctions [146]. The other method takes advantage of the extremely weak bonding between BiO_2 planes to form *c*-axis tunnel junctions. By pushing a sharp tip into the sample and subsequently releasing the pressure, a fracture between planes is formed about 100 μm below the surface [147]. Therefore, the junction is pristine and free of surface contaminations. Spectra taken on *c*-axis break junctions of Bi-2212 in the superconducting state have revealed a pronounced “peak-dip-hump” feature [147, 148, 149] consistent with the photoemission spectra on similar samples. We shall return to discuss the physical origin of the “peak-dip-hump” feature in later chapters.

Interlayer tunneling spectroscopy

Interlayer tunneling spectroscopy is also referred to as the intrinsic Josephson tunneling because it makes use of the extreme two dimensionality of certain cuprates, *e.g.*, Bi-2212, and measures their *c*-axis interlayer tunneling spectra. To avoid the complication in the interpretation of data, the sample thickness is controlled to contain less than 25 Josephson junctions. With the advance in fabrication technology, several groups [150, 69] have demonstrated the ability to reliably fabricate Bi-2212 mesas with as few as 9 Josephson junctions, corresponding to a thickness of ~ 15 nm. Like the break junctions, interlayer Josephson junctions are free of junction contaminations. Furthermore, the junction orientation is well-defined along the *c*-axis, and, therefore, it would appear to be the best configuration to study the *c*-axis tunneling of highly 2D Bi-2212 and Bi-2201 samples. Indeed, earlier intrinsic tunneling spectra on Bi-2212, which exhibited coexisting pseudogap and superconducting gap with disparate temperature evolutions [69, 151, 152], have drawn wide attention and intensified the debate of how pseudogap phase relates to high-temperature superconductivity.

However, the interpretation of the spectra is not without dispute. For instance, due to the poor thermal conductivity of Bi-2212, joule-heating has always been a main concern for possibly giving rise to non-intrinsic phenomena observed in the Bi-2212 mesas [153, 154]. Experimental efforts to reduce or calibrate away the effect of joule-heating include the use of short duty-cycle pulse measurements [155], the on-chip thermometry [156, 154], and the *in situ* temperature control [157].

3.3.2 Angle-resolved photoemission spectroscopy

Angle-resolved photoemission spectroscopy (ARPES) measures the single-particle spectral function. By shining a beam of monochromatized radiation (usually in the ultra-violet range) on a well-aligned single crystal sample, valence electrons are excited and escape into vacuum via the photoelectric effect. By analyzing the energy and angular distribution of the photoelectrons, the spectral function (convoluted with the one-electron dipole matrix element and the Fermi function) is derived. The spectral function $A(\vec{k}, \omega)$ is related to the retarded Green's function by the expression

$$A(\vec{k}, \omega) = -\frac{1}{\pi} \operatorname{Im} G^{\text{ret}}(\vec{k}, \omega), \quad (3.1)$$

where $G^{\text{ret}}(\vec{k}, \omega)$ is the momentum-space Fourier transform of the real-space retarded Green's function $G^{\text{ret}}(\vec{r}, \vec{r}, \omega)$ ²². Careful analysis of the ARPES spectra can yield information on the electron proper self-energy, $\Sigma(\vec{k}, \omega) = \Sigma'(\vec{k}, \omega) + \Sigma''(\vec{k}, \omega)$,

$$A(\vec{k}, \omega) = -\frac{1}{\pi} \frac{\Sigma''(\vec{k}, \omega)}{(\omega - e_k - \Sigma'(\vec{k}, \omega))^2 + (\Sigma''(\vec{k}, \omega))^2}. \quad (3.4)$$

The self-energy $\Sigma(\vec{k}, \omega)$ describes the energy renormalization and the finite lifetime of the quasiparticles, which serves as a useful comparison to other techniques that measure the scattering rate and

²²Let H be the total Hamiltonian of the system and $\psi_{\mathbf{q}}(\vec{r})$ the single-particle eigenstates. Then $G^{\text{ret}}(\vec{r}, \vec{r}, t)$ is defined as:

$$G^{\text{ret}}(\vec{r}, \vec{r}, t) = -i\theta(t) \sum_q \left\langle \vec{r} \left| e^{-i\hat{H}t/\hbar} \right| \psi_{\mathbf{q}} \right\rangle \langle \psi_{\mathbf{q}} | \vec{r} \rangle = -i\theta(t) \sum_q \left\langle \vec{r} \left| e^{-i\omega_q t/\hbar} \right| \psi_{\mathbf{q}} \right\rangle \langle \psi_{\mathbf{q}} | \vec{r} \rangle \quad (3.2)$$

and thus

$$G^{\text{ret}}(\vec{r}, \vec{r}, \omega) = \sum \frac{|\psi_{\mathbf{q}}(\vec{r})|^2}{\omega - \omega_q + i\delta}. \quad (3.3)$$

the relaxation rate.

Scanning tunneling spectroscopy and ARPES are complementary techniques in that STS measures local spectral function $N_s(\vec{r}, \omega)$ with high spatial resolution, while ARPES measures the spectral function $A(\vec{k}, \omega)$ with momentum resolution. It is worth noting that the angular resolution in ARPES comes at a price of reduced energy resolution [158]. Over the past decade, there has been an order-of-magnitude improvement in the energy resolution of ARPES to $\sim 5\text{meV}$. However, it is still far behind what STS could provide.

To ensure the best momentum and energy resolution, ARPES on cuprate material generally works at lower photon energies ($20 - 100$ eV). Consequently, the mean free path for ballistic photoelectrons is on the order of 5\AA , rendering ARPES extremely surface sensitive. To date, most of ARPES data on the cuprates have been taken on highly 2D samples because they could be easily cleaved to yield good surfaces. In particular, the ARPES data of the Bi-2212 families are among the most complete. It is known from STS measurements [67, 68] that Bi-2212 reveals strong spatially varying tunneling spectra possibly due to inhomogenous interstitial oxygen doping and competing order. On the other hand, ARPES averages over electrons ejected from a macroscopic area illuminated by the incoming photon beam. Thus, one must keep in mind that ARPES data as well as other bulk measurements on Bi-2212 present averaged information.

ARPES has been widely used by the high T_c community as means to survey the normal state properties, identify the Fermi surfaces, investigate the anisotropy of superconducting gap and pseudogap, and study the evolution of spectral function from below to above T_c . A comprehensive review on the recent progress can be found in Ref. [158]. In later chapters, we will draw on two ARPES observations, the peak-dip-hump structure [159] and the dichotomy between nodal and anti-nodal quasiparticle spectra in the pseudogap phase [160], and discuss how these novel phenomena relate to our STS results.

3.3.3 Neutron scattering

The proximity of cuprate superconductors to the anti-ferromagnetic Mott insulating phase gives rise to several interesting magnetic orders in cuprate systems. The studies of the doping-dependent magnetic properties can conceivably lead to important insight into the underlying pairing mechanism of cuprate superconductors. Neutron scattering has been the most widely used spectroscopic technique to investigate the dynamic and static magnetic correlations of cuprates by the high T_c community. Because neutrons are charge neutral, they interact weakly with the system under study, penetrate much deeper into the sample, and thus allow the bulk magnetic properties of sample to be explored. On the other hand, the weak interaction renders scattering cross sections small. Thus, high quality cm^3 size crystals are generally required to overcome the instrumentation noises. As a result, only two families of cuprates, $\text{La}_{2-x}\text{Sr}_x\text{CuO}_4$ and $\text{YBa}_2\text{Cu}_3\text{O}_{6+\delta}$, have been studied in detail to date.

Neutron scattering data contain contributions from both the phonon modes and the magnetic fluctuations. Because of the difference in the form factors, it is possible to distinguish magnetic scattering from phonon scattering by probing the angular dependence of the scattering cross section. In addition, polarized neutron scattering can be employed to filter out the phonon spectral weight completely. However, the signals of the polarized neutron scattering configuration are substantially smaller than those of the unpolarized configuration, and thus extracting signals from background noises can be very challenging for the polarized neutron scattering experiments.

Inelastic neutron scattering measures the dynamic scattering cross section, which is proportional to the dynamic structure factor and hence to the imaginary part of the generalized susceptibility:

$$\frac{\partial^2 \sigma}{\partial \Omega_f \partial E_f} \sim |f(\vec{Q})|^2 \frac{|\vec{k}_f|}{|\vec{k}_i|} \sum_{\alpha\beta} (\delta_{\alpha\beta} - \hat{Q}_\alpha \hat{Q}_\beta) S^{\alpha\beta}(\vec{Q}, \omega) \quad (3.5)$$

$$S^{\alpha\beta}(\vec{Q}, \omega) = \frac{1}{1 - e^{-\hbar\omega/kT}} \text{Im } \chi(\vec{Q}, \omega), \quad (3.6)$$

where $\vec{Q} = \vec{k}_f - \vec{k}_i$ and $f(\vec{Q})$ is the form factor. The elastic neutron scattering experiments measure the magnetic Bragg scattering from the sample, which can reveal long-range magnetic structures

such as the stripe order in $\text{Nd} - \text{La}_{2-x}\text{Sr}_x\text{CuO}_4$ [84] and the anti-ferromagnetic order in the undoped cuprate compounds [chap:introduction]. In fact, neutron scattering was the first technique to demonstrate the anti-ferromagnetic spin configurations of the undoped parent compounds [1], disproving the conjecture of a resonating-valence-bond spin liquid phase as the ground state for the undoped cuprates [20]. Comprehensive reviews on the earlier neutron scattering results of $\text{La}_{2-x}\text{Sr}_x\text{CuO}_4$ and $\text{YBa}_2\text{Cu}_3\text{O}_{6+\delta}$ can be found in Refs. [2, 161, 162, 163, 164].

Chapter 4

Tunneling Spectra of Hole-Doped $\text{YBa}_2\text{Cu}_3\text{O}_{6+\delta}$ ¹

4.1 Introduction

The proximity of cuprate superconductors to the Mott insulating phase gives rise to novel superconducting behavior enriched by the influence of additional orders from doping the Mott insulators [62]. Several important questions arise, concerning what characteristics these quantum orders possess, how different orders manifest themselves in various cuprates, how the competing orders relate to the superconducting order and the pseudogap phenomena, and how their presence contribute to the asymmetry of the phase diagram between the electron- (n-type) and hole-doped (p-type) cuprates. To address these issues, we study the scanning tunneling spectra of two model systems, the p-type $\text{YBa}_2\text{Cu}_3\text{O}_{6+\delta}$ and the n-type $\text{Sr}_{1-x}\text{La}_x\text{CuO}_2$, with the goal of contrasting the non-universal phenomena and extracting the common properties between the two types of cuprates.

The focus of this chapter is on the investigation of the hole-doped $\text{YBa}_2\text{Cu}_3\text{O}_{6+\delta}$. While in the superconducting (SC) phase the mean-field modified BCS theory and Ginzburg-Landau theory provide a fair description for the properties of p-type cuprate superconductors; their normal-state properties seem to defy the conventional Fermi liquid phenomenology. For instance, the pseudogap (PG) phase exhibits a suppression of the density of states (DOS) around the Fermi level and a loss of spectral weight in the spin and charge excitations [9], and the anomalous metallic phase

¹The main contents of this chapter are published as N.-C. Yeh, C.-T. Chen, *et al.* *Phys. Rev. Lett.* **87**, 087003 (2001), and N.-C. Yeh, C.-T. Chen, *et al.* *Physica C* **364-365**, 450 (2001).

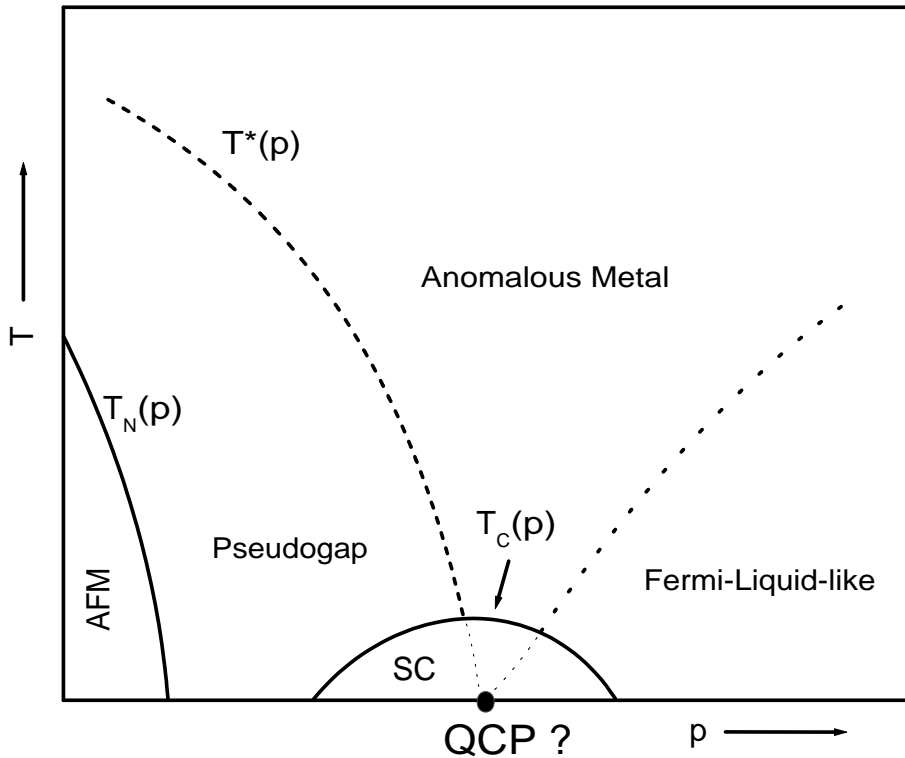


Figure 4.1: The generic temperature (T) vs. doping (p) phase diagram of the hole-doped cuprate superconductors. AFM: long-range commensurate anti-ferromagnetic order. SC stands for the superconducting state and p denotes the doping. T_N , T_c , and T^* are the Néel temperature, superconducting transition temperature, and pseudogap temperature.

exhibits the marginal Fermi liquid behavior [10] in which the single-particle and transport scattering rates are linear in frequency up to an energy comparable to the temperature [Fig. 4.1]. The linear scattering rates measured in the resistivity [165, 166] and optical conductivity [167] experiments suggest the presence of scale-invariant low-energy magnetic and density fluctuations around optimal doping above T_c . That temperature is the only energy scale dictating the fluctuation spectrum is reminiscent of the behavior of critical fluctuations associated with a quantum phase transition [168, 169]. The observation of the marginal Fermi liquid behavior [10, 74] and the PG phenomena leads to the conjecture of a quantum phase transition between the SC order and a competing order that is manifested as the PG phase, with the quantum critical point (QCP) located within the superconducting “dome” [74, 170].

Although the presence of critical fluctuations near the optimal doping level [171, 172] and the disparate physical properties between the underdoped and overdoped regimes are suggestive of the

presence of a QCP near the optimal doping, an unambiguous proof requires identifying the relevant broken symmetry associated with a critical doping p_c . Various theoretical studies have investigated the dependence of the competing ground states of doped Mott insulators on the doping level and the strength of exchange and Coulomb interactions [28, 173]. The relevant symmetries associated with the competing orders include electromagnetic $U(1)$, spin rotation-invariance $SU(2)$, square lattice space group C_{4v} , and time-reversal symmetry \mathcal{T} . Experimentally, while the $d_{x^2-y^2}$ pairing symmetry is known to dominate in the optimally doped p-type cuprates [6, 7, 174], possible doping-dependent pairing symmetry has been suggested [175]. At the time of writing, the existence of a QCP, the location of the critical doping p_c , and the nature of the quantum phase transition are still under debate.

We address some of these issues via studies of the directional and spatially resolved quasiparticle tunneling spectra on $\text{YBa}_2\text{Cu}_3\text{O}_{6+\delta}$ (YBCO) with a range of doping levels. Since YBCO has been examined extensively by various other experimental techniques and is proven less susceptible to doping-induced inhomogeneity [176] than other well-studied systems, such as $\text{La}_{2-x}\text{Sr}_x\text{CuO}_4$ (LSCO) and the highly two-dimensional (2D) $\text{Bi}_2\text{Sr}_2\text{CaCu}_2\text{O}_{8+\delta}$ (Bi-2212), its doping-dependent tunneling spectra should serve as a good reference for comparison with those of the electron-doped cuprates. By fitting to the quasiparticle momentum-dependent Blonder-Tinkham-Klapwijk (BTK) tunneling spectra of unconventional superconductors, the doping dependence of the pairing symmetry, pairing potential, and spatial homogeneity are derived. In the underdoped and optimally doped YBCO single crystals and thin-film samples, predominantly $d_{x^2-y^2}$ -wave-pairing spectral characteristics and long-range spatial homogeneity of the quasiparticle spectra are revealed. In overdoped ($(\text{Y}_{0.7}\text{Ca}_{0.3})\text{Ba}_2\text{Cu}_3\text{O}_{6+\delta}$) Ca-YBCO thin films, however, $(d_{x^2-y^2}+s)$ pairing symmetry is found with a significant s -wave admixture. We will discuss the implication of the doping-dependent pairing symmetry on the possibility of a quantum critical point in YBCO. In addition, we will present STS data on the non-magnetic-impurity-substituted $\text{YBa}_2(\text{Cu}_{0.9934}\text{Zn}_{0.0026}\text{Mg}_{0.0004})_3\text{O}_{6.9}$ [(Zn, Mg)YBCO], where microscopic spatial modulations and strong scattering near the Zn or Mg impurity sites are observed. The results are again consistent with a $d_{x^2-y^2}$ -wave pairing as observed in the underdoped

and optimally doped pure YBCO.

4.2 Sample preparation

The samples used in this investigation include three optimally doped YBCO single crystals with $T_c = 92.9 \pm 0.5$ K, three underdoped YBCO single crystals with $T_c = 60.0 \pm 2.5$ K, one underdoped YBCO *c*-axis film with $T_c = 85.0 \pm 1.0$ K, two overdoped Ca-YBCO *c*-axis films [177] with $T_c = 78.0 \pm 2.0$ K, and one optimally doped single crystal containing small concentrations of non-magnetic impurities, (Zn,Mg)-YBCO with $T_c = 82.0 \pm 1.5$ K. All single crystals are twinned except for the (Zn,Mg)-YBCO.

The pure YBCO crystals used for the experiment are grown by a crystal-pulling technique followed by a two-week oxygen annealing. Single crystallinity with twinning is verified by x-ray diffraction. Samples for in-plane {100} and {110} tunneling experiments are prepared in the following manner to have their surface normal vectors align along these two directions. First, the originally *c*-axis oriented single crystal samples are cast in transparent epoxy holders and aligned by identifying the twinning boundary with a polarized optical microscope. Surfaces with desirable crystalline orientations are then exposed using a diamond blade and polished to optical smoothness before re-annealing. The post-annealing condition for optimal doping is 450 °C in ultra-pure oxygen gas for 24 hours followed by gradual cooling. To reduce the doping of YBCO to $\delta \approx 0.5$, samples are post-annealed at 550 °C in flowing argon for 72 hours and quenched to room temperatures.

Before loading onto the STM probe, the sample surface is prepared by chemical etching with 1% bromine in absolute ethanol for one minute followed by ethanol rinsing [178, 179], and kept either in high-purity helium gas or under high vacuum. Our surface preparation has the advantage of terminating the YBCO top surface at the CuO₂ plane by chemically passivating the surface layer while retaining the bulk properties of the constituent elements [178, 179]. Thus it yields reproducible spectra for samples of the same bulk stoichiometry, although direct constant-current mode atomic imaging of the chemically inert surface becomes difficult. On the contrary, surface of vacuum-cleaved YBCO samples is found to terminate at the CuO-chain layer, which is prone to loss

of oxygen and the development of surface states [178, 179, 180, 37] that plague the STS and the angle-resolved photoemission spectroscopy (ARPES) experiments [181, 182, 180, 37]. In comparison, the surface of vacuum-cleaved Bi-2212 crystals typically terminates at the BiO layer, which protects the underlying CuO₂ from loss of oxygen. Therefore, reproducible tunneling spectra representative of the bulk properties are routinely obtained on cleaved Bi-2212 surfaces [183, 54].

4.3 Results of directional tunneling spectroscopy

The spectra of YBCO single crystals are taken primarily with the normal vector of the tunneling junction (and hence the average quasiparticle momentum) along three axes: the anti-nodal axes {100} or {010}, the nodal axis {110}, and the *c*-axis {001}, and those of the pure and Ca-YBCO films are taken along the *c*-axis. All data sets are acquired at $T = 4.2$ K with a solenoid-driven cryogenic scanning tunneling microscope and a mechanically sheared Pt/Ir tip.

4.3.1 Doping dependence of the pairing symmetry and pairing potential

Fig. 4.2 illustrates representative tunneling conductance (dI_{NS}/dV) versus voltage (V) raw data with high spatial resolution for YBCO samples at 4.2 K: (a) optimally doped YBCO crystal, with the average quasiparticle momentum $\vec{k} \parallel \{110\}$ and the tip scanning along {001}; (b) underdoped YBCO crystal, with the average quasiparticle momentum $\vec{k} \parallel \{100\}$ and scanning along {001}; and (c) Ca-YBCO film with $\vec{k} \parallel \{001\}$ and scanning along {100}. Fig. 4.3 shows the (dI_{NS}/dV) versus V spectra normalized to the high-voltage background: (a) underdoped YBCO crystal (upper panel) and (Zn,Mg)-doped YBCO crystal (lower panel) for $\vec{k} \parallel \{100\}$ together with BTK fitting curves (dashed lines); and (b) underdoped *c*-axis thin film (upper panel) and Ca-doped YBCO *c*-axis thin film (lower panel). Each set of the data is normalized relative to the polynomial fit to the high-voltage background conductance, as shown in Fig. 4.2(b) and (c) by the dashed curve.

For the optimally doped and underdoped YBCO, the STS exhibits long-range (~ 100 nm) spatial homogeneity and strong directionality, showing a zero-bias conductance peak (ZBCP) for $\vec{k} \parallel \{110\}$ [Fig. 4.2(a)], nearly “U-shape” gap features around the zero bias for $\vec{k} \parallel \{100\}$ [Fig. 4.2(b),

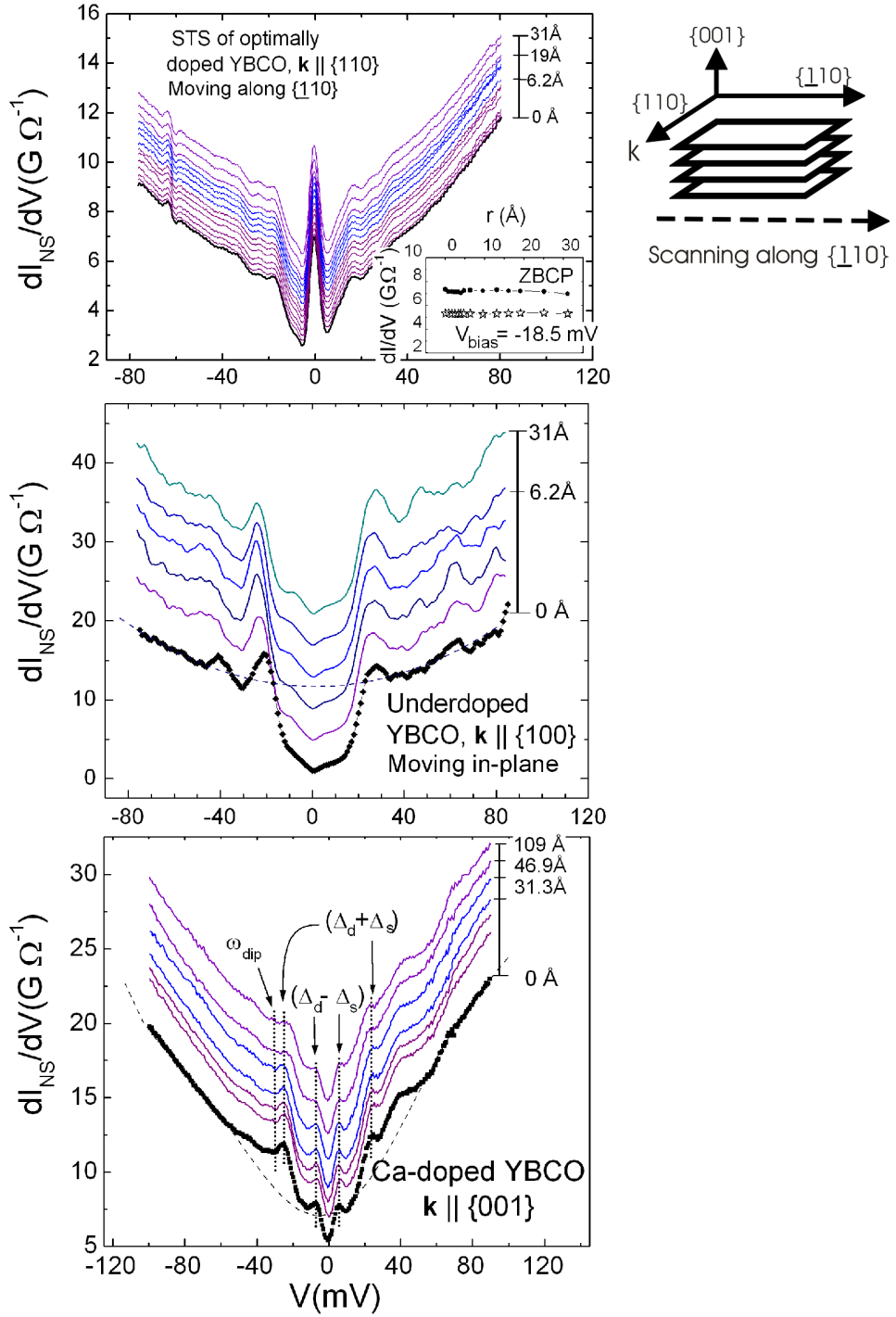


Figure 4.2: Spatially resolved (dI_{NS}/dV) vs. V spectra at 4.2 K: (a) Optimally doped YBCO crystal ($T_c = 92.0 \pm 0.5$ K) with the average quasiparticle momentum $\vec{k} \parallel \{110\}$. (b) Underdoped YBCO crystal ($T_c = 60.0 \pm 2.5$ K) with $\vec{k} \parallel \{100\}$. (c) c-axis Ca-YBCO film ($T_c = 78.0 \pm 2.0$ K). The dashed curves in (b) and (c) are the polynomial fit to the high-voltage background conductance.

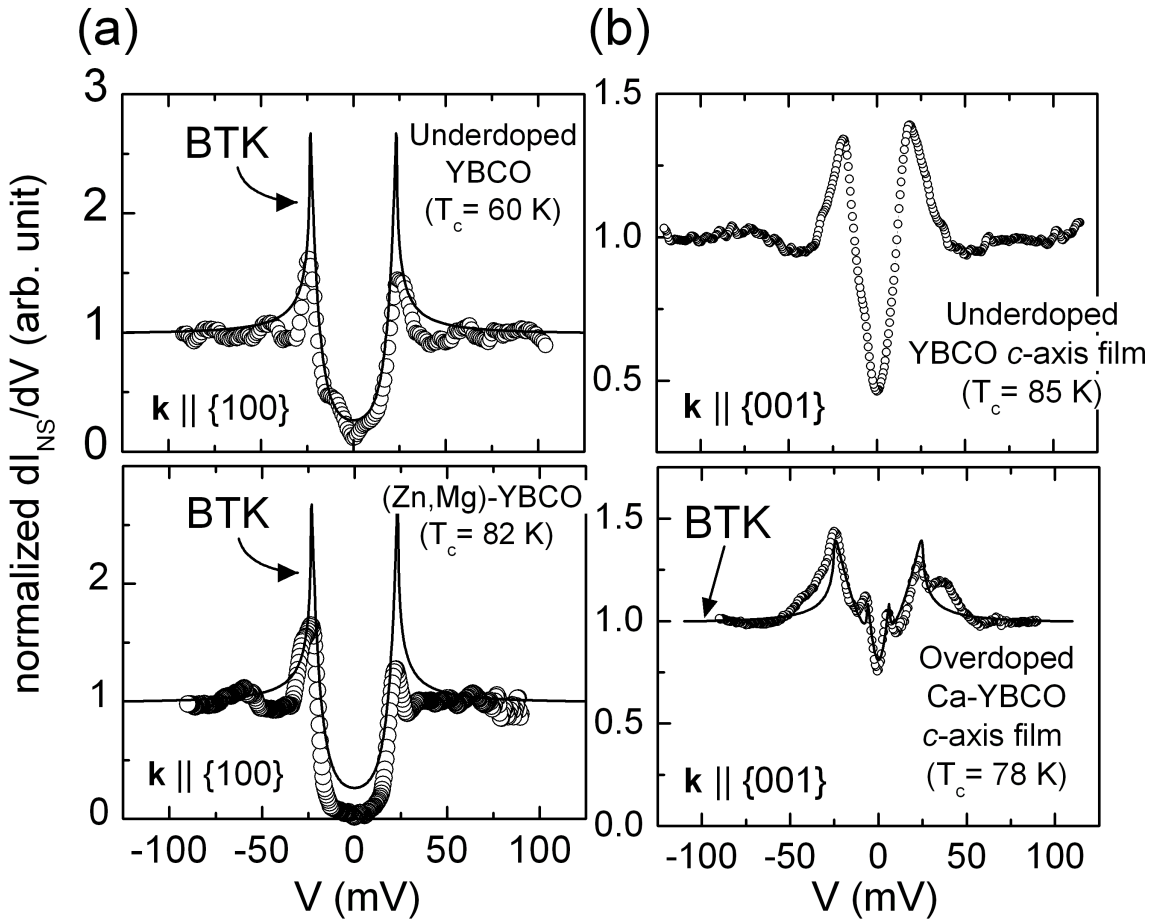
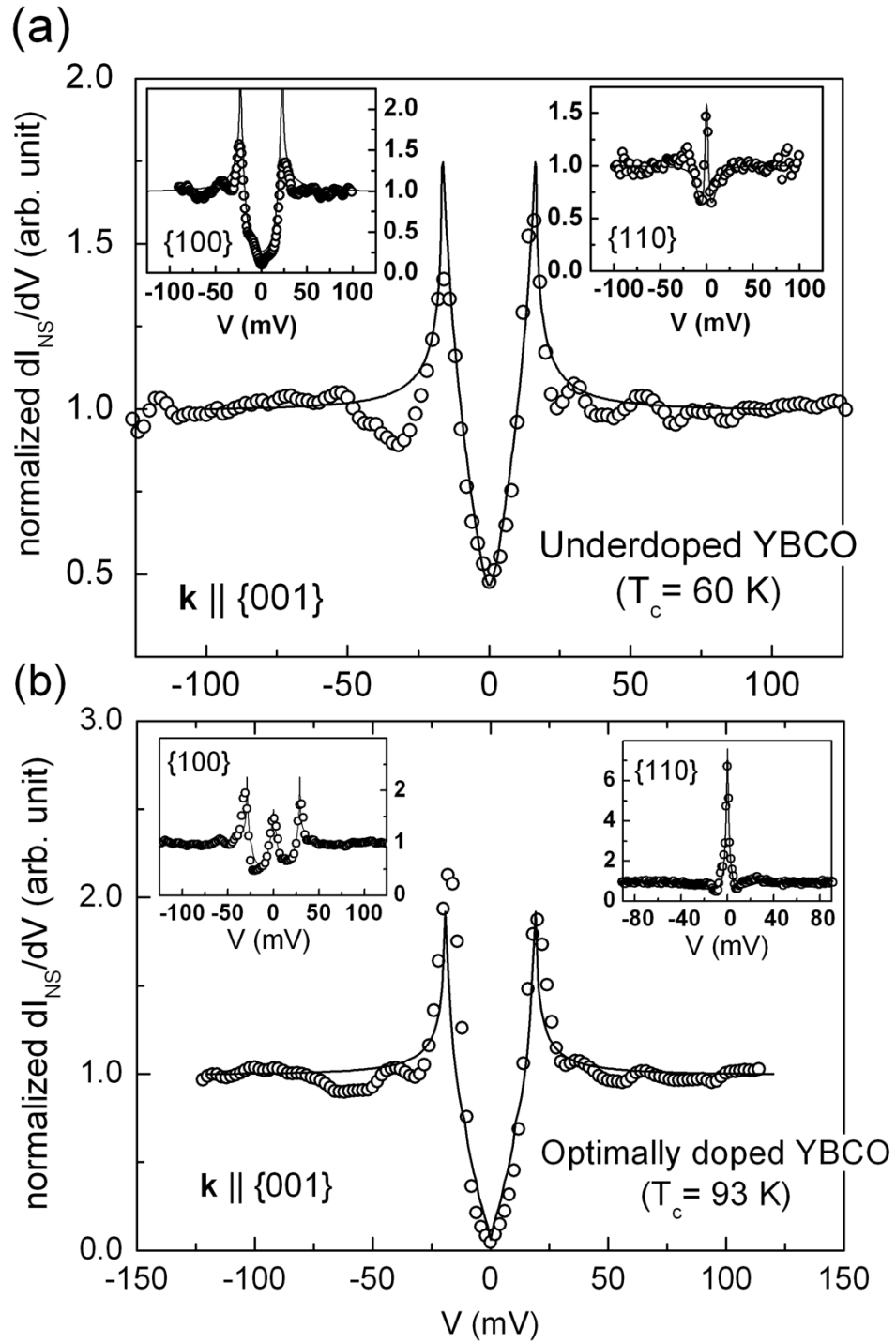


Figure 4.3: (a) Normalized $\{100\}$ spectra of an underdoped YBCO crystal with $T_c = 60.0 \pm 2.5$ K (upper panel) and that of a (Zn,Mg)-YBCO crystal with $T_c = 82.0 \pm 1.5$ K (lower panel) at 4.2 K together with a BTK fitting curve (solid line). (b) Normalized (dI_{NS}/dV) vs. V tunneling spectra of a c -axis underdoped film with $T_c = 85.0 \pm 1.0$ K (upper panel) and that of a Ca-YBCO film with $T_c = 78.0 \pm 2.0$ K (lower-panel) at 4.2K. For the BTK analysis, each data set is normalized relative to the polynomial fit to the high-voltage background conductance, as shown in Fig. 4.2 by the dashed curve. The tunneling cone [174, 184] of all data sets ranges from $(\pi/12)$ to $(\pi/8)$.



Adapted from Wei *et al.*, PRL 81, 2542 (1998)

Figure 4.4: (a) Normalized tunneling spectra of underdoped YBCO single crystal ($T_c = 60.0 \pm 2.5$ K) with BTK fitting curves. Main panel: c -axis tunneling spectrum. Top left inset: Tunneling spectrum with averaged quasiparticle momentum \vec{k} along the anti-nodal direction. Top right inset: Spectrum taken with \vec{k} along the nodal direction. (b) Adapted from Wei *et al.* [174]. Normalized tunneling spectra of optimally doped YBCO single crystal with BTK fitting curves. We note that the $\{100\}$ spectrum shows a ZBCP feature superposed on a U-shape gap because of surface microfaceting. The data points are plotted as open circle and the BTK fitting curves as solid line.

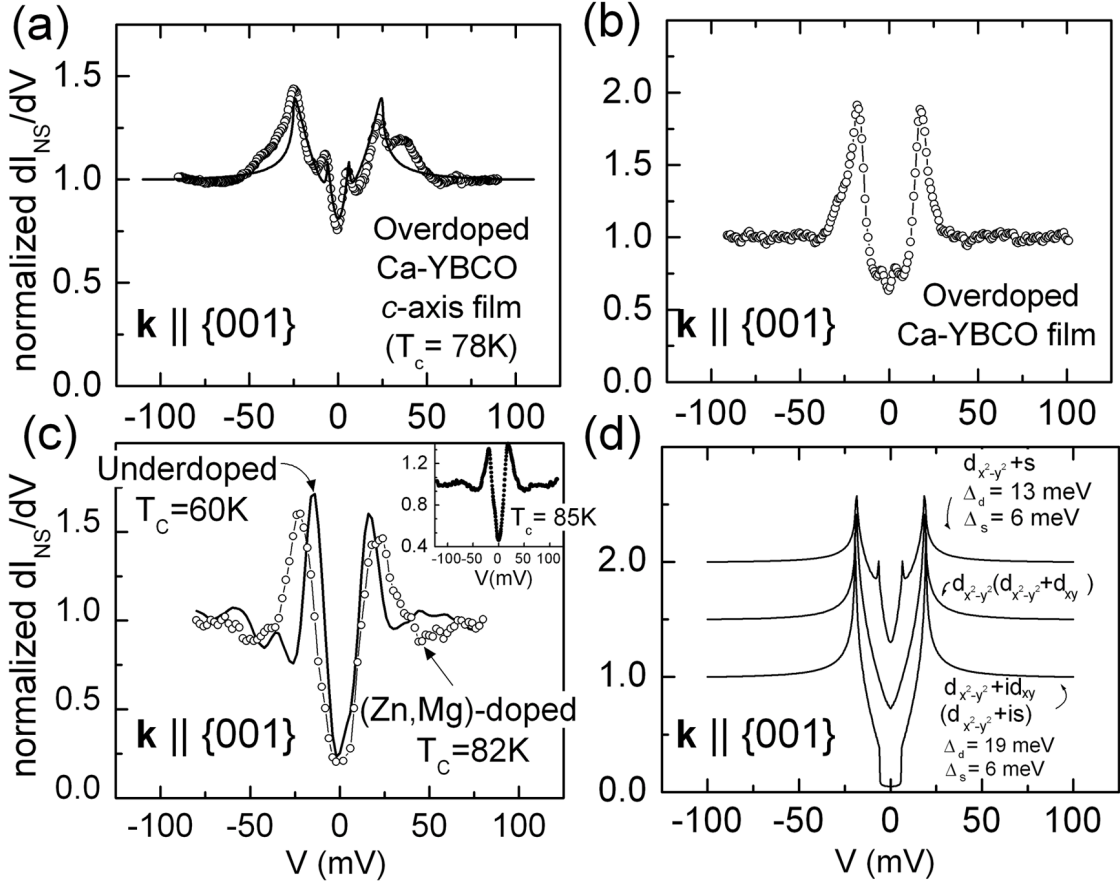


Figure 4.5: Representative c -axis tunneling spectra of YBCO. (a) Spectrum of Ca-YBCO films with $\Delta_d = 17$ meV and $\Delta_s = 9$ meV obtained by the BTK fitting (the thick solid line) to a $(d_{x^2-y^2} + s)$ -wave pairing. (b) Spectrum of YBCO films with $\Delta_d = 13$ meV and $\Delta_s = 6$ meV. (c) Normalized c -axis tunneling spectra of underdoped YBCO single crystal ($T_c = 60.0 \pm 2.5$ K) and (Zn,Mg)-YBCO ($T_c = 82.0 \pm 1.5$ K). Inset: Underdoped YBCO c -axis film ($T_c = 85.0 \pm 1.0$ K) (d) Calculated c -axis tunneling spectra for different pairing symmetries.

Fig. 4.3(a)], and “V-shape” features for $\vec{k} \parallel \{001\}$ [Fig. 4.3(b)]. By taking into account the finite transverse momentum distribution of the incident quasiparticles relative to the normal direction of the sample surface (i.e., by factoring in a finite “tunneling cone,” which typically ranges from 15° to 22.5° [174]), the prima features and the directionality of the spectra of all optimally doped and underdoped YBCO samples are consistent with d -wave pairing within the generalized BTK formalism [*cf.* §2.2] [124, 125, 123]. In Fig. 4.4, the normalized tunneling spectra of underdoped YBCO single crystal ($T_c = 60.0 \pm 2.5$ K) with BTK fitting curves are shown in comparison with the spectra of the optimally doped YBCO single crystal published by Wei *et al.* [174]. The pairing potential of the optimally doped YBCO is 25.0 – 29.0 meV, while that of the underdoped YBCO is

$22.0 - 24.0$ meV.

We note that when tunneling along the $\{100\}$ or $\{010\}$ anti-nodal direction, the theoretical BTK simulation predicts a perfect U-shape with sharp coherence peaks. In real underdoped samples, however, the coherence peaks are suppressed, and disorder-induced quasiparticle states with microscopic spatial variation can exist inside the U-shape gap [Fig. 4.2(b), Fig. 4.3(a)]. The resulting V-shape residual spectra suggest that gapless nodal quasiparticles are responsible for these subgap low-energy excitations.

For the Ca-doped YBCO epitaxial films, macroscopic spatial variation in the STS at a length scale of ~ 50 nm is observed, which correlates with the dimension of the growth islands according to images of atomic force microscopy [177], while the STS's within each island are spatially homogeneous, as exemplified by Fig. 4.2(c). Furthermore, the STS of Ca-YBCO exhibits *long-range symmetric subgap peaks*, which differ from the spectral contributions of local impurities or oxygen vacancies; the latter generally appear as asymmetric and short-range humps in the spectra. These spectral features are in good agreement with $(d_{x^2-y^2} + s)$ -pairing according to the generalized BTK analysis [124, 125], with a pairing potential $\Delta_k = \Delta_d \cos(2\theta_k) + \Delta_s$, where θ_k is the angle of \vec{k} relative to $\{100\}$. Two typical sets of spectra are obtained, one with $\Delta_d = 17$ meV and $\Delta_s = 9$ meV as illustrated in Fig. 4.5(a), and the other with $\Delta_d = 13$ meV and $\Delta_s = 6$ meV in Fig. 4.2(b).²

In comparison, long-range homogeneous spectra consistent with $d_{x^2-y^2}$ -wave pairing are confirmed on the optimally doped and underdoped *c*-axis epitaxial films, as exemplified in Fig. 4.3(b). The *c*-axis tunneling spectra of the underdoped YBCO single crystal, (Zn,Mg)-doped YBCO single crystal, and those of the underdoped YBCO film are also included in Fig. 4.5(c). For clarity, we depict the calculated *c*-axis tunneling spectra of different pairing symmetries in Fig. 4.5(d). Under the premise that the tunneling spectra are spatially homogeneous well beyond the coherence length and mean free path, we suggest that the long-range and symmetric subgap peaks in overdoped Ca-YBCO represent supporting evidence for doping-induced variations in the pairing symmetry from predominantly $d_{x^2-y^2}$ -wave to mixed $(d_{x^2-y^2} + s)$ -wave with a substantial *s*-component ($\geq 30\%$).

²We suspect that the dopant distribution of the heavily overdoped Ca-YBCO thin film may have phase segregation, which can account for the various gap values observed in this sample.

4.3.2 Impurity effect

Contrary to the long-range spatial homogeneity in the quasiparticle spectra of YBCO and Ca-YBCO, microscopic spatial variations have been observed in the (Zn,Mg)-YBCO single crystal near the Zn and Mg sites, where the coherent quasiparticle peaks for the *c*-axis tunneling spectra are strongly suppressed and replaced by a single impurity scattering peak at an energy $\Omega < \Delta_d$. The impurity scattering spectra may be classified into two types. One is associated with a resonant scattering at $\Omega_1 \approx (-10 \pm 2)$ meV and the other at $\Omega_2 \approx (4 \pm 2)$ meV, as shown in Fig. 4.6(a).

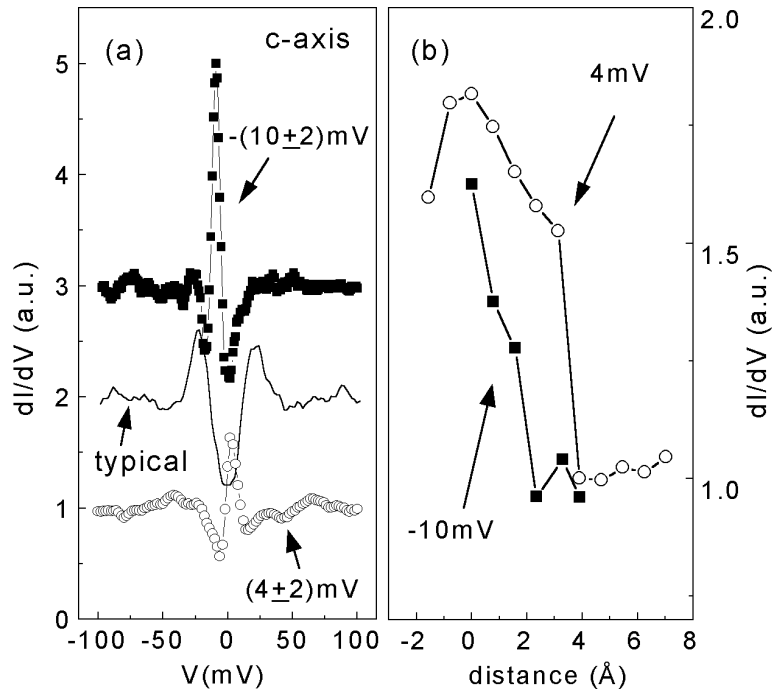


Figure 4.6: (a) Normalized *c*-axis tunneling spectra of the (Zn,Mg)-YBCO single crystal at and away from a local non-magnetic impurities. Two types of resonant energies are found at $\Omega \approx (-10 \pm 2)$ meV and $\Omega \approx (4 \pm 2)$ meV, corresponding to two different substitutions of Zn and Mg in the Cu – O planes. (b) Rapid decrease of the intensity of the resonant scattering peaks for displacement along $\{010\}$ away from an impurity site. The typical spectrum is recovered at ~ 3 nm away from the impurity site.

Assuming the position where the maximum intensity of a resonant peak occurs as an impurity site, we find that the peak persists over several lattice constants for displacement along either $\{100\}$ or $\{010\}$, the Cu – O bonding direction, and the peak intensity decreases rapidly within the Fermi wavelength, as shown in Fig. 4.6(b). For displacement along other directions, the spectral features become much more complicated. For example, the resonant scattering peak could appear to alternate

between energies of the same magnitude and opposite signs as the STM tip scans away from the local impurity [Fig. 4.7]. For STM tips significantly far away from any impurities, the usual c -axis quasiparticle tunneling spectrum is recovered, but the global superconducting gap Δ_d is suppressed to (22 ± 4) meV from $\Delta_d = (27 \pm 2)$ meV in pure YBCO.

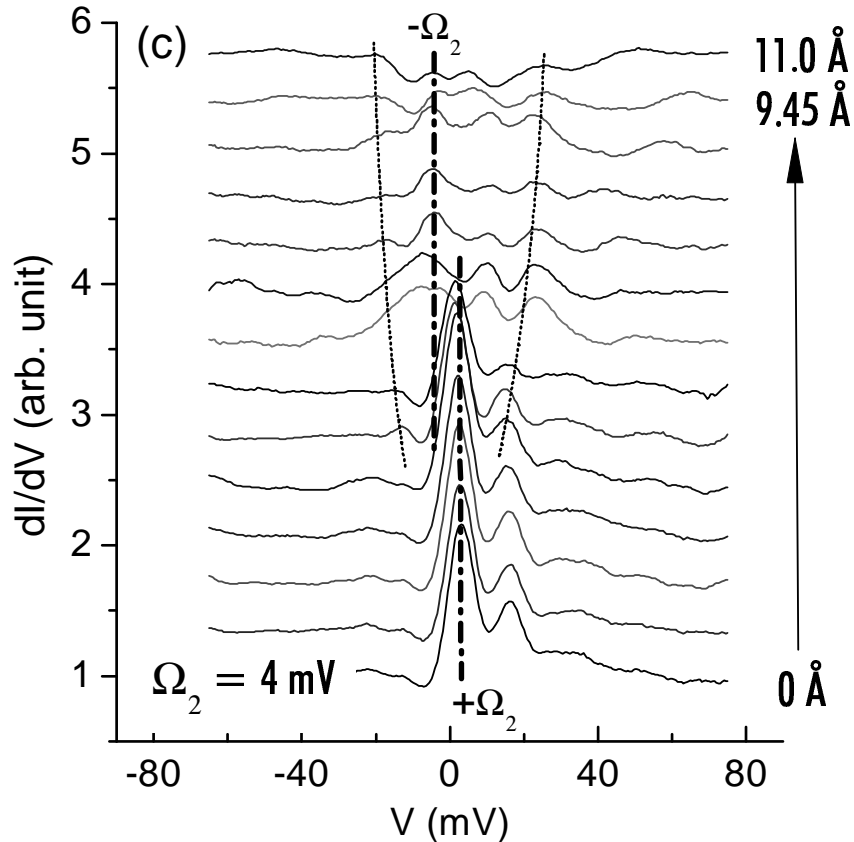


Figure 4.7: Spatial evolution of the c -axis tunneling spectra near a non-magnetic impurity with a scattering peak at $\Omega \approx +4$ meV.

4.4 Discussion

4.4.1 Pairing symmetry

It is shown in §2.2 by the generalized BTK formalism that, for superconductors with a small secondary pairing component, tunneling spectra along certain special axes can reveal the presence of the small admixture. For example, a small time-reversal-symmetry-breaking (TRSB) component,

such as is - or id_{xy} -admixture, would split the ZBCP when tunneling into the nodal direction of a predominantly d -wave superconductor [Fig. 4.8]. It would also change the gapless V-shape c -axis tunneling spectrum into a fully gapped U-shape spectrum around the Fermi level [Fig. 4.5(d)]. In comparison, the effect of an s -wave admixture in a predominantly d -wave superconductor, which breaks C_{4v} , can be manifested in the c -axis tunneling spectrum as two symmetric subgap peaks, while the spectral V-shape around the zero bias is retained [Fig. 4.5(b)].

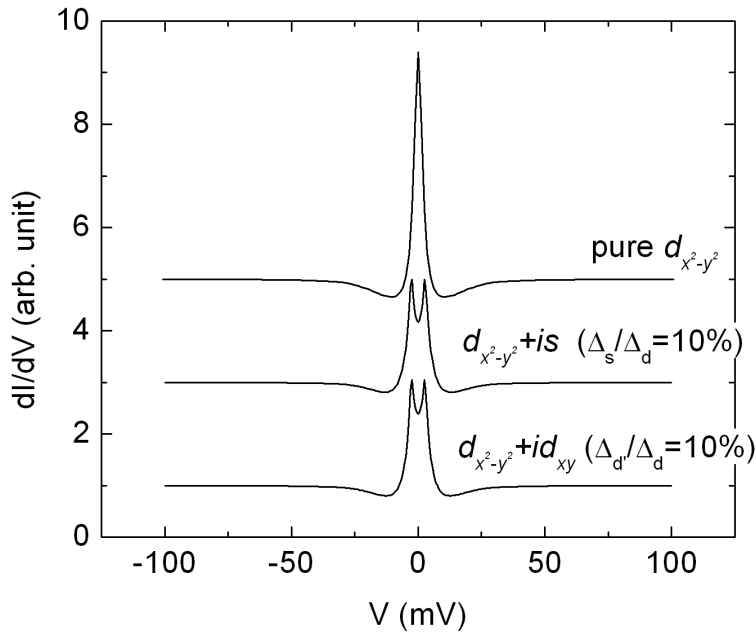


Figure 4.8: Numerical simulation of the tunneling spectra taken along $\{110\}$ for different pairing symmetries.

For convenience, the simulated $\{110\}$ spectrum for different pairing symmetries is reproduced in Fig. 4.8 as a reference. Comparing Fig. 4.8 and Fig. 4.5(d) with the experimental tunneling spectra [Fig. 4.2–4.5], we conclude that there is no TRSB component detected in either $\{110\}$ or c -axis tunneling within the STS resolution. In contrast, a significant amount of s -component ($\geq 30\%$) is revealed in the tunneling spectrum of overdoped Ca-YBCO samples.

Further experimental evidence of a mixed ($d + s$)-pairing in the overdoped YBCO family is provided by the ARPES of the fully oxygenated (lightly overdoped) YBCO single crystal [37] and the Raman spectroscopy of the heavily overdoped Ca-YBCO single crystal [38]. In addition, a sizable s -wave admixture in the SC order parameter of overdoped cuprates with tetragonal crystalline

structures, such as $\text{Bi}_2\text{Sr}_2\text{CaCu}_2\text{O}_{8+\delta}$ (Bi-2212) [38] and $\text{Tl}_2\text{Ba}_2\text{CuO}_{6+\delta}$ (Tl-2201) [185, 39], is also detected in Raman scattering experiments.

In the context of quantum criticality, our data of doping-dependent pairing symmetry is suggestive of a QCP with broken C_{4v} symmetry. However, a small s -pairing component beyond the resolution of our STS exists in the under- and optimally doped YBCO due to crystalline orthorhomicity, as identified to be $\leq 9\%$ by the recent scanning SQUID magnetometry measurement of the half-flux quantum effect [7] in YBCO/Au/Nb ramp-edge junction rings [186]. This result would imply that no obvious broken symmetry have taken place in YBCO when crossing over to the overdoped region. In contrast, the s -wave component found by Raman experiments on heavily overdoped tetragonal Bi-2212 and Tl-2201 crystals indicates that, in these two systems, there *is* a broken C_{4v} symmetry upon overdoping, thereby proving that s -wave mixing in the heavily overdoped limit is a generic feature, irrespective of sample crystalline symmetry. Although there is no obvious change of symmetry observed in YBCO with increasing hole-doping, the significant increase of s -component admixture in overdoped YBCO is indicative of an abrupt change in the ground state electronic properties with doping.

We remark that there have been suggestions of a possible QCP associated with broken time-reversal symmetry in the overdoped limit observed by macroscopic measurements including planar junctions and point-contact spectroscopy [175]. However, as mentioned above, our tunneling results are inconsistent with the existence of a secondary complex pairing component. In addition, other experimental techniques, such as the scanning SQUID magnetometry on three families of hole-doped cuprates including Ca-YBCO [187], yield no trace of the TRSB component in overdoped p-type cuprates. We note that the absence of either $(d_{x^2-y^2} + id_{xy})$ or $(d_{x^2-y^2} + is)$ in the tunneling spectra does not rule out the possibility of certain broken time-reversal-symmetry states, such as the staggered flux state [188, 189, 190] and the circulating current phase [74], for they cannot be detected directly by tunneling. To date, the only few experimental results supportive of a long-range staggered flux order (also referred to as a d -density wave order) [93, 94] or a circulating current phase [191] in the *underdoped* cuprates have been highly controversial. The latest neutron

scattering experiment on highly-ordered underdoped YBCO single crystal [87] contradicts the earlier result [93] and points to a short-range, dynamic spin density wave coexisting with SC instead of a long-range static *d*-density wave order.

Whether TRSB long-range order exists in the *underdoped* cuprates remains to be elucidated with future research efforts. However, it is fair to conclude that, in the *overdoped* limit, there is no experimental technique sensitive to bulk properties reporting its existence, alluding to an extrinsic origin of the complex pairing symmetry observed in certain surface sensitive tunneling experiments [175]. That is, surface degradation and faceting resulted from typical preparation of macroscopic tunneling junctions maybe responsible for the illusive and often non-reproducible TRSB components. On the other hand, an *s*-wave component that preserves the time-reversal symmetry while breaking the crystalline symmetry is revealed in various tunneling and bulk experiments. These observations strongly suggest a fundamental change of the ground state properties with doping. Combined with other bulk experimental results of underdoped YBCO single crystals, our tunneling spectra imply a transition from a coexisting phase of a predominantly *d*-wave SC order with a fluctuating competing order in the underdoped regime to a pure SC order with a sizable *s*-wave admixture in the heavily overdoped limit of YBCO. Consequently, while there is no obvious broken symmetry, a substantial increase of an *s*-wave component is observed in the tunneling spectra, which is consistent with the better charge screening, weaker on-site Coulomb repulsion, and more conventional normal-state behavior exhibited in the overdoped p-type cuprates [Fig. 4.1].

4.4.2 Spatial spectral homogeneity, pseudogap, and competing orders

In sharp contrast to the long-range homogeneous pairing potential manifested in the YBCO tunneling spectra [Fig.4.2] and the absence of inhomogeneous linewidth broadening in NMR studies [192, 193], the tunneling spectra of Bi-2212 exhibit nano-scale variations in the underdoped and optimally doped tunneling spectra [67, 68],

A simple comparison of the anisotropy ratio ξ_{ab}/ξ_c (ξ_{ab} : in-plane superconducting coherence length; ξ_c : *c*-axis superconducting coherence length) of YBCO ($\xi_{ab}/\xi_c \sim 5$) with that of Bi-2212

$(\xi_{ab}/\xi_c > 150)$ clearly indicates that YBCO has a much stronger three-dimensional electronic coupling. Furthermore, the ratio of the c -axis coherence length to the c -axis lattice constant of Bi-2212 is smaller than 0.01 while that of YBCO ranges from $0.2 - 0.7$, indicating that Bi-2212 is indeed highly two dimensional (2D). According to the Hohenberg-Mermin-Wagner theorem, in a 2D system any small disturbance can disrupt the superconducting (SC) long-range order. In particular, if there is a second phase close in energy to the SC phase, it can be locally stabilized by disorder, yielding a tunneling spectrum characteristic of that competing phase and thus resulting in nano-scale spectral variations.

Recent STS measurements on Bi-2212 single crystals confirmed that the nano-scale spectra variations are related to dopant-induced disorder in this system [194]. The perturbation caused by the oxygen dopants is strong enough to locally suppress the superconducting coherence peaks and give rise to a PG-like spectrum at low temperatures. Taking into account the interlayer tunneling spectroscopy (ITS) result [150, 69, 195], which states that the PG and the sharp SC coherence peaks coexist below T_c and, above T_c , the former persists while the latter disappear, it strongly suggests that the PG observed in the ITS (and other large-area tunneling spectroscopy) experiments is dominated by the PG-like spectra near the oxygen dopants observed in STS and that it is indicative of a fluctuating competing order pinned down by disorder in Bi-2212. We will present in Chapter 6 the theoretical modeling of phase-fluctuated d -wave superconductivity coexisting with the competing order, which yields pseudogap-like spectra as observed empirically 6.4. In contrast, because of the much stronger interlayer coupling in YBCO, the SC order is more robust against disorder-induced fluctuations. Therefore, the tunneling spectrum and the bulk electronic properties show long-range homogeneity in this system.

The stabilization of a fluctuating order in Bi-2212 by oxygen disorder also explains the disparate doping dependence of the quasiparticle spectral gap of the two systems. In YBCO, the maximum value of the d -wave gap Δ_d is non-monotonic with the doping level p [Fig. 4.9(a)], whereas the ratio $(2\Delta_d/k_B T_c)$ increases with decreasing doping, from ~ 7.8 for $p \approx 0.09$ to ~ 4.5 for $p \approx 0.22$, as illustrated in Fig. 4.9(b). On the other hand, tunneling experiments on Bi-2212 find an average

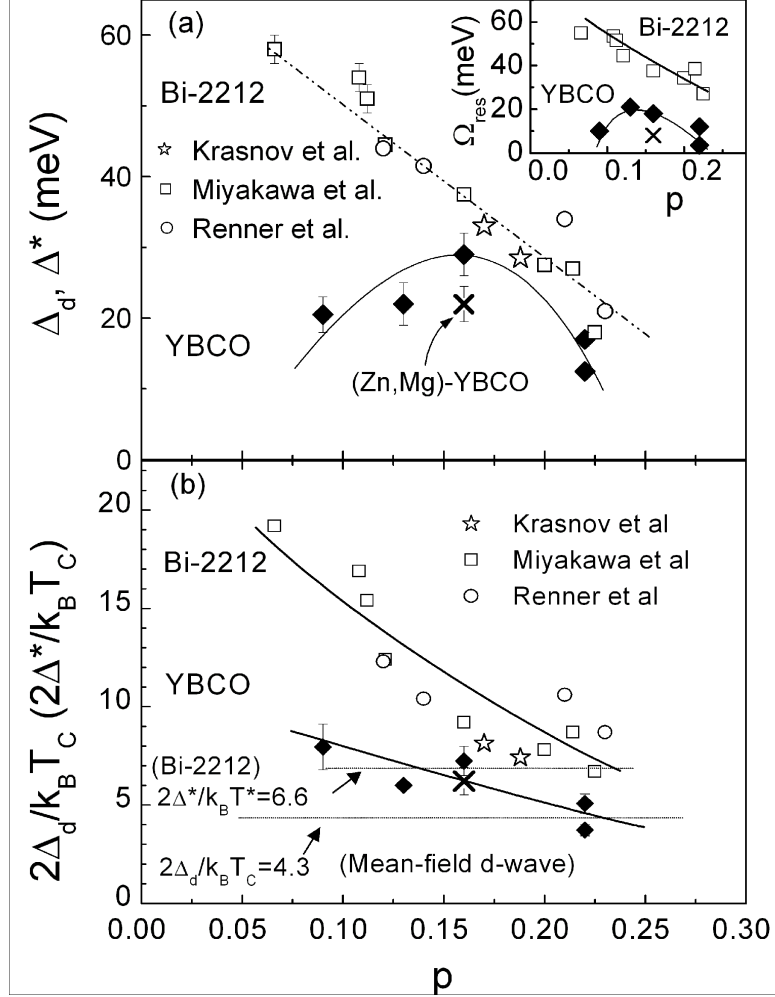


Figure 4.9: (a) Comparison of $\Delta_d(p)$ in YBCO with $\Delta^*(p)$ in Bi-2212. The doping level p is determined from the formula, $1 - T_c/T_{c,max} = 82.6(p - 0.16)^2$ [196, 197] with $T_{c,max} = 93.0$ K. Inset: Comparison of $\Omega_{res}(p)$ for YBCO and Bi-2212. (b) Doping-dependent $(2\Delta_d/k_B T_c)$ for YBCO and $(2\Delta^*/k_B T_c)$ for Bi-2212. The solid diamond denotes the YBCO data acquired in this study. The error bar associated with each doping level covers the range of Δ_d obtained from all spectra and the uncertainties of the BTK fitting. The open symbols are data extracted from three representative tunneling experiments of Bi-2212. (Open star: Krasnov *et al.* [69]. Open square: Miyakawa *et al.* [148]. Open circle: From Renner *et al.* [54]. The solid lines are guide to the eye.

gap Δ^* that increases with decreasing doping p , scales with the pseudogap temperature T^* , $2\Delta^* \sim 6.6k_B T^*$ [148, 57, 54, 198, 199, 200], and persists above T_c [9].

To understand the different trends in these two hole-doped cuprates, we examine the tunneling results on Bi-2212 in more detail. The low-temperature c -axis STM tunneling result of the optimally doped and underdoped Bi-2212 reveals two types of spectra [67, 68]. One shows sharp superconducting coherence peaks accompanied by the small satellite features located slightly above the spectral gap [67, 68] with the sharp peaks diminishing upon increasing temperatures [54]. The other type shows rounded spectral peaks [67] which resemble the PG spectra taken above T_c [54, 99]. As mentioned earlier, there is strong evidence that the nano-scale spectral variations are induced by oxygen dopants [194], and the resulting PG-like spectra are indicative of a pinned competing order coexisting with superconductivity. At the mean-field level, the spectral gap for the coexisting phase is $\Delta_{eff} \approx \sqrt{\Delta_d^2 + V_{co}^2}$, where V_{co} is the strength of the disorder-pinned competing order. As doping level decreases, because the SC pairing strength decreases, more and more regions become susceptible to disorder pinning of competing orders, which gives rise to PG-like spectra as shown in [68, 98]. Besides, the increasing strength of the competing order V_{co} starts to dominate over the diminishing Δ_d . Therefore, when the quasiparticle spectra are averaged over a macroscopic region, the average spectral gap Δ^* increases with decreasing doping, as manifested in the break-junction tunneling spectroscopy and the ARPES experiments [148, 57, 54, 198, 199, 200]. In contrast, for YBCO whose anisotropy ratio is much smaller, the superconducting order is much stiffer. Additional experiments in high fields also reveal that YBCO is farther away from quantum criticality than Bi-2212 [201, 202]. Thus, the effect of the competing phase is suppressed, and the mean-field BTK description is adequate to account for the low-energy characteristics of the tunneling spectra near and below the superconducting gap so that the measured energy gap Δ_d appears to track T_c better. In Chapter 6, we shall provide the theoretical foundation that justifies the conclusions drawn from experiments.

4.4.3 Satellite features

Although the generalized BTK analysis is suitable for deriving the pairing potential and the primary spectral characteristics, it cannot account for the satellite spectral features associated with many-body interactions [159, 203, 204]. In Bi-2212, the high-energy spectral “dip-and-hump” features [148, 57, 54, 198, 199, 200] are generally attributed to quasiparticle damping via interactions with collective bosonic excitations [159, 203, 204]. In the strong coupling limit, the spectral dip is expected to appear at the energy $\omega_{dip} = \Delta + \Omega_{res}$, where Δ is the measured gap, and Ω_{res} is associated with the resonance of the collective excitations [159, 203, 204]. If we adopt the notion that the ground state of YBCO is purely superconductivity and the bosonic excitations are responsible for the satellite features, we may define Ω_{res} as the energy difference between the primary peak (Δ) and the dip (ω_{dip}) [203], as indicated by the dotted lines in Fig. 4.2(c), and we find that Ω_{res} in YBCO decreases with decreasing p , as shown in the inset of Fig. 4.9(a).

There have been heated debates about the nature of these many-body bosonic modes [205, 206, 207]. The possible candidates of the bosonic excitations include the magnetic resonance mode [205], the B_{1g} phonon mode [208], and the longitudinal optical phonon mode [209]. They all have similar energy scales, and thus to distinguish between the three is non-trivial. According to the tunneling spectra of YBCO, the magnitude of the global Δ and Ω_{res} in (Zn,Mg)-YBCO both become smaller than those of the optimally doped YBCO, as shown in Fig. 4.9(a). The strong suppression of Ω_{res} by doping small amount of impurities with atomic masses similar to Cu but with different spin states suggests that if the satellite features arise from the bosonic modes, then it is the magnetic excitations, not phonons, that couple to the electrons and result in the “dip-and-hump” features. The latest ARPES data on Zn- and Ni-substituted Bi-2212 have demonstrated a significant reduction of the real part of the electron self-energy upon impurity substitution that disrupts the anti-ferromagnetic spin fluctuations in Bi-2212 [210], providing additional strong evidence for the magnetic origin of “dip-and-hump” features in p-type cuprates.

While in our earlier publications we had analyzed the satellite features of YBCO quasiparticle tunneling spectra in the context of bosonic excitations coupled with the quasiparticles of a pure su-

perconducting state, we notice that the energy scale of the bosonic mode deduced from the tunneling spectra is substantially smaller than that obtained directly from the bulk neutron scattering experiments. Thus, we adopt an alternative interpretation that views the ground state of the cuprates as a coexisting phase of superconductivity and a relevant competing order, so that the satellite features are in fact the manifestation of the competing order with an effective gap $\Delta_{eff} \approx \sqrt{\Delta_d^2 + V_{co}^2}$. This alternative view has the advantage of consistently accounting for the presence of pseudogap phenomena and satellite features in hole-doped cuprates versus the complete absence of both the pseudogap and satellite features in electron-doped cuprates by simply varying the relative strength of superconductivity to the competing order from hole- to electron-doped cuprate superconductors. The details of the theoretical modeling will be provided in Chapter 6.

4.4.4 Quantum impurities

In a conventional *s*-wave superconductor, according to Anderson's theorem [211], non-magnetic impurities (*i.e.*, spinless with $S = 0$, such as Zn^{2+} , Mg^{2+} , Li^+ and Al^{3+}) are weak pair breakers because the time-reversal symmetry is preserved. Pairing of the time-reversed degenerate states leads to the same T_c and the same BCS density of states (DOS) as that of a pure superconductor. It is the magnetic impurities that break the time-reversal symmetry, which strongly suppresses T_c and modifies the DOS [212].

In contrast, the gapless nature of the $d_{x^2-y^2}$ - or $(d_{x^2-y^2} + s)$ -pairing symmetry and the presence of gapless nodal quasiparticles in hole-doped cuprates result in their drastic response to the non-magnetic impurities. The spinless quantum impurities that substitute the Cu^{2+} ions in the CuO_2 plane incur strong suppression of superconductivity due to the resulting potential scattering of the nodal quasiparticles [213, 214]. In addition, Kondo effects are expected because of the induced magnetic moments [215, 216, 217, 218] associated with the non-magnetic impurities in the background of nearest-neighbor paired singlets. The induced magnetic moments can significantly perturb the immediate vicinity of the impurity site, yielding suppression of superconductivity below T_c and a strong effect on the spin dynamics above T_c [219].

That the non-magnetic impurities, such as Zn^{2+} and Mg^{2+} in YBCO, are strong pair breakers suppressing the coherence peaks and modifying the superconducting density of states [Fig. 4.6] is supportive of the presence of nodal quasiparticles in a pure d -wave superconductor [220, 216, 214, 213, 221, 217, 222, 223]. Furthermore, the single scattering peak at a non-magnetic impurity site is incompatible with any broken T -symmetry component in the pairing potential, for the latter would result in two excitation peaks at peaks at $\pm\Omega$ [221]. Hence the absence of double peaks in the quasiparticle spectra of both YBCO [8] and Bi-2212 [183] provides additional confirmation of a gapless Fermi surface in the superconducting state of the hole-doped cuprates.

4.5 Summary

In conclusion, we have demonstrated the long-range spatial homogeneity in the tunneling spectra of YBCO samples with a number of doping levels. In contrast, the spectral characteristics of the (Zn,Mg)-YBCO exhibit microscopic variations indicating strong pairing breaking effects near the Zn and Mg impurities. The quasiparticle spectral features and the impurity scattering effects in the optimally doped and underdoped YBCO are consistent with a predominantly $d_{x^2-y^2}(> 95\%)$ -wave pairing, whereas those of the overdoped Ca-YBCO exhibit $d_{x^2-y^2}$ pairing with a significant s -component mixing ($\geq 30\%$), indicative of a change of ground state properties. Except for the higher-energy satellite features, all low-energy spectral characteristics are well captured by the generalized BTK theory, indicating that critical fluctuations play a minor role in determining the single-particle low-energy excitation spectra and that mean field theory provides a reasonable description for the subgap quasiparticle tunneling spectra in the superconducting state of YBCO. The notion is further corroborated by the studies of the vortex-state quantum fluctuations in various cuprate superconductors, which reveal that YBCO is further away from quantum criticality than most other families of cuprate superconductors.

Chapter 5

Tunneling Spectra of Electron-Doped $\text{Sr}_{1-x}\text{La}_x\text{CuO}_2$ ¹

5.1 Introduction

In the previous chapter, we have addressed the doping-dependent pairing symmetry, pairing potential and the spectral response to non-magnetic impurities in hole-doped (p-type) YBCO. Both the low-energy spectral characteristics of pure YBCO and the resonant impurity scattering spectra of the (Zn,Mg)-YBCO suggest that the superconducting order parameter is predominantly *d*-wave, with gapless nodal quasiparticles as the low-energy excitations. Furthermore, the significant increase of *s*-wave component in the overdoped Ca-YBCO and the pronounced high-energy satellite features in underdoped and optimally doped YBCO are indicative of their proximity to a quantum phase transition from the overdoped superconducting phase to the underdoped coexisting phase of superconductivity and a competing order. The satellite features that we interpret as a manifestation of the competing order evolve into the pseudogap above T_c in underdoped p-type cuprates. The commonly observed incommensurate spin-density-wave is one of the possible candidates for the competing order of the underdoped and optimally doped p-type cuprates.

The predominantly $d_{x^2-y^2}$ pairing symmetry [7, 6], the pseudogap phenomena [224, 9], and the existence of incommensurate spin fluctuations in the CuO₂ planes [224, 169] in the underdoped and optimally p-type cuprates have been widely conceived as essential to high-temperature supercon-

¹The main contents of this chapter are published as C.-T. Chen, *et al.* *Phys. Rev. Lett.* **88**, 227002 (2002).

ductivity. However, the pairing symmetry of the one-layer electron-doped (n-type) cuprates, such as $\text{Nd}_{1.85}\text{Ce}_{0.15}\text{CuO}_{4-\delta}$ (NCCO) and $\text{Pr}_{1.85}\text{Ce}_{0.15}\text{CuO}_{4-\delta}$ (PCCO), remains controversial [§1.2.1]. While the tunneling spectra of bicrystal grain-boundary junctions [40, 225] and point-contact tunneling spectroscopy [41] on nominally optimally doped NCCO report the absence of the zero-bias conductance peak along the $\{110\}$ direction and a momentum-independent pairing potential, tricrystal scanning SQUID magnetometry [43] on nominally optimally doped NCCO and PCCO and grain-boundary Josephson junction spectroscopy on nearly optimally doped $\text{La}_{2-x}\text{Ce}_x\text{CuO}_{4-y}$ ($x = 0.105$) (LCCO) [226] support the d -wave pairing symmetry. Results from the bulk penetration measurements have also been contradictory. Some experiments exhibit s -wave pairing in underdoped and nearly optimally doped PCCO [227, 228] while others reveal d -wave pairing [229, 230]. Furthermore, doping-dependent pairing symmetry is observed by point-contact spectroscopy [47] and penetration depth measurements [48], where the change from d -wave pairing in the underdoped to s -wave or $d + is(id')$ -pairing in optimally doped and overdoped one-layer PCCO has been suggested.

Concerning the pseudogap phenomena in the electron-doped cuprates, contrary to the normal-state low-energy spectral gap commonly observed in the hole-doped cuprates, no discernible loss of low-energy spectral weight above T_c has been demonstrated in quasiparticle tunneling spectroscopy of PCCO and NCCO [16, 17, 18]. On the other hand, magnetic-field-induced pseudogap-like features have been reported by tunneling spectroscopy on PCCO and LCCO in the normal state [17, 18], and these phenomena all occur below T_c in contrast to the findings in underdoped p-type cuprates. Moreover, no Nernst effect above $H_{c2}(T)$ or T_c has been found in any n-type cuprates, which is consistent with the absence of pseudogap phenomena. The behavior of the spin excitations in one-layer electron-doped cuprates is also distinctly different. While hole-doped cuprates display incommensurate low-energy spin fluctuations and an inward dispersion toward a magnetic resonance with increasing energy [231, 232], electron-doped NCCO [89] and $\text{Pr}_{0.88}\text{LaCe}_{0.12}\text{CuO}_{4-\delta}$ (PLCCO) [85, 92] display commensurate spin fluctuations with possible coexistence of a residual three-dimensional anti-ferromagnetic order [89, 233, 234].

A possible explanation for conflicting experimental observations of the pairing symmetry in n-

type cuprate superconductors is associated with difficulties in producing consistent material properties. Specifically, we note that in the growth of NCCO, PLCCO, and PCCO, it is necessary to subject the samples to a post-annealing oxygen reduction process in order to turn the non-superconducting as-grown crystals into superconductors. The uncertainty in the oxygen reduction renders a precise determination of the doping level difficult, and controversies arise over the nature of the charge carriers introduced to the CuO₂ planes because of possible self-doping of holes from the in-plane oxygen vacancies created by the oxygen reduction [235]. Besides, the formation of magnetic impurity phases during the reduction procedure casts doubts on some neutron scattering results [236]. The existence of magnetic ions, Nd³⁺ and Pr³⁺, further complicates the interpretation of conflicting experimental observations of the one-layer electron-doped cuprates.

In comparison, the electron-doped infinite-layer cuprate Sr_{0.9}La_{0.1}CuO₂ (SLCO) is superior in that it contains only one metallic monolayer of Sr or La with no excess charge reservoir block between CuO₂ planes [Fig. 5.1]. The as-grown samples are free of magnetic ions and are superconducting without the need for oxygen reduction. Thus, scanning tunneling spectroscopy of SLCO should provide valuable information on the investigation of the asymmetry between n-type and p-type cuprates and on the universality of the pairing symmetry and pseudogap phenomena.

In this chapter, we report quasiparticle tunneling spectra of the n-type infinite-layer pure and impurity-doped SLCO that reveal characteristics which counter a number of common phenomena in the hole-doped cuprates. The nearly optimally doped SLCO with $T_c = 43$ K exhibits a momentum-independent superconducting gap $\Delta = 13.0 \pm 2.0$ meV that substantially exceeds the BCS value, and the spectral characteristics indicate the complete absence of satellite features above the spectral gap in the superconducting state and the absence of pseudogap in the normal state. The spectral response to quantum impurities at the Cu sites also differs fundamentally from that of the p-type cuprates with $d_{x^2-y^2}$ -wave pairing symmetry.

5.2 Crystalline structure and sample preparation

Despite significant progress in the studies of cuprate superconductivity, the research on the simplest form of cuprates, the infinite-layer system $\text{Sr}_{1-x}\text{Ln}_x\text{CuO}_2$ ($\text{Ln} = \text{La}, \text{Gd}, \text{Sm}$), has been limited [237, 238, 239] due to the difficulties in making single-phase bulk samples with complete superconducting volume. Recently, a breakthrough in high-pressure (4 GPa), high-temperature (950 C°) synthesis technique [240] has yielded single-phase polycrystalline samples of $\text{Sr}_{0.9}\text{La}_{0.1}\text{CuO}_2$ with nearly 100% superconducting volume and a sharp superconducting transition temperature at $T_c = 43$ K, thus enabling reliable spectroscopic studies of the pairing symmetry and the effects of quantum impurities.

These single-phased infinite-layer cuprates are n-type with P4/mmm symmetry, which differ significantly from other cuprates in that no excess charge reservoir block exists between consecutive CuO_2 planes except for a single layer of Sr (La) ions, as illustrated in Fig. 5.1. Contrary to the one-layer n-type cuprates, the oxygen distribution in the infinite-layer polycrystalline SLCO is perfectly stoichiometric, without oxygen vacancies in the CuO_2 planes and excess interstitial oxygen in the Sr (La) layer [237]. Furthermore, the c -axis superconducting coherence length ($\xi_c = 0.53$ nm) is found to be longer than the c -axis lattice constant ($c_0 = 0.347$ nm) [241], in stark contrast to other cuprate superconductors with $\xi_c \ll c_0$. Hence, the superconducting properties of the infinite-layer system are expected to be more three-dimensional, as opposed to the quasi-two-dimensional nature of all other cuprates.

The samples studied in this work included high-density granular samples of $\text{Sr}_{0.9}\text{La}_{0.1}\text{CuO}_2$ (SLCO), $\text{Sr}_{0.9}\text{La}_{0.1}(\text{Cu}_{0.99}\text{Zn}_{0.01})\text{O}_2$ (1% Zn-SLCO), and $\text{Sr}_{0.9}\text{La}_{0.1}(\text{Cu}_{0.99}\text{Ni}_{0.01})\text{O}_2$ (1% Ni-SLCO). X-ray diffraction (XRD) measurements confirm the single-phase nature of all samples, and both XRD and scanning electron microscopy (SEM) [240, 242] reveal random grain orientation and a typical grain size of a few micrometers in diameter. Magnetization studies reveal nearly 100% superconducting volume for all samples, with $T_c = 43$ K and $\Delta T_c \leq 1.0$ K for SLCO and 1% Zn-SLCO, and $T_c = 32$ K, $\Delta T_c \sim 1.0$ K for 1% Ni-SLCO. Structurally, the infinite-layer system is stoichiometrically homogeneous with up to < 3% Zn or Ni substitution [243].

The sample surface is prepared by non-aqueous chemical etching with 0.5% bromine in absolute

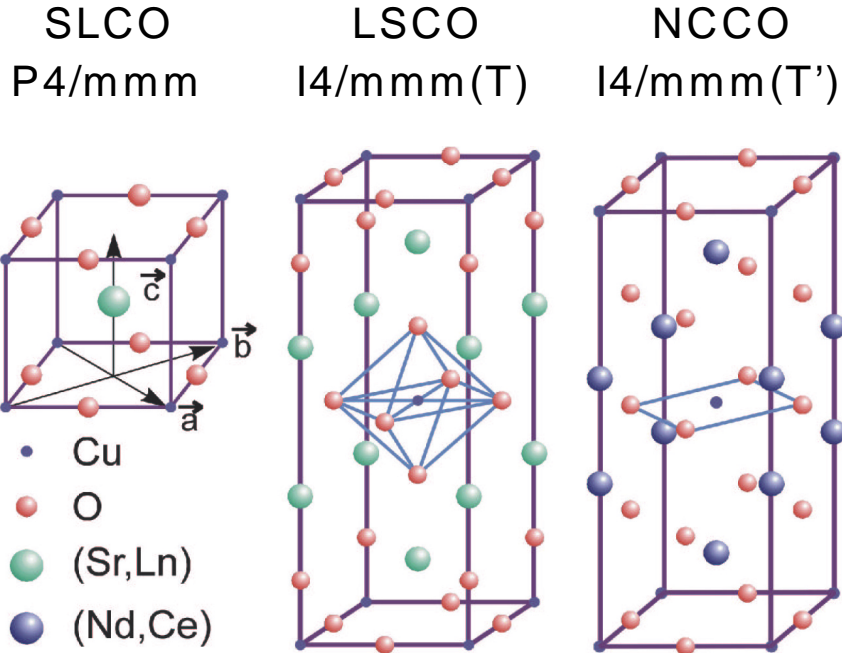


Figure 5.1: Comparison of the structure of the infinite-layer system $\text{Sr}_{1-x}\text{Ln}_x\text{CuO}_2$, ($\text{Ln} = \text{La}, \text{Gd}, \text{Sm}$), with those of the one-layer p-type (T-phase) and one-layer n-type (T'-phase) cuprates.

ethanol for less than 30 seconds [242], rinsed in pure ethonal, blown dry with high-purity helium or nitrogen, and transferred to the STM probe in a glove box with dry N_2 at ambient pressure. Nearly stoichiometric surface is confirmed with X-ray photoemission spectroscopy (XPS) [242]. We note that because of the polycrystalline nature of the sample, a shorter etching time is required in order to avoid damaging the grain boundaries and yielding disconnected crystallites on the surface.

5.3 Results of scanning tunneling spectroscopy

Quasiparticle tunneling spectra presented in this chapter are acquired with two low-temperature scanning tunneling microscopes, one of which is a solenoid-driven gas-cooled STM operating at 4.2 K, and the other is the variable-temperature shear-piezo-driven STM as described in Chapter 3. Tunneling spectra are taken on hundreds of randomly oriented grains for the three different infinite-layer compounds so as to sample a range of quasiparticle momenta relative to the crystalline axes of the local grains. A typical surface topography of the pure SLCO sample for our spectroscopic studies with sub-nanometer flatness is exemplified in the left panel of Fig. 5.2(a), and a zoom-out

view of this area is illustrated in Fig. 5.2(b). Confirming the local flatness for the tunneling spectra ensures that the average momentum of the incident quasiparticles relative to the crystalline axes of a grain is well-defined.

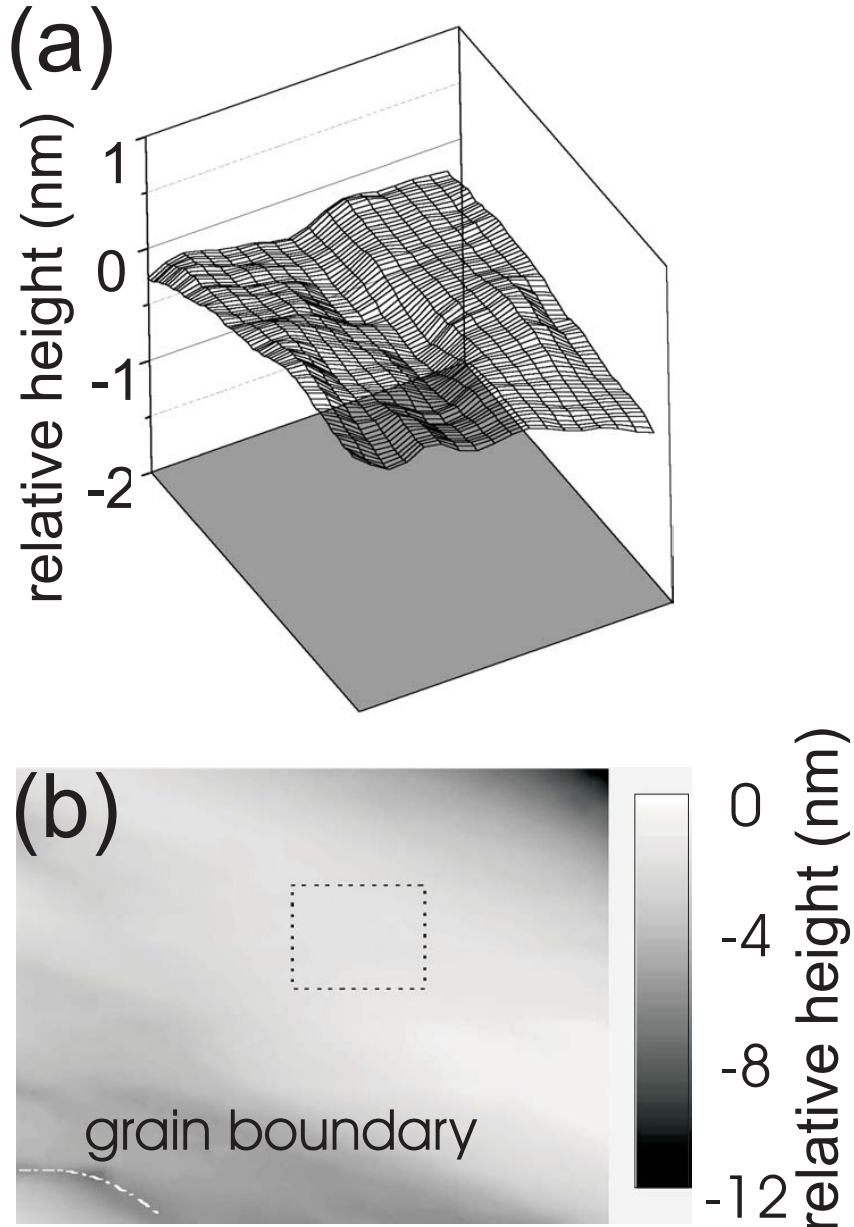


Figure 5.2: (a) A representative surface topography of an area of SLCO with sub-nanometer flatness. The typical area with atomic-scale flatness where most tunneling spectra were taken was greater than $(20 \text{ nm} \times 20 \text{ nm})$, and the work function of the spectra was $0.1 \sim 1 \text{ eV}$. (b) A zoom-out view of the region shown in part (a) (indicated by the dashed box) over an area $(49 \text{ nm} \times 40 \text{ nm})$. Also shown in the lower left corner is a grain boundary.

5.3.1 Pairing symmetry and pairing potential of pure $\text{Sr}_{1-x}\text{La}_x\text{CuO}_2$

A set of representative differential conductance (dI/dV) versus biased voltage (V) spectra for a locally flat area is depicted in Fig. 5.3(a). The waterfall plot displays a line cut of tunneling spectra taken at equally spaced locations with a separation of 1.5 nm. The curves are displaced vertically for clarity except for the bottom curve. We note that the low zero-bias conductance value indicates that the surface disorder is small and the chemical etching procedure is effective.

For the set of data shown in Fig. 5.3(a), both the low-energy spectral gap and the high-energy background are spatially homogeneous up to ~ 100 nm. In general, all spectral characteristics reveal long-range (> 50 nm) spatial homogeneity within each grain. The variations in the spectral gap ($\Delta = 13.0 \pm 2.5$ meV) across hundreds of randomly oriented grains are relatively small, which suggests that the pairing symmetry of SLCO is momentum-independent. Here $(2\Delta/e)$ is defined as the conductance peak-to-peak separation in the spectra. This observation is in sharp contrast to the findings of strongly momentum-dependent spectra in the p-type cuprates with $d_{x^2-y^2}$ pairing symmetry [§4]. The absence of the zero-bias conductance peak (ZBCP), a hallmark for unconventional pairing symmetry, for over 1000 spectra provides additional support for a fully gapped Fermi surface.

By normalizing a typical spectrum in Fig. 5.3(a) relative to the background conductance shown in the left inset of Fig. 5.3(a), we compare the quasiparticle density of states (DOS) of SLCO with the BCS theoretical curve, as illustrated in Fig. 5.3(b). The spectral weight of SLCO for quasiparticle energies at $|E| \geq \Delta$ is smaller than the BCS prediction, whereas excess low-energy DOS appears for $|E| < \Delta$ and the DOS approaches zero at the Fermi level (i.e., $V = 0$). Such behavior cannot be accounted for by the simple inclusion of disorder in the BCS weak-coupling limit, because the latter would have only broadened the width of the conductance peaks and also increased the DOS near $V = 0$ substantially. The spectra also differ fundamentally from those of pure $d_{x^2-y^2}$ -wave cuprates [8] because of the absence of ZBCP and the lack of discernible gap variations in all spectra taken on random grain orientations. Even in a special case of c -axis tunneling, $|d^2I/dV^2|_{V \rightarrow 0^\pm}$ would have been a positive constant in a $d_{x^2-y^2}$ -wave superconductor, as simulated by the thin solid line in

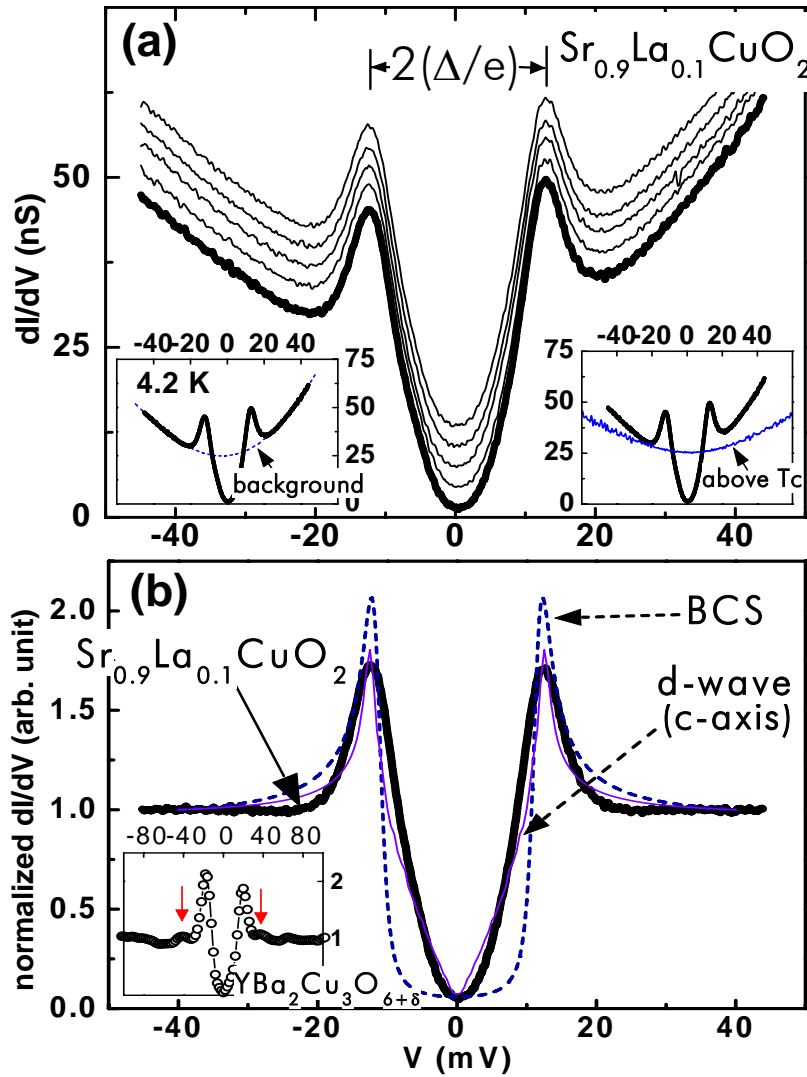


Figure 5.3: (a) Representative (dI/dV) vs. (V) quasiparticle spectra of SLCO taken at 4.2 K. The curves correspond to spectra taken at ~ 1.5 nm equally spaced locations within one grain, and have been displaced vertically for clarity except the lowest curve. Left inset: a typical spectrum taken at 4.2 K (solid line) compared with the corresponding high-voltage background (dashed line). Right inset: comparison of a typical spectrum taken at 4.2 K with one taken slightly above T_c . (b) A spectrum normalized relative to the high-voltage background given in the left inset of (a), together with a BCS theoretical curve for the normalized DOS at $(T/T_c) = 0.1$ and a corresponding c -axis tunneling spectrum for a pure $d_{x^2-y^2}$ -wave superconductor (thin solid line). Left inset: a normalized c -axis tunneling spectrum of an optimally doped $\text{YBa}_2\text{Cu}_3\text{O}_{6+\delta}$ ($T_c = 92.5 \pm 0.5$ K). The red arrows point to the satellite features referred to in the text.

Fig. 5.3(b), which is in contrast to the finding of $|d^2I/dV^2|_{V \rightarrow 0^\pm} = 0$ in SLCO.

In short, the tunneling spectra of SLCO reveal a momentum-independent gap, absence of the Andreev bound state associated with the line nodes and the sign change of unconventional pairing

symmetry, and a smooth change of slope near zero bias as opposed to a discontinuous V-shape in the *c*-axis tunneling spectra of a *d*-wave superconductor [Fig. 5.3(b) inset]. These findings are suggestive of isotropic *s*-wave pairing symmetry. Nevertheless, the excess low-energy excitations signify the breakdown of mean-field BCS theory for the low-energy physics in SLCO, and the unusually large ratio of $(2\Delta/k_B T_c) \approx 7.0$, as compared with the BCS ratio of 3.5, is indicative of strong coupling effects. Interestingly, recent Knight shift data from NMR studies of similar samples have revealed a much smaller normal-state density of states at the Fermi level ($\sim 25\%$ that of YBCO) as compared with those of other cuprates [79], which implies poor screening of the Coulomb repulsion and stronger electronic correlations in SLCO, further corroborating the inapplicability of weak-coupling BCS theory in this system.

5.3.2 Spectral characteristics of pure $\text{Sr}_{1-x}\text{La}_x\text{CuO}_2$

Comparing the tunneling spectra of SLCO with those of the hole-doped YBCO, we find that the commonly observed “satellite features” in the quasiparticle spectra of p-type cuprate superconductors [§4.4.3], as indicated by the arrows in the left inset of Fig. 5.3(b), are invisible in SLCO. Furthermore, when the temperature rises above T_c , the tunneling gap Δ completely vanishes, with no apparent energy scale associated with any depression of the density of states (DOS) at $T > T_c$, as shown in the right inset of Fig. 5.3(a). The normal-state tunneling spectrum remains featureless from just above T_c to ~ 110 K, though the slope of the normal-state high-energy background decreases slightly with increasing temperature due to decreasing conductance with temperature. The absence of any spectroscopic pseudogap in the n-type infinite-layer SLCO is independently verified by the NMR studies on similar samples, showing temperature-independent Knight shift above T_c [79].

The evolution of the tunneling gap with temperature is plotted in Fig. 5.4 for SLCO, PCCO [16], and Bi-2212 [69]. A comparison with the BCS prediction reveals a rapid decrease of spectral gap in SLCO, which is indicative of the deviation from the mean-field description and is consistent with the large $(2\Delta/k_B T_c) \approx 7.0$ ratio found in this system. We note that the temperature dependence of the tunneling gap in NCCO [41] (not shown) and PCCO [16] is well captured by the BCS theory

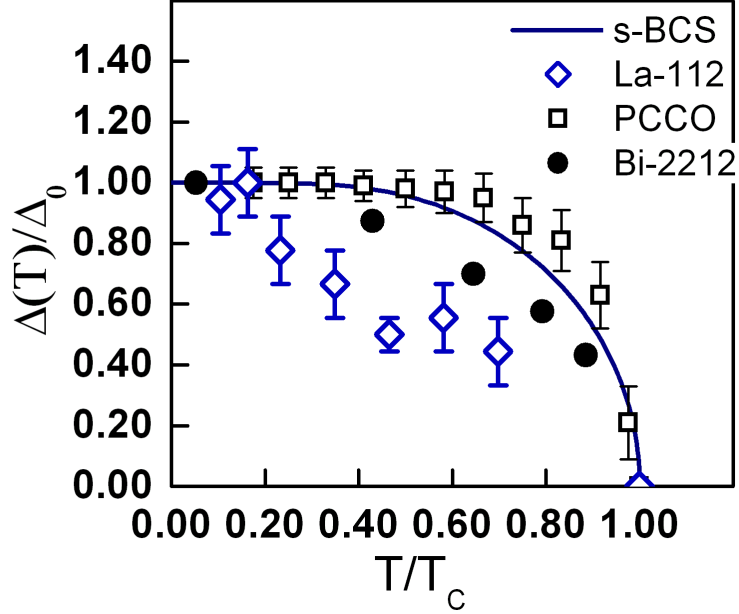


Figure 5.4: Comparison of the temperature dependence of the normalized spectral gap for PCCO [16], Bi-2212 [69] and SLCO. $\Delta(T)$ is the spectral gap measured at temperature T , and Δ_0 represents the zero temperature tunneling gap.

with an s -wave pairing. A detail analysis of the NCCO tunneling spectra using the BTK formalism yields a nearly perfect fit with $(2\Delta/k_B T_c) \approx 3.3$ [41] comparable to the BCS value.

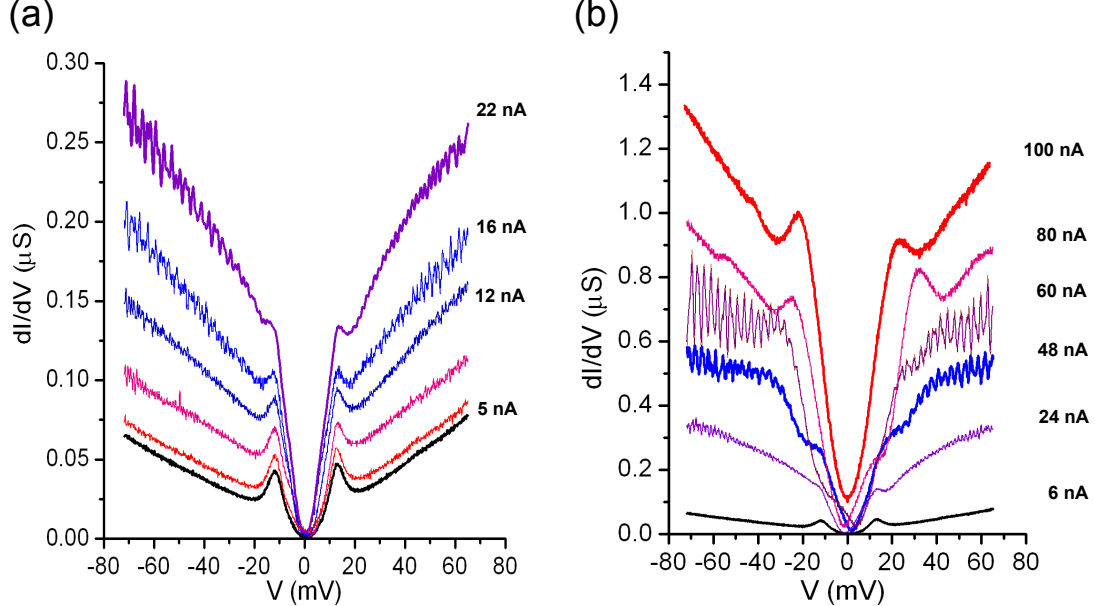


Figure 5.5: The evolution of tunneling spectra with increasing injection current.

In Figure 5.5, an interesting phenomenon associated with the current dependence of the tunneling

spectra is depicted. Each spectrum is labeled by its corresponding set-point tunneling current at the fixed-bias voltage, 100 mV, and taken with the feedback loop disabled so that the tunneling matrix is kept at a constant value within each acquisition. The spectra acquired at lower injection current values show that the height of the spectral peaks slowly reduced with increasing current, whereas the energy gap value remains the same. The sharp spectral peaks indicative of quasiparticle coherence persist up to $I \leq \sim 22$ nA and are fully suppressed as the injection current passes ~ 24 nA. A broad high-energy “pseudogap”-like feature emerges and gradually dominates over the remnant low-energy feature. After the low-energy gap completely disappears, the “pseudogap” sharpens up whereas the gap value slightly decreases to ~ 23 meV at $I = 100$ nA.

We note that the spectral response to large injection current is fully reversible, with the high-energy “pseudogap” vanishing and the low-energy gap recovering with decreasing tunneling current, as exemplified by the bottom curve in Fig. 5.5(b). Therefore, it is unlikely that the injection current induces structural or chemical changes that give rise to the spectral changes. Further, we can rule out local heating as the cause of the anomalous current-induced “pseudogap” because, as shown in Fig. 5.4, the low-energy superconducting gap decreases rapidly with increasing temperatures, as opposed to the large “pseudogap” revealed by high current injection.

The spectral characteristics of the tunneling spectra under large current injection are reminiscent of those observed in the pseudogap phase of the underdoped p-type cuprates. Thus, we speculate that, similar to the high-energy satellite features in the superconducting spectra of p-type cuprates, the current-induced “pseudogap” is indicative of the underlying coexisting state, where the superconductivity is gradually suppressed while the strength of the competing order promoted with increasing current [§5.4.3].

5.3.3 Tunneling spectra of Zn- and Ni-doped $\text{Sr}_{1-x}\text{La}_x\text{CuO}_2$

The tunneling spectra taken on the 1% Zn-doped SLCO reveal long-range spatially homogeneous spectral characteristics and a similar gap value ($\Delta = 13.0 \pm 2.5$ meV) for randomly sampled areas in different grains, as exemplified in Fig. 5.6. Given that the average separation among Zn

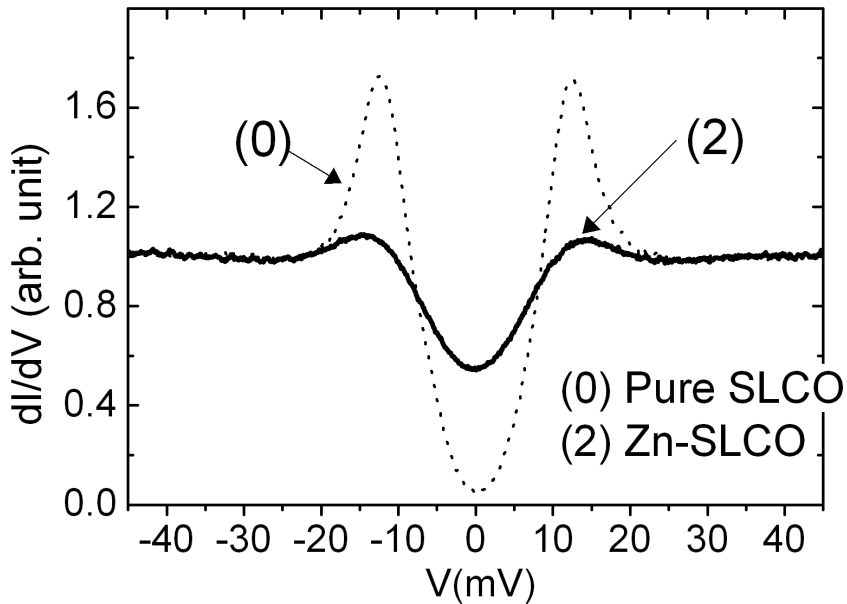


Figure 5.6: Comparison of quasiparticle tunneling spectra of 1% Zn-SLCO and pure SLCO, showing significant residual conductance in the subgap region and broadened spectral peaks indicating reduced quasiparticle lifetime due to disorder for the Zn-SLCO.

impurities is $\sim (1.8 \times 1.8 \times 1.6)$ nm³, our exhaustive spectral studies should have covered a significant number of Zn impurities. However, no significant local variations are found in the spectra of the 1% Zn-SLCO, which differs fundamentally from our observation of atomic-scale spectral variations in a YBa₂(Cu_{0.9934}Zn_{0.0026}Mg_{0.004})₃O_{6.9} single crystal near non-magnetic Zn or Mg impurities[Fig. 4.3.2]. Nevertheless, the conductance peaks in 1% Zn-SLCO are significantly broadened relative to pure SLCO, with a substantial increase in the low-energy DOS for $|E| < \Delta$, as illustrated in Fig. 5.6. These features suggest that Zn impurities result in reduced quasiparticle lifetime while retaining T_c , similar to the response of conventional *s*-wave superconductors to non-magnetic impurities [211, 244].

In contrast, two types of spectra are observed in 1% Ni-SLCO, As illustrated in the main panel of Fig. 5.7(a), the majority spectra ($> 90\%$) exhibit suppressed coherence peaks, large zero bias residual conductance, strong electron-hole spectral asymmetry, and gradual spatial evolution over a long range. In contrast, the minority spectra ($< 10\%$) exhibit sharp spectral peaks, small zero-bias conductance, and varying electron-hole spectral asymmetry over a short range (< 1 nm), as

exemplified in the inset of Fig. 5.7(a) for two representative minority spectra. The significant spectral asymmetry in the majority spectra implies different phase shifts in the electron-like and hole-like quasiparticle states as the result of broken time-reversal symmetry [244, 212], which may be responsible for the global suppression of the superconducting phase coherence and thus a reduction in T_c .

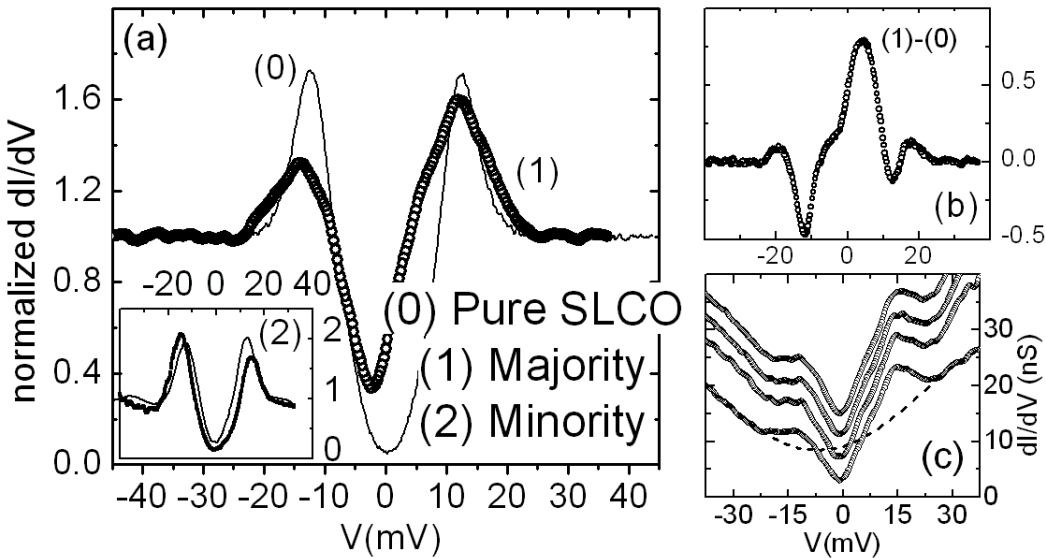


Figure 5.7: (a) Main panel: Comparison of a normalized majority spectrum of 1% Ni-SLCO and that of pure SLCO at 4.2 K. The normalization was made relative to the background conductance shown by the dashed line in part (c). Inset: Two minority spectra with different electron-hole asymmetry. (b) Spectral differences of the majority and minority spectra relative to that of the pure SLCO. (c) A series of spectra taken on the same grain of 1% Ni-SLCO at ~ 3 nm apart. The conductance of all curves except the lowest one has been displaced up for clarity.

Assuming homogeneous Ni impurity distributions, the average Ni-Ni separation would be $d_{Ni} \sim 1.8$ nm in the ab -plane and ~ 1.6 nm along the c -axis in each grain. The impurity wavefunction with poor screening from the carriers would have extended over a coherence volume $(\xi_{ab}^2 \xi_c)$ [244, 212]. Given the coherence lengths $\xi_{ab} \sim 4.8$ nm and $\xi_c \sim 0.53$ nm [241], $\sim 30\%$ volume probability in each grain could be considered as under significantly weaker impurity influence. In the limit of completely random grain orientation in 1% Ni-SLCO, the STM studies of the grain surfaces would have 10–20% probability for finding surface regions with weak impurity influence and spatial extension over a short range (~ 0.5 nm) along the c -axis. This simple estimate is in reasonable agreement with our observation of $\sim 10\%$ minority spectra with short-range (< 1 nm) spatial homogeneity. However,

due to the lack of direct information for the Ni distribution on the sample surface, the true origin for two types of spectra in 1% Ni-SLCO remains uncertain.

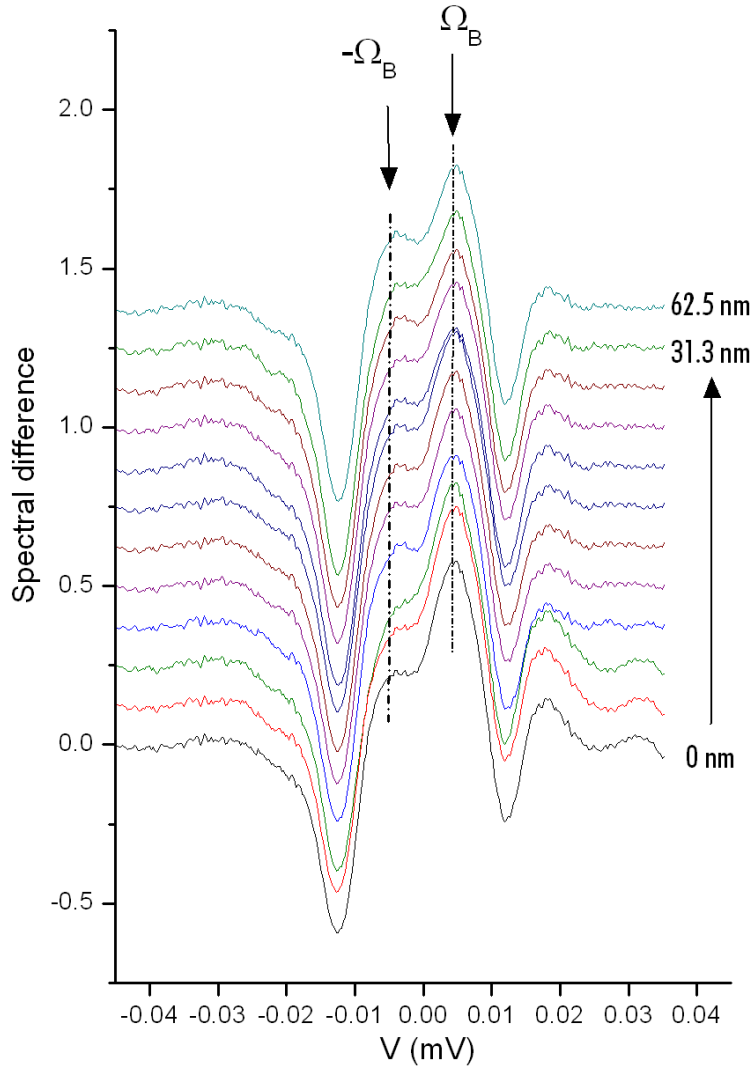


Figure 5.8: The spatial evolution of the spectral difference in the vicinity of the Ni impurity, showing long-range impurity bound states at energy $\pm\Omega_B$ similar to the Shiba states of the magnetic impurity bands in a conventional superconductor.

Considering the spectral difference between the majority spectrum of 1% Ni-SLCO and that of pure SLCO [Fig. 5.7(b)], we find that the spectral characteristics resemble the findings in Ref. [244] and are representative of magnetic impurity-induced state. Since the average Ni-Ni separation (~ 1.8 nm) is smaller than the in-plane coherence length (~ 4.8 nm), the Ni impurities can be considered as forming a magnetic impurity band. According Shiba's theory [245], the bound state energy

associated with the Ni-impurity band in an *s*-wave superconductor locates at $\pm\Omega_B$ as depicted in Fig. 5.8, where a set of spectra illustrating the slow variations in spectral difference around the Ni impurity is given. The weak screening owing to the low carrier density and the strong overlap of impurity wavefunctions explain the slow-varying spectra shown in Fig 5.7(c) and Fig. 5.8.

5.4 Discussion

5.4.1 Pairing symmetry

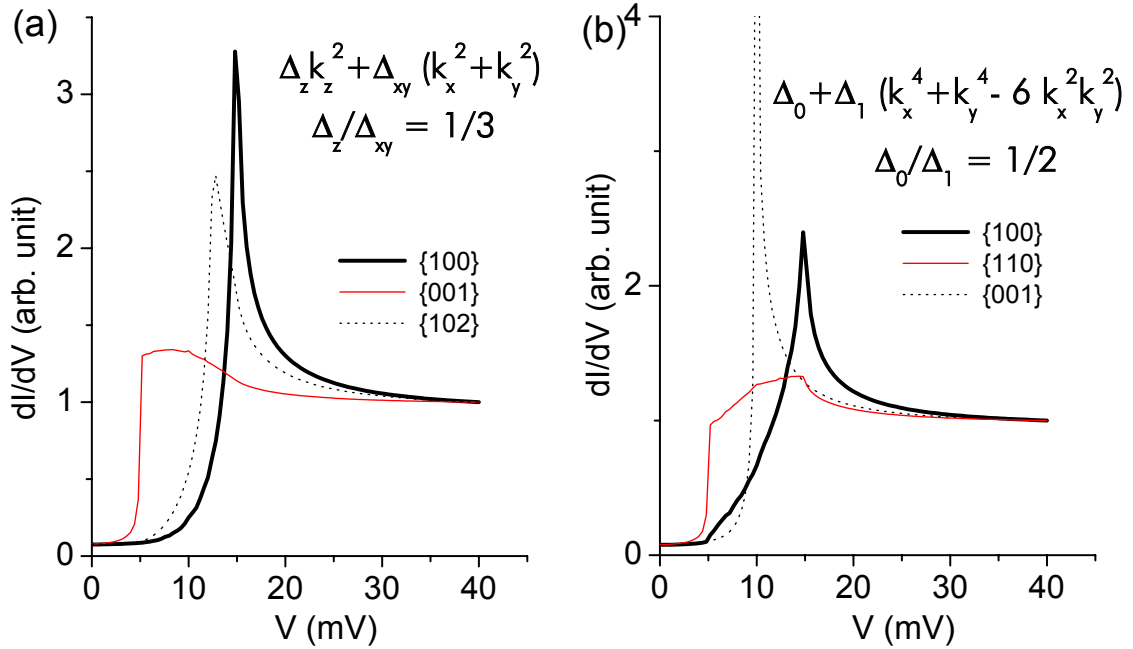


Figure 5.9: Simulated tunneling spectra along different crystalline axes for (a) an anisotropic *s*-wave pairing with uniaxial symmetry $\Delta_{\vec{k}} = \Delta_{xy}(k_x^2 + k_y^2) + \Delta_z k_z^2$, and (b) an anisotropic *s*-wave pairing with four-fold in-plane modulation $\Delta_{\vec{k}} = \Delta_0 + \Delta_1(k_x^4 + k_y^4 - 6k_x^2k_y^2)$.

The lack of spectral variations with crystalline orientations, the absence of ZBCP, and the distinctly different bulk and local spectral response to non-magnetic and magnetic impurity substitution suggest that SLCO is a fully gapped *s*-wave superconductor. To explore the possibility of any anisotropy in the pairing symmetry, we use the generalized BTK formalism to derive the tunneling spectra for the anisotropic order parameters permitted by the crystalline symmetry. In the case of the infinite-layer SLCO, the point group of the lattice is D_{4h} . We consider the lowest energy con-

figurations of the order parameter with orbital angular momenta $l = 0, 2, 4$. For $l = 0$, the pairing symmetry is isotropic s . For $l = 2$ and $l = 4$, the relevant anisotropic pairing potentials are the uniaxial symmetric anisotropic s -pairing, $\Delta_{\vec{k}} = \Delta_{xy}(k_x^2 + k_y^2) + \Delta_z k_z^2$, and the in-plane four-fold symmetric anisotropic s -pairing, $\Delta_{\vec{k}} = \Delta_0 + \Delta_1(k_x^4 + k_y^4 - 6k_x^2 k_y^2)$. The calculated spectra of anisotropic s -wave superconductors with quasiparticles tunneling along different crystalline axes are illustrated in Fig. 5.9. For tunneling spectra taken on randomly oriented crystallites of an anisotropic s -wave superconductor, the variations in the tunneling gap values can be resolved if the anisotropy in the pairing potential is appreciable. By comparing the numerical result with the STS data and taking into account the experimental resolution, we estimate that the upper bound for the anisotropy of the pairing potential is less than 8%, so that the pairing potential of SLCO is essentially isotropic.

5.4.2 Impurity substitution and pairing symmetry

An important consequence of either $d_{x^2-y^2}$ or $(d_{x^2-y^2} + s)$ -wave pairing is that the resulting nodal quasiparticles can interact strongly with the quantum impurities in the CuO₂ planes [214, 213, 246], such that a small concentration of impurities can lead to strong suppression of superconductivity. The scattering of quasiparticles by the non-magnetic impurities dramatically modifies the local spectral response, yielding a low-energy resonance feature while suppressing the superconducting coherence peaks [8, 220] as observed in the tunneling spectra of (Zn,Mg)-YBCO [§4.3.2]. Furthermore, the induced magnetic moments that are confined to the vicinity of the non-magnetic impurities [215, 247, 216, 217, 218] can couple with the Bogoliubov quasiparticles and give rise to Kondo physics [222, 219]. Such strong response to non-magnetic impurities is in sharp contrast to that of conventional s -wave superconductivity [211, 244].

In comparison, the T_c of the infinite-layer SLCO has little dependence on the non-magnetic Zn substitutions up to 3%, but it is drastically suppressed with only 1% of magnetic Ni substitutions [243]. Figure 5.10 illustrates the suppression of T_c upon impurity substitution observed by the bulk susceptibility measurements. While 1% of Zn substitutions hardly changes the transition temperature, 1% of Ni substitutions decreases T_c from 43 K to ≤ 32 K. With 2% of Ni substitutions,

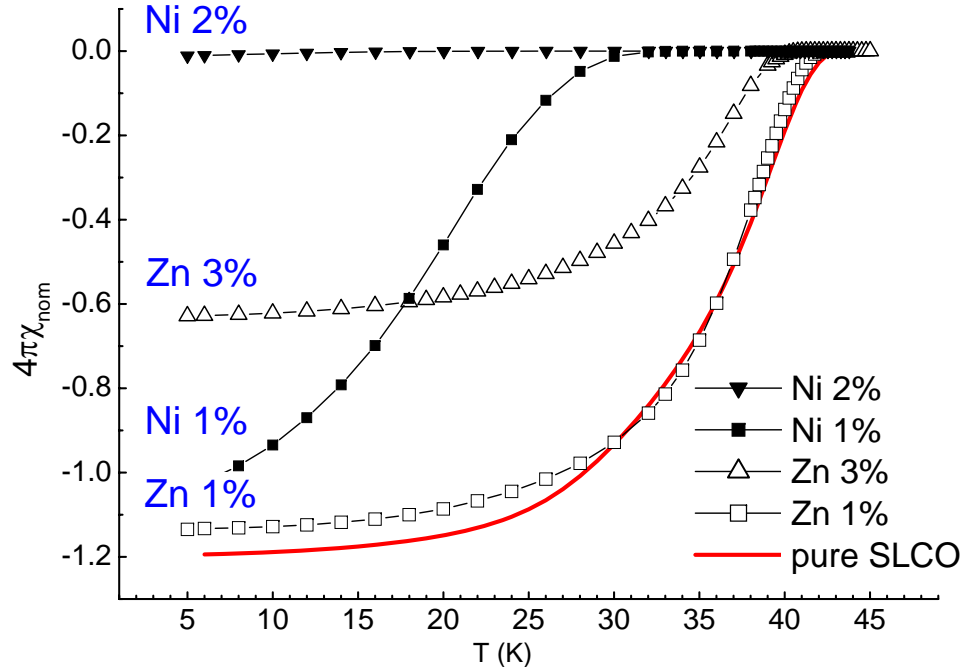


Figure 5.10: (Adapted from Fig. 1(b) of Ref. [240].) Magnetic susceptibility data of pure and impurity doped SLCO. The superconducting transition temperature has little variation upon Zn doping up to 3%, while superconductivity is completely suppressed with 2% of Ni doping.

superconductivity is completely suppressed. Thus, the global response of SLCO to impurities is different from that in the p-type cuprates and is similar to that in an *s*-wave superconductor [211].

Microscopically, the effect of non-magnetic Zn impurities on the tunneling spectra [Fig. 5.6] can be accounted for with the increase of the quasiparticle lifetime broadening which smears out the superconducting peaks without changing the nature of the eigenstates, a behavior completely different from that in a *d*-wave superconductor where resonance bound states associated with impurity scattering are generally observed.

In comparison, the majority spectra [Fig. 5.7] found in the 1% Ni-SLCO show strong electron-hole asymmetry with spectral contributions from the magnetic impurities reminiscent of those in an *s*-wave superconductor [244]. However, the slow spatial variations in Ni-SLCO due to weak screening effects and strong overlapping of Ni wavefunctions are markedly different from the rapidly diminishing impurity bound states observed near the isolated Mn or Gd atom on the surface of the conventional superconductor Nb [244] and also from the strong atomic-scale spectral variations near Ni impurities in the p-type cuprate $\text{Bi}_2\text{Sr}_2\text{Ca}(\text{Cu}_{1-x}\text{Ni}_x)_2\text{O}_{8+x}$ [248]. The contrast in the spatial extension of the

Ni-impurity effects may be attributed to the variation in the impurity coupling strength and range, and also to the degree of impurity screening by carriers. Overall, both bulk and microscopic studies of Zn and Ni substituted SLCO corroborate our findings on pure SLCO that the infinite-layer n-type cuprate superconductors exhibit *s*-wave pairing symmetry.

5.4.3 Satellite features, pseudogap phenomena, and competing orders

In the previous chapter [§4.4.3], we have mentioned that the “dip-hump” features in the tunneling spectra of hole-doped cuprates are generally attributed to quasiparticle interaction with background bosonic excitations. Within the quasiparticle damping scenario, there are two possible bosonic modes in the cuprate superconductors that quasiparticles can couple to. One is the magnetic resonance mode, and the other is the phonon mode. A recent study of the angular-resolved photoemission spectroscopy (ARPES) on Bi-2212, Pb-doped Bi-2212, Pb-doped $Bi_2Sr_2CuO_6$, and LSCO reveals an abrupt change of the electron group velocity in the $50 \sim 80$ meV energy range [206]. The similar energy scales exhibited in these four different systems prompt some physicists to speculate that the longitudinal optical oxygen phonon modes in the CuO_2 planes are responsible for the change of slope in the quasiparticle dispersion [206] and the satellite features in tunneling spectra. However, as shown in §4.4.3, it is unlikely that the satellite features are associated with the phonon modes, since the strong suppression of the “dip” energy observed in (Zn,Mg)-YBCO [8] and the significant reduction of the electron self-energy in Bi-2212 [210] upon impurity substitution with similar atomic masses cannot be reconciled with the phonon mediation scenario. On the other hand, the energy of the resonance mode extracted from the Bi-2212 tunneling spectra are consistent with the resonant energy measured by magnetic neutron scattering measurements [149], thereby providing convincing evidence for the magnetic damping scenario in Bi-2212.

Besides the high-energy “dip-hump” features, additional *lower-energy* satellite features are revealed in the tunneling spectra of underdoped Bi-2212 [183, 220, 68] at an energy scale comparable to the pseudogap observed above T_c . These low-energy features sometimes dominate over the superconducting sharp peaks and form the pseudogap-like spectra [68] [Fig. 6.4(d)]. The coexistence

of these pseudogap-like features with the pure superconducting spectra suggests that they are the manifestation of the competing orders in the underdoped Bi-2212. The tunneling spectra on YBCO exhibit similar lower-energy spectral features at energies slightly above the superconducting gap. If we attribute these lower-energy satellite features to the magnetic resonance mode in YBCO, the resonance frequency from the tunneling experiment would be appreciably smaller than that obtained from the neutron scattering results [83] (*cf.* inset of Fig. 5.10(a)). For this reason, we propose to interpret the satellite features in YBCO as a manifestation of coexisting competing orders.

For a competing order strength comparable to or larger than the superconducting pairing potential, the spectral gap of the coexisting state would take place at an energy slightly higher than the superconducting gap, which corresponds to the satellite features in the superconducting state of YBCO and Bi-2212. Furthermore, as the stiffness of the competing order increases while that of superconductivity decreases with underdoping, the spectral gap associated with the competing order would sustain beyond the superconducting transition temperature, giving rise to the pseudogap observed in the normal of the underdoped p-type cuprates.

On the other hand, if the strength of the competing state is small compared to the superconducting pairing potential, the spectral gap associated with the coexisting competing order would be buried in the pronounced superconducting peaks and rendered invisible, which accounts for the absence of satellite features in the electron-doped infinite-layer SLCO and one-layer compounds. Furthermore, as the temperature increases, the coexisting order would vanish before superconductivity disappears, which explains why no discernible pseudogap is observed above T_c .

The absence of the zero-field pseudogap in SLCO is consistent with similar findings in the one-layer electron-doped NCCO and PCCO [16, 18]. It is shown that, in the one-layer systems, the application of a magnetic field that destroys superconductivity reveals a suppression of DOS near the Fermi level in the field-driven normal state [18], which signifies the existence of a competing order. By taking into account the spectral smearing, it is found that the strength of the field-induced pseudogap is smaller than the zero-temperature superconducting gap, which accounts for the observation that the onset temperature of the “pseudogap” opening in the field-driven normal

state is smaller than the superconducting transition temperature in zero field.

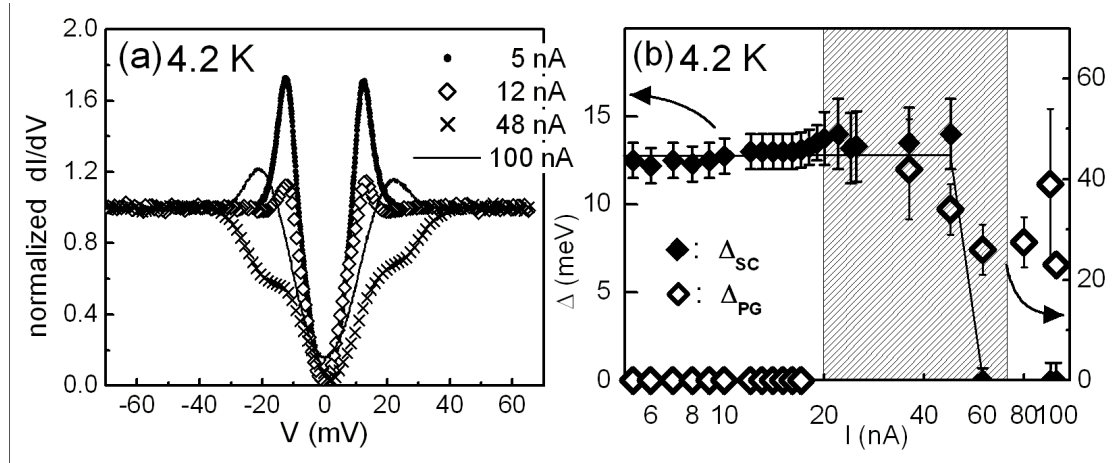


Figure 5.11: (a) Representative normalized quasiparticle tunneling spectra of SLCO with increasing tunneling current I . (b) Evolution of the low-energy superconducting gap Δ_{SC} and the high-energy current-induced pseudogap Δ_{PG} of SLCO with I . The shaded region is where quantum fluctuations are strong and the two orders coexist.

The current-induced “pseudogap” in the tunneling spectra of SLCO can be understood within the same picture. Figure 5.11(a) shows a set of representative normalized spectra taken from Fig. 5.5. In the low-current limit, superconductivity dominates over the competing order so that there are no discernible satellite features, the appearance of which would have been indicative of a competing order energy scale exceeding that of superconductivity. As the current increases, the Bogoliubov quasiparticles gradually lose coherence (as manifested by the diminished coherence peaks) probably due to increasing local fields induced by the large tunneling currents, and the competing order gains strength. When the magnitude of the competing order becomes significant, the high-energy satellite features emerge at the energy $\Delta_{PG} \sim \sqrt{\Delta_{SC}^2 + V_{CO}^2}$ and coexist with the low-energy remnant gap Δ_{SC} [Fig. 5.5(b)]. Eventually, the injection current renders the superconducting order parameter sufficiently small, and the high-energy “pseudogap” dominates over the negligible remnant superconducting gap. A rigorous theoretical foundation for the notion described here will be provided in Chapter 6.

Thus, by tuning the relative strength of the competing order to superconductivity, the presence of the zero-field pseudogap in p-type cuprates, and the field- and current-induced pseudogap in n-type

cuprates can be explained in a coherent way.

5.4.4 Low-energy excitations, quantum fluctuations, and quantum criticality

We have noted in §5.3.1 that despite the observation of the momentum-independent quasiparticle tunneling spectra supportive of *s*-wave pairing symmetry, the spectral characteristics of SLCO deviate significantly from the conventional *s*-wave BCS prediction [Fig. 5.3(b)]. The excess low-energy excitations manifested in the low-temperature quasiparticle spectra are indicative of substantial quantum fluctuations resulting from the presence of a competing order close in energy to superconductivity.

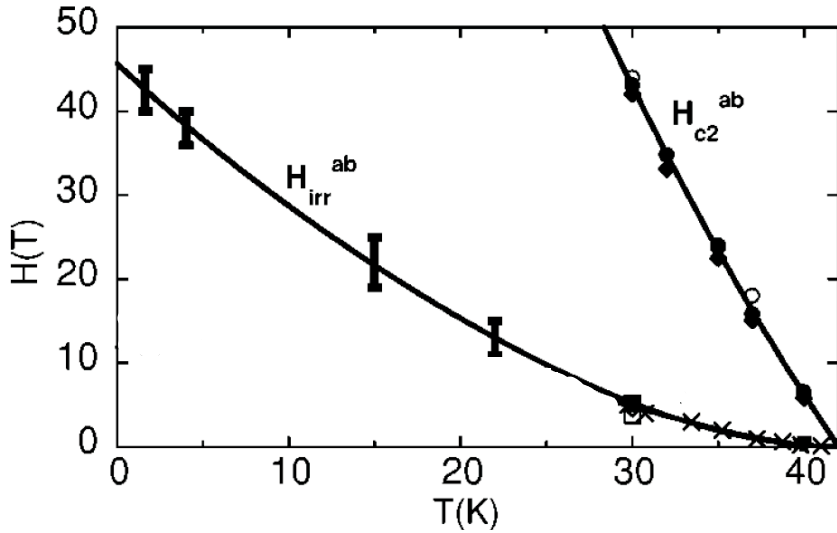


Figure 5.12: (Adapted from Fig. 3 of Ref. [107].) The vortex phase diagram of electron-doped infinite-layer SLCO for $H \parallel ab$ showing significant reduction of the in-plane irreversibility field (H_{irr}^{ab}) relative to the in-plane higher critical field (H_{c2}^{ab}).

High-field vortex dynamics measurements on SLCO provide additional evidence for strong quantum fluctuations [107, 201, 202]. These experiments are conducted with the magnetic field parallel to the CuO₂ planes, so that the fluctuations due to disorder pinning are minimized by the strong confinement of vortices along the periodic CuO₂ planes. In the absence of quantum fluctuations, the in-plane irreversibility field (H_{irr}^{ab}) is expected to approach the in-plane upper critical field (H_{c2}^{ab}) as $T \rightarrow 0$, where thermal depinning mechanism is quenched. Therefore, our experimental finding of a

large reduction of $H_{irr}^{ab}(T \rightarrow 0)$ relative to $H_{c2}^{ab}(T \rightarrow 0)$ in SLCO [Fig. 5.12] must be attributed to field-induced quantum fluctuations that suppress the phase stiffness of superconductivity. Specifically, large magnetic fields induce strong transverse phase fluctuations that suppress superconductivity phase coherence and enhance the competing order even at $T = 0$. Thus, the strong quantum phase fluctuations prevent the superconductor from supporting a well-defined supercurrent in high fields, leading to $H_{irr}^{ab}(T = 0) < H_{c2}^{ab}(T = 0)$. On the other hand, although transverse phase fluctuations are negligible in the zero-field limit at $T = 0$, the coupling of quasiparticles with longitudinal quantum phase fluctuations can account for the excess low-energy spectral weight manifested in the tunneling spectrum [§6].

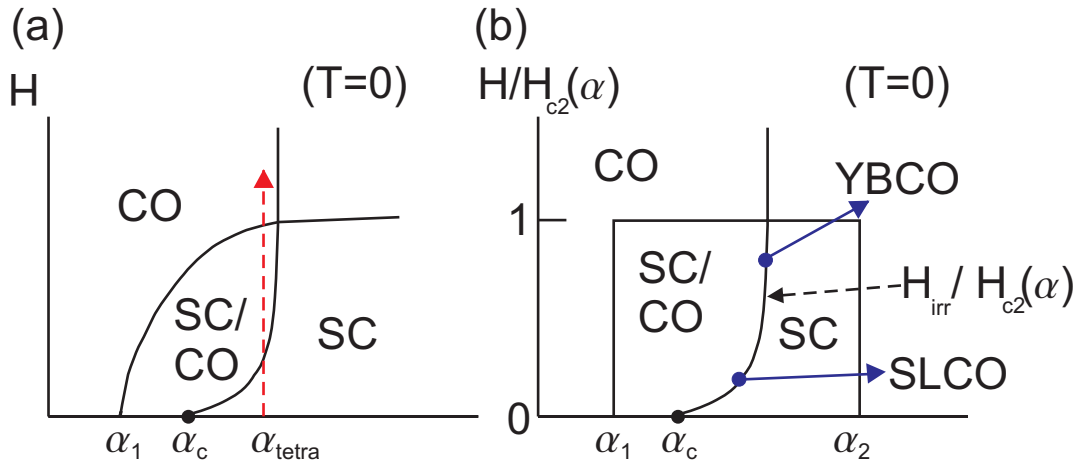


Figure 5.13: (a) Schematic H vs. α phase diagram at $T = 0$ showing the field-induced quantum phase transition from a superconducting phase with a dynamic competing order to a coexisting phase with superconductivity and a static competing order. α : relevant material specific parameter, such as doping level, disorder, electronic anisotropy and on-site Coulomb repulsion; α_i ($i = 1, 2, c$): quantum critical point; α_{tetra} : tetra-critical point; SC/CO: superconducting phase with coexisting static competing order; SC: superconducting phase (with coexisting dynamic competing order when $\alpha < \alpha_{tetra}$). (b) Reduced field $H/H_{c2}(\alpha)$ vs. α phase diagram at $T = 0$ showing the relative proximity to the quantum critical point α_c for SLCO and YBCO.

We can further use the degree of quantum fluctuations extracted from the high-field thermodynamic measurements to characterize the proximity to quantum criticality for individual cuprate compounds. Theoretical investigations [249, 250, 251] indicate that in the presence of a competing order energetically comparable to superconductivity, the application of a magnetic field would induce a phase transition from the coexisting phase with the dynamic competing order to one with

static long-range order [Fig.5.13(a)]. In the vicinity of the critical line where the fluctuations of the competing order are significant, the superconducting order parameter that couples with the competing order [252] would also fluctuate substantially. Therefore, by examining the suppression of H_{irr}^{ab} with respect to H_{c2}^{ab} in the zero-temperature limit for various cuprate compounds, we can map out their relative proximity to quantum criticality. Comparing the high-field vortex phase diagram of SLCO [107] to that of YBCO [253, 254], we find that SLCO is much closer to the quantum critical point than YBCO [Fig.5.13(b)], and therefore the low-energy excitation spectra of SLCO deviate considerably from the mean-field BCS theory, while that in YBCO is well described by the mean-field generalized BTK theory.

5.5 Summary

In conclusion, we present the quasiparticle tunneling spectra of the electron-doped infinite-layer cuprate SLCO that demonstrate a momentum-independent pairing potential $\Delta = 13.0 \pm 2.5$ meV with an anisotropy $< 8\%$. The global and local spectral response to impurity substitution is consistent with *s*-wave pairing symmetry. The absence of satellite features, the absence of zero-field pseudogap, and the emergence of the current-induced pseudogap suggest that, in SLCO, superconductivity coexists with a small fluctuating competing order revealed only upon the suppression of superconductivity by external perturbations. The proximity of the ground state to the quantum critical point gives rise to significant quantum fluctuations, as manifested in the high-field vortex dynamics measurement. The coupling of quasiparticles to the quantum phase fluctuations of the superconducting order parameter results in excess low-energy excitations observed in the tunneling spectra. We shall present further supporting evidence from the theoretical modeling of quasiparticle tunneling spectra in the presence of strong quantum fluctuations and competing orders in the following chapter.

Chapter 6

Competing Orders, Quantum Phase Fluctuations, and Quasiparticle Tunneling Spectra

6.1 Introduction

In the previous two chapters, we have presented the scanning tunneling spectroscopic studies of hole-doped YBCO [§4] and electron-doped SLCO [§5] that reveal several contrasting spectroscopic features. Specifically, the quasiparticle tunneling spectra of YBCO exhibit spectral characteristics well captured by the mean-field d -wave [or $(d+s)$ -wave] generalized BTK formalism. In SLCO, the quasiparticle tunneling spectra are consistent with isotropic s -wave pairing symmetry while excess low-energy spectral weight that deviates significantly from the mean-field BCS theory is present. In accordance with the low-energy spectral anomaly, high-field low-temperature vortex dynamics measurements on SLCO reveal sizable reduction of H_{irr}^{ab} with respect to H_{c2}^{ab} at $T \rightarrow 0$, implying strong field-induced quantum phase fluctuations. In comparison, relatively weaker quantum phase fluctuations associated with YBCO is consistent with the applicability of mean-field theory to its low-energy spectral characteristics. The satellite features and the “pseudogap”-like spectral dip around the Fermi level manifested in the tunneling spectra of p-type cuprates are suggestive of the presence of a pinned competing order with an energy scale comparable to or larger than that of superconductivity. On the other hand, the complete absence of the satellite features and zero-field pseudogap, and the appearance of current- or field-induced “pseudogap” in n-type SLCO and other

one-layer compounds signify a small coexisting competing order revealed only upon the suppression of superconductivity. Based on these findings and the notion that the varying degrees of quantum phase fluctuations are indicative of the varying degrees of proximity to quantum criticality, we conjecture that the non-universal spectral features among n- and p-type cuprates can be accounted for by tuning the relative energy scales of competing orders to superconductivity.

In this chapter, the aforementioned conjecture is put to test by means of a calculation of the low-energy single-particle spectra that incorporates quantum phase fluctuations into superconductivity with coexisting density waves as the competing order. To date, most theoretical investigations on the tunneling spectra of cuprate superconductors generally address competing orders and superconducting phase fluctuations separately. One approach takes the BCS-like Hamiltonian as the unperturbed mean-field state and treats the disorder-pinned competing order as the weak perturbative scattering potential for the Bogoliubov quasiparticles [249, 255, 256, 257, 258, 259, 260, 101, 261] [§6.3]. Another approach begins with the BCS-like Hamiltonian and includes superconducting phase fluctuations in the proper self-energy correction without any consideration of competing orders [262, 263, 264]. By allowing both the competing orders and the superconducting phase fluctuations in the superconducting state [§6.2], we find that the low-energy excitations thus derived differ from conventional Bogoliubov quasiparticles, and various seemingly puzzling and non-universal phenomena in the hole- and electron-type cuprates, such as the excess subgap low-energy excitations [§5.3.1] below T_c and pseudogap phenomena [§5.4.3], can be coherently explained. We further consider the low-energy limit in d -wave superconductors where the Bogoliubov quasiparticles are the dominating low-energy excitations and disorder-pinned competing orders maybe treated perturbatively, and find that calculated quasiparticle interference spectra reveal modulated density of states due to the presence of competing order, consistent with experimental observations. Therefore, we conclude that the presence of competing orders is indisputable at least in the quasi-2D Bi-2212.

6.2 Competing orders and quantum phase fluctuations on low-energy excitations

We first consider a simple case of coexisting *s*-wave superconductivity (SC) and charge density waves (CDW) with finite quantum phase fluctuations at $T = 0$. That charge density wave is the relevant competing order to *s*-wave superconductivity is because the symmetry of *s*-wave superconductivity is compatible with that of CDW. Under certain conditions, such as in the half-filled Hubbard model with negative U , the two orders can further rotate into each other without modifying the low-energy spectrum and hence be unified under a higher SO(4) symmetry [265]. Empirically, the coexistence has been known in NbSe₂ [266, 267], although the energy scale of CDW in NbSe₂ is much larger than that of superconductivity and therefore does not directly affect the low-energy excitations of the superconducting order. The simple case of *s*-wave superconductivity coexisting with CDW can be extended straightforwardly to $d_{x^2-y^2}$ -wave superconductivity with a competing order being either CDW [252, 73], spin-density waves (SDW) [268, 249], or *d*-density waves (DDW) [75]. Nevertheless, compatibility in the symmetry of the superconductivity order parameter with that of the relevant competing order is important for determining which competing states is pertinent under a given superconducting pairing symmetry.

In subsequent discussions we shall associate realistic band structures of n-type cuprate superconductors with the scenario of coexisting *s*-wave SC and CDW, and those of p-type cuprates with the scenario of coexisting $d_{x^2-y^2}$ -wave SC with disorder-pinned SDW. We further assume that the exact degree of quantum phase fluctuations depends on microscopic coupling mechanism between superconductivity and competing orders, which is not fully understood and is therefore left as a variable to be determined empirically.

6.2.1 Formalism

In the case of coexisting *s*-wave SC and CDW, the mean-field Hamiltonian is given by:

$$\begin{aligned}
\mathcal{H}_{MF} &= \mathcal{H}_{SC} + \mathcal{H}_{CDW} \\
&= \sum_{\mathbf{k},\sigma} \xi_{\mathbf{k}} c_{\mathbf{k},\sigma}^\dagger c_{\mathbf{k},\sigma} - \sum_{\mathbf{k}} \Delta \left(c_{\mathbf{k},\uparrow}^\dagger c_{-\mathbf{k},\downarrow}^\dagger + c_{-\mathbf{k},\downarrow} c_{\mathbf{k},\uparrow} \right) \\
&\quad + \sum_{\mathbf{k},\sigma} V \left(c_{\mathbf{k},\sigma}^\dagger c_{\mathbf{k}+\mathbf{Q},\sigma} + c_{\mathbf{k}+\mathbf{Q},\sigma}^\dagger c_{\mathbf{k},\sigma} \right) \\
&= \sum_{\mathbf{k}} \left(c_{\mathbf{k},\uparrow}^\dagger c_{-\mathbf{k},\downarrow}^\dagger c_{\mathbf{k}+\mathbf{Q},\uparrow}^\dagger c_{-(\mathbf{k}+\mathbf{Q}),\downarrow} \right) \begin{pmatrix} \xi_{\mathbf{k}} & -\Delta & -V & 0 \\ -\Delta & -\xi_{\mathbf{k}} & 0 & V \\ -V & 0 & \xi_{\mathbf{k}+\mathbf{Q}} & -\Delta \\ 0 & V & -\Delta & -\xi_{\mathbf{k}+\mathbf{Q}} \end{pmatrix} \begin{pmatrix} c_{\mathbf{k},\uparrow} \\ c_{-\mathbf{k},\downarrow}^\dagger \\ c_{\mathbf{k}+\mathbf{Q},\uparrow} \\ c_{-(\mathbf{k}+\mathbf{Q}),\downarrow}^\dagger \end{pmatrix} \\
&\equiv \sum_{\mathbf{k}} \Psi_{\mathbf{k},\mathbf{Q}}^\dagger H_0 \Psi_{\mathbf{k},\mathbf{Q}},
\end{aligned}$$

where $\xi_{\mathbf{k}}$ is the normal-state energy of particles of momentum \mathbf{k} relative to the Fermi energy, σ is the spin index, c^\dagger and c are the fermion creation and annihilation operators, \mathbf{Q} is the wave vector of the CDW, and Δ and V denote the SC energy gap and CDW energy scale, respectively. H_0 is the (4×4) matrix, and the adjoint of Ψ represents a (1×4) matrix $\Psi_{\mathbf{k},\mathbf{Q}}^\dagger \equiv (c_{\mathbf{k},\uparrow}^\dagger c_{-\mathbf{k},\downarrow}^\dagger c_{\mathbf{k}+\mathbf{Q},\uparrow}^\dagger c_{-(\mathbf{k}+\mathbf{Q}),\downarrow})$. We have further imposed the condition $\xi_{\mathbf{k}} \xi_{-(\mathbf{k}+\mathbf{Q})} < 0$ to ensure that CDW excitations only involve particle-hole sectors. The mean-field Hamiltonian in Eq. (6.1) can be exactly diagonalized so that the bare Green's function $G_0(\mathbf{k}, \omega)$ is given by

$$G_0^{-1} = \omega I - H_0 = \begin{pmatrix} \omega - \xi_{\mathbf{k}} & \Delta & V & 0 \\ \Delta & \omega + \xi_{\mathbf{k}} & 0 & -V \\ V & 0 & \omega - \xi_{\mathbf{k}+\mathbf{Q}} & \Delta \\ 0 & -V & \Delta & \omega + \xi_{\mathbf{k}+\mathbf{Q}} \end{pmatrix}, \quad (6.1)$$

where I denotes the (4×4) unit matrix.

Next, we introduce phase fluctuations to the superconducting order parameter $\Delta(\mathbf{r}) = |\Delta(\mathbf{r})| e^{i\theta(\mathbf{r})}$.

In order to couple quasiparticles explicitly to the phase field $\theta(\mathbf{r})$, we follow Ref. [262] and perform

a gauge transformation to the fermion operators: $c_\sigma(\mathbf{r}) \rightarrow c_\sigma(\mathbf{r})e^{i\theta(\mathbf{r})/2}$. After integrating out the fast momentum degrees of freedom with variations larger than $1/\xi_0$ (ξ_0 : superconducting coherence length) [269], the resulting low-energy effective theory contains the mean-field theory of coexisting SC and CO, the Gaussian theory of the phase fluctuations, and the coupling term between the two [262]:

$$\begin{aligned}\mathcal{H}_{eff} &= \mathcal{H}_0 + \mathcal{H}_I, \\ \mathcal{H}_0 &= \mathcal{H}_{MF} + \frac{1}{2} \sum_{\mathbf{q}} \frac{n_f}{4m} \mathbf{q}^2 \theta(\mathbf{q}) \theta(-\mathbf{q}), \\ \mathcal{H}_I &= \sum_{\mathbf{k}, \mathbf{q}, \sigma} m \mathbf{v}(\mathbf{k}) \cdot \mathbf{v}_s(\mathbf{q}) c_{\mathbf{k}+\mathbf{q}, \sigma}^\dagger c_{\mathbf{k}, \sigma},\end{aligned}\quad (6.2)$$

where m is the free electron mass, $\mathbf{v}(\mathbf{k}) = \nabla_{\mathbf{k}} \xi_{\mathbf{k}} / \hbar$ is the normal-state group velocity, and $\mathbf{v}_s = \int d^2r e^{-i\mathbf{q} \cdot \mathbf{r}} \nabla \theta(\mathbf{r}) / 2m$ is the superfluid velocity.

Expressed in the basis of Ψ , $\mathcal{H}_I = \sum_{\mathbf{k}, \mathbf{q}} \Psi_{\mathbf{k}, \mathbf{Q}}^\dagger H_I(\mathbf{k}, \mathbf{q}) \Psi_{\mathbf{k}, \mathbf{Q}}$ where

$$\begin{aligned}H_I &\propto \begin{pmatrix} i\theta_{\mathbf{q}} \mathbf{q} \cdot \nabla_{\mathbf{k}} \xi_{\mathbf{k}} & 0 & 0 & 0 \\ 0 & i\theta_{\mathbf{q}} \mathbf{q} \cdot \nabla_{\mathbf{k}} \xi_{\mathbf{k}} & 0 & 0 \\ 0 & 0 & i\theta_{\mathbf{q}} \mathbf{q} \cdot \nabla_{\mathbf{k}} \xi_{\mathbf{k}+\mathbf{Q}} & 0 \\ 0 & 0 & 0 & i\theta_{\mathbf{q}} \mathbf{q} \cdot \nabla_{\mathbf{k}} \xi_{\mathbf{k}+\mathbf{Q}} \end{pmatrix} \\ &\approx i\theta_{\mathbf{q}} \mathbf{q} \cdot \nabla_{\mathbf{k}} \xi_{\mathbf{k}} \begin{pmatrix} 1 & 0 & 0 & 0 \\ 0 & 1 & 0 & 0 \\ 0 & 0 & -1 & 0 \\ 0 & 0 & 0 & -1 \end{pmatrix}.\end{aligned}\quad (6.3)$$

In deriving Eq. (6.3), we have taken the approximation $\xi_{\mathbf{k}+\mathbf{Q}} \approx -\xi_{\mathbf{k}}$ to simplify the calculation, which holds for electrons around the Fermi surface along the $\{100\}$ and $\{010\}$ axes where CDW couples most strongly with SC.

With Eq. (6.3), we can now write down the proper self-energy for the electrons:

$$\begin{aligned}\Sigma^*(\mathbf{k}) &= \sum_{\mathbf{q}} H_I(\mathbf{k}, \mathbf{q}) G(\mathbf{k} + \mathbf{q}, \omega) H_I(\mathbf{k} + \mathbf{q}, -\mathbf{q}) \\ &= \sum_{\mathbf{q}} \frac{1}{16} \langle \theta_{\mathbf{q}} \theta_{-\mathbf{q}} \rangle (\mathbf{q} \cdot \nabla_{\mathbf{k}} \xi_{\mathbf{k}})(\mathbf{q} \cdot \nabla_{\mathbf{k}} \xi_{\mathbf{k}+\mathbf{q}}) \begin{pmatrix} G_{11}(\mathbf{k}, \omega) & -G_{12}(\mathbf{k}, \omega) \\ -G_{21}(\mathbf{k}, \omega) & G_{22}(\mathbf{k}, \omega) \end{pmatrix},\end{aligned}\quad (6.4)$$

where $G_{ij}(\mathbf{k}, \omega)$'s are the (2×2) matrices composing the full Green's function

$$G(\mathbf{k}, \omega) = \begin{pmatrix} G_{11}(\mathbf{k}, \omega) & -G_{12}(\mathbf{k}, \omega) \\ -G_{21}(\mathbf{k}, \omega) & G_{22}(\mathbf{k}, \omega) \end{pmatrix}.$$

In Eqs. (6.3) and (6.4), only the longitudinal phase fluctuations are retained because at $T = 0$ in the zero field limit, the transverse phase fluctuations are energetically very costly and therefore may be neglected. After summing over an infinite series of ring diagrams [Fig. 6.1(a)], the phase field correlation function $\langle \theta_{\mathbf{q}} \theta_{-\mathbf{q}} \rangle$ is given by [264]

$$\langle \theta_{\mathbf{q}} \theta_{-\mathbf{q}} \rangle \approx \frac{4m \omega_p}{\hbar n_s^{2D} \Omega} \frac{1}{q^2}, \quad (6.5)$$

where n_s^{2D} the two-dimensional superfluid density, ω_p the plasma frequency, and Ω the sample volume.

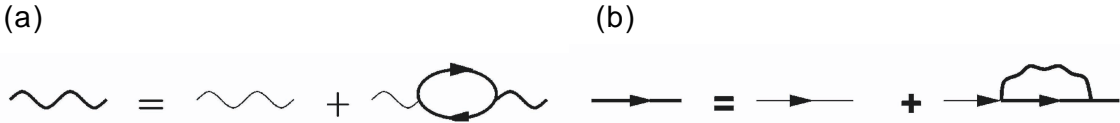


Figure 6.1: (From Figs. 3 and 4 of Ref. [262].) (a) The infinite sum of the ring diagrams for the superfluid velocity field propagator. (b) The Dyson's equation for the fermion Green's function. The thin (thick) wiggly line is the bare (full) velocity field propagator, and the thin (thick) solid line is the bare (full) fermion Green's function.

Thus, we obtain the full Green's function $G(\mathbf{k}, \omega)$ self-consistently through the Dyson's equation

[Fig. 6.1(b)]:

$$\begin{aligned}
G^{-1}(\mathbf{k}, \tilde{\omega}) &= G_0^{-1}(\mathbf{k}, \omega) - \Sigma^* \\
&= G_0^{-1}(\mathbf{k}, \omega) - \eta \sum_{\mathbf{q}} \frac{1}{q^2} (\mathbf{q} \cdot \nabla_{\mathbf{k}} \xi_{\mathbf{k}}) (\mathbf{q} \cdot \nabla_{\mathbf{k}} \xi_{\mathbf{k}+\mathbf{q}}) \begin{pmatrix} G_{11}(\mathbf{k}, \tilde{\omega}) & -G_{12}(\mathbf{k}, \tilde{\omega}) \\ -G_{21}(\mathbf{k}, \tilde{\omega}) & G_{22}(\mathbf{k}, \tilde{\omega}) \end{pmatrix} \\
&= \begin{pmatrix} \tilde{\omega} - \tilde{\xi}_{\mathbf{k}} & \tilde{\Delta} & \tilde{V} & 0 \\ \tilde{\Delta} & \tilde{\omega} + \tilde{\xi}_{\mathbf{k}} & 0 & -\tilde{V} \\ \tilde{V} & 0 & \tilde{\omega} - \tilde{\xi}_{\mathbf{k}+\mathbf{Q}} & \tilde{\Delta} \\ 0 & -\tilde{V} & \tilde{\Delta} & \tilde{\omega} + \tilde{\xi}_{\mathbf{k}+\mathbf{Q}} \end{pmatrix}, \tag{6.6}
\end{aligned}$$

Here $\tilde{\omega}$ denotes the energy renormalized by the phase fluctuations, and $\eta \equiv m\omega_p/4\hbar n_s^{2D}\Omega q^2$ is a parameter indicative of the magnitude of fluctuations. Equation (6.6) can be solved self-consistently for each ω and each \mathbf{k} -value in the Brillouin zone. Summing over a finite phase space in \mathbf{q} near each \mathbf{k} , we use the iterative Newton's method to find the corresponding $\tilde{\xi}_{\mathbf{k}}$, $\tilde{\omega}$, \tilde{V} and $\tilde{\Delta}$ to the full Green's function $G(\mathbf{k}, \tilde{\omega})$ [270]. The converged Green's function thus yields the spectral density function $A(\mathbf{k}, \tilde{\omega}) \equiv -\text{Im}[G(\mathbf{k}, \tilde{\omega})]/\pi$ and the DOS $\mathcal{N}(\tilde{\omega}) \equiv \sum_{\mathbf{k}} A(\mathbf{k}, \tilde{\omega})$.

In the case of $d_{x^2-y^2}$ -wave SC, similar derivations can be made if we replace in Eq. (6.1) Δ by $\Delta_d(\cos k_x a - \cos k_y a)$ and V by the disorder-pinned $g^2 V_{SDW}$, where a is the square lattice constant, and g is the coupling strength between SDW and disorder. The periodicity \mathbf{Q} of the charge modulations caused by the disorder-pinned SDW is twice that of the SDW.

6.2.2 Numerical results

For a given cuprate band structure with a known doping level, the quasiparticle DOS calculated from the aforementioned approach depends primarily on two variables: the ratio Δ/V and the magnitude of the quantum phase fluctuations represented by η . For an s -wave electron-doped superconductivity with $\Delta > V$, finite quantum phase fluctuations can induce substantial subgap DOS even if the mean-field SC and CDW orders are fully gapped, as illustrated in Fig. 6.2(a). Comparing the single-particle excitation spectrum derived from §6.2.1 with the BCS curve, we see

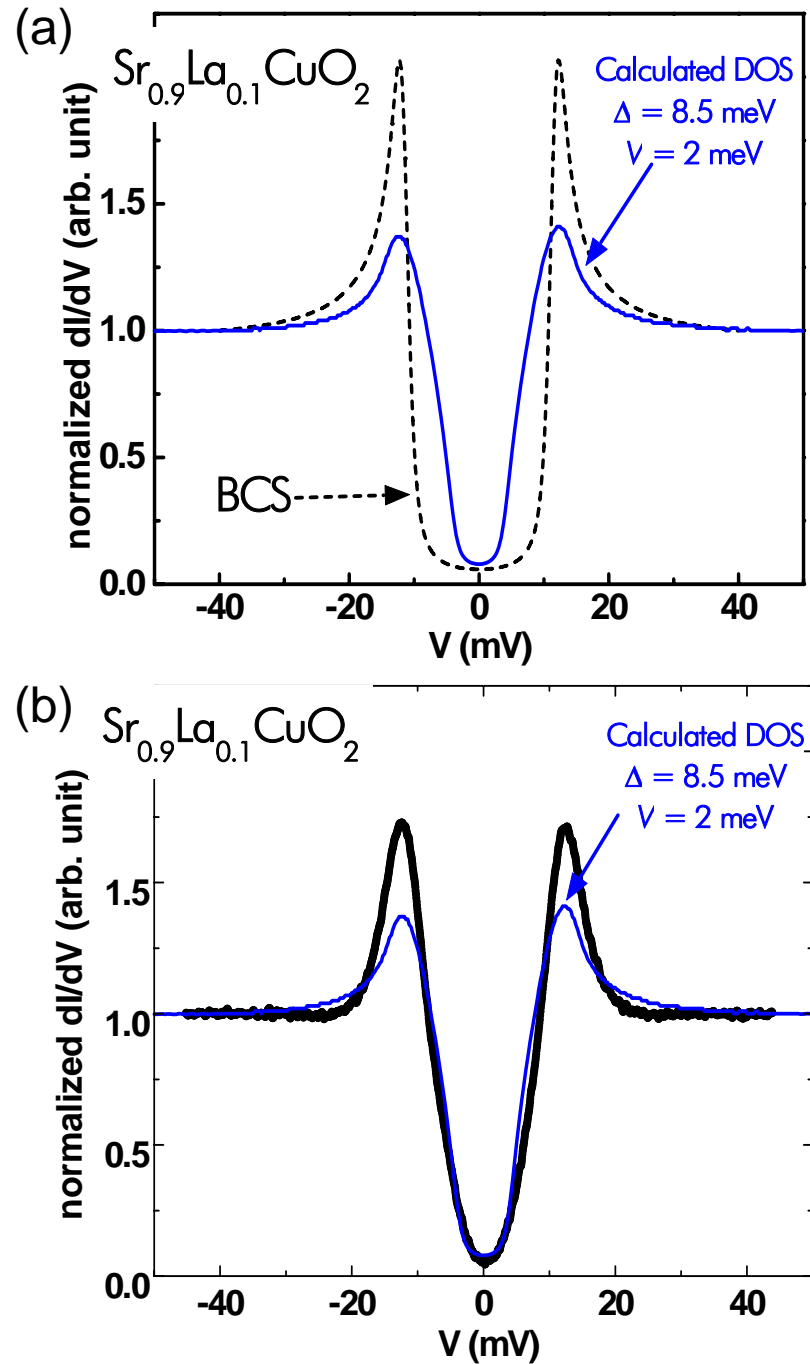


Figure 6.2: Comparison of the calculated quasiparticle DOS with experimental spectra on SLCO: (a) The calculated DOS for coexisting *s*-wave SC and CDW with quantum fluctuations is compared with the BCS prediction (dashed line). We note that finite subgap DOS can be induced by quantum fluctuations even if the mean-field DOS is fully gapped. (b) Momentum-independent quasiparticle tunneling spectrum of the electron-doped cuprate SLCO (thick line) is compared with the calculated DOS. The bare parameters are $\Delta = 8.5 \text{ meV}$, $V = 2 \text{ meV}$, and the fluctuation strength $\eta = 0.0001/16\pi$.

that, under finite quantum fluctuations, the spectral weight shifts from above the mean-field gap to lower energies and the spectral peaks are suppressed. The bare superconducting gap value and bare charge density wave energy for this set of simulation are chosen to be 8.5 meV and 2 meV, respectively, to match the experimentally observed peak position. The spectral peak of the phase-fluctuated SC with coexisting CDW locates at ~ 13.5 meV, but the effective gap $\Delta_{eff} = \sqrt{\Delta^2 + V^2}$ is only $\sim (9 - 11.5)$ meV when all uncertainties in fitting parameters are included. Therefore, in the presence of fluctuations, the subgap density of states is filled in and the peak-to-peak separation of the single-particle spectrum appears larger than the actual spectral gap, which is characteristic of any fluctuation-smeared tunneling spectrum.

In Fig. 6.2(b), we plot the normalized quasiparticle tunneling spectrum of SLCO with the simulation result. The calculated spectrum fits the low-energy excitations of the experimental data fairly well, while the calculated peak height is lower than the observed peak height. Since the calculated spectrum conserves the density of states when compared with the mean-field BCS prediction and yields a reasonable $2\Delta/k_B T_c \sim 4.85$ ratio, we believe that the simulation captures all major low-energy physics of SLCO and that the discrepancy in peak height between the calculated and the observed spectra may have originated from the tunneling matrix effect and the uncertainty in background normalization.

We further investigate how the quasiparticle tunneling spectra of an *s*-wave superconductor evolve under varying V/Δ ratio and a constant magnitude of quantum phase fluctuations. Given the degrees of phase fluctuation characterized by $\eta = 0.0001/16\pi$, the calculated spectra for $V/\Delta < 1$, such as those for $V/\Delta = 2.0/8.5$ and $V/\Delta = 8.0/8.5$, exhibit similar spectral characteristics [Fig. 6.3(a)]. They all exhibit substantial subgap low-energy excitations but no discernible satellite features. For a larger $V/\Delta > 1$, the satellite features designated by the red circle in Fig. 6.3(b) appear above the spectral gap, which is indicative of the coexisting CDW. Therefore, the absence of satellite features in the superconducting state tunneling spectra of electron-doped cuprates implies that the energy scale of the coexisting order is smaller than that of superconductivity. Consequently, as the temperature increases, the competing order vanishes before the system turns normal, which explains the absence

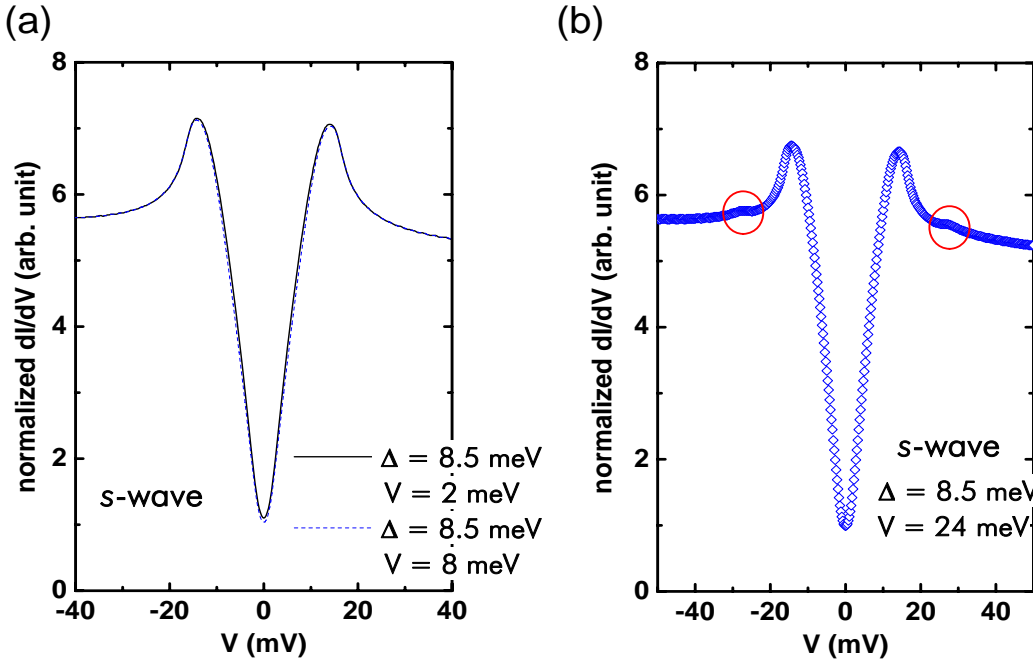


Figure 6.3: A scenario for the occurrence of the satellite features as the consequence of coexisting CO and SC in the ground state with $V \geq \Delta$: Evolution of the quasiparticle tunneling spectra for an s -wave superconductor from absence of the satellite features to appearance of which with increasing (V/Δ) and a constant magnitude of quantum phase fluctuations $\eta = 0.0001/16\pi$.

of pseudogap in their normal-state tunneling spectra.

For a $d_{x^2-y^2}$ -wave hole-doped superconductors, we find that by taking into account a coexisting disorder-pinned density wave with $g^2V_{SDW} > \Delta$, our model can reproduce the experimentally observed satellite features [as indicated by the red circles in Fig. 6.4(b)] in the limit of vanishing phase fluctuations [Fig. 6.4(a)]. The incorporation of varying degrees of quantum phase fluctuations would give rise to various types of “pseudogap”-like spectra revealed in the scanning tunneling spectra on Bi-2212 [Fig. 6.4(d)] [68]. A specific example that displays double peaks of comparable height is given in Fig. 6.4(c) to compare with the empirically observed double-peak structure, as indicated by the arrows in Fig. 6.4(d). Decreasing the phase fluctuations and CO would recover the sharp superconducting coherence peaks, as shown in spectra denoted by thin red lines in Fig. 6.4(d) and in Fig. 6.4(a). In contrast, increasing phase fluctuations while maintaining the strengths of both orders smears the double-peak feature into a big broad “pseudogap” peak as shown in Fig. 6.4(e). By comparing the calculated spectra of a d -wave hole-doped cuprate superconductor [Fig. 6.4(a,c,e)]

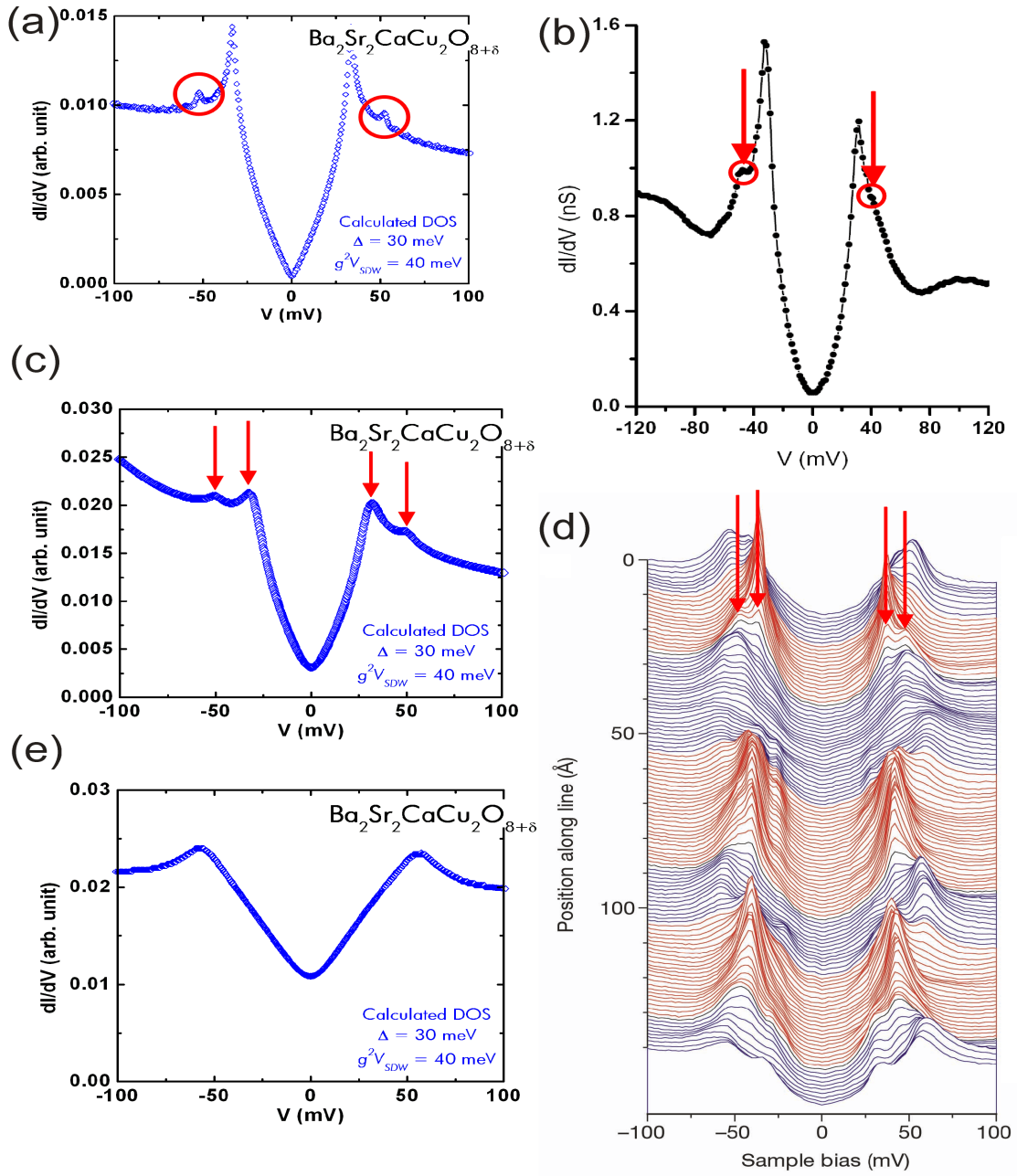


Figure 6.4: Comparison of the calculated quasiparticle DOS with experimental spectra on Bi-2212: (a) Calculated d -wave mean-field DOS using parameters $\Delta = 30$ meV, $g^2V_{SDW} = 40$ meV, and $\eta = 0$. (b) (Adapted from Fig. 2 of Ref. [183].) Quasiparticle c -axis tunneling spectrum of the hole-doped d -wave superconductor Bi-2212 in Ref. [183], showing satellite features as marked by arrows. (c) Calculated d -wave DOS with phase fluctuations using parameters $\Delta = 30$ meV, $g^2V_{SDW} = 40$ meV, and $\eta = 0.001/16\pi$. (d) (Adapted by permission from Macmillan Publishers Ltd: Nature [68], copyright (2002).) Quasiparticle c -axis tunneling spectrum of $\text{Bi}_2\text{Sr}_2\text{Ca}\text{Cu}_2\text{O}_x$ in Ref. [68], showing "pseudogap"-like features and the coexistence of two gaps as indicated by the red arrows. (e) Calculated d -wave DOS with phase fluctuations using parameters $\Delta = 30$ meV, $g^2V_{SDW} = 40$ meV, and $\eta = 0.0025/16\pi$. We note that the double-peak structure in (c) merges into one broad peak, yielding a pseudogap-like spectrum.

with the empirically observed ‘‘pseudogap’’-like spectra [Fig. 6.4(d)] [68]], we see clearly that the nano-scale variations in the spectral gap of Bi-2212 originate from the interplay of the competing order with the phase-fluctuated superconducting order, whose fluctuation strength varies at nano-scale possibly due to random disorder in this high-2D system. The energy scale of the competing order is larger than that of superconductivity, and hence the spectral gap associated with the coexisting order sustains above the superconducting transition temperature, giving rise to the pseudogap observed in the normal-state tunneling spectra of Bi-2212 [54].

6.2.3 Summary

In summary, we recapitulate the implications of the coexistence of SC and CO on the origin of pseudogap phenomena and the satellite features in cuprate superconductors. For arbitrary values of Δ and V , the poles associated with \mathcal{H}_{MF} in Eq. (6.1) generally give rise to two sets of peaks at $\omega = \pm\Delta_{\text{eff}}$ and $\omega = \pm\Delta$ in the quasiparticle DOS. For $\Delta \gg V$, we find that $\Delta_{\text{eff}} \approx \Delta$ so that only one set of peaks can be resolved in the quasiparticle spectra, particularly under finite quantum fluctuations. In this case, the magnitude of Δ_{eff} in the quasiparticle spectra is expected to decrease with increasing T and completely vanishes at T_c , which is consistent with the general findings in the electron-type cuprate superconductors [49, 16, 271]. On the other hand, for $V \geq \Delta$, two distinct sets of peaks can be resolved at $T \ll T_c$ and for limited quantum phase fluctuations. With increasing T or quantum phase fluctuations, the peaks at $\omega = \pm\Delta$ diminish while those at $\omega = \pm\Delta_{\text{eff}} \sim \pm V$ are broadened by fluctuations thus appear to remain nearly invariant in position, similar to the findings of pseudogap phenomena in underdoped $\text{Bi}_2\text{Sr}_2\text{CaCu}_2\text{O}_x$ (Bi-2212) cuprates above T_c [54]. In short, these results corroborate our conjecture that $V \ll \Delta$ is associated with the absence of pseudogap and the satellite features in electron-doped cuprates, whereas $V \geq \Delta_d$ is responsible for their presence in under- and optimally doped hole-doped cuprates. Thus, the experimental observation of non-universal pseudogap phenomena in the cuprates can be reconciled by coexisting CO and SC of different relative strengths.

6.3 Collective modes and quasiparticle interference on the local density of states of cuprate superconductors¹

The presence of competing orders and the proximity to quantum criticality [249, 62, 202] have significant consequences on the unconventional low-energy excitation spectra of the cuprates, including weakened superconducting phase stiffness [73], the occurrence of excess subgap quasiparticle density of states (DOS) [49], and the presence (absence) of pseudogap [49, 54, 16] and Nernst effect in the hole (electron)-type cuprates above the SC transition [64, 65]. Other experimental observables of the coexisting orders involve various spin and charge ordering revealed in the neutron scattering and scanning tunneling spectroscopy measurements as mentioned in §1.2.3. In this section, we examine the effect of coexisting spin/charge density waves on recent scanning tunneling spectroscopic studies of the Fourier transformed (FT) quasiparticle local density of states (LDOS) in nearly optimally doped Bi-2212 [95, 97, 272] and find that while Bogoliubov quasiparticle interference [256, 258, 101, 273, 274, 275] apparently plays an important role in the observed FT-LDOS in the superconducting state, certain spectral details of the LDOS cannot be accounted for unless collective modes such as spin/charge density waves are considered [256, 258, 101]. More importantly, the observations of four high-intensity Bragg peaks remaining above T_c in the FT-LDOS map of Bi-2212 [99] cannot be reconciled with quasiparticles being the sole low-energy excitations. By comparing the experimental data to the calculated energy (E), momentum transfer (q) and temperature (T) dependence of the FT-LDOS modulations of a d -wave superconductor with random disorder, we conclude that collective modes such as spin/charge density waves are relevant low-energy excitations which contribute to the aforementioned LDOS modulations in Bi-2212.

6.3.1 Model

We begin our model construction by recalling that substantial nano-scale spectral variations are observed in the low-temperature tunneling spectroscopy of under- and optimally doped Bi-2212 single

¹The main contents of this section are published as C.-T. Chen and N.-C. Yeh, *Phys. Rev. B* **68**, 220505(R) (2003).

crystals [Fig. 6.4(d)] [276, 67, 68, 194] which exhibits two types of spatially separated regions. In the last section, we have shown that for regions with double-peak or rounded hump-like “pseudogap” features at larger energies Δ_{eff} , quantum phase fluctuations resulting from pinned density waves coexisting with superconductivity are important, where as for region with sharp quasiparticle coherence peaks at smaller energies Δ_d , Bogoliubov quasiparticle spectra with a well-defined d -wave pairing order parameter Δ_k dominate over the collective modes. Our model therefore assumes that, embedded in the predominantly superconducting regions, there are “puddles” of spatially confined “pseudogap regions” with a quasiparticle scattering potential modulated by the pinned density waves along the Cu-O bonding directions [§6.5]. The spatial modulations can be of either the ‘checkerboard’ pattern [256, 258] or ‘charge nematic’ with short-range stripes [277, 73] at a periodicity of four lattice constants, as inferred from neutron scattering experiments in a variety of p-type cuprates [84, 278, 279, 280, 281, 282, 85]. The calculation is implemented on a (400×400) sample area with either 24 randomly distributed point impurities or 24 randomly distributed puddles of charge modulations that cover approximately 6% of the sample area.²

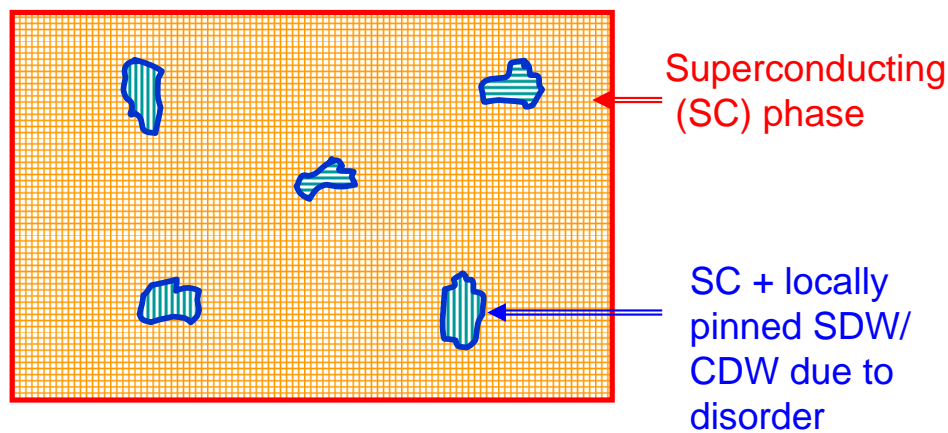


Figure 6.5: Disorder-pinned density waves forming “puddles” of “pseudogap” regions embedded in the predominantly superconducting region.

The Hamiltonian of the two-dimensional superconductor is given by $\mathcal{H} = \mathcal{H}_{BCS} + \mathcal{H}_{imp}$, where

²For simplicity, we do not take into account the effect of disorder on either suppressing the local pairing potential $\Delta_d(r)$ or altering the nearest-neighbor hopping coefficient (t) in the band structure of Bi-2212, although such effects reflect the internal structures of charge modulations [101, 273].

\mathcal{H}_{BCS} denotes the unperturbed BCS Hamiltonian of the d -wave superconductor,

$$\mathcal{H}_{BCS} = \sum_{\mathbf{k}\sigma} (\epsilon_{\mathbf{k}} - \mu) c_{\mathbf{k}\sigma}^\dagger c_{\mathbf{k}\sigma} + \sum_{\mathbf{k}} \Delta_{\mathbf{k}} [c_{\mathbf{k}\uparrow}^\dagger c_{-\mathbf{k}\downarrow}^\dagger + c_{-\mathbf{k}\downarrow} c_{\mathbf{k}\uparrow}], \quad \Delta_{\mathbf{k}} \approx \Delta_d \cos 2\theta_{\mathbf{k}}, \quad (6.7)$$

and \mathcal{H}_{imp} is the perturbation Hamiltonian associated with impurity-induced quasiparticle scattering potential [258, 273, 274]. In Eq. (6.7), Δ_d is the maximum gap value and $\theta_{\mathbf{k}}$ is the angle between the quasiparticle wavevector \mathbf{k} and the anti-node direction. Using the T-matrix method, the Green's function \mathcal{G} associated with \mathcal{H} is given by $\mathcal{G} = \mathcal{G}_0 + \mathcal{G}_0 T \mathcal{G}_0$, where \mathcal{G}_0 is the Green's function of \mathcal{H}_{BCS} and $T = \mathcal{H}_{imp}/(1 - \mathcal{G}_0 \mathcal{H}_{imp})$ [cf. Appendix C]. We remark that the perturbative approach adopted here for the competing order is justifiable for low-energy (*i.e.*, $E < \Delta_d$) excitations in d -wave superconductors, because the gapless nodal Bogoliubov quasiparticles are the dominant low-energy excitations in this limit, as manifested in Fig. 6.4(a). In other words, the perturbative approach is a special case of the exact self-consistent treatment described in §6.2.

To proceed, we note that the Hartree perturbation potential for single scattering events in the diagonal part of \mathcal{H}_{imp} is

$$V_\alpha(\mathbf{q}) = \sum_i V_{s,m} e^{i\mathbf{q}\cdot\mathbf{r}_i}$$

for non-interacting non-magnetic (V_s) and magnetic (V_m) impurities at locations \mathbf{r}_i [274], whereas that for puddles with short stripe-like modulations centering at \mathbf{r}_j is³

$$V_\beta(\mathbf{q}) = \sum_j V_0 e^{i\mathbf{q}\cdot\mathbf{r}_j} \frac{2 \sin(q_{y,x} R_j) \sin(q_{x,y} R_j)}{q_{y,x} \sin(2q_{x,y})}, \quad (6.8)$$

and that for checkerboard modulations is

$$V_\gamma(\mathbf{q}) = \sum_j V_0 e^{i\mathbf{q}\cdot\mathbf{r}_j} \left[\frac{2 \sin(q_y R_j) \sin(q_x R_j)}{q_y \sin(2q_x)} + (q_x \leftrightarrow q_y) \right]. \quad (6.9)$$

Here all lengths are expressed in units of the lattice constant a , R_j is the averaged radius of the

³For coexisting superconductivity and CDW, $V_\beta(\mathbf{q})$ represents the second-order effect of quasiparticle interference with pinned CDW. The first-order effect of CDW has been discussed in Ref. [101].

j -th puddle, and V_0 denotes the magnitude of the scattering potential by pinned collective modes. Empirically, for nearly optimally doped Bi-2212, R_j ranges from $5 \sim 10$ [68]. Here we take different values for R_j with a mean value $\langle R_j \rangle = 10$. In the context of our discussion in §6.2, the Hartree potentials contains information of the mean-field competing order and the self-energy correction that couples the superconducting phase fluctuations to the fermionic excitations of the coexisting state.

For simplicity, we neglect the energy dependence of $V_{\alpha,\beta,\gamma}$ and assume that V_s , V_m and V_0 are sufficiently small so that no resonance occurs in the FT-LDOS [273]. For sufficiently large scattering potentials, full T-matrix calculations become necessary as in Ref. [274]. However, large $V_{s,m}$ would result in strong spectral asymmetry between positive and negative bias voltages [274], which differs from experimental observation [95, 97, 272]. We also note that the energy dependence of $V_{\beta,\gamma}$ reflects the spectral characteristics of the collective modes and their interaction with quasiparticles and impurities. For instance, we expect $V_\gamma \sim \zeta g^2$ for pinned SDW, where ζ is the impurity pinning strength and g is the coupling amplitude of quasiparticles with SDW fluctuations [256, 258].

In the limit of weak perturbations, given the Hamiltonian and the scattering potentials $V_{\alpha,\beta,\gamma}(\mathbf{q})$, we find that the FT of the LDOS $\rho(\mathbf{r}, E)$ that involves elastic scattering of quasiparticles from momentum \mathbf{k} to $\mathbf{k} + \mathbf{q}$ is

$$\begin{aligned} \rho_{\mathbf{q}}(\omega) = & -\frac{1}{\pi N^2} \lim_{\delta \rightarrow 0} \sum_{\mathbf{k}} V_{\alpha,\beta,\gamma}(\mathbf{q}) \times \\ & \left\{ u_{\mathbf{k}+\mathbf{q}} u_{\mathbf{k}} (u_{\mathbf{k}+\mathbf{q}} u_{\mathbf{k}} \mp v_{\mathbf{k}+\mathbf{q}} v_{\mathbf{k}}) \text{Im} \left[\frac{1}{(\omega - E_{\mathbf{k}} + i\delta)(\omega - E_{\mathbf{k}+\mathbf{q}} + i\delta)} \right] \right. \\ & + u_{\mathbf{k}+\mathbf{q}} v_{\mathbf{k}} (u_{\mathbf{k}+\mathbf{q}} v_{\mathbf{k}} \pm v_{\mathbf{k}+\mathbf{q}} u_{\mathbf{k}}) \text{Im} \left[\frac{1}{(\omega + E_{\mathbf{k}} + i\delta)(\omega - E_{\mathbf{k}+\mathbf{q}} + i\delta)} \right] \\ & + v_{\mathbf{k}+\mathbf{q}} u_{\mathbf{k}} (u_{\mathbf{k}+\mathbf{q}} v_{\mathbf{k}} \pm v_{\mathbf{k}+\mathbf{q}} u_{\mathbf{k}}) \text{Im} \left[\frac{1}{(\omega - E_{\mathbf{k}} + i\delta)(\omega + E_{\mathbf{k}+\mathbf{q}} + i\delta)} \right] \\ & \left. - v_{\mathbf{k}+\mathbf{q}} v_{\mathbf{k}} (u_{\mathbf{k}+\mathbf{q}} u_{\mathbf{k}} \mp v_{\mathbf{k}+\mathbf{q}} v_{\mathbf{k}}) \text{Im} \left[\frac{1}{(\omega + E_{\mathbf{k}} + i\delta)(\omega + E_{\mathbf{k}+\mathbf{q}} + i\delta)} \right] \right\} \end{aligned} \quad (6.10)$$

in the first-order T-matrix approximation for infinite quasiparticle lifetime. Here N is the total number of unit cells in the sample, and $\text{Im}[\dots]$ denotes the imaginary part of the quantity within the brackets, which is related to the equal-energy quasiparticle joint density of states. The upper (lower) sign in the coherence factor applies to spin-independent (spin-dependent) interactions. $u_{\mathbf{k}}$

and $v_{\mathbf{k}}$ are the Bogoliubov quasiparticle coefficients, $u_{\mathbf{k}}^2 + v_{\mathbf{k}}^2 = 1$, $u_{\mathbf{k}}^2 = [1 + (\xi_{\mathbf{k}}/E_{\mathbf{k}})]/2$, where $\xi_{\mathbf{k}} \equiv \epsilon_{\mathbf{k}} - \mu$, $E_{\mathbf{k}} = \sqrt{\xi_{\mathbf{k}}^2 + \Delta_{\mathbf{k}}^2}$, μ is the chemical potential, and $\epsilon_{\mathbf{k}}$ is the tight-binding energy of the normal state of Bi-2212 according to Norman *et al.* [283],

$$\begin{aligned}\epsilon_{\mathbf{k}} = & \frac{t_1}{2}(\cos k_x + \cos k_y) + t_2 \cos k_x \cos k_y + \frac{t_3}{2}(\cos 2k_x + \cos 2k_y) \\ & + \frac{t_4}{2}(\cos 2k_x \cos k_y + \cos k_x \cos 2k_y) + t_5 \cos 2k_x \cos 2k_y,\end{aligned}$$

$$t_{1-5} = -0.5951, 0.1636, -0.0519, -0.1117, 0.0510 \text{ eV.}$$

6.3.2 Numerical results

Using Eq. (6.10) and $V_{\alpha,\beta,\gamma}(\mathbf{q})$, we obtain the energy-dependent FT-LDOS maps in the first Brillouin zone for non-magnetic point impurities in Fig. 6.6 with two different superconducting gap values, $\Delta_d = 20$ and 40 meV, and $T = 0$. The most intense modulation q -values are associated with the elastic scattering events connecting quasiparticle momenta k located around the tips of the constant-energy contours where the available phase space is maximized, as illustrated in Fig. 6.6(c). Comparing Fig. 6.6(a) with Fig. 6.6(b), we find that the polarity of the bias voltages does not change the primary features of the FT-LDOS plots, consistent with experimental findings. However, because of the directionality of the coherence factors [$u_{\mathbf{k}+\mathbf{q}}u_{\mathbf{k}}(u_{\mathbf{k}+\mathbf{q}}u_{\mathbf{k}} - v_{\mathbf{k}+\mathbf{q}}v_{\mathbf{k}})$], the intensities associated with \mathbf{q}_B and \mathbf{q}_C are much stronger than those of \mathbf{q}_A [Fig. 6.6(a)(b)] and also in Fig. 6.7(a), which differs from the STM observation [95, 97] that reveals comparable intensities associated with \mathbf{q}_A and \mathbf{q}_B , and weaker intensities with \mathbf{q}_C . Interestingly, the intensity of \mathbf{q}_A becomes larger than that of \mathbf{q}_B if one assumes magnetic point impurity scattering, as illustrated in Fig. 6.7(b). However, there is no evidence of magnetic scattering in the samples used in Refs. [95, 97]. In contrast, the presence of pinned collective modes, regardless of CDW or SDW, gives rise to much stronger intensities for \mathbf{q}_A (by about two orders of magnitude), as shown in Fig. 6.8 for pinned SDW (with spin-dependent coherence factors). Thus, the empirical FT-LDOS maps [95, 97] cannot be solely attributed to quasiparticle scattering by non-magnetic point impurities and should contain contributions from the pinned density waves. For reference, an example of the real-space LDOS modulations corre-

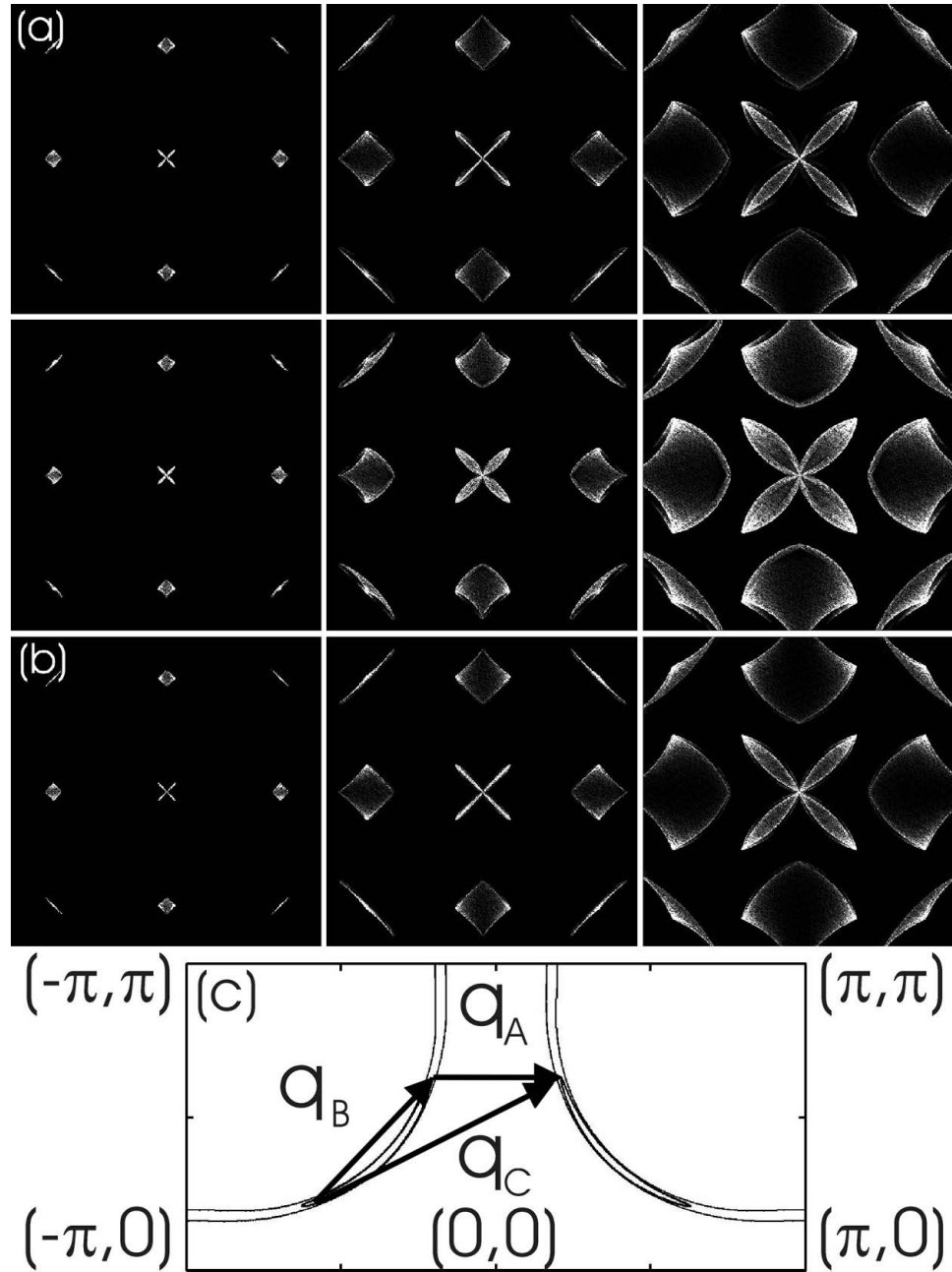


Figure 6.6: Calculated energy-dependent Fourier transform (FT) maps of quasiparticle LDOS in the first Brillouin zone with randomly distributed non-magnetic point defects using Eq. (6.10) and V_α : (a) $\Delta_d = 40$ meV and $(\omega/\Delta_d) = \pm 0.15, \pm 0.45, \pm 0.75$ (up and down from left to right); (b) $\Delta_d = 20$ meV and $(\omega/\Delta_d) = 0.15, 0.45, 0.75$ (left to right). (c) Schematic illustration of the equal-energy contours and representative modulation wavevectors \mathbf{q}_A , \mathbf{q}_B , and \mathbf{q}_C , which correspond to \mathbf{q}_1 , \mathbf{q}_7 , and \mathbf{q}_2 in Refs. [95, 97].

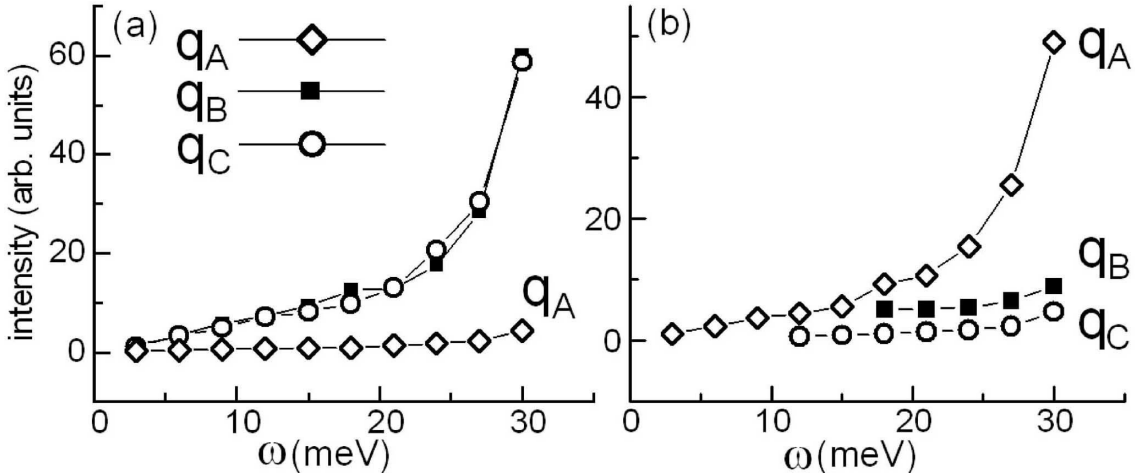


Figure 6.7: Evolution of the relative intensities of FT-LDOS with energy (ω) for q_A , q_B and q_C as defined in Fig.1(c) and V_s , V_m and V_0 all taken to be unity: quasiparticle scattering by (a) single non-magnetic point impurity, and (b) single magnetic point impurity.

sponding to quasiparticle scattering by the three types of random disorders $V_{\alpha,\beta,\gamma}(\mathbf{q})$ is included in Figs. 6.9(a)–(c), though a detail comparison between experiments and calculations must be done through the FT-LDOS maps.

The relevance of collective modes becomes indisputable when we consider the temperature dependence of the FT-LDOS. In calculating the FT-LDOS at finite temperatures, we assume $\Delta_d(T) = \Delta_d(0) [1 - (T/T_c)]^{1/2}$, and the coherence factors change with temperature accordingly:

$$u_{\mathbf{k}}^2 = \frac{1}{2} \left[1 + \frac{\xi_{\mathbf{k}}}{E_{\mathbf{k}}} \right] = \frac{1}{2} \left[1 + \frac{\xi_{\mathbf{k}}}{\sqrt{\xi_{\mathbf{k}}^2 + \Delta_d^2(T)}} \right], \quad v_{\mathbf{k}}^2 = \frac{1}{2} \left[1 - \frac{\xi_{\mathbf{k}}}{E_{\mathbf{k}}} \right] = \frac{1}{2} \left[1 - \frac{\xi_{\mathbf{k}}}{\sqrt{\xi_{\mathbf{k}}^2 + \Delta_d^2(T)}} \right].$$

The thermal smearing of quasiparticle tunneling conductance (dI/dV) is obtained by using

$$(dI/dV) \propto \left| \int \rho_{\mathbf{q}}(E) (df/dE)|_{(E-eV)} dE \right|,$$

where $f(E)$ denotes the Fermi function. As shown in Fig. 6.10(a), for point impurity scattering, the q -values contribute to the FT-LDOS map become significantly extended and smeared at $T = 0.75T_c$. In the limit of $T \rightarrow T_c^-$, the FT-LDOS contains hardly any feature except for the weak residual modulations encoding normal-state Fermi surface information. In contrast, pinned SDW yields

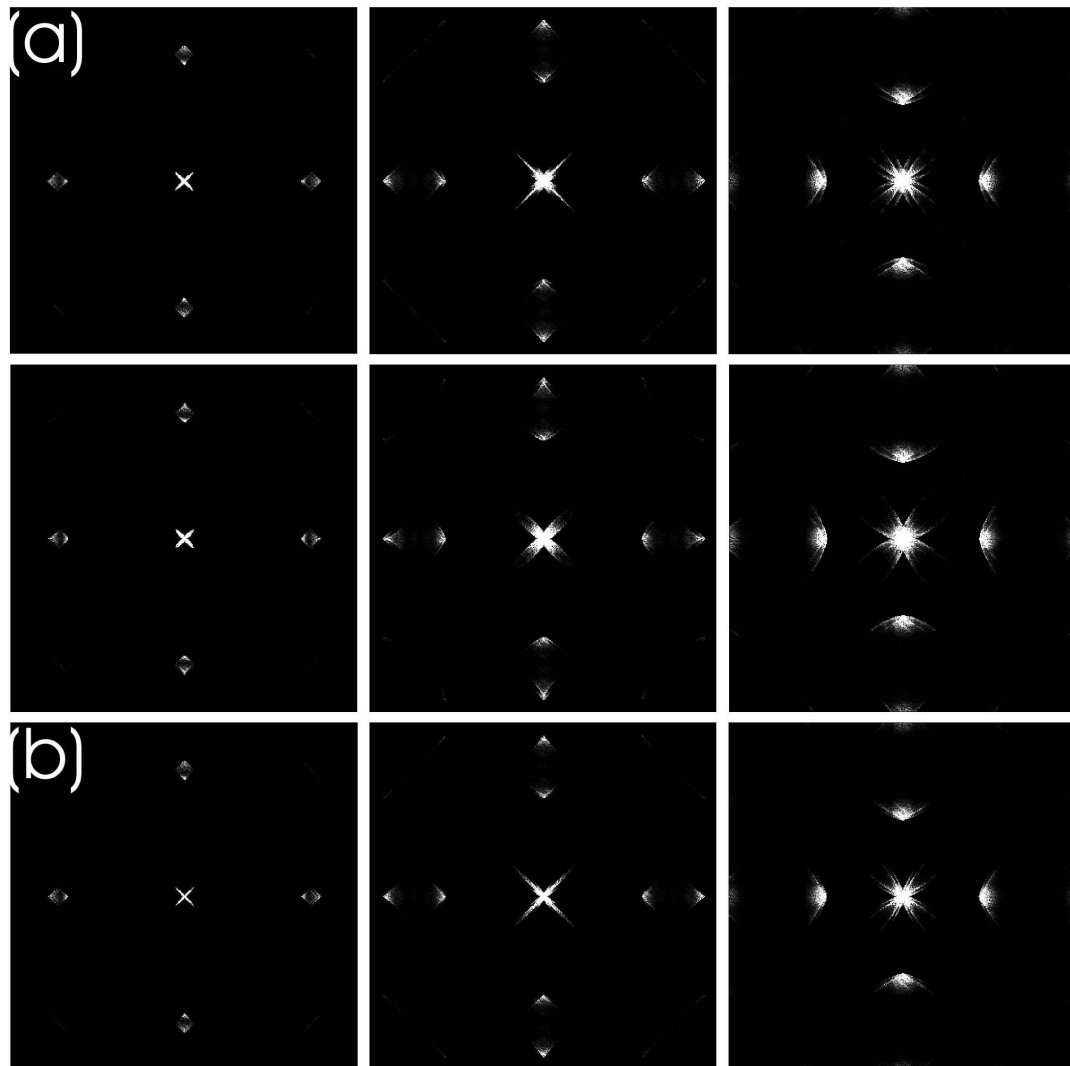


Figure 6.8: Energy-dependent FT-LDOS maps with randomly distributed pinned SDW using Eq. (6.10) and V_γ : (a) $\Delta_d = 40$ meV and $(\omega/\Delta_d) = \pm 0.15, \pm 0.45, \pm 75$, up and down from left to right; (b) $\Delta_d = 20$ meV and $(\omega/\Delta_d) = 0.15, 0.45, 0.75$, from left to right. The FT-LDOS does not exhibit discernible differences in the spectral characteristics except the total intensities if we simply replace V_γ by V_β and assume non-magnetic coherence factors in Eq. (6.10).

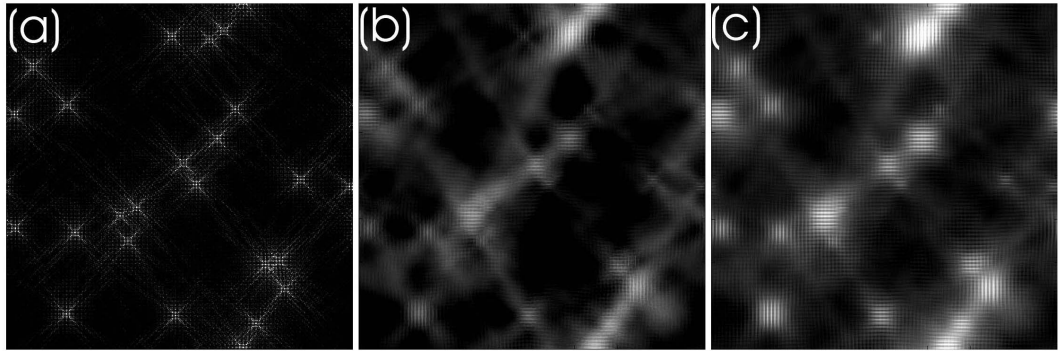


Figure 6.9: Real space quasiparticle LDOS for a (400×400) area at $T = 0$ due to scattering by (a) non-magnetic point impurities, (b) pinned CDW, and (c) pinned SDW, for $\Delta_d = 40$ meV and $\omega = 30$ meV.

strong intensities in the FT-LDOS map only at \mathbf{q}_A for $T \geq T_c$, as shown in Fig. 6.10(b). The overall energy dispersion due to pinned SDW is weaker than that due to point impurities, as shown in Fig. 6.10(c) for $|\mathbf{q}_A|$ versus V (biased voltage) at both $T = 0$ and $T = T_c$. In particular, we note that the dispersion is further reduced at T_c . These findings are consistent with recent experimental observation of 4 nearly non-dispersive Bragg peaks above T_c by Vershinin *et al.* [99].

6.3.3 Summary

The energy, momentum, and temperature dependence of our calculated FT-LDOS in Figs. 6.6–6.10 is supportive of spatially modulated collective modes being relevant low-energy excitations in cuprates besides quasiparticles. In the superconducting state, the high intensities of the Bragg peaks along the principle axes cannot be explained by point-impurity as the sole scattering source. Furthermore, we must invoke the presence of pinned collective modes in order to account for the observation of 4 non-dispersive Bragg peaks in the FT-LDOS map above T_c .

6.4 Conclusion

In summary, we have analyzed the effect of quantum phase fluctuations and competing orders on cuprate superconductivity. By incorporating both superconductivity (SC) and competing orders (CO) in the bare Green's function and quantum phase fluctuations in the self-energy, we obtain

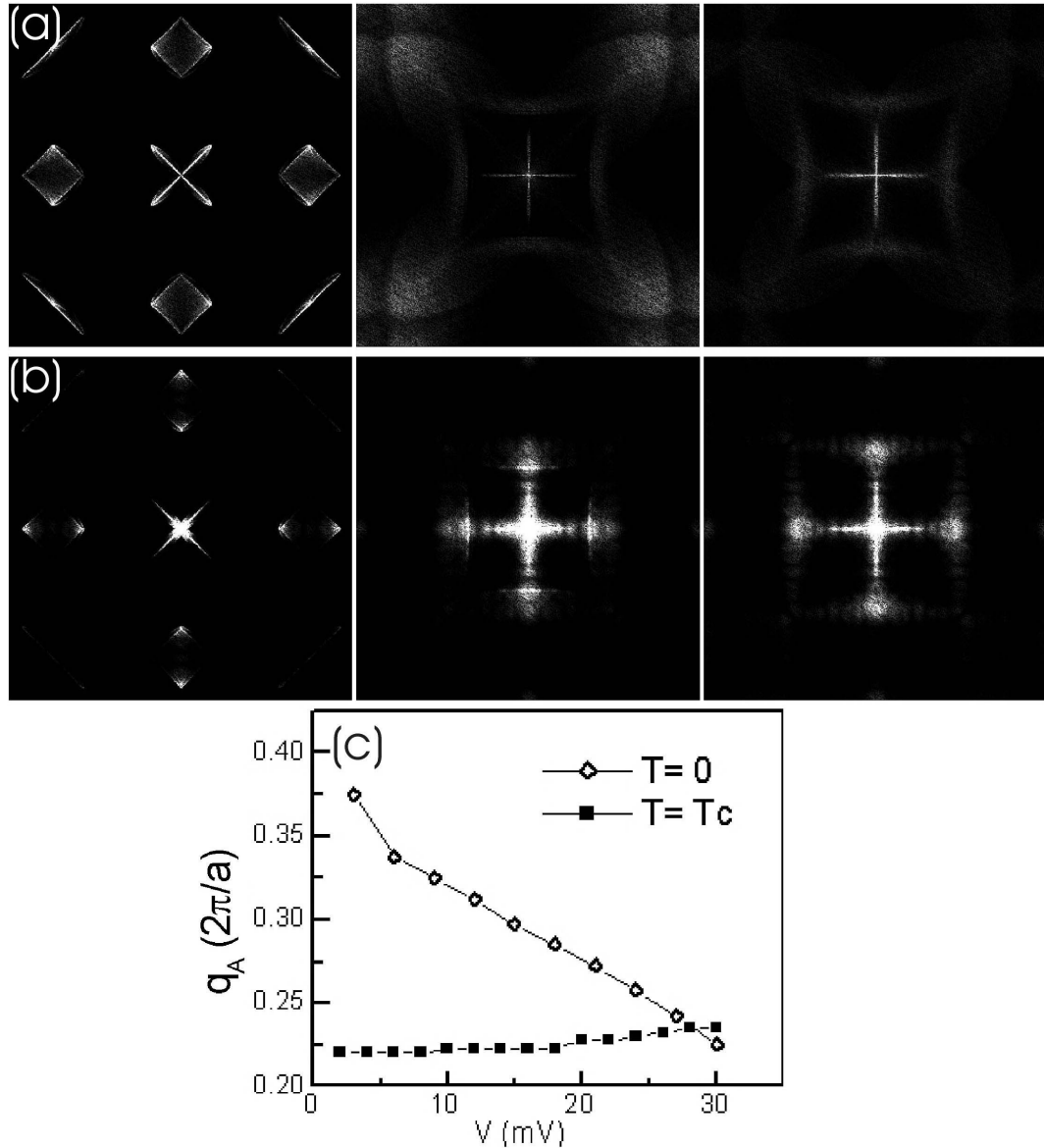


Figure 6.10: The FT-LDOS maps at $T = 0, 0.75T_c$ and T_c (from left to right) for (a) point impurities $V_\alpha(q)$ and (b) pinned SDW $V_\gamma(q)$. We assume $\Delta_d(T) = \Delta_d(0)[1 - (T/T_c)]^{1/2}$, $\Delta_d(0) = 40$ meV, tunneling biased voltage = 18 mV, and $T_c = 80$ K. Besides temperature-dependent coherence factors, the thermal smearing of quasiparticle tunneling conductance (dI/dV) is obtained by using $(dI/dV) \propto |\int \rho_{\mathbf{q}}(E)(df/dE)|_{(E-eV)} dE|$, where $f(E)$ denotes the Fermi function. (c) $|q_A|$ -vs.- V (biased voltage) dispersion relation for pinned SDW at $T = 0$ and T_c .

excess subgap quasiparticle density of states even for fully gapped SC and CO. Moreover, we find that the occurrence (absence) of pseudogap phenomena above T_c or H_{c2} in the hole (electron)-type cuprate superconductors may be a natural consequence of a competing order energy scale being larger (smaller) than the superconducting energy gap. We further investigate the modulations in the quasiparticle FT-LDOS of cuprates as a function of energy, momentum and temperature using the first-order T-matrix approximation in which the pinned CO is treated as a small perturbation. The latter approach is a special case of the self-consistent calculations and is justifiable when we consider the low-energy ($E < \Delta_d$) quasiparticle scattering in d -wave superconductors. Our results suggest that a full account for all aspects of experimental observation in hole-doped d -wave cuprates below T_c must include CO as relevant low-energy excitations besides Bogoliubov quasiparticles, and that only the pinned CO can account for the observed FT-LDOS above T_c .

Conclusion

High-temperature cuprate superconductors exhibit interesting coexisting phases originating from doping the strongly correlated Mott insulating parent compounds. We address how these competing orders contribute to the apparent non-universal phenomena among the electron- and hole-doped cuprates via the scanning tunneling spectroscopic studies of two representative cuprate families, the hole-doped YBCO and the electron-doped SLCO. We focus on the detailed analyses of the spectral evidence for the pairing symmetry and pseudogap phenomena of the two systems. The quasiparticle spectral features and the impurity scattering effects in the optimally doped and underdoped YBCO are consistent with a predominantly $d_{x^2-y^2}$ ($> 95\%$)-wave pairing, whereas those of the overdoped Ca-YBCO exhibit $d_{x^2-y^2}$ pairing with a significant s -component mixing ($> 30\%$), indicative of a change of ground state properties. While the satellite features in the tunneling spectra of YBCO above the spectral gap imply the existence of a competing order comparable in strength to superconductivity, the low-energy quasiparticle spectral characteristics are well-captured by the mean-field generalized BTK theory, indicating that quantum fluctuations are less significant in describing the low-energy physics of YBCO.

On the contrary, quasiparticle tunneling spectra of the n-type infinite-layer pure and impurity-doped SLCO support an isotropic s -wave pairing potential, and the spectral characteristics demonstrate the complete absence of satellite features in the superconducting state and the absence of pseudogap in the normal state. The emergence of the current-induced pseudogap suggest that, in SLCO, superconductivity coexists with a small competing order, which manifests itself only upon the suppression of superconductivity by external perturbations. The small amplitude of the competing order is consistent with the invisible pseudogap phenomena and satellite features in zero field.

The excess low-energy excitations revealed by tunneling spectroscopy deviate significantly from the mean-field prediction, which indicates the presence of strong quantum fluctuations as corroborated by the high-field vortex dynamic measurements.

To understand the distinctly different physical properties between the two types of cuprate, we consider a simple model of density waves as competing orders coexisting with superconductivity. By taking into account the varying proximity to quantum criticality and the varying degree of quantum fluctuations, numerical results of the theoretical proposal reproduce the excess subgap low-energy excitations of SLCO below T_c . Furthermore, we show that, by tuning the relative strength of competing orders and superconductivity, the proposal reconciles the occurrence of pseudogap phenomena above T_c or H_{c2} in the hole-doped cuprates with their absence in the electron-doped cuprates and thus provides a unified explanation for the seemingly non-universal behavior among the cuprate superconductors.

Appendix A

Blonder-Tinkham-Klapwijk Formalism

The Bogoliubov-de Gennes (BdG) equations generalize the BCS formalism to treat superconductors with spatially varying pairing strength $\Delta(x)$, chemical potential $\mu(x)$, and Hartree potential $V(x)$.

The excitation described by the operator $\gamma_{e,k+\uparrow}^\dagger = u_{k+} c_{k+\uparrow}^\dagger - v_{k+} S^\dagger c_{-k+\downarrow}$ with charge e is represented as a two-element column vector

$$\psi_k = \begin{bmatrix} u_k(x,t) \\ v_k(x,t) \end{bmatrix}, \quad (\text{A.1})$$

where u_k and v_k satisfy the equations

$$\begin{cases} \left[-\frac{\hbar^2}{2m} \nabla^2 + V(x) - \mu(x) \right] u_k(x,t) + \Delta(x) v_k(x,t) &= i\hbar \frac{\partial u_k(x,t)}{\partial t} \\ - \left[-\frac{\hbar^2}{2m} \nabla^2 + V(x) - \mu(x) \right] v_k(x,t) + \Delta^*(x) u_k(x,t) &= i\hbar \frac{\partial v_k(x,t)}{\partial t}. \end{cases} \quad (\text{A.2})$$

Deep in the superconducting electrode where $\Delta(x)$, $\mu(x)$, and $V(x)$ are constants, the solutions to (A.2) are time-independent plane waves. Let $u_k(x,t) = u_k e^{ikx-iE_k t/\hbar}$ and $v_k(x,t) = v_k e^{ikx-iE_k t/\hbar}$.

For $V(x) = 0$, (A.2) reads

$$\begin{cases} E_k u_k &= \left[-\frac{\hbar^2 k^2}{2m} - \mu \right] u_k + \Delta v_k \\ E_k v_k &= - \left[-\frac{\hbar^2 k^2}{2m} - \mu \right] v_k + \Delta u_k. \end{cases} \quad (\text{A.3})$$

For each energy E_k , there are 4 corresponding k values, $\pm k_{\pm}$, where

$$\frac{\hbar^2 k_{\pm}^2}{2m} = \mu \pm \sqrt{E_k^2 - |\Delta|^2}. \quad (\text{A.4})$$

In Eq. (A.4), k_+ labels the electron-like quasiparticles, and k_- labels the hole-like quasiparticles,

since

$$\begin{cases} u_{k_+}^2 &= \frac{1}{2}(1 + \frac{\sqrt{E_k^2 - \Delta^2}}{E_k}) \equiv u_{k0}^2 > \frac{1}{2} \\ v_{k_+}^2 &= \frac{1}{2}(1 - \frac{\sqrt{E_k^2 - \Delta^2}}{E_k}) \equiv v_{k0}^2 < \frac{1}{2} \end{cases} \quad (\text{A.5})$$

$$\begin{cases} u_{k_-}^2 &= \frac{1}{2}(1 - \frac{\sqrt{E_k^2 - \Delta^2}}{E_k}) = v_{k0}^2 < \frac{1}{2} \\ v_{k_-}^2 &= \frac{1}{2}(1 + \frac{\sqrt{E_k^2 - \Delta^2}}{E_k}) = u_{k0}^2 > \frac{1}{2}. \end{cases} \quad (\text{A.6})$$

The corresponding wavefunctions are

$$\psi_{\pm k_{\pm}}^S = \begin{bmatrix} u_{\pm k_{\pm}}(x) e^{-iE_k t/\hbar} \\ v_{\pm k_{\pm}}(x) e^{-iE_k t/\hbar} \end{bmatrix} = e^{\pm i k_{\pm} x} \begin{bmatrix} \sqrt{\frac{1}{2}(1 \pm \frac{\sqrt{E_k^2 - \Delta^2}}{E_k})} \\ \sqrt{\frac{1}{2}(1 \mp \frac{\sqrt{E_k^2 - \Delta^2}}{E_k})} \end{bmatrix} e^{-iE_k t/\hbar}. \quad (\text{A.7})$$

Similarly, in the normal electrode sufficiently far away from the interface, $V(x) = \Delta(x) = 0$, and $\frac{\hbar^2 k_{\pm}^2}{2m} = \mu \pm E_k$. The wavefunctions are

$$\psi_{\pm k_+}^N = \begin{bmatrix} u_{\pm k_+}(x) e^{-iE_k t/\hbar} \\ v_{\pm k_+}(x) e^{-iE_k t/\hbar} \end{bmatrix} = e^{\pm i k_+ x} \begin{bmatrix} 1 \\ 0 \end{bmatrix} e^{-iE_k t/\hbar} \quad (\text{electron-branch}) \quad (\text{A.8})$$

$$\psi_{\pm k_-}^N = \begin{bmatrix} u_{\pm k_-}(x) e^{-iE_k t/\hbar} \\ v_{\pm k_-}(x) e^{-iE_k t/\hbar} \end{bmatrix} = e^{\pm i k_- x} \begin{bmatrix} 0 \\ 1 \end{bmatrix} e^{-iE_k t/\hbar} \quad (\text{hole-branch}), \quad (\text{A.9})$$

where

$$E_k = \begin{cases} \frac{\hbar^2 k_{\pm}^2}{2m} - \mu, & (|k_{\pm}| > k_f) \\ \mu - \frac{\hbar^2 k_{\pm}^2}{2m}, & (|k_{\pm}| < k_f). \end{cases} \quad (\text{A.10})$$

To model the N-S interface, BTK follows Demers and Griffin [284, 285] and represents the interface by a repulsive delta-function potential $V(x) = H\delta(0)$. We restrict our discussion to elastic

tunneling processes. The constraint that, for an incident particle with a positive group velocity ($dE_k/\hbar dk$) only transmitted particles with positive group velocities and reflected ones with negative group velocities can be generated, narrows down the number of allowed processes to four [Fig. A.1]. Given an incident electron from the normal electrode, it can be Andreev-reflected as an hole, normal-reflected as an electron, transmitted as an electron-like quasiparticle, or transmitted as a hole-like quasiparticle. Therefore, for electrons traveling from N to S, the wavefunctions of the normal and superconducting electrodes consist of

$$\begin{aligned}\psi_{\text{inc}}^N &= \begin{bmatrix} 1 \\ 0 \end{bmatrix} e^{ik_+ x}, \\ \psi_{\text{refl}}^N &= a \begin{bmatrix} 0 \\ 1 \end{bmatrix} e^{ik_- x} + b \begin{bmatrix} 1 \\ 0 \end{bmatrix} e^{-ik_+ x}, \\ \psi_{\text{trans}}^S &= c \begin{bmatrix} u_{k0}^2 \\ v_{k0}^2 \end{bmatrix} e^{ik_+ x} + d \begin{bmatrix} v_{k0}^2 \\ u_{k0}^2 \end{bmatrix} e^{-ik_- x},\end{aligned}\quad (\text{A.11})$$

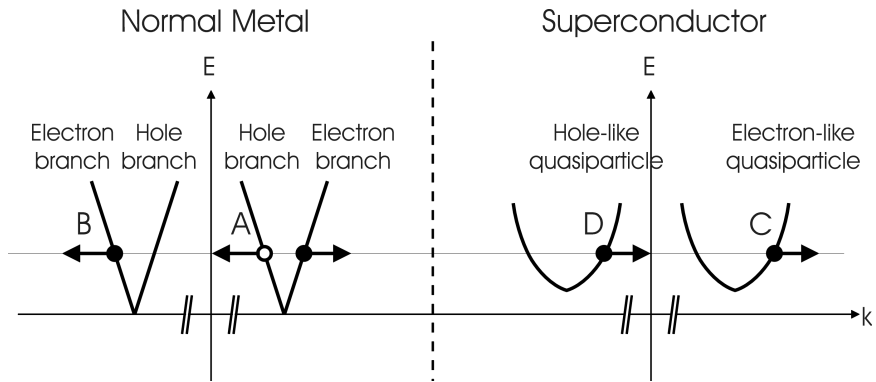


Figure A.1: Schematic diagram of energy vs. momentum at N-S interface modified from Fig. 4 in [122]. The open circles denote holes, and closed circles electrons, and the arrows point in the direction of the group velocity. The figure illustrates the four allowed processes for an incident electron at (0): the Andreev-reflected hole (A), the normal-reflected electron (B), the transmitted electron-like quasiparticle (C) and the transmitted hole-like quasiparticle (D).

Apply the following boundary conditions to solve for the prefactors $a - d$: (1) The wavefunction values are continuous at the interface $x = 0$: $\psi^N(0) = \psi^S(0) = \psi(0)$. (2) The derivative of the wavefunctions satisfies $\frac{\hbar}{2m} \frac{d\psi^S(0)}{dx} - \frac{\hbar}{2m} \frac{d\psi^N(0)}{dx} = H\psi(0)$. We obtain the probability current for

Andreev reflection $A(E)$ and that for normal reflection $B(E)$

$$\left. \begin{aligned} A(E) &= |a(E)|^2 = \frac{u_0^2 v_0^2}{\gamma^2} \\ B(E) &= |b(E)|^2 = \frac{(u_0^2 - v_0^2)^2 Z^2 (1+Z^2)}{\gamma^2} \end{aligned} \right\} (E > \Delta) \quad (\text{A.12})$$

$$\left. \begin{aligned} A(E) &= |a(E)|^2 = \frac{\Delta^2}{E^2 + (\Delta^2 - E^2)(1+2Z^2)^2} \\ B(E) &= |b(E)|^2 = 1 - A \end{aligned} \right\} (E < \Delta), \quad (\text{A.13})$$

where the dimensionless barrier height $Z = mH/\hbar^2 k_f$, $\gamma = u_0^2 + (u_0^2 - v_0^2)Z^2$, and the subscript k has been dropped.

Consequently, when a bias voltage is applied, the total current flowing from the normal to the superconducting electrode is

$$I(V) \propto N(0) \int_{-\infty}^{\infty} [f(E - eV) - f(E)] \left[1 + |a(E)|^2 - |b(E)|^2 \right] dE. \quad (\text{A.14})$$

Equation (A.14) shows that Andreev reflection increases the current transmission while the normal reflection reduces tunneling current. The zero-temperature differential tunneling conductance $\frac{dI}{dV}(V) \propto \left[1 + |a(E)|^2 - |b(E)|^2 \right]$ versus bias voltage V for a number of barrier heights Z is plotted in Fig. A.2. In the limit of zero-barrier height, the conductance within the superconducting gap nearly doubles because most of the incident electrons are Andreev-reflected and the transmitted electron pairs across the interface carries double the amount of charge of the incident electrons. On the contrary, in the high-barrier limit, the result given by the BTK formalism is essentially the same as that of the transfer Hamiltonian (*cf.* the conductance plot for $Z = 5.0$ in Fig. A.2).

We remark that the BTK theory is a mean-field theory, for it is based on the Bogoliubov-de Gennes equation. Therefore, residual interactions, such as quasiparticle scattering and quasiparticle coupling with the bosonic modes of the system, are not accounted for. The original BTK theory describes the tunneling process between a normal metal and a conventional *s*-wave superconductor. To investigate the consequence of unconventional pairing symmetries, in particular the *d*-wave pairing

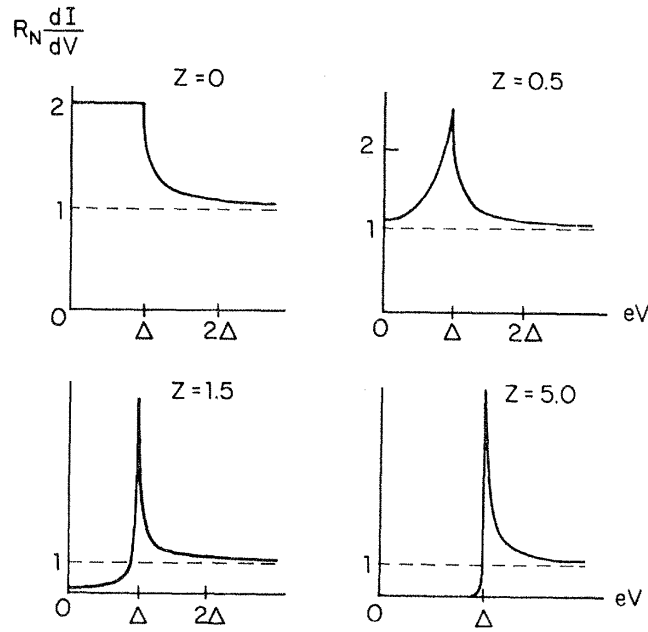


Figure A.2: Differential tunneling conductance vs. bias voltage for various normalized barrier heights Z at zero temperature. Figure taken from [122].

in the hole-doped cuprates, we resort to the generalized BTK formalism developed by Tanaka and Kashiwaya [124, 125] introduced in §2.2.1.

Appendix B

Tip Preparation, Piezo Calibration, and Thermal Drifting

B.1 Tip preparation

The STM tips for this thesis study were made of 15 mil Pt/Ir (.85/.15) wires. A number of tip preparation procedures were trialed to optimize the tip quality. Different tips suit different samples. To image a flat sample, such as that of a highly ordered pyrolytic graphite (HOPG), a simple mechanically cut Pt/Ir tip can produce good atomic images as long as the apex of the tip is free of undesirable atoms or molecules. Thus, before calibrating the piezo-tube scanner against HOPG, we cleaned the mechanically sheared tips in saturated hydrochloric acid (HCl) to remove unwanted material. A exemplary image of a tip after cleaning is shown in Fig. B.1(a).

To image rough surfaces, tips with a sharp and well-defined shape are preferable. Electrochemical etching has been proven to yield sharp tungsten tips. For inert metals, such as the Pt/Ir wires, well-controlled etching can be tricky. We had several trials on various etching methods, including the micro-polishing technique [286], before we successfully produced a sharp tip with good aspect ratio following the three-step recipe given by [287] (Fig. B.1(b)).

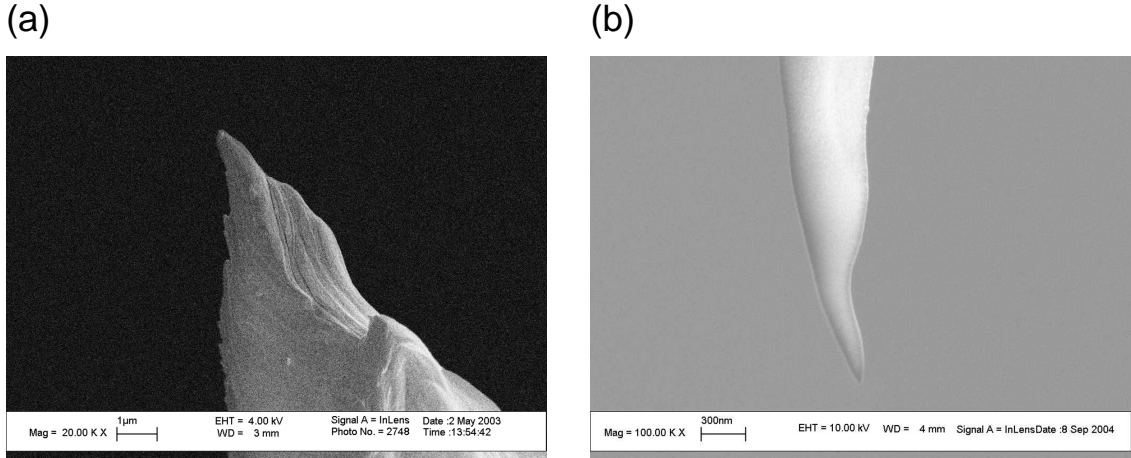


Figure B.1: (a) SEM image of a mechanically cut Pt/Ir tip after HCl cleaning. (b) SEM image of a tapered tip after the three-step electrochemical etching.

B.2 Piezo calibration and HOPG images

To calibrate the shear-piezos of the coarse approach motor, a Michelson interferometer is set up to measure both their polarization and displacement coefficient. We use type EBL #2 piezos purchased from Staveley sensor whose shear-coefficient ranges from 5 Å/V to 10 Å/V. Among all piezos, we pick those with similar coefficients ($\sim 7 - 8 \text{ \AA/V}$) for the STM head construction.

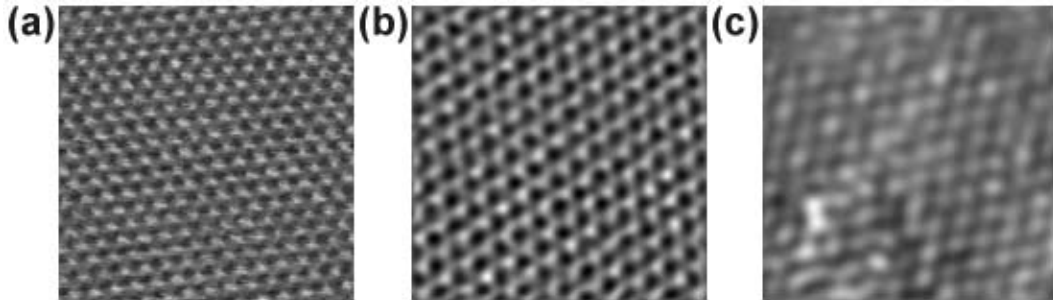


Figure B.2: (a) STM topographic images of highly ordered pyrolytic graphite at 295K ($37 \text{ \AA} \times 37 \text{ \AA}$), (b) at 77K ($29 \text{ \AA} \times 29 \text{ \AA}$), and (c) at 4.2K ($30 \text{ \AA} \times 30 \text{ \AA}$).

A 0.125" O.D., 0.6" long, 20 mil thick EBL#2 tube serves as our STM scanner. To calibrate the piezo-tube scanner, atomic-resolved images on HOPG are taken at 295K, 77K, and 4.2K (Fig. B.2). Knowing the carbon-carbon separation in graphite, we then extract the piezo coefficient for lateral scanning and plot them in Fig. B.3. Notice that the coefficient decreases linearly with decreasing temperatures. Therefore, at any intermediate temperatures, a simple linear interpolation is sufficient

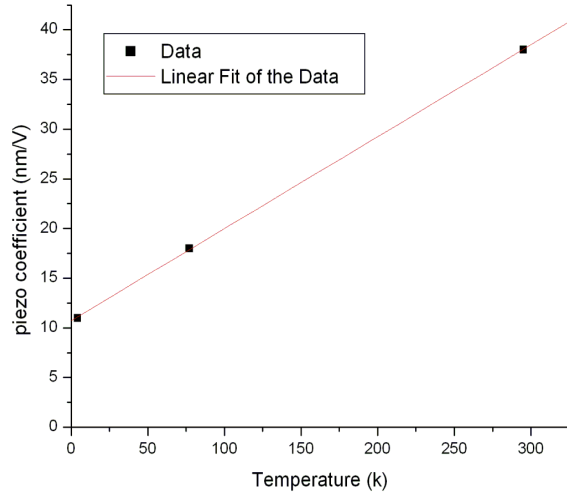


Figure B.3: The temperature dependence of the coefficient of the STM piezo-tube scanner is linear.

to rescale the STM images.

B.3 Thermal drifting calibration and gold images

It is preferable that we can return to the same location under study after withdrawing the tip for helium transfer. Figure B.4 demonstrates that the STM head is capable of retrieving the feature of interest upon re-approach. we find that the biggest source of drifting upon re-approach comes from the misalignment between the vertical axis of the tip holder and the normal direction of the sample holder. We reduce this problem by restricting the servo range to make sure that the piezo tube is under roughly the same amount of extension every time the tip reaches tunneling range. Figure B.4 shows that this trick helps to reduce the undesirable displacement to less than 10 Å.

In order to perform scanning tunneling spectroscopy at elevated temperatures, it is necessary to make sure that the thermal drifting of the tip relative to the sample can be compensated by the piezo tube scanner. We present the STM images of gold taken at the temperature range 10 – 35 K with a 5 K interval, which demonstrate that the STM head is capable of tracing the feature of interest upon the increase of temperatures [Fig. B.5]. The origin of the image taken at 15 K and 35 K have been shifted so as to demonstrate the ability of the STM to compensate for thermal drifting. The estimated drifting between 10 K and 15 K is $\sim (90 \text{ \AA}, 110 \text{ \AA})$, between 15

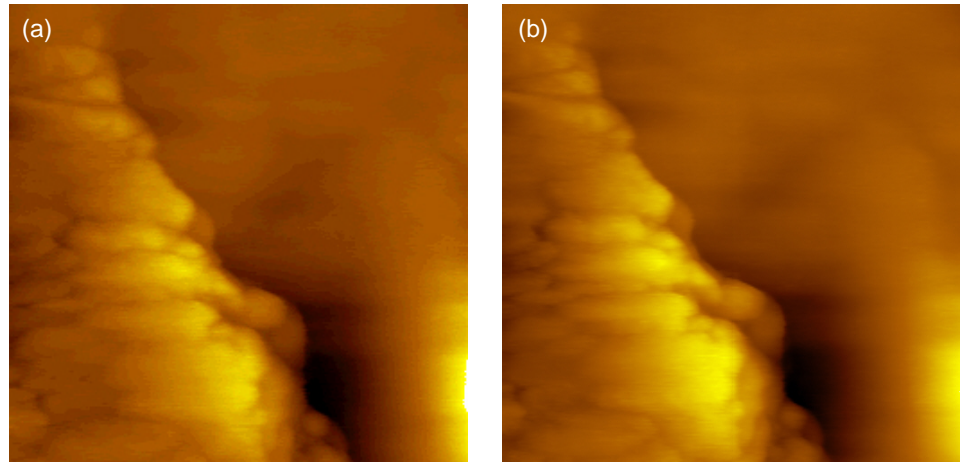


Figure B.4: Gold images ($200 \text{ \AA} \times 200 \text{ \AA}$) taken at 10 K (a) before and (b) after we withdraw the tip for $\sim 50 \mu\text{m}$ and re-approach. The displacement between frames is no more than 10 \AA .

K and 20 K $\sim (110 \text{ \AA}, 60 \text{ \AA})$, between 20 K and 25 K $\sim (155 \text{ \AA}, -65 \text{ \AA})$, between 25 K and 30 K $\sim (145 \text{ \AA}, -215 \text{ \AA})$, and between 30 K and 35 K $\sim (135 \text{ \AA}, -110 \text{ \AA})$, where (x, y) denotes the displacement along the x- and y-axes respectively. We note that the piezo coefficient of the tube scanner does not change much with the sample temperatures, indicative of good thermal isolation between the sample stage and the rest of the STM probe. During each temperature increment, the STM tip is retracted out of the tunneling range by $\sim 500 \text{ nm}$ before ramping up the temperature in order to avoid crashing the tip onto the sample. In general, each temperature increment takes about half 15 – 30 minutes to reach thermal equilibrium and to fully relax the piezo tube.

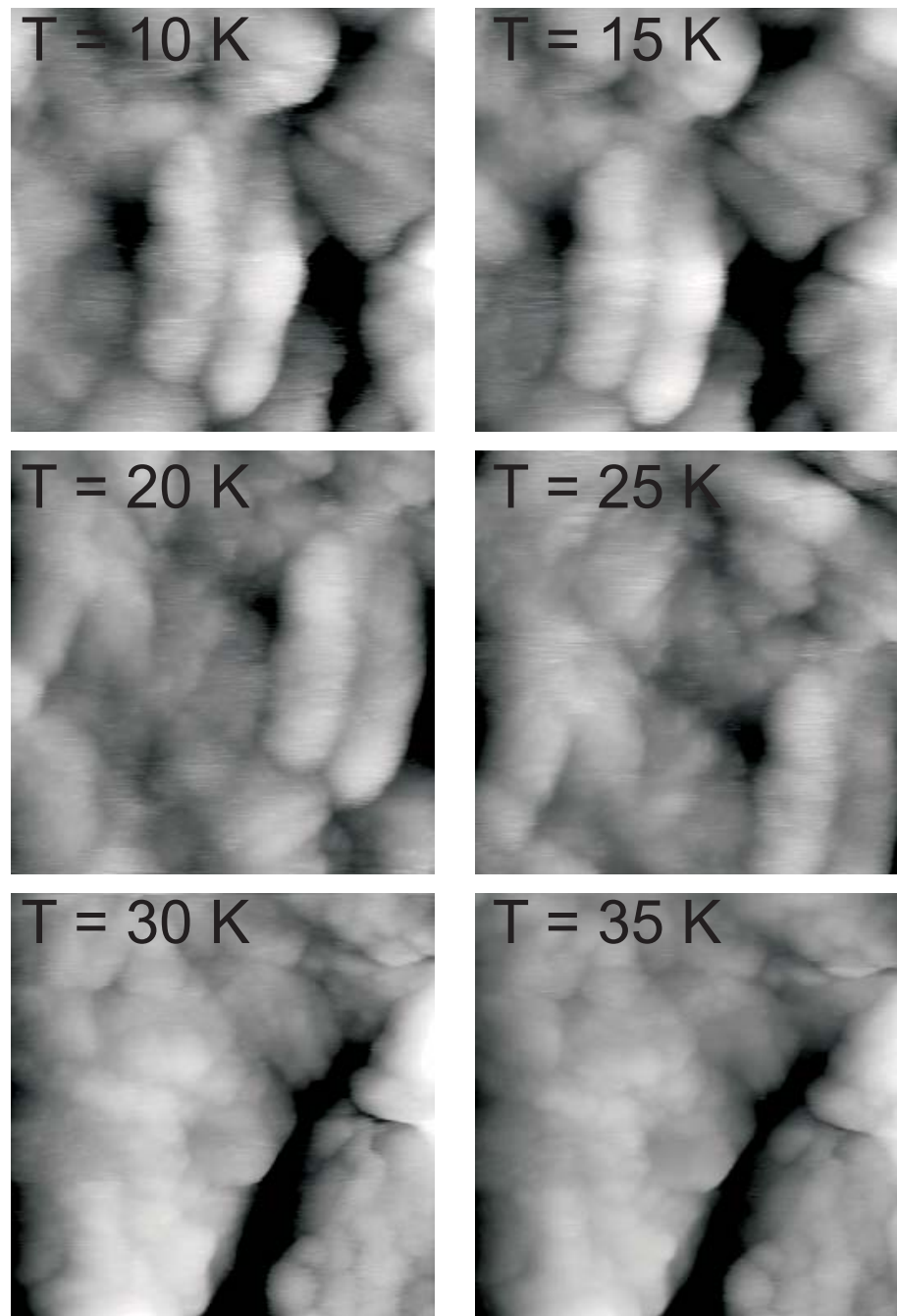


Figure B.5: STM topographic images of gold ($400 \text{ \AA} \times 400 \text{ \AA}$) taken at various temperatures to calibrate for thermal drifting.

Appendix C

Modeling the STS data in the presence of impurities

To extract information encoded in the the spatially resolved scanning tunneling spectroscopy, we recall that, for tunneling into a superconductor, the tunneling current is given by

$$I(V) \propto \int_{-\infty}^{\infty} d\xi |D|^2 [f(\xi) - f(\xi + eV)] N_S(\xi + eV), \quad (\text{C.1})$$

where $N_S(\xi)$ is the density of states of the superconducting electrode, and Δ is the energy gap of the superconductor. Assuming D varies slightly with energy, the tunneling conductance $\frac{dI}{dV}(\vec{r}, V)$ measures the local density of states (LDOS) directly in the low temperature limit:

$$\frac{dI}{dV}(\vec{r}, V) \propto |D|^2 N_S(\vec{r}, eV). \quad (\text{C.2})$$

The LDOS is related to the retarded Green's function through

$$N_S(\vec{r}, \omega) = -\frac{1}{\pi} \text{Im} [G^{\text{ret}}(\vec{r}, \vec{r}, \omega)], \quad (\text{C.3})$$

where $G^{\text{ret}}(\vec{r}, \vec{r}, \omega)$ is the Fourier transform of $G^{\text{ret}}(\vec{r}, \vec{r}, t)$. Let H be the total Hamiltonian of the system and $\psi_{\mathbf{q}}(\vec{r})$ the single-particle eigenstates. Then $G^{\text{ret}}(\vec{r}, \vec{r}, t)$ is defined as:

$$G^{\text{ret}}(\vec{r}, \vec{r}, t) = -i\theta(t) \sum_q \left\langle \vec{r} \left| e^{-i\hat{H}t/\hbar} \right| \psi_{\mathbf{q}} \right\rangle \langle \psi_{\mathbf{q}} | \vec{r} \rangle = -i\theta(t) \sum_q \left\langle \vec{r} \left| e^{-i\omega_q t/\hbar} \right| \psi_{\mathbf{q}} \right\rangle \langle \psi_{\mathbf{q}} | \vec{r} \rangle \quad (\text{C.4})$$

and thus

$$G^{\text{ret}}(\vec{r}, \vec{r}, \omega) = \sum_q \frac{|\psi_{\mathbf{q}}(\vec{r})|^2}{\omega - \omega_q + i\delta} \quad (\text{C.5})$$

$$N_S(\vec{r}, \omega) = \sum_q |\psi_{\mathbf{q}}(\vec{r})|^2 \delta(\omega - \omega_q). \quad (\text{C.6})$$

In a perfect crystal where the $\psi_q(\vec{r})$'s are Bloch states, $|\psi_q(\vec{r})|^2 = 1$, and the LDOS $N_s(\vec{r}, \omega)$ depends only on the energy ω . When there are impurities or defects in the system, scattering off the impurities results in the interference between the outgoing and the backscattered waves, which leads to spatial modulations in the LDOS and the topography map.

The first STM images of the wavelike features on the metallic surfaces were carried out in Ei- gler's group at IBM [130]. In cuprate superconductors, the analysis of the energy-dependent Fourier transformed LDOS (FT-LDOS) of $\text{Bi}_2\text{Sr}_2\text{CaCu}_2\text{O}_{8+\delta}$ single crystals [95, 97, 272, 99] based on the quasiparticle interference model has yielded segments of the Fermi surface and energy gap $\Delta_d(\vec{k})$ consistent with results of the angular-resolved photoemission spectroscopy [95, 97, 274]. Furthermore, detailed examination of the FT-LDOS has revealed a charge order coexisting with superconductivity below T_c in $\text{Bi}_2\text{Sr}_2\text{CaCu}_2\text{O}_{8+\delta}$ [257, 258, 256, 101, 73], and the charge order was demonstrated to survive well above T_c [99], as shown in §6.3. In the following paragraph, the theoretical formalism for computing the LDOS is summarized.

In the presence of an impurity potential \mathcal{H}_{imp} , we use perturbation expansion to calculate the LDOS, *i.e.*, the imaginary part of the retarded Green's function. Define \mathcal{G} as the total thermal Green's function associated with the total Hamiltonian $\mathcal{H} = \mathcal{H}_0 + \mathcal{H}_{\text{imp}}$ and \mathcal{G}_0 the unperturbed thermal Green's function associated with the Hamiltonian of a perfect crystal \mathcal{H}_0 . Dyson's equation reads, in the operator notation,

$$\mathcal{G} = \mathcal{G}_0 + \mathcal{G}_0 \mathcal{H}_{\text{imp}} \mathcal{G} = \mathcal{G}_0 + \mathcal{G}_0 \mathcal{H}_{\text{imp}} \mathcal{G}_0 + \mathcal{G}_0 \mathcal{H}_{\text{imp}} \mathcal{G}_0 \mathcal{H}_{\text{imp}} \mathcal{G}_0 + \dots \quad (\text{C.7})$$

(C.7) can be further rearranged into

$$\mathcal{G} = \mathcal{G}_0 + \mathcal{G}_0(\mathcal{H}_{\text{imp}} + \mathcal{G}_0\mathcal{H}_{\text{imp}}\mathcal{G}_0 + \dots)\mathcal{G}_0 = \mathcal{G}_0 + \mathcal{G}_0T\mathcal{G}_0. \quad (\text{C.8})$$

When the impurity potential is weak, the first order T -matrix expansion is generally sufficient. Thus,

$$\mathcal{G} \approx \mathcal{G}_0 + \mathcal{G}_0\mathcal{H}_{\text{imp}}\mathcal{G}_0, \quad (\text{C.9})$$

which is the familiar Born approximation. In the real-space representation, (C.9) reads

$$\mathcal{G}(\vec{r}, \vec{r}, i\omega) \approx \mathcal{G}_0(\vec{r}, \vec{r}, i\omega) + \int d^2\vec{r}_1 \mathcal{G}_0(\vec{r}, \vec{r}_1, i\omega) \mathcal{H}_{\text{imp}}(\vec{r}_1) \mathcal{G}_0(\vec{r}_1, \vec{r}, i\omega), \quad (\text{C.10})$$

where $i\omega$ is the Matsubara frequency. The thermal Green's function $\mathcal{G}(\vec{r}, \vec{r}, i\omega)$ is analytically continued in the upper half of the complex ω plane ($i\omega \rightarrow \omega + i\delta$) to determine the finite-temperature retarded Green's function $\mathcal{G}^{\text{ret}}(\vec{r}, \vec{r}, \omega)$. The Fourier transform of $\mathcal{G}^{\text{ret}}(\vec{r}, \vec{r}, \omega)$ in turn gives us the energy-dependent FT-LDOS.

At very low temperatures, we can avoid the use of thermal Green's functions and derive similar results from Dyson's equation of the zero-temperature Green's function $G(\vec{r}, \vec{r}, \omega)$. The imaginary part of $G(\vec{r}, \vec{r}, \omega)$ is related to that of the zero-temperature retarded Green's function $G^{\text{ret}}(\vec{r}, \vec{r}, \omega)$ by

$$\text{Im} [G(\vec{r}, \vec{r}, \omega)] = \text{sgn}(\omega) \text{ Im} [G^{\text{ret}}(\vec{r}, \vec{r}, \omega)], \quad (\text{C.11})$$

from which the FT-LDOS in §6.3 is deduced.

Bibliography

- [1] D. Vaknin, S. K. Sinha, D. E. Moncton, D. C. Johnston, J. M. Newsam, C. R. Safinya, and J. H. E. King, Phys. Rev. Lett. **58**, 2802 (1987).
- [2] M. A. Kastner, R. J. Birgeneau, G. Shirane, and Y. Endoh, Rev. Mod. Phys. **70**, 897 (1998), and references therein.
- [3] T. Thio, T. R. Thurston, N. W. Preyer, P. J. Picone, M. A. Kastner, H. P. Jenssen, D. R. Gabbe, C. Y. Chen, and R. J. Birgeneau, Phys. Rev. B **38**, 905 (1988).
- [4] T. Yildirim, A. B. Harris, O. Entin-Wohlman, and A. Aharony, Phys. Rev. Lett. **72**, 3710 (1994), and references therein.
- [5] H.-Q. Ding, Phys. Rev. Lett. **68**, 1927 (1992), and references therein.
- [6] D. J. VanHarlingen, Rev. Mod. Phys. **67**, 515 (1995).
- [7] C. C. Tsuei and J. R. Kirtley, Rev. Mod. Phys. **72**, 969 (2000), and references therein.
- [8] N.-C. Yeh, C.-T. Chen, G. Hammerl, J. Mannhart, A. Schmehl, C. W. Schneider, R. R. Schulz, S. Tajima, K. Yoshida, D. Garrigus, et al., Phys. Rev. Lett. **87**, 087003 (2001).
- [9] T. Timusk and B. Statt, Rep. Prog. Phys. **62**, 61 (1999), and references therein.
- [10] C. M. Varma, P. B. Littlewood, S. Schmitt-Rink, E. Abrahams, and A. E. Ruckenstein, Phys. Rev. Lett. **63**, 1996 (1989).
- [11] C. M. Varma, Phys. Rep. **361**, 267 (2002), and references therein.

- [12] M. Matsuda, Y. Endoh, , K. Yamada, H. Kojima, I. Tanaka, R. J. Birgeneau, M. A. Kastner, and G. Shirane, Phys. Rev. B **45**, 12548 (1992).
- [13] B. Keimer, A. Aharony, A. Auerbach, R. J. Birgeneau, A. Cassanho, Y. Endoh, R. W. Erwin, M. A. Kastner, and G. Shirane, Phys. Rev. B **45**, 7430 (1992).
- [14] B. Keimer, N. Belk, R. J. Birgeneau, A. Cassanho, C. Y. Chen, M. Greven, M. A. Kastner, A. Aharony, Y. E. R. W. Erwin, and G. Shirane, Phys. Rev. B **46**, 14034 (1992).
- [15] A. Aharony, R. J. Birgeneau, A. Coniglio, M. A. Kastner, and H. E. Stanley, Phys. Rev. Lett. **60**, 1330 (1988).
- [16] S. Kleefisch, B. Welter, A. Marx, L. Alff, R. Gross, and M. Naito, Phys. Rev. B **63**, 100507 (2001).
- [17] A. Biswas, P. Fournier, V. N. Smolyaninova, R. C. Budhani, J. S. Higgins, and R. L. Greene, Phys. Rev. B **64**, 104519 (2001).
- [18] L. Alff, Y. Krockenberger, B. Welter, M. Schonecke, R. Gross, D. Manske, and M. Naito, Nature **422**, 698 (2003).
- [19] V. J. Emery, Phys. Rev. Lett. **58**, 2794 (1987).
- [20] P. W. Anderson, Science **235**, 1196 (1987).
- [21] F. C. Zhang and T. M. Rice, Phys. Rev. B **37**, 3759 (1988).
- [22] T. Tohyama and S. Maekawa, Phys. Rev B **49**, 3596 (1994).
- [23] T. Tohyama, Phys. Rev B **70**, 174517 (2004), and references therein.
- [24] R. J. Gooding, K. J. E. Vos, and P. W. Leung, Phys. Rev B **50**, 12866 (1994).
- [25] M. S. Hybertsen, E. Stechel, M. Schuter, and D. Jennison, Phys. Rev B **41**, 11068 (1990).
- [26] O. K. Andersen, S. Y. Savrasov, O. Jepsen, and A. I. Liechtenstein, J. Low Temp. Phys. **105**, 285 (1996).

- [27] E. Pavarini, I. Dasgupta, T. Saha-Dasgupta, O. Jepsen, and O. K. Andersen, Phys. Rev. Lett. **87**, 047003 (2001).
- [28] M. Vojta, Y. Zhang, and S. Sachdev, Phys. Rev. B **62**, 6721 (2000).
- [29] M. Takigawa, P. C. Hammel, R. H. Heffner, and Z. Fisk, Phys. Rev. B **39**, 7371 (1989).
- [30] S. E. Barrett, D. J. Durand, C. H. Pennington, C. P. Slichter, T. A. Friedmann, J. P. Rice, and D. M. Ginsberg, Phys. Rev. B **41**, 6283 (1990).
- [31] H. Ding, M. R. Norman, J. C. Campuzano, M. Randeria, A. F. Bellman, T. Yokoya, T. Takahashi, T. Mochiku, and K. Kadokawa, Phys. Rev. B **54**, 9678 (1996).
- [32] L. Taillefer, B. Lussier, R. Gagnon, K. Behnia, and H. Aubin, Phys. Rev. Lett. **79**, 483 (1997).
- [33] W. N. Hardy, D. A. Bonn, D. C. Morgan, R. Liang, and K. Zhang, Phys. Rev. Lett. **70**, 3999 (1993).
- [34] D. A. Wollman, D. J. V. Harlingen, W. C. Lee, D. M. Ginsberg, and A. J. Leggett, Phys. Rev. Lett. **71**, 2134 (1993).
- [35] D. A. Wollman, D. J. V. Harlingen, J. Giapintzakis, and D. M. Ginsberg, Phys. Rev. Lett. **74**, 797 (1995).
- [36] C. C. Tsuei, J. R. Kirtley, C. C. Chi, L. S. Yu-Jahnes, A. Gupta, T. Shaw, J. Z. Sun, and M. B. Ketchen, Phys. Rev. Lett. **73**, 593 (1994).
- [37] D. H. Lu, D. L. Feng, N. P. Armitage, K. M. Shen, A. Damascelli, C. Kim, F. Ronning, Z. X. Shen, D. A. Bonn, R. Liang, et al., Phys. Rev. Lett. **86**, 4370 (2001).
- [38] T. Masui, M. Limonov, H. Uchiyama, S. Lee, S. Tajima, and A. Yamanaka, Phys. Rev. B **68**, 060506 (2003).
- [39] L. V. Gasparov, P. Lemmens, N. N. Kolesnikov, and G. Gntherodt, Phys. Rev. B **58**, 11753 (1998).

- [40] L. Alff, A. Beck, R. Gross, A. Marx, S. Kleefisch, T. Bauch, H. Sato, M. Naito, and G. Koren, Phys. Rev. B **58**, 11197 (1998).
- [41] L. Shan, Y. Huang, H. Gao, Y. Wang, S. L. Li, P. C. Dai, F. Zhou, J. W. Xiong, W. X. Ti, and H. H. Wen, Phys. Rev. B **72**, 144506 (2005).
- [42] B. Stadlober, G. Krug, R. Nemetschek, R. Hackl, J. L. Cobb, and J. T. Markert, Phys. Rev. Lett. **74**, 4911 (1995).
- [43] C. C. Tsuei and J. R. Kirtley, Phys. Rev. Lett. **85**, 182 (2000).
- [44] N. P. Armitage, D. H. Lu, D. L. Feng, C. Kim, A. Damascelli, K. M. Shen, F. Ronning, Z.-X. Shen, Y. Onose, Y. Taguchi, et al., Phys. Rev. Lett. **86**, 1126 (2001).
- [45] H. Matsui, K. Terashima, T. Sato, T. Takahashi, M. Fujita, and K. Yamada, Phys. Rev. Lett. **95**, 017003 (2005).
- [46] G. Blumberg1, A. Koitzsch, A. Gozar, B. S. Dennis, C. A. Kendziora, P. Fournier, and R. L. Greene, Phys. Rev. Lett. **88**, 107002 (2002).
- [47] A. Biswas, P. Fournier, M. M. Qazilbash, V. N. Smolyaninova, H. Balci1, and R. L. Greene, Phys. Rev. Lett. **88**, 207004 (2002).
- [48] J. A. Skinta, M.-S. Kim, T. R. Lemberger, T. Greibe, and M. Naito, Phys. Rev. Lett. **88**, 207005 (2002).
- [49] C.-T. Chen, P. Seneor, N.-C. Yeh, R. P. Vasquez, L. D. Bell, C. U. Jung, J. Y. Kim, M. S. Park, H. J. Kim, and S. I. Lee, Phys. Rev. Lett. **88**, 227002 (2002).
- [50] N.-C. Yeh, Bulletin of Associations of Asia Pacific Physical Societies **12**, 2 (2002), cond-mat/0210656, and references therein.
- [51] J. W. W. Warren, R. E. Walstedt, G. F. Brennert, R. J. Cava, R. Tycko, R. F. Bell, and G. Dabbagh, Phys. Rev. Lett. **62**, 1193 (1989).
- [52] H. Alloul, T. Ohno, and P. Mendels, Phys. Rev. Lett. **63**, 1700 (1989).

- [53] C. C. Homes, T. Timusk, R. Liang, D. A. Bonn, and W. N. Hardy, Phys. Rev. Lett. **71**, 1645 (1993).
- [54] C. Renner, B. Revaz, J. Y. Genoud, K. Kadowaki, and O. Fischer, Phys. Rev. Lett. **80**, 149 (1998).
- [55] D. H., Y. T., J. C. Campuzano, T. T., R. M., M. R. Norman, M. T., K. K., and G. J., Nature **382**, 51 (1996).
- [56] A. G. Loeser, Z.-X. Shen, D. S. Dessau, D. S. Marshall, C. H. Park, F. P., and K. A., Science **273**, 325 (1996).
- [57] N. Miyakawa1, J. F. Zasadzinski, L. Ozyuzer, P. Guptasarma, D. G. Hinks, C. Kendziora, and K. E. Gray, Phys. Rev. Lett. **83**, 1018 (1999).
- [58] P. A. Lee, N. Nagaosa, and X. G. Wen, Rev. Mod. Phys **78**, 17 (2006), and references therein.
- [59] I. Affleck and J. B. Marston, Phys. Rev. B **37**, 3774 (1988).
- [60] I. Affleck, Z. Zou, T. Hsu, and P. W. Anderson, Phys. Rev. B **38**, 745 (1988).
- [61] A. Rigamonti, R. Borsa, and P. Carretta, Rep. Prog. Phys. **61**, 1367 (1998).
- [62] S. Sachdev, Rev. Mod. Phys **75**, 913 (2003).
- [63] V. J. Emery and S. Kivelson, Nature **374**, 434 (1995).
- [64] Y. Wang, Z. A. Xu, T. Kakeshita, S. Uchida, S. Ono, Y. Ando, and N. P. Ong, Phys. Rev. B **64**, 0224519 (2001).
- [65] Y. Wang, L. Li, and N. P. Ong, Phys. Rev. B **73**, 024510 (2006).
- [66] F. Rullier-Albenque, R. Tourbot, H. Alloul, P. Lejay, D. Colson, and A. Forget, Phys. Rev. Lett. **96**, 067002 (2006).
- [67] S. H. Pan, J. P. O'Neal, R. L. Badzey, C. Chamon, H. Ding, J. R. Engelbrecht, Z. Wang, H. Eisaki, S. Uchida, A. K. Gupta, et al., Nature **413**, 282 (2001).

- [68] K. M. Lang, V. Madhavan, J. E. Hoffman, E. W. Hudson, H. Eisaki, S. Uchida, and J. C. Davis, *Nature* **415**, 412 (2002).
- [69] V. M. Krasnov, A. Yurgens, D. Winkler, P. Delsing, and T. Claeson, *Phys. Rev. Lett.* **84**, 5860 (2000).
- [70] T. Sato, T. Yokoya, Y. Naitoh, T. Takahashi, K. Yamada, and Y. Endoh, *Phys. Rev. Lett.* **83**, 2254 (1999).
- [71] J. L. Tallon and J. W. Loram, *Physica C* **349**, 53 (2001), and references therein.
- [72] V. J. Emery, S. A. Kivelson, and J. M. Tranquada, *Proc. Natl. Acad. Sci.* **96**, 8814 (1999).
- [73] S. A. Kivelson, I. Bindloss, E. Fradkin, V. Oganesyan, J. M. Tranquada, A. Kapitulnik, and C. Howald, *Rev. Mod. Phys.* **75**, 1201 (1997).
- [74] C. M. Varma, *Phys. Rev. B* **55**, 14554 (1997), and references therein.
- [75] S. Chakravarty, R. B. Laughlin, D. K. Morr, and C. Nayak, *Phys. Rev. B* **63**, 094503 (2001).
- [76] E. Demler, W. Hanke, and S. C. Zhang, *Rev. Mod. Phys.* **76**, 909 (2004).
- [77] N. P. Armitage, D. H. Lu, C. Kim, A. Damascelli, K. M. Shen, F. Ronning, D. L. Feng, P. Bogdanov, Z.-X. Shen, Y. Onose, et al., *Phys. Rev. Lett.* **87**, 147003 (2001).
- [78] H. Balci, C. P. Hill, M. M. Qazilbash, and R. L. Greene, *Phys. Rev. B* **68**, 054520 (2003).
- [79] G. V. M. Williams, R. Dupree, A. Howes, S. Krmer, H. J. Trodahl, C. U. Jung, M.-S. Park, and S.-I. Lee, *Phys. Rev. B* **65**, 224520 (2002).
- [80] S. Wakimoto, G. Shirane, Y. Endoh, K. Hirota, S. Ueki, K. Yamada, R. J. Birgeneau, M. A. Kastner, Y. S. Lee, P. M. Gehring, et al., *Phys. Rev. B* **60**, 769 (1999).
- [81] Y. S. Lee, R. J. Birgeneau, M. A. Kastner, Y. Endoh, S. Wakimoto, K. Yamada, R. W. Erwin, S.-H. Lee, and G. Shirane, *Phys. Rev. B* **60**, 3643 (1999).
- [82] S. Wakimoto, R. J. Birgeneau, Y. S. Lee, and G. Shirane, *Phys. Rev. B* **63**, 172501 (2001).

- [83] P. C. Dai, H. A. Mook, R. D. Hunt, and F. Dogan, Phys. Rev. B **63**, 054525 (2001).
- [84] J. M. Tranquada, B. J. Sternlieb, J. D. Axe, Y. Nakamura, and S. Uchida, Nature **375**, 561 (1995).
- [85] M. Fujita, H. Goka, K. Yamada, J. M. Tranquada, and L. P. Regnault, Phys. Rev. B **70**, 104517 (2004).
- [86] K. Yamada, C. H. Lee, K. Kurahashi, J. Wada, S. Wakimoto, S. Ueki, H. Kimura, Y. Endoh, S. Hosoya, G. Shirane, et al., Phys. Rev. B **57**, 6165 (1998).
- [87] C. Stock, W. J. L. Buyers, Z. Tun, R. Liang, D. Bonn, W. N. Hardy, and L. Tailleurfer, Phys. Rev. B **66**, 024505 (2004).
- [88] C. Stock, W. J. L. Buyers, R. A. Cowley, P. S. Clegg, R. Coldea, C. D. Frost, R. Liang, D. Peets, D. Bonn, W. N. Hardy, et al., Phys. Rev. B **71**, 024522 (2005).
- [89] K. Yamada, K. Kurahashi, T. Uefuji, M. Fujita, S. Park, S.-H. Lee, and Y. Endoh, Phys. Rev. Lett. **90**, 137004 (2003).
- [90] M. Fujita, M. Matsuda, S. Katano, and K. Yamada, Phys. Rev. Lett. **93**, 147003 (2004).
- [91] H. J. Kang, P. Dai, H. A. Mook, D. N. Argyriou, V. Sikolenko, J. W. Lynn, Y. Kurita, S. Komiya, and Y. Ando, Phys. Rev. B **71**, 214512 (2005).
- [92] S. D. Wilson, S. Li, H. Woo, P. Dai, H. A. Mook, C. D. Frost, S. Komiya, and Y. Ando, Phys. Rev. Lett. **96**, 157001 (2006).
- [93] H. A. Mook, P. C. Dai, and F. Dogan, Phys. Rev. B **64**, 012502 (2001).
- [94] H. A. Mook, P. C. Dai, S. M. Hayden, A. Hiess, S.-H. Lee, and F. Dogan, Phys. Rev. B **69**, 134509 (2004), and references therein.
- [95] J. E. Hoffman, K. McElroy, D. H. Lee, K. M. Lang, H. Eisaki, S. Uchida, and J. C. Davis, Science **297**, 1148 (2002).

- [96] J. E. Hoffman, E. W. Hudson, K. M. Lang, V. Madhavan, H. Eisaki, S. Uchida, and J. C. Davis, *Science* **295**, 466 (2002).
- [97] K. McElroy, R. W. Simmonds, J. E. Hoffman, D. H. Lee, J. Orenstein, H. Eisaki, S. Uchida, and J. C. Davis, *Nature* **422**, 592 (2003).
- [98] K. McElroy, D. H. Lee, J. E. Hoffman, K. M. Lang, J. Lee, E. W. Hudson, H. Eisaki, S. Uchida, and J. C. Davis, *Phys. Rev. Lett.* **94**, 197005 (2005).
- [99] M. Vershinin, S. Misra, S. Ono, Y. Abe, Y. Ando, and A. Yazdani, *Science* **303**, 1995 (2004).
- [100] T. Hanaguri, C. Lupien, Y. Kohsaka, D.-H. Lee, M. Azuma, M. Takano, H. Takagi, and J. Davis, *Nature* **430**, 1001 (2004).
- [101] D. Podolsky, E. Demler, K. Damle, and B. I. Halperin, *Phys. Rev. B* **67**, 094514 (2003).
- [102] T. Senthil and M. P. A. Fisher, *Phys. Rev. B* **62**, 7850 (2000).
- [103] T. Senthil and P. A. Lee, *Phys. Rev. B* **71**, 174515 (2005).
- [104] T. Senthil and M. P. A. Fisher, *Phys. Rev. Lett.* **86**, 292 (2001).
- [105] D. A. Bonn, J. C. Wynn, B. W. Gardner, Y.-J. Lin, R. Liang, W. N. Hardy, J. R. Kirtley, and K. A. Moler, *Nature* **414**, 867 (2001).
- [106] J. C. Wynn, D. A. Bonn, B. W. Gardner, Y.-J. Lin, R. Liang, W. N. Hardy, J. R. Kirtley, and K. A. Moler, *Phys. Rev. Lett.* **87**, 197002 (2001).
- [107] V. S. Zapf, N.-C. Yeh, A. D. Beyer, C. R. Hughes, C. H. Mielke, N. Harrison, M. S. Park, K. H. Kim, and S.-I. Lee., *Phys. Rev. B* **71**, 134526 (2005).
- [108] L. Esaki, *Phys. Rev.* **109**, 603 (1958).
- [109] I. Giaever, *Science* **183**, 1253 (1974).
- [110] I. Giaever, *Phys. Rev. Lett.* **5**, 147 (1960).
- [111] J. Bardeen, *Phys. Rev. Lett.* **6**, 57 (1961).

- [112] M. H. Cohen, L. M. Falicov, and J. C. Phillips, Phys. Rev. Lett. **8**, 316 (1962).
- [113] G. D. Mahan, *Many-Particle Physics* (Kluwer Academic/Platinum Publishers, New York, 2000).
- [114] J. R. Schrieffer, D. J. Scalapino, and J. W. Wilkins, Phys. Rev. Lett **10**, 336 (1963).
- [115] C. B. Duke, *Tunneling in Solids* (Academic Press, New York and London, 1969).
- [116] W. A. Harrison, Phys. Rev. **123**, 85 (1961).
- [117] E. L. Wolf, *Principles of Electron Tunneling Spectroscopy* (Oxford University Press, USA, 1985).
- [118] R. E. Prange, Phys. Rev. **131**, 1083 (1963).
- [119] T. E. Feuchtwang, Phys. Rev. B **10**, 4121 (1974).
- [120] B. D. Josephson, Phys. Lett. **1**, 251 (1962).
- [121] A. F. Andreev, Soviet Physics JETP **19**, 1228 (1964).
- [122] G. E. Blonder, M. Tinkham, and T. M. Klapwijk, Phys. Rev. B **25**, 4515 (1982).
- [123] C. R. Hu, Phys. Rev. Lett. **72**, 1526 (1994).
- [124] Y. Tanaka and S. Kashiwaya, Phys. Rev. Lett. **74**, 3451 (1995).
- [125] S. Kashiwaya and Y. Tanaka, Phys. Rev. B **53**, 2667 (1996).
- [126] S. Kashiwaya and Y. Tanaka, Rep. Prog. Phys. **63**, 1641 (2000).
- [127] C. Bruder, Phys. Rev. B **41**, 4017 (1990).
- [128] G. Binnig and H. Rohrer, Surf. Sci. **126**, 236 (1983).
- [129] K. Takayanagi, Y. Tanishiro, M. Takahashi, and S. Takahashi, Surf. Sci. **164**, 367 (1985).
- [130] M. F. Crommie, C. Lutz, and D. Eigler, Science **262**, 218 (1993).

- [131] H. C. Manoharan, C. Lutz, and D. Eigler, *Nature* **403**, 512 (2000).
- [132] V. Madhavan, W. Chen, T. Jamneala, M. F. Crommie, and N. S. Wingreen, *Science* **280**, 567 (1998).
- [133] H. F. Hess, R. B. Robinson, R. C. Dynes, J. J. M. Valles, and J. V. Waszczak, *Phys. Rev. Lett.* **62**, 214 (1989).
- [134] H. F. Hess, R. B. Robinson, and J. V. Waszczak, *Phys. Rev. Lett.* **64**, 2711 (1990).
- [135] C. Renner, G. Aeppli, B.-G. Kim, Y.-A. Soh, and S.-W. Cheong, *Nature* **416**, 518 (2002).
- [136] G. Binnig and H. Rohrer, *Rev. Mod. Phys.* **59**, 615 (1987).
- [137] G. Binnig, H. Rohrer, C. Gerber, and E. Weibel, *Appl. Phys. Lett.* **40**, 178 (1982).
- [138] C. J. Chen, *Introduction to Scanning Tunneling Microscopy* (Oxford University Press, New York, 1993).
- [139] R. Wiesendanger, *Scanning Probe Microscopy and Spectroscopy: Methods and Applications* (Cambridge University Press, 1994).
- [140] S. H. Pan, International Patent Publication Number WO 93/19494 (1993).
- [141] S. H. Pan, E. W. Hudson, and J. C. Davis, *Rev. Sci. Instrum.* **70**, 1459 (1999).
- [142] J. M. Martinis, M. H. Devoret, and J. Clarke, *Phys. Rev. B* **35**, 4682 (1987).
- [143] I. B. Spielman, Ph.D. thesis, California Institute of Technology (2004), appendix E.
- [144] M. Covington, M. Aprili, E. Paraoanu, L. H. Greene, F. Xu, J. Zhu, and C. A. Mirkin, *Phys. Rev. Lett.* **79**, 277 (1997).
- [145] G. Deutscher, *Rev. Mod. Phys.* **77**, 109 (2005), and references therein.
- [146] S. I. Vedeneev and D. K. Maude, *Phys. Rev. B* **72**, 144519 (2005).
- [147] Y. DeWilde, N. Miyakawa, P. Guptasarma, M. Iavarone, L. Ozyuzer, J. F. Zasadzinski, P. Romano, D. G. Hinks, C. Kendziora, G. W. Crabtree, et al., *Phys. Rev. Lett.* **80**, 157 (1998).

- [148] N. Miyakawa, P. Guptasarma, J. F. Zasadzinski, D. G. Hinks, and K. E. Gray, Phys. Rev. Lett. **80**, 157 (1998).
- [149] J. F. Zasadzinski, L. Ozyuzer, N. Miyakawa, K. E. Gray, D. G. Hinks, and C. Kendziora, Phys. Rev. Lett. **87**, 067005 (2001).
- [150] M. Suzuki, T. Watanabe, and A. Matsuda, Phys. Rev. Lett. **82**, 5361 (1999).
- [151] V. M. Krasnov, A. E. Kovalev, A. Yurgens, and D. Winkler, Phys. Rev. Lett. **86**, 2657 (2001).
- [152] M. Suzuki and T. Watanabe, Phys. Rev. Lett. **85**, 4787 (2000).
- [153] V. N. Zavaritsky, Phys. Rev. B **72**, 094503 (2005).
- [154] V. M. Krasnov, M. Sandberg, and I. Zogaj, Phys. Rev. Lett. **94**, 077003 (2005).
- [155] K. Anagawa, Y. Yamada, T. Shibauchi, M. Suzuki, and T. Watanabe, Appl. Phys. Lett. **83**, 2381 (2003).
- [156] A. Yurgens, D. Winkler, T. Claeson, S. Ono, and Y. Ando, Phys. Rev. Lett. **92**, 259702 (2004).
- [157] M.-H. Bae, J.-H. Choi, and H.-J. Lee, Appl. Phys. Lett. **86**, 232502 (2005).
- [158] A. Damascelli, Z. Hussain, and Z.-X. Shen, Rev. Mod. Phys. **75**, 403 (2003), and references therein.
- [159] M. R. Norman, H. Ding, J. C. Campuzano, T. Takeuchi, M. Randeria, T. Yokoya, and T. Takahashi, Phys. Rev. Lett. **79**, 3506 (1997), and references therein.
- [160] X. J. Zhou, T. Yoshida, D.-H. Lee, W. L. Yang, V. Brouet, F. Zhou, W. X. Ti, J. Xiong, Z. X. Zhao, T. Sasagawa, et al., Phys. Rev. Lett. **92**, 187001 (2004).
- [161] L. P. Regnault, P. Bourges, and P. Burlet, in *Neutron Scattering in Layered Copper-Oxide Superconductors* (Kluwer Academic Publishers, 1998), pp. 85–134.
- [162] S. M. Hayden, in *Neutron Scattering in Layered Copper-Oxide Superconductors* (Kluwer Academic Publishers, 1998), pp. 140–161.

- [163] J. M. Tranquada, in *Neutron Scattering in Layered Copper-Oxide Superconductors* (Kluwer Academic Publishers, 1998), pp. 225–260.
- [164] L. Pintschovius and W. Reichardt, in *Neutron Scattering in Layered Copper-Oxide Superconductors* (Kluwer Academic Publishers, 1998), pp. 165–223.
- [165] S. Martin, A. T. Fiory, R. M. Fleming, L. F. Schneemeyer, and J. V. Waszczak, Phys. Rev. B **41**, 846 (1990).
- [166] J. W. Loram, A. Mirza, J. M. Wade, J. R. Cooper, and W. Y. Liang, Physica C **235-240, Part I**, 134 (1994).
- [167] A. V. Puchkov, D. N. Basov, and T. T., J. Phys.: Condens. Matter **8**, 10049 (1996).
- [168] S. Sachdev, *Quantum Phase Transition* (Cambridge University Press, USA, 1999).
- [169] S. Sachdev, Science **288**, 475 (2000).
- [170] C. M. Varma, Phys. Rev. Lett. **83**, 3538 (1999).
- [171] T. Valla, A. V. Fedorov, P. D. Johnson, B. O. W. amd S. L. Hulbert, Q. Li, G. D. Gu, and N. Koshizuka, Science **285**, 2110 (1999).
- [172] T. Valla, A. V. Fedorov, P. D. Johnson, Q. Li, G. D. Gu, and N. Koshizuka, Phys. Rev. Lett. **85**, 828 (2000).
- [173] M. Vojta and S. Sachdev, Phys. Rev. Lett. **83**, 3916 (1999).
- [174] J. Y. T. Wei, N. C. Yeh, D. F. Garrigus, and M. Strasik, Phys. Rev. Lett. **81**, 2542 (1998).
- [175] G. Deutscher, Nature **397**, 410 (1999).
- [176] M. Sutherland, D. G. Hawthorn, R. W. Hill, F. Ronning, S. Wakimoto, H. Zhang, C. Proust, E. Boaknin, C. Lupien, L. Taillefer, et al., Phys. Rev. B **67**, 174520 (2003).
- [177] C. W. Schneider, R. R. Schulz, B. Goetz, A. Schmehl, H. Bielefeldt, H. Hilgenkamp, and J. Mannhart, Appl. Phys. Lett. **75**, 850 (1999).

- [178] R. P. Vasquez, B. D. hunt, and M. C. Foote, *Appl. Phys. Lett.* **54**, 2373 (1989).
- [179] R. P. Vasquez, M. C. Foote, and B. D. Hunt, *Appl. Phys. Lett.* **55**, 1801 (1989).
- [180] D. J. Derro, E. W. Hudson, K. M. Lang, S. H. Pan, J. C. Davis, J. T. Markert, and A. L. D. Lozanne, *Phys. Rev. Lett.* **86**, 097002 (2001).
- [181] H. L. Edwards, J. T. Markert, and A. L. DeLozanne, *Phys. Rev. Lett.* **69**, 2967 (1992).
- [182] H. L. Edwards, A. L. Barr, J. T. Markert, and A. L. DeLozanne, *Phys. Rev. Lett.* **73**, 1154 (1994).
- [183] S. H. Pan, E. W. Hudson, A. K. Gupta, K. W. Ng, H. Eisaki, S. Uchida, and J. C. Davis, *Phys. Rev. Lett.* **85**, 1536 (2000).
- [184] N.-C. Yeh, J. Y. T. Wei, C.-T. Chen, W. D. Si, and X. X. Xi, *Physica C* **341**, 1639 (2000).
- [185] C. Kendziora, R. J. Kelley, and M. Onellion, *Phys. Rev. Lett.* **77**, 727 (1996).
- [186] J. R. Kirtley, C. C. Tsuei, A. Ariando, C. J. M. Verwijs, S. Harkema, and H. Hilgenkamp, *Nature Phys.* **2**, 190 (2006).
- [187] C. C. Tsuei, J. R. Kirtley, G. Hammerl, J. Mannhart, H. Raffy, and Z. Z. Li, *Phys. Rev. Lett.* **93**, 187004 (2004).
- [188] S. Chakravarty and H. Y. Kee, *Phys. Rev. B* **61**, 14821 (2000).
- [189] I. Affleck, Z. Zou, T. Hsu, and P. W. Anderson, *Phys. Rev. B* **38**, 745 (1988).
- [190] J. Kishine, P. A. Lee, and X.-G. Wen, *Phys. Rev. Lett.* **86**, 5188 (2001).
- [191] A. Kaminski, S. Rosenkranz, H. M. Fretwell, J. C. Campuzano, Z. Li, H. Raffy, W. G. Cullen, H. You, C. G. Olson, C. M. Varma, et al., *Nature* **416**, 610 (2002).
- [192] J. Bobroff, H. Alloul, S. Ouazi, P. Mendels, A. Mahajan, N. Blanchard, G. Collin, V. Guillen, and J.-F. Marucco, *Phys. Rev. Lett.* **89**, 157002 (2002).
- [193] J. W. Loram, J. L. Tallon, and W. Y. Liang, *Phys. Rev. B* **69**, 060502 (2004).

- [194] K. McElroy, J. Lee, J. A. Slezak, D. H. Lee, H. Eisaki, S. Uchida, and J. C. Davis, Science **309**, 1048 (2005).
- [195] M.-H. Bae, J.-H. Choi, and H.-J. Lee, cond-mat/0512664.
- [196] M. R. Presland, J. L. Tallon, R. G. Buckley, R. S. Liu, and N. E. Flower, Physica C **176**, 95 (1991).
- [197] R. Liang, D. Bonn, and W. N. Hardy, cond-mat/0510674.
- [198] M. R. Norman and H. Ding, Phys. Rev. B **57**, R11089 (1998), and references therein.
- [199] A. V. Fedorov, T. Valla, P. D. Johnson, Q. Li, G. D. Gu, and N. Koshizuka, Phys. Rev. Lett. **82**, 2179 (1999).
- [200] Z. X. Shen and D. S. Dessau, Phys. Rep. **253**, 2 (1995), and references therein.
- [201] N.-C. Yeh, C.-T. Chen, V. S. Zapf, A. D. Beyer, C. R. Hughes, M.-S. Park, K.-H. Kim, and S.-I. Lee, Chinese Journal of Physics **43**, 505 (2005).
- [202] N.-C. Yeh, C.-T. Chen, V. S. Zapf, A. D. Beyer, and C. R. Hughes, Int'l. Journal of Modern Physics B **19**, 285 (2005).
- [203] A. V. Chubukov, N. Gemelke, and A. Abanov, Phys. Rev. B **61**, R6467 (2000), and references therein.
- [204] C. L. Wu, C. Y. Mou, and D. Chang, Phys. Rev. B **63**, 172503 (2001).
- [205] A. V. Chubukov and M. R. Norman, Phys. Rev. B **70**, 174505 (2004).
- [206] A. Lanzara1, P. V. Bogdanov, X. J. Zhou, S. A. Kellar, D. L. Feng, E. D. Lu, T. Yoshida, H. Eisaki, A. Fujimori, K. Kishio, et al., Nature **412**, 510 (2001).
- [207] M. R. Norman and C. Pepin, Rep. Prog. Phys **66**, 1547 (2003), and references therein.
- [208] T. P. Devereaux, T. Cuk, Z.-X. Shen, and N. Nagaosa, Phys. Rev. Lett. **93**, 117004 (2004).

- [209] R. J. McQueeney, Y. Petrov, T. Egami, M. Yethiraj, G. Shirane, and Y. Endoh, Phys. Rev. Lett. **82**, 628 (1999).
- [210] K. Terashima, H. Matsui, D. Hashimoto, T. Sato, T. Takahashi, H. Ding, T. Yamamoto, and K. Kadowaki, Nature Physics **2**, 27 (2006), and references therein.
- [211] P. W. Anderson, J. Phys. Chem. Sol. **11**, 26 (1959).
- [212] A. A. Abrikosov and L. P. Gov'kov, Soviet Phys. JETP **12**, 1243 (1961).
- [213] M. E. Flatte and J. M. Byers, Phys. Rev. Lett. **80**, 4546 (1998).
- [214] A. V. Balatsky, M. I. Salkola, and A. Rosengren, Phys. Rev. B **51**, 15547 (1995).
- [215] H. Alloul, P. Mendels, H. Casalta, J. F. Marucco, and J. Arabskiand, Phys. Rev. Lett. **67**, 3140 (1991).
- [216] H. F. Fong, P. Bourges, Y. Sidis, L. P. Regnault, A. Ivanov, G. D. Gu, N. Koshizuka, and B. Keimer, Nature **398**, 588 (1999).
- [217] Y. Sidis, P. Bourges, H. F. Fong, B. Keimer, L. P. Regnault, J. Bossy, A. Ivanov, B. Hennion, P. Gautier-Picard, G. Collin, et al., Phys. Rev. Lett. **84**, 5900 (2000).
- [218] W. A. MacFarlane, J. Bobroff, H. Alloul, P. Mendels, N. Blanchard, G. Collin, and J. F. Marucco, Phys. Rev. Lett. **85**, 1108 (2000).
- [219] M. Vojta and R. Bulla, Phys. Rev. B **65**, 014511 (2001).
- [220] S. H. Pan, E. W. Hudson, K. M. Lang, H. Eisaki, S. Uchida, and J. C. Davis, Nature **403**, 746 (2000).
- [221] M. I. Salkola and J. R. Schrieffer, Phys. Rev. B **58**, R5952 (1998).
- [222] A. Polkovnikov, S. Sachdev, and M. Vojta, Phys. Rev. Lett. **86**, 296 (2001).
- [223] S. Haas and K. Maki, Phys. Rev. Lett. **85**, 2172 (2000).
- [224] J. Orenstein and A. J. Millis, Science **288**, 468 (2000), and references therein.

- [225] L. Alff, S. M. and S. Kleefisch, U. Schoop, A. Marx, H. Sato, M. Naito, and R. Gross, Phys. Rev. Lett. **83**, 2644 (1999).
- [226] B. Chesca, M. Seifried, T. Dahm, N. Schopoh, D. Koelle, R. Kleiner, and A. Tsukada, Phys. Rev. B **71**, 104504 (2005).
- [227] J. A. Skinta, M.-S. Kim, T. R. Lemberger, T. Greibe, and M. Naito, Phys. Rev. Lett. **88**, 207003 (2002).
- [228] M.-S. Kim, J. A. Skinta, T. R. Lemberger, A. Tsukada, and M. Naito, Phys. Rev. Lett. **91**, 087001 (2003).
- [229] R. Prozorov, R. W. Giannetta, P. Fournier, and R. L. Greene, Phys. Rev. Lett. **85**, 3700 (2000).
- [230] A. Snezhko, R. Prozorov, D. D. Lawrie, R. W. Giannetta, J. Gauthier, J. Renaud, and P. Fournier, Phys. Rev. Lett. **92**, 157005 (2005).
- [231] J. M. Tranquada, H. Woo, T. G. Perring, H. Goka, G. D. Gu, G. Xu, M. Fujita, and K. Yamada, Nature **429**, 534 (2004).
- [232] S. M. Hayden, H. A. Mook, P. Dai, T. G. Perring, and F. Doan, Nature **429**, 531 (2004).
- [233] H. J. Kang, P. C. Dai, J. W. Lynn, M. Matsuura, J. R. Thompson, S. C. Zhang, D. N. Argyriou, Y. Onose, and Y. Tokura, Nature **423**, 522 (2003).
- [234] P. C. Dai, H. J. Kang, H. A. Mook, M. Matsuura, J. W. Lynn, Y. Kurita, S. Komiya, and Y. Ando, Phys. Rev. B **71**, 100502 (2005).
- [235] P. Richard, G. Riou, I. Hetel, S. Jandl, M. Poirier, and P. Fournier, Phys. Rev. B **70**, 064513 (2004).
- [236] P. K. Mang, S. Larochelle, A. Mehta, O. P. Vajk, A. S. Erickson, L. Lu, W. J. L. Buyers, A. F. Marshall, K. Prokes, and M. Greven, Phys. Rev. B **70**, 094507 (2004).

- [237] J. D. Jorgensen, P. G. Radaelli, D. G. Hinks, J. L. Wagner, S. Kikkawa, G. Er, and F. Kanamaru, Phys. Rev. B **47**, 14654 (1993).
- [238] T. Siegrist, S. M. Zahurak, D. W. Murphy, and R. S. Roth, Nature **334**, 231 (1988).
- [239] M. G. Smith, A. Manthiram, J. Zhou, J. B. Goodenough, and J. T. Markert, Nature **351**, 549 (1991).
- [240] C. U. Jung, J. Y. Kim, M.-S. Park, M.-S. Kim, H.-J. Kim, S. Y. Lee, and S.-I. Lee, Phys. Rev. B **65**, 172501 (2002).
- [241] M.-S. Kim, C. Jung, J. Kim, J.-H. Choi, and S.-I. Lee, Solid State Commun. **123**, 17 (2002).
- [242] R. P. Vasquez, C. U. Jung, J. Y. Kim, M.-S. Park, H.-J. Kim, and S.-I. Lee, J. Phys.: Condens. Matter **13**, 7977 (2001).
- [243] C. U. Jung, J. Y. Kim, M.-S. Kim, M.-S. Park, H.-J. Kim, Y. Yao, S. Y. Lee, and S.-I. Lee, Physica C **366**, 299 (2002).
- [244] A. Yazdani, B. A. Jones, C. P. Lutz, M. F. Crommie, and D. M. Eigler, Science **275**, 1767 (1997).
- [245] H. Shiba, Prog. Theor. Phys. **40**, 435 (1968).
- [246] M. E. Flatte, Phys. Rev. B **61**, 14920 (2000).
- [247] K. Ishida, Y. Kitaoka, K. Yamazoe, K. Asayama, and Y. Yamada, Phys. Rev. Lett. **76**, 531 (1996).
- [248] E. W. Hudson, K. M. Lang, V. Madhavan, S. H. Pan, H. Eisaki, S. Uchida, and J. C. Davis, Nature **411**, 920 (2001).
- [249] E. Demler, S. Sachdev, and Y. Zhang, Phys. Rev. Lett. **87**, 067202 (2001).
- [250] Y. Zhang, E. Demler, and S. Sachdev, Phys. Rev. B **66**, 094501 (2002).
- [251] S. A. Kivelson, D.-H. Lee, E. Fradkin, and V. Oganesyan, Phys. Rev. B **66**, 1445016 (2002).

- [252] D. H. Lee, Phys. Rev. Lett. **88**, 227003 (2000).
- [253] N.-C. Yeh, W. Jiang, D. S. Reed, U. Kriplani, and F. Holtzberg, Phys. Rev. B **47**, 6146 (1993).
- [254] J. L. O'Brien, H. Nakagawa, A. S. Dzurak, R. G. Clark, B. E. Kane, N. E. Lumpkin, R. P. Starrett, N. Muira, E. E. Mitchell, J. D. Goettie, et al., Phys. Rev. B **61**, 1584 (2000).
- [255] Y. Chen, H.-Y. Chen, and C. S. Ting, Phys. Rev. B **66**, 104501 (2002).
- [256] A. Polkovnikov, M. Vojta, and S. Sachdev, Phys. Rev. B **65**, 220509 (2002).
- [257] C.-T. Chen and N.-C. Yeh, Phys. Rev. B **68**, 220505(R) (2003), and references therein.
- [258] A. Polkovnikov, S. Sachdev, and M. Vojta, Physica C **388**, 19 (2003).
- [259] K. Park and S. Sachdev, Phys. Rev. B **64**, 184519 (2001).
- [260] J.-X. Zhu, I. Martin, and A. R. Bishop, Phys. Rev. Lett. **89**, 067003 (2002).
- [261] S. Misra, M. Vershinin, P. Phillips, and A. Yazdani, Phys. Rev. B **70**, 220503 (2004).
- [262] H.-J. Kwon and A. T. Dorsey, Phys. Rev. B **59**, 6438 (1999).
- [263] H.-J. Kwon, Phys. Rev. B **59**, 13600 (1999).
- [264] H.-J. Kwon and A. T. Dorsey, Phys. Rev. Lett. **86**, 3875 (2001).
- [265] C. N. Yang and S. C. Zhang, Mod. Phys. Lett. B **4**, 759 (1990).
- [266] G. S. Grest, K. Levin, and M. J. Nass, Phys. Rev. B **25**, 4562 (1982).
- [267] C. Berthier, P. Molinie, and D. Jerome, Solid State Comm. **18**, 1393 (1976).
- [268] S. C. Zhang, Science **275**, 1089 (1997).
- [269] R. Shankar, Rev. Mod. Phys. **66**, 129 (1994).
- [270] A. D. Beyer, C. T. Chen, and N.-C. Yeh, in preparation.
- [271] Y. Y. Wang, N. P. Ong, Z. A. Xu, T. Kakeshita, S. Uchida, D. A. Bonn, R. Liang, and W. N. Hardy, Phys. Rev. Lett. **88**, 257003 (2002).

- [272] C. Howald, H. Eisaki, N. Kaneko, M. Greven, and A. Kapitulnik, Phys. Rev. B **67**, 014533 (2003).
- [273] D. G. Zhang and C. S. Ting, Phys. Rev. B **67**, 100506 (2003).
- [274] Q. H. Wang and D. H. Lee, Phys. Rev. B **67**, 020511 (2003).
- [275] L. Capriotti, D. J. Scalapino, and R. D. Sedgewick, Phys. Rev. B **68**, 014508 (2003).
- [276] C. Howald, P. Fournier, and A. Kapitulnik, Phys. Rev. B **64**, 100504 (2001).
- [277] N.-C. Yeh and C.-T. Chen, Int. J. Mod. Phys. B **17**, 3575 (2003).
- [278] H. F. Fong, P. Bourges, Y. Sidis, L. P. Regnault, A. Ivanov, G. D. Gu, N. Koshizuka, and B. Keimer, Nature **398**, 588 (1999).
- [279] B. Lake, G. Aeppli, K. N. Clausen, D. F. McMorrow, K. Lefmann, N. E. Hussey, N. Mangkorntong, M. Nohara, H. Takagi, T. E. Mason, et al., Science **291**, 1759 (2001).
- [280] H. A. Mook, P. C. Dai, and F. Dogan, Phys. Rev. Lett. **88**, 097004 (2002).
- [281] M. Fujita, H. Goka, K. Yamada, and M. Matsuda, Phys. Rev. Lett. **88**, 167008 (2002).
- [282] B. Lake, H. M. Ronnow, N. B. Christensen, G. Aeppli, K. Lefmann, D. F. McMorrow, P. Vorderwisch, P. Smeibidl, N. Mangkorntong, T. Sasagawa, et al., Nature **415**, 299 (2002).
- [283] M. R. Norman, M. Randeria, H. Ding, and J. C. Campuzano, Phys. Rev. B **52**, 615 (1995).
- [284] J. Demers and A. Griffin, Can. J. Phys. **49**, 285 (1970).
- [285] A. Griffin and J. Demers, Phys. Rev. B **4**, 2202 (1971).
- [286] L. Libioulle, Y. Houbion, and M. G. J, Rev. Sci. Instrum. **66**, 97 (1995).
- [287] J. Lindahl, T. Takanen, and L. Montelius, J. Vac. Sci. Technol. B **16**, 3077 (1998).